

## Dissertation

# Stress resultant plasticity model and mixed kinematic description in roll forming simulations

carried out for the purpose of obtaining the degree of Doctor technicae  
(Dr. techn.), submitted at TU Wien, Faculty of Mechanical and  
Industrial Engineering

**Emin KOGBAY**

Mat. Nr.: 01325795

under the supervision of

Univ.Prof. Mag. Dr. habil. Yury Vetyukov  
Institute of Mechanics and Mechatronics, E325

Vienna, October 2023

reviewed by

Associate Prof. D.Sc. Alexander Belyaev  
Peter the Great St.Petersburg Polytechnic University  
Polytechnicheskaya St., 29, Saint-Petersburg, Russia  
Associate Prof. Dipl.-Ing.in Dr.in techn. Melanie Todt  
Technische Universität Wien (TU Wien)  
Getreidemarkt 9, 1060 Wien, Austria



I confirm, that going to press of this thesis needs the confirmation of the examination committee.

*Affidavit*

I declare in lieu of oath, that I wrote this thesis and performed the associated research myself, using only literature cited in this volume. I confirm that this work is original and has not been submitted elsewhere for any examination, nor is it currently under consideration for a thesis elsewhere. I acknowledge that the submitted work will be checked using suitable and state-of-the-art means (plagiarism detection software).

Vienna, 05.12.2023

City, date

Signature

## Danksagung

Zunächst gebührt mein tiefster Dank meiner Familie die mich unter jeden Umständen bedingungslos unterstützt und mein Studium erst ermöglicht hat.

Außerdem möchte ich mich herzlich bei den Kolleginnen und Kollegen des Instituts für Mechanik und Mechatronik der TU Wien und vorallem auch des Forschungsbereichs für Mechanik fester Körper, für die gute Zusammenarbeit und das äußerst angenehme Arbeitsklima bedanken. Herrn Univ.Ass. Dipl.-Ing. Dr.techn. Jakob Scheidl möchte ich insbesondere hervorheben und mich bedanken für die reibungslose und stilvolle Zusammenarbeit sowohl in der Forschung als auch in der Lehre.

Abschließend, möchte ich einen ganz besonderen Dank dem Betreuer meiner Dissertation, welcher auch gleichzeitig der Leiter des Forschungsbereichs für Mechanik fester Körper ist, nämlich Herrn Univ.Prof. Mag. Dr. Yury Vetyukov, widmen. Yury Vetyukov, den ich nicht nur aufgrund seiner angenehmen Persönlichkeit und seines Führungsstils sehr schätze, sondern insbesondere auch aufgrund dessen, dass er durch ein enormes Maß an Erfahrung und Fachkompetenz ausgezeichnet ist, hat sich stets Zeit für meine Anliegen und Fragen genommen und mich in bester Weise betreut.

## Contents

<b>1. Introduction and scientific context</b>	<b>1</b>
<b>2. Problem statement and research goals</b>	<b>3</b>
<b>3. Geometrically nonlinear theory of Kirchhoff–Love shells</b>	<b>4</b>
<b>4. Mixed Eulerian–Lagrangian kinematic description of Kirchhoff–Love shells in axial motion</b>	<b>6</b>
<b>5. Frictionless contact with rolls</b>	<b>9</b>
<b>6. Elastoplasticity of Kirchhoff–Love metal shells</b>	<b>11</b>
<b>7. Numerical solution scheme</b>	<b>15</b>
<b>8. Summary of the journal articles</b>	<b>18</b>
<b>9. Scientific impact</b>	<b>20</b>
<b>Paper A</b>	<b>23</b>
<b>Paper B</b>	<b>51</b>
<b>Paper C</b>	<b>73</b>

## Abstract

In this cumulative thesis we develop a shell stress resultant plasticity model. This model is designed for bending dominant applications and as particular use case we choose the roll forming of sheet metals. Although tools to simulate the roll forming process exist, they mainly make use of full continuum models with Lagrangian kinematic description and therefore lack efficiency, which is highly unfavorable for the engineering practice from the point of view of time consumption. Therefore, our motivation is to develop a fully structural shell model in the mixed Eulerian–Lagrangian kinematic scheme, in which both aspects significantly contribute to the efficiency and speed of the simulations. Such model would pose a highly useful addition to the conventional time and labor extensive methods (e.g. experiments) to analyze and optimize the roll forming process.

The ultimately desired model is obtained by incrementally increasing the model complexity in three essential steps. We begin with the linear static plate bending model. For this plate model we find a stress resultant plasticity formulation by exploiting known analytical continuum solutions of simple bending experiments like uniaxial bending. By doing so we identify functions which are meaningful for the structural plasticity formulation and thus obtain a pure stress resultant plasticity formulation. Here we also make use of basic principles like additive decomposition of strain measures and the associated flow rule. No further nonlinearities, such as contact or large deformations, are considered at this stage.

In the second step the previous research is augmented such, that it is applicable for the geometrically nonlinear scheme and also for applications with normal contact with rigid bodies (the roll profiles) by means of the contact penalty approach. Therefore, we now employ a nonlinear shell theory which is in line with the classical Kirchhoff–Love shell theory. For the kinematic description we do not make use of the Lagrangian formulation, but instead apply the mixed Eulerian–Lagrangian kinematic description, which is numerically more efficient for the description of axially moving continua like it is the case for roll forming. Thus, we are able to exploit an axial mesh refinement scheme because the mesh is now fixed in axial direction. Furthermore, we avoid numerical oscillations which are related to the pure Lagrangian kinematic description. The inelastic material behavior is however treated in a continuum plasticity approach by virtue of treating the flow rule in the integration points along the thickness and through-the-thickness integration. This model is validated against reference computations with commercial software Abaqus and also against physical experiments.

In the final step we extend previous research such, that it features a pure stress resultant plasticity formulation in order to avoid the tedious through-the-thickness integration and arrive at a multiple times more efficient simulation model. This stress resultant shell plasticity formulation makes use of the previously developed plate stress resultant plasticity model and extends it such, that membrane forces also enter the elastic-plastic constitutive laws. The obtained yield criterion can also be thought as an extension of the widely known Ilyushin and Crisfield yield criterions. We validate and compare the obtained results against various other models and conclude that the newly proposed model is advantageous from the point of view of efficiency and robustness of time integration.

## Kurzfassung

In dieser kumulativen Dissertation entwickeln wir ein anwendungsorientiertes und strukturmechanisches Schalenplastizitätsmodell für biegedominante Anwendungen. Als besonderen Anwendungsfall wählen wir das Rollformen (Walzprofilieren) von Blechen. Obwohl es Werkzeuge zur Simulation des Rollformprozesses gibt, basieren diese hauptsächlich auf Kontinuumsmodellen mit Lagrangescher Beschreibung der Kinematik und sind daher sehr ineffizient, was für die Ingenieurspraxis aus wirtschaftlicher Sicht höchst ungünstig ist. Durch diese Aspekte motivieren wir die Entwicklung eines strukturmechanischen Schalenmodells, welches außerdem auf der gemischt Euler-Lagrangeschen Kinematik basiert. Beide Maßnahmen führen zur merklichen Steigerung der Effizienz und zur Reduktion der Rechenzeit. Ein solches Modell würde sich daher als äußerst nützliche Ergänzung zur Analyse und Optimierung des ansonsten sehr arbeits- und zeitintensiven (Aufbau, Experimente, etc.) Rollformprozesses erweisen.

Das letztendlich gewünschte Modell wird durch schrittweise Erhöhung der Modellkomplexität erhalten, welche in drei wesentlichen Schritten passiert. Grundlage und erster Schritt unserer Forschung ist ein Modell zur Simulation der inelastischen Biegung von geometrisch linearen Platten. Für dieses Modell gelingt es uns eine strukturmechanische Formulierung des inelastischen Materialverhaltens, basierend auf analytischen Kontinuumslösungen für einfache Biegefälle, zu identifizieren. Hier werden außerdem grundlegende Konzepte wie die additive Dekomposition der Verzerrungsmaße und die assoziierte Fließregel verwendet. Zu diesem Zeitpunkt stellt die einzige Nichtlinearität im Modell das Materialverhalten dar.

Im zweiten Schritt erweitern wir das vorherige Modell einerseits, dass es im geometrisch nichtlinearen Rahmen, das heißt für große Verformungen, anwendbar ist und andererseits durch Implementierung von reibungsfreiem Normalkontakt mit ideal starren Körpern (Rollen) mittels des Penaltyverfahrens. Es wird nun eine nichtlineare Schalentheorie, welche konform mit der klassischen Kirchhoff-Love Schalentheorie ist, zugrunde gelegt. Anstatt der Lagrangeschen Beschreibung der Kinematik wird außerdem die gemischt Euler-Lagrangesche Betrachtungsweise gewählt, welche für axial bewegliche Strukturen, wie es im Rollformen der Fall ist, vorteilhaft ist. Dadurch sind wir auch in der Lage eine adaptive Netzverfeinerung in axialer Richtung auszunutzen, weil das Netz axial unbeweglich ist und außerdem vermeiden wir numerisch induzierte Oszillationen welche im Falle der Lagrangeschen Betrachtungsweise auftreten würden. Das inelastische Materialverhalten wird zum jetzigen Zeitpunkt durch die klassische kontinuumsmechanische Methodik durch Einführung von Integrationspunkten über die Dicke der Schale aufgelöst. Dieses Modell wird dann gegenüber Referenzlösungen welche mit der kommerziellen Software Abaqus generiert werden und durch physikalische Experimente validiert.

Im finalen Schritt erweitern wir das Modell dahingehend, dass das inelastische Materialverhalten nun strukturmechanisch, das heißt durch die Spannungsresultanten der Schale beschrieben wird. Dadurch ersparen wir uns die sehr ineffiziente Dickenintegration, welche in der kontinuumsmechanischen Plastizitätsmodellierung durchzuführen ist. Das so entwickelte Schalenplastizitätsmodell basiert auf dem zuvor entwickelten Plat-

tenplastizitätsmodell, allerdings erweitert auf den geometrisch nichtlinearen Fall, also unter Berücksichtigung der Kopplung der Membrankräfte in den Materialgleichungen. Die gefundene Fließfunktion kann auch als Erweiterung der weit bekannten Fließfunktionen von Ilyushin und Crisfield angesehen werden. Letztendlich validieren wir und vergleichen das Modell gegenüber diversen anderen Plastizitätsmodellen und stellen fest, dass es für das Rollformen aufgrund der gesteigerten Effizienz und der Robustheit der Zeitintegration von Vorteil ist.



## List of Figures

1. Visualization of roll forming simulation: As it passes through a single roll stand, the flat sheet is bent into a symmetric V-shaped profile. At  $x = 0$  (clamped edge), material particles enter the control domain with the constant transport rate  $v$ . The bending angle  $\varphi$ , at the opposite free end  $x = L$  of the domain, is used as post-processing variable . . . . . 3
2. Mixed Eulerian–Lagrangian kinematic description of the deformation of the metal sheet, featuring the three different configurations and the multiplicative decomposition of the deformation gradient tensor  $\mathbf{F}$  . . . . . 7
3. Visualization of the contact parameters, with:  $\gamma$  being the current penetration depth at an integration point and  $\mathbf{e}_\gamma$  being the surface normal vector. The roll geometry is described by the radial profile  $R(y)$ . . . . . 10
4. Algorithmic visualization of the quasistatic time-stepping procedure, which follows a two-step solution in each time increment by first invoking the return-mapping scheme and then concluding by the convective update . . 16

*License remarks:* Figures Fig. 1, Fig. 2, Fig. 3 and Fig. 4 are taken from *Paper B: Thin-Walled Structures*; <https://doi.org/10.1016/j.tws.2023.110662>

© 2023 the Authors, published as an open access article by Elsevier Ltd. under the creative commons license CC BY, see <https://creativecommons.org/licenses/by/4.0/>



## 1. Introduction and scientific context

Roll forming is an industrial forming process, which allows the highly economical production of various steel sections (profiles) in high quantity and quality. Here a coiled steel sheet is uncoiled and fed through a roll forming line – a sequence of roll stands, which are typically made up of upper and lower profiled rolls that constitute a roll gap. In each roll stand the axially moving and initially flat, thin sheet metal is receiving an incremental elastic-plastic bending deformation, which is kinematically imposed by the roll shapes such, that in the end the desired profile is obtained. It is important to note that this process must not be confused with rolling, as the deformation is bending dominant and the thickness of the metal sheet does not change significantly [1]. Within this cumulative thesis a non-material shell finite element model, featuring a novel description of inelastic behavior of the sheet at the level of structural mechanics, is developed to simulate the roll forming process.

State-of-the-art simulations for roll forming, typically make use of continuum elements in a Lagrangian kinematic framework, see [2, 3]. The same approach is also implemented in the commercial software *COPRA FEA RF*<sup>1</sup>, which possesses a leadership role for roll forming simulations, see [4] for an application. For use cases with axially moving continua the Lagrangian kinematic description is however computationally inefficient due to the motion of the finite elements and problems associated with that, e.g. mesh refinement. Furthermore, it gives cause to numerical oscillations, due to material particles entering or leaving the contact zones repeatedly, see [5].

In order to remediate these drawbacks associated with the Lagrangian kinematic description, the traditional Arbitrary Lagrangian Eulerian (ALE) formalism is used in problems of axially moving continua, see e.g. [6] for application in roll forming. The two-step solution scheme is comprised by a Lagrangian step, which is succeeded by a Eulerian step, within a single time increment [7]. The latter step is used to transport all mechanical fields, including material density and stresses to a new mesh. Therefore, the approach becomes complicated and the risk of accuracy loss during the time integration is elevated. In the present cumulative thesis we introduce a computational scheme for the roll forming process with three novel features:

1. The mixed Eulerian–Lagrangian (MEL) kinematic description [8–10], representing a sub-class of the ALE methods, exploits a special variable transformation and thus makes it possible to only transport the inelastic (plastic) variables instead of all the mechanical fields during the Eulerian step of a time increment. The finite element mesh does not move in axial direction and may be refined in the vicinity of the roll stands. Therefore, the accuracy of the time integration is improved and the model complexity is reduced.
2. The discretization of the sheet metal in form of a nonlinear Kirchhoff–Love shell finite element model, in which the number of degrees of freedom is reduced and the

---

<sup>1</sup><https://www.datam.de/en/products/software-division/fea-simulation>

treatment of the elastoplastic constitutive laws becomes more efficient in comparison to a full 3D volumetric analysis.

3. The application specific shell stress resultant plasticity model for bending dominated problems, which avoids the usually employed numerically expensive treatment of plasticity on the continuum level by the introduction of integration points through the thickness of the shell, hence the computational efficiency is further increased here.

The metal sheet is modeled as a nonlinear Kirchhoff–Love shell (material surface) in the spirit of the direct approach, see [11, 12]. The mesh of the numerical model is regular and consists of rectangular  $C^1$  continuous four-node shell finite elements. These elements represent an extension of the known Bogner-Fox-Schmit plate finite elements with bi-cubic Hermitian shape functions [11, 13]. The transient simulation comprises a sequence of statically and plastically admissible equilibrium states; inertia effects are negligible due to the typically slow transport rates in roll forming. Hence, the simulation procedure follows a quasistatic time-stepping scheme; in each time increment first the minimization of the total potential energy is carried out and then the convective transport of plastic variables along the streamlines of material flow concludes the time increment.

Regarding the contact interactions at the roll stands, we assume that the rolls are rigid and that the contact is frictionless. Due to the lack of information on the elastic stiffness of the roll stands and on the frictional conditions in the roll gaps, these simplifying assumptions are the usually adapted ones in the open literature, see [14, 15]. The contact interaction is implemented by the penalty regularization method and resolved in the integration points of the finite elements.

Elastic-plastic behavior of structures, such as plates and shells, is a challenging topic and various research articles regarding that can be found in the open literature, see [16–18]. Generally the continuum plasticity approach (through-the-thickness integration approach), which evaluates the well-established relations of plane stress elastoplasticity in chosen integration points through the thickness, is employed, see again [18]. And although this approach accurately resolves the 3D plastic state, it is disadvantageous because it comes at a significant computational cost. In order to mitigate this drawback, the so-called stress resultant plasticity models were developed, see [16, 19–22]. In these models the yield criterion as well as the elastoplastic constitutive laws are formulated purely on the structural level, by means of stress resultants and further state variables. Several approaches exist in the open literature and many make use of the classical Ilyushin yield criterion [19], which corresponds to the plane stress von Mises yield criterion. As this yield criterion can only distinguish between an elastic or fully plastic through-the-thickness element and is unable to capture the gradual spreading of plastic zones along the thickness during bending, Crisfield [16] augmented it with a pseudo-hardening variable. Similarly, we develop our own shell stress resultant plasticity model, aimed at bending dominant applications, by the introduction of an isotropic hardening function in the yield criterion, which essentially determines the growth of the yield surface. This function is identified by continuum reference solutions for simple cases such as uniaxial bending. We developed

the stress resultant plasticity model first for linear plate bending and then extended it to the case of nonlinear shell bending by augmenting it accordingly such that the yield criterion and the constitutive laws also account for membrane forces and the coupling. It should be noted that the actual production lines are designed such, that the membrane forces remain possibly low to avoid extensive irreversible stretching of the sheet, which may otherwise result into the buckling of the ready product. Nevertheless, experience shows that the membrane forces still need to be taken into account in the flow rule of the structural model to achieve better correspondence to the 3D simulations and physical experiments.

Finally, various roll forming simulations with different models were carried out and compared against each other, which lead to the conclusion that the newly proposed stress resultant plasticity model produces convincing results at significantly reduced computation times.

## 2. Problem statement and research goals

Within this cumulative thesis, the conducted research focuses on the development of an efficient simulation tool for roll forming simulations, see Fig. 1 for an illustration of the simulation with one roll stand. The motivation is rooted in the engineering practice of roll

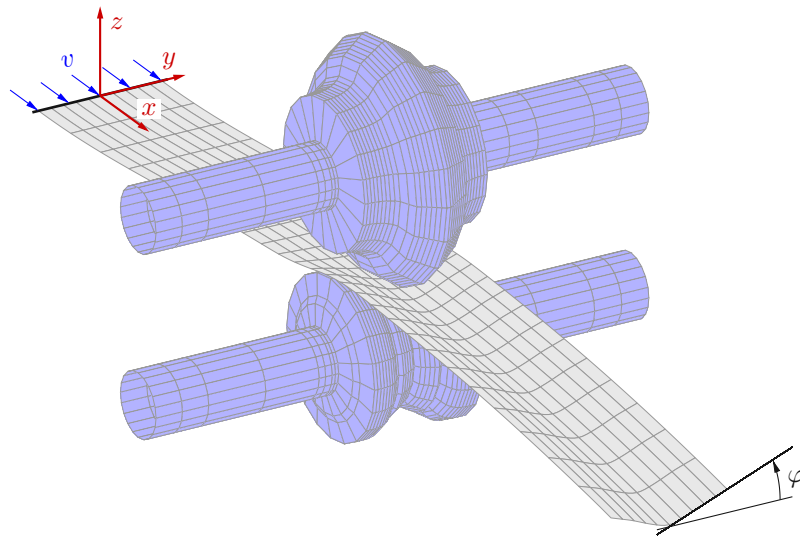


Figure 1: Visualization of roll forming simulation: As it passes through a single roll stand, the flat sheet is bent into a symmetric V-shaped profile. At  $x = 0$  (clamped edge), material particles enter the control domain with the constant transport rate  $v$ . The bending angle  $\varphi$ , at the opposite free end  $x = L$  of the domain, is used as post-processing variable

forming, as currently the setup and control of the process mainly rely on experiments and

the experience of the operator of the roll forming line and therefore an efficient simulation tool is highly desirable. The scientific novelties and highlights of the carried out research may be summarized as:

- The development of a novel (geometrically linear) plate bending stress resultant plasticity model for bending dominant applications, see *Paper A*.
- The extension of that model to the geometrically nonlinear setting and augmentation to problems with frictionless contact, see *Paper B*.
- The implementation of a finite element scheme for roll forming in the mixed Eulerian–Lagrangian kinematic (MEL) framework, see *Paper B*.
- The development of a shell stress resultant plasticity model for bending dominant applications, by appropriate extension of the previous research regarding the plate model, see *Paper C*.

In the following sections we will methodically outline the fundamentals of this thesis by briefly presenting the necessary theoretical background. Although we employ global Cartesian coordinates  $x$ ,  $y$  and  $z$  (see Fig. 1) for the mathematical description of this special application oriented theory, the underlying general physical theory must be indifferent to the chosen type of coordinates. Thus, wherever it is deemed to be purposeful and feasible, the mathematical equations are presented in a concise, general and coordinate invariant form utilizing the notation of the direct tensor calculus, see e.g. [23], which is conventional in the theory of elasticity or in structural mechanics.

In Sect. 3 we address the nonlinear Kirchhoff–Love shell theory in the material (Lagrangian) description, which is commonly used in this form in solid mechanics. Then we proceed with Sect. 4 where the particular form of the MEL kinematic description shall be presented, which is specifically designed for roll forming simulations. We carry on with a brief discussion of the treatment of frictionless contact with rigid rolls in Sect. 5. Furthermore, in Sect. 6 the theory regarding Kirchhoff–Love metal shells in the elastic-plastic regime is discussed. Finally, a brief discussion about the underlying numerical solution strategy and finite element scheme takes place in Sect. 7. In total, three publications (scientific papers) comprise the thesis, see Sect. 8 for a brief summary of the papers and the contribution of the author of this dissertation.

### 3. Geometrically nonlinear theory of Kirchhoff–Love shells

Here, we briefly recapitulate the essentials of the traditional nonlinear Kirchhoff–Love shell theory, according to *Paper C*. The shell is viewed as a material surface in the framework of the direct approach, we refer to [12, 24] for the derivation of the governing equations.

The Lagrangian kinematics of the Kirchhoff–Love shell is defined as a mapping between the reference (undeformed) configuration of the material surface and its actual (deformed) configuration:  $\mathbf{r}(\hat{\mathbf{r}})$ . Here,  $\hat{\mathbf{r}}$  and  $\mathbf{r}$  correspond to the position vectors and are used to

identify material particles for the reference and the actual state, respectively. Hence, two corresponding differential operators  $\overset{\circ}{\nabla}$  and  $\nabla$  may be defined with the help of the total differential of a field quantity  $\phi$  (which can be of arbitrary tensor rank) on the surface:

$$d\phi = d\overset{\circ}{\mathbf{r}} \cdot \overset{\circ}{\nabla}\phi = d\mathbf{r} \cdot \nabla\phi. \quad (1)$$

The material surface is typically parametrized by two material (Lagrangian) coordinates, hence the planar operators of (1) implicitly contain the derivatives with respect to those coordinates. The first metric tensors are then found as the gradients of  $\overset{\circ}{\mathbf{r}}$  and  $\mathbf{r}$ :

$$\overset{\circ}{\mathbf{a}} = \overset{\circ}{\nabla}\overset{\circ}{\mathbf{r}}, \quad \mathbf{a} = \nabla\mathbf{r}, \quad (2)$$

which correspond to the in-plane metric and whose components define lengths and angles of the surface in the two configurations. Evaluating (1) for  $\phi = \mathbf{r}$ , the deformation gradient tensor  $\mathbf{F}$ , which provides a mapping between the differential line elements, is identified:

$$d\mathbf{r} = \mathbf{F} \cdot d\overset{\circ}{\mathbf{r}}, \quad \mathbf{F} = \overset{\circ}{\nabla}\mathbf{r}^T. \quad (3)$$

The gradient (rate of change) of the unit normal vector to the deformed surface  $\mathbf{n}$  defines the bending deformation from a planar reference state in terms of the classical (unsharable) Kirchhoff–Love theory and is expressed by the second metric tensor  $\mathbf{b}$ :

$$\mathbf{b} = -\nabla\mathbf{n}, \quad (4)$$

where  $\mathbf{n}$  is orthogonal to the tangent plane  $\mathbf{a} \cdot \mathbf{n} = 0$ . Using the principle of virtual work one may show, that the internal forces and moments in the shell are work conjugate to the changes of the components of both metric tensors from the reference state to the actual one. This allows to identify the appropriate strain measures, namely the membrane strain tensor  $\mathbf{E}$  and the bending strain tensor  $\mathbf{K}$ . Their invariant forms read:

$$\mathbf{E} = \frac{1}{2} \left( \mathbf{F}^T \cdot \mathbf{F} - \overset{\circ}{\mathbf{a}} \right), \quad \mathbf{K} = \mathbf{F}^T \cdot \mathbf{b} \cdot \mathbf{F}, \quad (5)$$

where a plane reference configuration is assumed in the definition of the curvature tensor  $\mathbf{K}$ . If the reference configuration in fact would be a curved one, the second metric tensor of the undeformed state  $\overset{\circ}{\mathbf{b}} = -\overset{\circ}{\nabla}\overset{\circ}{\mathbf{n}}$  would not vanish and (5) must be complemented accordingly.

Since we aim to exploit a variational formalism within the framework of the finite element analysis, see Sect. 7, we omit the discussion of the strong form of the equilibrium equations and boundary conditions (see [24] for a detailed presentation), which are equivalent to the variational problem statement and proceed directly to the constitutive equations of the shell. The strain energy density (per unit reference area) of the elastic and isotropic shell may be stated as a quadratic form in the elastic strain measures:

$$U = \frac{1}{2} \left( A_1 (\text{tr}\mathbf{E})^2 + A_2 \mathbf{E} \cdot \mathbf{E} + D_1 (\text{tr}\mathbf{K})^2 + D_2 \mathbf{K} \cdot \mathbf{K} \right), \quad (6)$$

in which  $A_\alpha$  and  $D_\alpha$  are the usual elastic stiffness coefficients, see [24]. Strictly speaking, the quadratic form confines the here adopted theory to small local strains (small strain assumption), otherwise the strain energy density must be complemented by higher order terms, see again [24]. We remark, however, that the theory is nevertheless suited and applicable in the geometrically nonlinear setting, as the small strain assumption does not preclude large overall deformations. Finally, the shell stress resultants, in the form of membrane forces  $\mathbf{N}$  and bending moments  $\mathbf{M}$ , follow as partial derivatives of the strain energy density:

$$\mathbf{N} = \frac{\partial U}{\partial \mathbf{E}} = A_1 \hat{\mathbf{a}} \text{tr} \mathbf{E} + A_2 \mathbf{E}, \quad \mathbf{M} = \frac{\partial U}{\partial \mathbf{K}} = D_1 \hat{\mathbf{a}} \text{tr} \mathbf{K} + D_2 \mathbf{K}. \quad (7)$$

#### 4. Mixed Eulerian–Lagrangian kinematic description of Kirchhoff–Love shells in axial motion

In problems that treat continua, which are in axial motion (e.g. metal sheet in roll forming mill), one is often only interested in what happens in a certain bounded and spatially fixed control domain and does not need nor wish to track the motion of every material particle in the classical sense. For such purposes, instead of the Lagrangian kinematic formalism (see Sect. 3 and [12, 25]) the MEL kinematic formulation has been proposed in [8]. Here we outline the essentials of the very same non-material kinematic description and refer to *Paper B* and *Paper C*. We consider the special case of a planar and infinitely long rectangular reference configuration, which corresponds to the initially flat metal sheet and use global spatial Cartesian coordinates  $x, y$  and  $z$  with corresponding orthonormal basis vectors  $\mathbf{i}, \mathbf{j}$ , and  $\mathbf{k}$ . Instead of having a direct mapping from reference configuration to the actual configuration, the idea here is to isolate the axial motion by the introduction of another configuration, namely the intermediate one, see Fig. 2. Thus, the intermediate configuration is a spatially fixed domain with the spatial coordinate  $0 \leq x \leq L$  in which  $L$  is the length of the domain and the material coordinate  $-w/2 \leq \hat{y} \leq w/2$ , with  $w$  being the width of the planar and rectangular intermediate state (width of the sheet metal). Speaking in terms of the finite element method, this would translate to the fact that if we discretize the metal sheet in the intermediate state, then the nodes of the finite element mesh will not move in the axial direction, but will follow the deformation of the structure in the lateral (horizontal) and the transverse (vertical) directions. This means, that we now indeed employ a mixed kinematic description with the axial coordinate  $x$  as the Eulerian one, whereas the other coordinates  $y$  and  $z$  remain Lagrangian.

We proceed with the mathematical formulation of the previously verbally outlaid idea; the material particles in the infinitely long reference configuration are identified by their material coordinates  $\hat{x}$  and  $\hat{y}$ :

$$\hat{\mathbf{r}} = \hat{x} \mathbf{i} + \hat{y} \mathbf{j}, \quad -w/2 \leq \hat{y} \leq w/2. \quad (8)$$

The spatially fixed intermediate configuration, which occupies a planar rectangular domain,



is described by:

$$\tilde{\mathbf{r}} = \tilde{x}\mathbf{i} + \tilde{y}\mathbf{j}, \quad 0 \leq \tilde{x} \leq L, \quad -w/2 \leq \tilde{y} \leq w/2. \quad (9)$$

As active material volume we denote the material particles that currently reside in the control domain  $0 \leq x \leq L$ . It is apparent that the active material volume changes during the process, as material particles keep entering and leaving the control domain due to the axial motion. The entire deformation is now decomposed into two steps, see Fig. 2. First, to arrive at the intermediate state from the reference state, the axial displacement

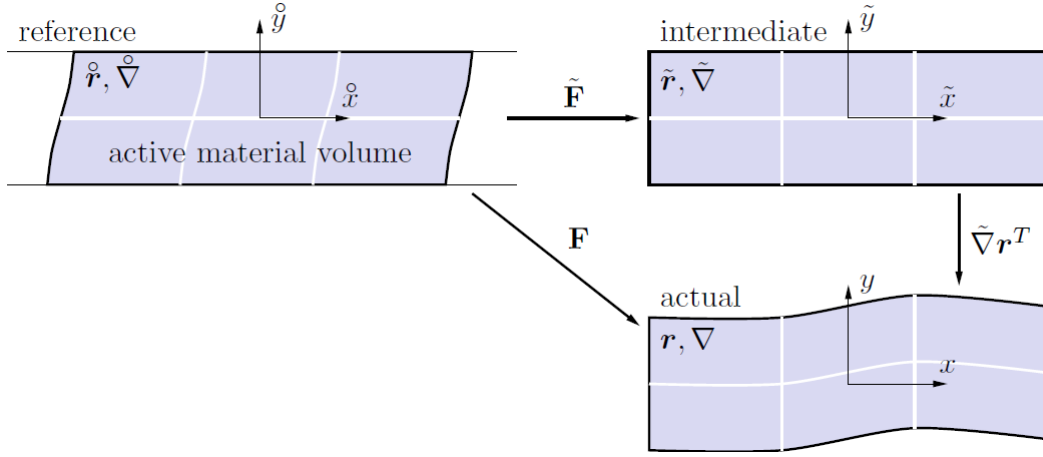


Figure 2: Mixed Eulerian–Lagrangian kinematic description of the deformation of the metal sheet, featuring the three different configurations and the multiplicative decomposition of the deformation gradient tensor  $\mathbf{F}$

$u_x$  must be taken into account,

$$\tilde{\mathbf{r}} = \hat{\mathbf{r}} + u_x \mathbf{i}, \quad \tilde{x} = \hat{x} + u_x, \quad \tilde{y} = \hat{y}. \quad (10)$$

Secondly, we need to amend for the two additional displacement components, which then lead to the actual state with in-plane deformations and bending:

$$\mathbf{r} = \tilde{\mathbf{r}} + u_y \mathbf{j} + u_z \mathbf{k}, \quad x = \tilde{x}, \quad y = \tilde{y} + u_y, \quad z = u_z. \quad (11)$$

With the finite element implementation in mind (see Sect. 7), the aim of the MEL-description is that all mechanical fields are considered as functions of the coordinates in the intermediate configuration; the mapping from the reference configuration to the actual state is defined implicitly as

$$\hat{\mathbf{r}} = \hat{\mathbf{r}}(\tilde{\mathbf{r}}), \quad \mathbf{r} = \mathbf{r}(\tilde{\mathbf{r}}). \quad (12)$$

The displacement vector and its Cartesian components

$$\mathbf{u}(x, \overset{\circ}{y}, t) = u_x(x, \overset{\circ}{y}, t)\mathbf{i} + u_y(x, \overset{\circ}{y}, t)\mathbf{j} + u_z(x, \overset{\circ}{y}, t)\mathbf{k} \quad (13)$$

act as primary unknowns.

By adapting this mixed parametrization we essentially gain the ability of a spatial resolution of the deformations imposed by the roll stands at given  $x$ -positions. This translates to the fact that material particles are free to travel through the finite element mesh, which is fixed in axial direction. Due to the use of new (mixed) coordinates a corresponding transformation of the basic kinematic relations is necessary. In particular, the material differential operator needs to be reformulated in terms of the partial derivatives with respect to  $x$  and  $\overset{\circ}{y}$ :

$$\overset{\circ}{\nabla} = \mathbf{i}(1 - \partial_x u_x)^{-1} \partial_x + \mathbf{j} \partial_{\overset{\circ}{y}}, \quad (14)$$

such that  $\overset{\circ}{\nabla} \overset{\circ}{r}$  with  $\overset{\circ}{x} = x - u_x$  still yields the planar unit tensor  $\overset{\circ}{\mathbf{a}} = \mathbf{i}\mathbf{i} + \mathbf{j}\mathbf{j}$ . The first coefficient in the brackets represents the derivative of the material coordinate  $\overset{\circ}{x}$  with respect to its Eulerian counterpart  $x$ , this essentially determines the Jacobian and is used to transform the material area integral for the total strain energy:

$$U^\Sigma = \iint U d\overset{\circ}{x} d\overset{\circ}{y} = \int_0^L dx \int_{-w/2}^{w/2} (1 - \partial_x u_x) U d\overset{\circ}{y}. \quad (15)$$

This transformation is necessary, because when speaking in terms of the finite element method again, all the field variables and also the strain energy density are functions of the coordinates of the intermediate configuration. The unknowns then constitute to the nodal variables of a single four-node rectangular finite element, which resides in the intermediate configuration. They comprise the displacements, their first derivatives and the mixed second derivative with respect to the local finite element coordinates. This choice of nodal degrees of freedom paired up with bi-cubic polynomial shape functions guarantees a  $C^1$  continuous approximation of the position vector, which is the requirement of the underlying shell theory.

Before we conclude this section, we need to address the Eulerian step within each time increment, which succeeds the Lagrangian step and in which the plastic variables are transported. This is necessary because the plastic variables are strictly attached to the material particles, which in turn are in axial motion. Thus, the plastic states that are stored in the axially fixed integration points must be updated accordingly. The total (material) time derivative of a plastic variable (plastic strains and hardening variables)  $\mathbf{p}$  reads:

$$\dot{\mathbf{p}} = \partial_x \mathbf{p} \dot{u}_x + \partial_t \mathbf{p}, \quad (16)$$

where  $\dot{\mathbf{p}}$  denotes the time rate of  $\mathbf{p}$ , which is registered at a moving material particle; it consists of a local change  $\partial_t \mathbf{p}$  at  $\{x, \overset{\circ}{y}\}$  and a convective transport term. Since (16) is the material derivative of any variable, regardless of what is substituted for  $\mathbf{p}$ , we set  $\mathbf{p} = u_x$  and rearrange (16) to find  $\dot{u}_x = v(1 - \partial_x u_x)^{-1}$ . Here,  $v$  is defined as the constant axial

material transport rate  $v = \partial_t u_x$ . We remark that stating  $v = \partial_t u_x = \text{const.}$  is slightly inaccurate during the transient phase of the simulation. Nevertheless, we accept  $v$  as a constant model parameter and justify the approach by the fact that we are only interested in the steady-state solution where the assumption is justified. The advection problem (16) can now be reformulated as:

$$\partial_t \mathbf{p} = \dot{\mathbf{p}} - v(1 - \partial_x u_x)^{-1} \partial_x \mathbf{p}. \quad (17)$$

In order to solve the advection equation, a forward in time and backwards in space finite difference method is used for the incremental time integration of this equation, which mathematically represents the Eulerian step of the current time increment in the solution scheme, see Sect. 7.

## 5. Frictionless contact with rolls

For the contact treatment and algorithm, we refer to *Paper B*. The penalty regularization method is used to account for frictionless contact, the contact potential reads:

$$V^\Sigma = \int_0^L dx \int_{-w/2}^{w/2} (1 - \partial_x u_x) V d\hat{y}, \quad (18)$$

where  $V$  is the contact potential per unit reference area and is accepted as a quadratic form in the penetration depth  $\gamma$ :

$$V = \frac{1}{2} P \gamma^2. \quad (19)$$

$P$  denotes the contact penalty and essentially penalizes any penetration  $\gamma$  of the deformable solid (shell) into the rigid counterpart (rolls); for the limiting case of  $P \rightarrow \infty$ , the impenetrability condition is exactly fulfilled. We note that the integral of (18) is in principle of the same form as the one of the total strain energy (15); the material area integral has been transformed in the same manner, by the use of the Jacobian, see Sect. 4.

The  $3 \times 3$  Gaussian quadrature rule is used for the numerical integration of (18). For that purpose the contact kinematics at each integration point must be resolved, see Fig. 3, for an illustration. The penetration depth  $\gamma$  is essentially defined by the difference of the profile radius  $R(y)$  and the radial distance  $|\mathbf{d}|$  of the current integration point. Projecting this difference in direction of the normal vector to the roll surface  $\mathbf{e}_\gamma$ , we obtain:

$$\gamma = \max \left\{ 0, \frac{R(y) - |\mathbf{d}|}{\sqrt{1 + R'(y)^2}} \right\}, \quad \mathbf{d} = \mathbf{r} - \mathbf{r}_0 - \mathbf{r} \cdot \mathbf{j} \mathbf{j}, \quad (20)$$

in which  $\mathbf{r}$  and  $\mathbf{r}_0$  denote the position vector (11) and the vector to the center of the roll axis at  $y = 0$ , respectively. The factor with the square root ensures that the difference  $R(y) - |\mathbf{d}|$  is projected in normal direction  $\mathbf{e}_\gamma$  and thus amounts to the cosine of the inclination angle of the roll profile  $R(y)$ .  $\gamma$  is simply set to zero if there is no penetration,

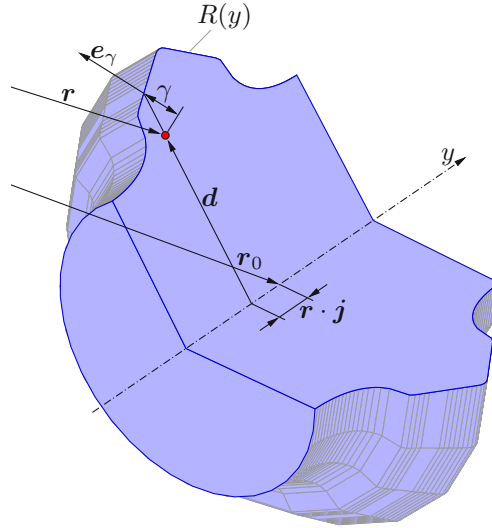


Figure 3: Visualization of the contact parameters, with:  $\gamma$  being the current penetration depth at an integration point and  $\mathbf{e}_\gamma$  being the surface normal vector. The roll geometry is described by the radial profile  $R(y)$ .

which prevents the occurrence of non-vanishing contact forces in the event of no contact. Upon established contact, the variation of  $\gamma$  is computed by the virtual displacement in direction of the normal vector  $\mathbf{e}_\gamma$ :

$$\delta\gamma = -\mathbf{e}_\gamma \cdot \delta\mathbf{r} = -\mathbf{e}_\gamma \cdot (\delta u_y \mathbf{j} + \delta u_z \mathbf{k}), \quad \mathbf{e}_\gamma = \frac{(\mathbf{d}/|\mathbf{d}| - R'(y)\mathbf{j})}{|\mathbf{d}/|\mathbf{d}| - R'(y)\mathbf{j}|}, \quad (21)$$

which does not contain a variation of the axial displacement  $u_x$  owing to the mixed kinematic description, as the integration points are axially fixed.

Since the rolls are axisymmetric bodies of revolution, their geometry can be fully defined and implemented by means of discretizing their radial profile  $R(y)$  as a sequence of cubic polynomials:

$$R(y) = p_i(y), \quad y_i \leq y < y_{i+1}. \quad (22)$$

At their boundaries these polynomials fulfill continuity conditions

$$\{p_i(y_i), p_i'(y_i), p_i(y_{i+1}), p_i'(y_{i+1})\} = \{R_i, R_i', R_{i+1}, R_{i+1}'\}. \quad (23)$$

For simplicity sake, the radii and inclinations  $R_i$  and  $R_i'$  are defined on an equidistant grid

$$y_i = -l/2 + i \Delta y, \quad \Delta y = \frac{l}{N}, \quad 0 \leq i \leq N, \quad (24)$$

in which  $l$  and  $N$  are the length of the roll axis and the total number of cubic polynomials,

respectively.

## 6. Elastoplasticity of Kirchhoff–Love metal shells

In this section we briefly address the elastoplastic behavior of metal shells at bending. For brevity sake and as this is not something essential for the applicability of the presented theory (however, still essential for the process and simulation of roll forming) we omit the consideration of material hardening and view elastic-ideal plastic material behavior. Material hardening, see [26] for common strain hardening models, can however be easily included within the presented theory, we refer to *Paper A* and *Paper B* for an elaborate view. In the literature generally there are two different ways of treating elastoplastic bending of shells:

1. The predominant and established continuum plasticity with the through-the-thickness integration approach, for applications see [17, 18, 27].
2. The more efficient but in general still immature and therefore less common stress resultant plasticity approaches, for applications see [21, 22, 28].

Within this cumulative thesis we gradually developed a novel shell plasticity model that belongs to the latter class of the stress resultant plasticity approaches; we will discuss it below, after the classical continuum plasticity approach is introduced as it is essential for the theoretical foundation.

We start by discussing the first approach. In terms of the continuum plasticity with the through-the-thickness integration approach, the shell is considered a continuum with non-vanishing thickness, that however still obeys the structural kinematics of a Kirchhoff–Love shell. By doing so, it is possible to accurately resolve the elastic-plastic rate equations on the continuum level. The in-plane part of the strain tensor of the 3D body  $\boldsymbol{\varepsilon}_\perp$  is, according to the Kirchhoff kinematic hypothesis, a linear function of the material thickness coordinate  $\zeta$ :

$$\boldsymbol{\varepsilon}_\perp = \mathbf{E} - \zeta \mathbf{K}. \quad (25)$$

The small strain assumption allows us to additively decompose the total strains in elastic and plastic parts:

$$\boldsymbol{\varepsilon}_\perp = \boldsymbol{\varepsilon}_\perp^e + \boldsymbol{\varepsilon}_\perp^p. \quad (26)$$

We already made use of this assumption above by stating the strain energy density in its quadratic form, see (6), of Sect. 3. Here, this implies that the membrane strains  $\mathbf{E}$  must remain small and the bending strains  $\mathbf{K}$  may be moderate. This however, again does by no means preclude large overall deformations, as the thickness coordinate is confined to vary in the small range  $-h/2 \leq \zeta \leq h/2$  due to the thinness of the shell. For metal plasticity it is common to use the (here for plane stress) von Mises yield criterion, which in an invariant form reads:

$$f_\sigma = \frac{3}{2} \boldsymbol{\sigma} \cdots \boldsymbol{\sigma} - \frac{1}{2} (\text{tr} \boldsymbol{\sigma})^2 \leq k^2. \quad (27)$$

Since we omit material hardening, the yield strength  $k$  remains a constant value, the yield surface does not change. For an elastic state  $f_\sigma < k^2$  holds and plastic flow sets in at  $f_\sigma = k^2$ . The planar stress tensor  $\boldsymbol{\sigma}$  is connected to the elastic part of the planar strain tensor by the elastic law for the plane stress assumption:

$$\boldsymbol{\sigma} = \frac{E}{1+\nu} \boldsymbol{\varepsilon}_\perp^e + \frac{E\nu}{1-\nu^2} \hat{\mathbf{a}} \text{tr} \boldsymbol{\varepsilon}_\perp^e = {}^4\mathbb{C} \cdot \boldsymbol{\varepsilon}_\perp^e, \quad (28)$$

with the elastic modulus  $E$  and the Poisson ratio  $\nu$ . An alternative form of the elastic law features  ${}^4\mathbb{C}$ , the fourth rank plane stress elasticity tensor, that connects elastic strain tensor to stress tensor by means of a double contraction.  ${}^4\mathbb{C}$  can easily be derived from (28) as  ${}^4\mathbb{C} = \frac{\partial \boldsymbol{\sigma}}{\partial \boldsymbol{\varepsilon}_\perp^e}$  and reads:

$$\begin{aligned} {}^4\mathbb{C} &= \frac{E}{2(1+\nu)} (\mathbf{e}_\alpha \mathbf{e}_\beta \mathbf{e}_\alpha \mathbf{e}_\beta + \mathbf{e}_\alpha \mathbf{e}_\beta \mathbf{e}_\beta \mathbf{e}_\alpha) + \frac{E\nu}{1-\nu^2} \mathbf{e}_\alpha \mathbf{e}_\alpha \mathbf{e}_\beta \mathbf{e}_\beta \\ &= \frac{E}{2(1+\nu)} (\mathbf{e}_\alpha \mathbf{e}_\beta \mathbf{e}_\alpha \mathbf{e}_\beta + \mathbf{e}_\alpha \hat{\mathbf{a}} \mathbf{e}_\alpha) + \frac{E\nu}{1-\nu^2} \hat{\mathbf{a}} \hat{\mathbf{a}}, \end{aligned} \quad (29)$$

here  $\alpha$  and  $\beta$  are summation indices with  $\mathbf{e}_1 = \mathbf{i}$  and  $\mathbf{e}_2 = \mathbf{j}$ , hence the planar unit tensor  $\hat{\mathbf{a}}$  can be identified as  $\hat{\mathbf{a}} = \mathbf{e}_\alpha \mathbf{e}_\alpha = \mathbf{e}_\beta \mathbf{e}_\beta = \mathbf{i}\mathbf{i} + \mathbf{j}\mathbf{j}$ , which allows to simplify the expression as shown above. We note the slight inconsistency introduced through (28), as here the Cauchy stresses  $\boldsymbol{\sigma}$  are directly related to the strain measure, although the stress tensor should be expressed on the deformed surface and the strains are referred to the reference one. However, owing to the small strain assumption this subtle distinction is irrelevant; see *Paper B* for a more detailed discussion. We close the system of equations by providing the associated flow rule, which determines the evolution of the plastic strains and is a consequence of the postulate of maximum plastic dissipation, see [29]:

$$\dot{\boldsymbol{\varepsilon}}_\perp^p = \dot{\lambda} \frac{\partial f_\sigma}{\partial \boldsymbol{\sigma}}, \quad \frac{\partial f_\sigma}{\partial \boldsymbol{\sigma}} = 3\boldsymbol{\sigma} - \hat{\mathbf{a}} \text{tr} \boldsymbol{\sigma}. \quad (30)$$

The consistency parameter  $\dot{\lambda}$  is non-negative and either zero (elastic state,  $\dot{\boldsymbol{\varepsilon}}_\perp^p = 0$ ) or positive (elastic-plastic state,  $\dot{\boldsymbol{\varepsilon}}_\perp^p \neq 0$ ). At yield the stress state must remain on the yield surface, which is ensured by the consistency condition  $\dot{f}_\sigma = 0$ . Evaluation of the consistency condition, see e.g [29], yields the stress-strain relation in terms of time rates for elastoplastic states:

$$\dot{\boldsymbol{\sigma}} = \left( {}^4\mathbb{C} - \frac{{}^4\mathbb{C} \cdot \frac{\partial f_\sigma}{\partial \boldsymbol{\sigma}} \frac{\partial f_\sigma}{\partial \boldsymbol{\sigma}} \cdot {}^4\mathbb{C}}{\frac{\partial f_\sigma}{\partial \boldsymbol{\sigma}} \cdot {}^4\mathbb{C} \cdot \frac{\partial f_\sigma}{\partial \boldsymbol{\sigma}}} \right) \cdot \dot{\boldsymbol{\varepsilon}}_\perp. \quad (31)$$

The tensor (term in brackets) that connects strain and stress rates in the elastoplastic regime, is called the fourth rank tangent stiffness tensor and is symmetric due to the use of the associated flow rule, see [30]. Within this continuum plasticity approach, the strain

energy density per unit reference area reads:

$$U = \int_{-h/2}^{h/2} \frac{1}{2} \boldsymbol{\varepsilon}_{\perp}^e \cdot \mathbb{C} \cdot \boldsymbol{\varepsilon}_{\perp}^e d\zeta, \quad \boldsymbol{\varepsilon}_{\perp}^e = \boldsymbol{\varepsilon}_{\perp} - \boldsymbol{\varepsilon}_{\perp}^p. \quad (32)$$

Since the energy density of the shell and also the shell stress resultants  $\mathbf{N}$  and  $\mathbf{M}$  are obtained via a thickness integration (see *Paper B*), this continuum plasticity approach is also referred as the through-the-thickness integration approach. The integration is carried out numerically within the finite element scheme by means of a Gaussian quadrature rule with several points  $\zeta_i$  in thickness direction, see *Paper B*. This rate equation system now fully describes the load history dependent stress and strain state of the shell without material hardening.

We proceed with the discussion on the second method to handle shell plasticity, namely the stress resultant plasticity approaches. Instead of carrying out the computationally demanding time integration of the elastoplastic constitutive equations in multiple points over the thickness, inherent to the continuum plasticity approach discussed above, we propose to treat elastoplasticity directly in the framework of the direct approach featuring the shell as material surface, see *Paper C*. The strain energy density of the shell is then sought as a quadratic form in the elastic parts of the shell strain measures  $\mathbf{E}^e$  and  $\mathbf{K}^e$ , as in (6), which stands in contrast to the definition (32) used in the through-the-thickness integration approach. Similar to (26) the additive decomposition of shell strain measures

$$\mathbf{E} = \mathbf{E}^e + \mathbf{E}^p, \quad \mathbf{K} = \mathbf{K}^e + \mathbf{K}^p \quad (33)$$

is based on the assumption of small local strains. In *Paper A* we derived a plate stress resultant plasticity model for the geometrically linearized framework, where  $\mathbf{N}$  can be neglected and only the bending moments  $\mathbf{M}$  need to be considered. Knowing that this simplification is no longer reasonable in the context of the geometrically nonlinear shell theory we amended the yield criterion accordingly in *Paper C*. In what follows we will provide the governing equations of the theory and refer to *Paper A* and *Paper C*. First we define invariants of the stress resultants as following:

$$\begin{aligned} I_N &= \frac{1}{N_0^2} \left( \frac{3}{2} \mathbf{N} \cdot \mathbf{N} - \frac{1}{2} (\text{tr} \mathbf{N})^2 \right), \\ I_{NM} &= \frac{1}{N_0 M_0} \left( \frac{3}{2} \mathbf{N} \cdot \mathbf{M} - \frac{1}{2} \text{tr} \mathbf{N} \text{tr} \mathbf{M} \right), \\ I_M &= \frac{1}{M_0^2} \left( \frac{3}{2} \mathbf{M} \cdot \mathbf{M} - \frac{1}{2} (\text{tr} \mathbf{M})^2 \right). \end{aligned} \quad (34)$$

The expressions are made dimensionless with the help of the membrane force  $N_0$  and the bending moment  $M_0$  that correspond to first yield under the distinguished load cases of

uniaxial tension and uniaxial bending, respectively:

$$N_0 = kh, \quad M_0 = \frac{kh^2}{6}. \quad (35)$$

After some theoretical considerations (see *Paper C*), we propose the yield criterion of the shell stress resultant plasticity in following form:

$$f = I_N + \frac{1}{\sqrt{3} \frac{k_M(A^P)}{M_0}} |I_{NM}| + \frac{1}{\frac{k_M^2(A^P)}{M_0^2}} I_M - 1, \quad (36)$$

where the isotropic hardening function  $k_M(A^P)$  is identified such, that it reproduces the elastic-plastic response of a plate at pure uni-axial bending:

$$k_M^2(A^P) = -\frac{1}{36} h^3 \left( 3EA^P - 3\sqrt{EA^P} \sqrt{2hk^2 + EA^P} + 2\sqrt{3}hk^2 \arctan \frac{\sqrt{EA^P}}{\sqrt{6hk^2 + 3EA^P}} \right) + \frac{h^4 k^2}{36}, \quad (37)$$

see *Paper A*. Here  $A^P$  is the dissipation work per unit reference area and is essentially used to govern the structural hardening (not to be confused with material hardening, which is independent thereof) effect of the shell, meaning that the gradual spreading of plastic zones along the thickness of the shell can now be accounted for. This implementation in the spirit of work hardening not only captures initial yield ( $k_M^2 = M_0^2$ ,  $A^P = 0$ ) and limit yield ( $k_M^2 = M_L^2$ ,  $A^P \rightarrow \infty$ ) accurately for the case of pure bending, but also straightforwardly enables the account of actual isotropic material hardening by means of augmentation of  $k_M^2(A^P)$ , see *Paper A*. Moreover, the contribution of plastic membrane strains to the strain hardening can be rigorously accounted for in the definition of the dissipation power:

$$\dot{A}^P = \mathbf{N} \cdot \dot{\mathbf{E}}^P + \mathbf{M} \cdot \dot{\mathbf{K}}^P. \quad (38)$$

We proceed with the statement of two equations of the associated flow rules with a single consistency parameter  $\dot{\lambda}$  that govern the evolution of the plastic strain rates:

$$\dot{\mathbf{E}}^P = \dot{\lambda} \frac{\partial F}{\partial \mathbf{N}}, \quad \dot{\mathbf{K}}^P = \dot{\lambda} \frac{\partial F}{\partial \mathbf{M}}, \quad (39)$$

where instead of  $f = 0$  we exploit a modified yield equation of the form  $F(\mathbf{N}, \mathbf{M}) = k_M^2(A^P)$ , which reads:

$$F = \frac{h^4 k^2 \left( |I_{NM}| + \sqrt{12I_M(1 - I_N) + I_{NM}^2} \right)^2}{432(1 - I_N)^2} = k_M^2(A^P). \quad (40)$$

We note that the here defined yield criterion simplifies to the plate stress resultant



plasticity yield criterion of *Paper A* for  $\mathbf{N} = 0$ . Due to the now established separation of yield criterion and effective yield strength, the consistency condition can be evaluated in a straightforward manner:

$$\dot{F} = \frac{\partial F}{\partial \mathbf{N}} \cdot \dot{\mathbf{N}} + \frac{\partial F}{\partial \mathbf{M}} \cdot \dot{\mathbf{M}} = 2k_M k'_M \dot{A}^P, \quad (41)$$

which confines the stress state to the actual yield surface in case of plastic flow. Proceeding, with the dissipation power given in (38), we evaluate the constitutive law (7) in order to relate the rates of the stress and strain resultants:

$$\begin{aligned} \dot{\mathbf{N}} &= A_1 \hat{\mathbf{a}}_{\text{tr}} \dot{\mathbf{E}}^e + A_2 \dot{\mathbf{E}}^e = \frac{\partial \mathbf{N}}{\partial \mathbf{E}^e} \cdot (\dot{\mathbf{E}} - \dot{\mathbf{E}}^P), \\ \dot{\mathbf{M}} &= D_1 \hat{\mathbf{a}}_{\text{tr}} \dot{\mathbf{K}}^e + D_2 \dot{\mathbf{K}}^e = \frac{\partial \mathbf{M}}{\partial \mathbf{K}^e} \cdot (\dot{\mathbf{K}} - \dot{\mathbf{K}}^P), \end{aligned} \quad (42)$$

here the elastic strain rates are replaced according to the additive decomposition (26). We note that in analogy to the elasticity tensor  ${}^4\mathbf{C}$  of the continuum theory of (28), the tensor derivatives of  $\mathbf{N}$  and  $\mathbf{M}$  with respect to the corresponding elastic strain tensors constitute two fourth order tensors. By substituting the rates of the stress resultants (42) as well as the dissipation power (38) written in terms of strain rates, into the flow rules (39), we are able to solve (41) for the consistency parameter:

$$\dot{\lambda} = \frac{\frac{\partial F}{\partial \mathbf{N}} \cdot \frac{\partial \mathbf{N}}{\partial \mathbf{E}^e} \cdot \dot{\mathbf{E}} + \frac{\partial F}{\partial \mathbf{M}} \cdot \frac{\partial \mathbf{M}}{\partial \mathbf{K}^e} \cdot \dot{\mathbf{K}}}{\frac{\partial F}{\partial \mathbf{N}} \cdot \frac{\partial \mathbf{N}}{\partial \mathbf{E}^e} \cdot \frac{\partial F}{\partial \mathbf{N}} + \frac{\partial F}{\partial \mathbf{M}} \cdot \frac{\partial \mathbf{M}}{\partial \mathbf{K}^e} \cdot \frac{\partial F}{\partial \mathbf{M}} + 2k_M k'_M \left( \mathbf{N} \cdot \frac{\partial F}{\partial \mathbf{N}} + \mathbf{M} \cdot \frac{\partial F}{\partial \mathbf{M}} \right)}. \quad (43)$$

Similar to (31), backward substitution in (42) yields the tangential elastic-plastic constitutive law in the framework of the shell stress resultant plasticity theory, which is essential for the numerical implementation of the Newton method featuring tangent stiffness matrix of the finite element model. The coupling of the membrane and bending deformations in the elastoplastic regime, can be noticed by the fact that both of the total strain rates  $\dot{\mathbf{E}}$  and  $\dot{\mathbf{K}}$  contribute to (43). Thus, according to the flow rules of (39), curvature rates will in general give rise to plastic membrane strains even when membrane forces are small and vice versa.

Now the shell stress resultant theory is complete and can be implemented within a numerical solution scheme, which features a return-mapping algorithm in the spirit of *Paper A*, see also Sect. 7 for a brief discussion of the numerical implementation within the framework of the finite element analysis.

## 7. Numerical solution scheme

Here we give a short overview of the implemented numerical solution scheme, that features a finite element model within the mixed Eulerian–Lagrangian framework. The shell is discretized using four-node rectangular finite elements, which reside in the axially

fixed intermediate configuration (see Sect. 4). The nodal degrees of freedom contain the displacements, their first derivatives and the mixed second derivative with respect to the local finite element coordinates. We achieve the necessary  $C^1$  continuous approximation of the position vector by the use of bi-cubic polynomial shape functions. The used kind of element therefore is an extension of the well known Bogner-Fox-Schmit plate element, see [11, 13], adapted to the case of a Kirchhoff–Love shell.

Since we view the whole process as quasistatic, we basically exploit the variational principle of minimum potential energy as a part of the solution scheme within each time increment, see Fig. 4. The total potential energy of the system comprises the sum of the total strain energy (15) and the contact potential (18). In what follows we will highlight the two-step solution procedure, algorithmically depicted in Fig. 4. The variables  $\mathbf{q}$  and

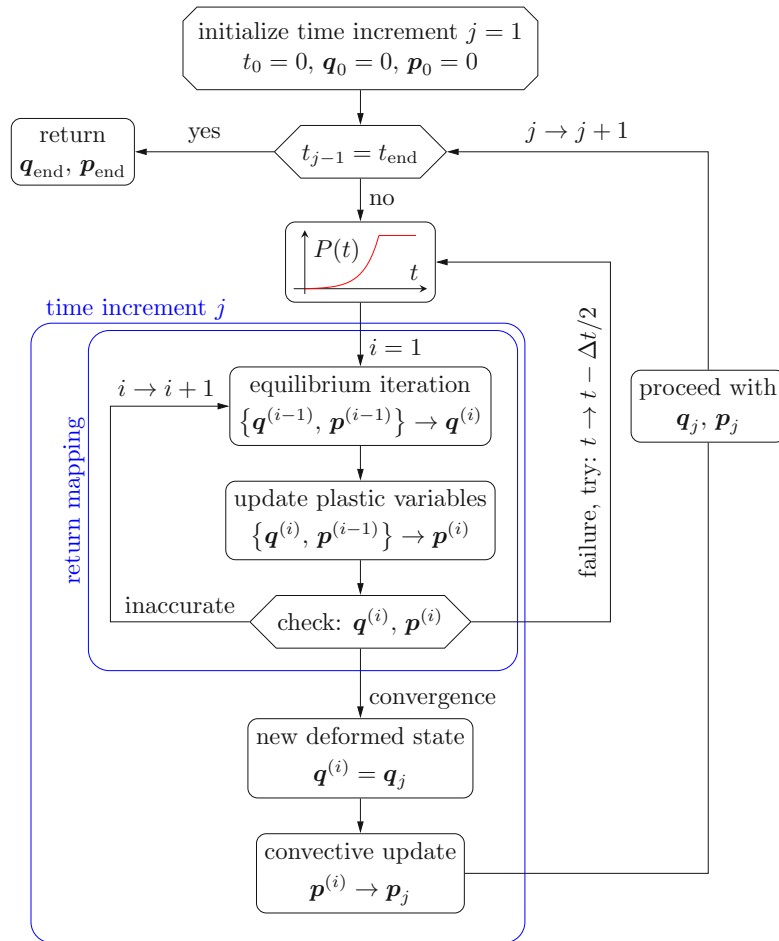


Figure 4: Algorithmic visualization of the quasistatic time-stepping procedure, which follows a two-step solution in each time increment by first invoking the return-mapping scheme and then concluding by the convective update

$\mathbf{p}$  comprise an array of all the nodal degrees of freedom and an array of all the plastic variables (stored in integration points), respectively. The simulation is driven such, that the rolls are in their final position, forming the desired roll gap from the very beginning, while the contact penalty  $P$  is incremented in each time increment until at some time value the desired contact penalty is reached. Therefore, the source of loading is the incrementation of the contact penalty. In the first step of each time increment  $j$  we evoke a return-mapping scheme (see *Paper A* and *Paper B*) in which within a Newton loop first an equilibrium iteration (in which the plastic state is frozen) is carried out and then since the newly obtained nodal state  $\mathbf{q}^{(i)}$  doubtlessly perturbs the previous frozen plastic state, an update of the plastic variables is carried out to obtain new plastic variables  $\mathbf{p}^{(i)}$ , where  $i$  is the iteration index. Then, the newly obtained state  $\{\mathbf{q}^{(i)}, \mathbf{p}^{(i)}\}$  is checked whether it is a converged statically and plastically admissible state in order to determine to proceed with the obtained state or to carry out another iteration. Failure, see Fig. 4, occurs upon divergence or if the plastic flow exceeds a certain threshold value; since we carry out the update of the plastic variables in a linearized manner, the yield surface must not be exceeded by far for this algorithm (which is slightly different than the classical return mapping scheme proposed by [31]) for the sake of accuracy of time integration, see *Paper B* for a detailed discussion. In the second step of each time increment  $j$ , since the material particles travel with an axial transport rate  $v$ , the plastic variables must simply be transported forward by means of a convective update. Therefore, the advection equation, see Sect. 4, is solved to transport the plastic variables according to the axial motion increment  $v\Delta t$ . At this simulation stage there is no active plastic flow and the only "source of loading" is the material motion, meaning that from the perspective of a moving material particle no change of its plastic state is registered; this amounts to  $\dot{\mathbf{p}} = 0$  in (17). The repetition of this two-step sequence in each time increment effectively keeps up the transient simulation. After a sufficient number of time increments, the stationary state is obtained, in which no more changes can be detected within the control domain from the perspective of a spatially fixed observer and the simulation is finished.

## 8. Summary of the journal articles

### Paper A

*Stress resultant plasticity for plate bending in the context of roll forming of sheet metal*

Emin Kocbay, Yury Vetyukov

International Journal for Numerical  
Methods in Engineering  
<https://doi.org/10.1002/nme.6760>

In this first publication, with the aim of roll forming simulations in mind, we develop a novel plate stress resultant plasticity model with isotropic material hardening for the geometrically linear bending of plates, which stands in contrast to the usually applied continuum plasticity with the through-the-thickness integration approach. The derivation features the analytical identification of the isotropic hardening function, by means of comparison against exactly available solutions for a continuum through-the-thickness element for simple load cases like uniaxial bending. With the help of this function and few additional steps, a complete formulation of the plate stress resultant plasticity model is established. The model is first applied in local numerical experiments on a through-the-thickness element and the responses are compared against numerical results of the continuum plasticity approach. The comparison highlights very good correspondence to the latter results. In order to further investigate the model as part of a structural mechanics simulation, we implemented it in a plate finite element scheme and applied it on some static benchmark problems, with mechanical loads. The results of comparison against commercial software as well as against other models from the open literature were convincing and in favor of the newly proposed plate stress resultant plasticity model.

*Emin Kocbay is responsible for:* writing of the original draft; derivation of the model equations, numerical experiments and validation; comparative finite element computations; visualization and presentation of the results.

### Paper B

*Mixed Eulerian–Lagrangian modeling of sheet metal roll forming*

Emin Kocbay, Jakob Scheidl, Fabian Riegler,  
Martin Leonhartsberger, Matthias Lamprecht,  
Yury Vetyukov

Thin-Walled Structures  
<https://doi.org/10.1016/j.tws.2023.110662>

In this second research paper we now take more concrete steps towards the goal of roll forming simulations. This means, that we here extend the previous research of *Paper A* and implement a simulation tool that features the geometrically nonlinear setting within the framework of the mixed Eulerian–Lagrangian kinematic description. Furthermore, we account for the contact interaction with the rigid rolls by means of the penalty regularization method. We propose a quasistatic time-stepping procedure that comprises a two-step solution within each time increment and utilizes the return mapping scheme. Various parameter studies are carried out in order to gain a profound process knowledge and furthermore we achieved to reproduce certain effects that are known to occur in the

engineering practice of roll forming. Regarding the constitutive models; the previous plate stress resultant plasticity model as well as the here (nonlinear case) more appropriate continuum plasticity approach were implemented and tested. We found that the results of the plate stress resultant plasticity model are not sufficiently accurate for the nonlinear case in which membrane forces (albeit small in roll forming) should be introduced to the elastoplastic constitutive equations. Finally, finite element results are validated against commercial software as well as against physical experiments, which were carried out on an industrial roll forming test rig.

*Emin Kocbay is responsible for:* writing of the original draft; development of software, performing simulations, numerical validation and visualization of results.

## Paper C

*An enhanced stress resultant plasticity model for shell structures with application in sheet metal roll forming*

Emin Kocbay, Jakob Scheidl, Fabian Schwarzinger,  
Yury Vetyukov

The International Journal of Advanced  
Manufacturing Technology  
<https://doi.org/10.1007/s00170-023-12544-1>

In this final publication, we build upon *Paper A* and *Paper B* and essentially extend the plate stress resultant plasticity model to a bending dominant application oriented nonlinear Kirchhoff–Love shell stress resultant plasticity model. In doing so, we derive a yield criterion, which resembles the one previously proposed by Crisfield [16], in which membrane forces are introduced. Thus, we obtain a generalization of the yield criterion of *Paper A*. Furthermore, instead of using the hardening variable that Crisfield came up with, we use the isotropic hardening function of *Paper A*. Subsequently we apply the model in numerical experiments on a through-the-thickness element. The comparison of the results between our model, the model of *Paper A*, the continuum plasticity model and the Crisfield model demonstrates certain advantages of the here presented model in terms of accuracy and numerical efficiency. Upon testing the model on practical finite element simulations (using the same software as in *Paper B* but with replacing the constitutive model) with one and three roll stands we ascertain a significant improvement against the model of *Paper A* and furthermore an excellent correspondence in comparison to the continuum plasticity model in regard of the predictivity of the final geometry of the sheet metal profile and forces on the roll stands.

*Emin Kocbay is responsible for:* writing of the original draft; derivation of the model equations, development of software, numerical experiments; finite element computations; visualization and presentation of the results.

## 9. Scientific impact

Within this cumulative thesis we were able to develop and introduce a novel simulation strategy, developed for the purpose of roll forming simulations. The novelties comprise the discretization of the sheet metal as a Kirchhoff–Love shell within a mixed Eulerian–Lagrangian kinematic finite element framework. Furthermore, the description of the inelastic constitutive equations features a new shell stress resultant plasticity model, which is applicable for bending dominant applications. Thus, the usually employed time consuming approaches that utilize classical Lagrangian kinematic formulation and furthermore a finite element discretization on the continuum level are elegantly evaded.

During this research work we systematically developed the simulation tool and are able to briefly summarize following scientific highlights and impacting factors in the order they were implemented:

- The development of a new plate stress resultant plasticity finite element model for the geometrically linear setting.
- The extension to the nonlinear Kirchhoff–Love shell theory within the mixed Eulerian–Lagrangian kinematic formalism.
- The account for the contact interaction with the rigid rolls by means of the penalty regularization method.
- The testing of the software with the previously developed and other constitutive models (continuum plasticity approach) in practical roll forming simulations and validations of those against commercial software results as well as physical experiments.
- The extension towards a nonlinear Kirchhoff–Love shell stress resultant plasticity formalism, building upon the previous research and finally obtaining an accurate and still computationally efficient simulation tool for roll forming.

## References

- [1] G. T. Halmos. Roll forming handbook. CRC Press, 2005.
- [2] F. Heislitz et al. Simulation of roll forming process with the 3-D FEM code PAM-STAMP. *Journal of Materials Processing Technology* 59.1 (1996), 59–67. DOI: [10.1016/0924-0136\(96\)02287-X](https://doi.org/10.1016/0924-0136(96)02287-X).
- [3] Q. Bui and J. Ponthot. Numerical simulation of cold roll-forming processes. *Journal of Materials Processing Technology* 202.1 (2008), 275–282. DOI: [10.1016/j.jmatprotec.2007.08.073](https://doi.org/10.1016/j.jmatprotec.2007.08.073).
- [4] J. Cheng et al. The flower pattern and rolls design for ERW pipes with the different specification in the flexible roll forming process. *Thin-Walled Structures* 154 (2020), 106809. DOI: [10.1016/j.tws.2020.106809](https://doi.org/10.1016/j.tws.2020.106809).

- [5] E. Oborin, Y. Vetyukov and I. Steinbrecher. Eulerian description of non-stationary motion of an idealized belt-pulley system with dry friction. *International Journal of Solids and Structures* 147 (2018), 40–51. DOI: [10.1016/j.ijsolstr.2018.04.007](https://doi.org/10.1016/j.ijsolstr.2018.04.007).
- [6] Y. Crutzen et al. Lagrangian and arbitrary Lagrangian Eulerian simulations of complex roll-forming processes. *Comptes Rendus Mécanique* 344.4 (2016), 251–266. DOI: [10.1016/j.crme.2016.02.005](https://doi.org/10.1016/j.crme.2016.02.005).
- [7] J. Donea et al. Arbitrary Lagrangian-Eulerian Methods. *Encyclopedia of Computational Mechanics*. Ed. by E. Stein, R. de Borst and T. Hughes. Vol. 1: Fundamentals. John Wiley & Sons, Ltd, 2004. Chap. 14.
- [8] Y. Vetyukov, P. Gruber and M. Krommer. Nonlinear model of an axially moving plate in a mixed Eulerian-Lagrangian framework. *Acta Mechanica* 227 (2016), 2831–2842. DOI: <https://doi.org/10.1007/s00707-016-1651-0>.
- [9] Vetyukov, Yu. and Gruber, P. G. and Krommer, M. and Gerstmayr, J. and Gafur, I. and Winter, G. Mixed Eulerian–Lagrangian description in materials processing: deformation of a metal sheet in a rolling mill. *International Journal for Numerical Methods in Engineering* 109.10 (2017), 1371–1390. DOI: [10.1002/nme.5314](https://doi.org/10.1002/nme.5314).
- [10] J. Scheidl et al. Mixed Eulerian–Lagrangian shell model for lateral run-off in a steel belt drive and its experimental validation. *International Journal of Mechanical Sciences* 204 (2021), 106572. DOI: [10.1016/j.ijmecsci.2021.106572](https://doi.org/10.1016/j.ijmecsci.2021.106572).
- [11] Y. Vetyukov. Finite element modeling of Kirchhoff-Love shells as smooth material surfaces. *ZAMM - Journal of Applied Mathematics and Mechanics / Zeitschrift für Angewandte Mathematik und Mechanik* 94.1-2 (2014), 150–163. DOI: [10.1002/zamm.201200179](https://doi.org/10.1002/zamm.201200179).
- [12] V. V. Eliseev and Y. M. Vetyukov. Finite deformation of thin shells in the context of analytical mechanics of material surfaces. *Acta Mechanica* 209.1-2 (2010), 43. DOI: [10.1007/s00707-009-0154-7](https://doi.org/10.1007/s00707-009-0154-7).
- [13] F. K. Bogner, R. L. Fox and L. A. Schmit. The generation of interelement compatible stiffness and mass matrices by the use of interpolation formulae. *Proc. Conf. Matrix Methods in Struct. Mech., Airforce Inst. Of Tech.* Wright Patterson AF Base, Ohio. 1965.
- [14] C. Mueller et al. Influence of Friction on the Loads in a Roll Forming Simulation with Compliant Rolls. *Material Forming ESAFORM 2014*. Vol. 611. Key Engineering Materials. Trans Tech Publications Ltd, 2014, 436–443. DOI: [10.4028/www.scientific.net/KEM.611-612.436](https://doi.org/10.4028/www.scientific.net/KEM.611-612.436).
- [15] R. Safdarian and H. Moslemi Naeini. The effects of forming parameters on the cold roll forming of channel section. *Thin-Walled Structures* 92 (2015), 130–136. DOI: [10.1016/j.tws.2015.03.002](https://doi.org/10.1016/j.tws.2015.03.002).
- [16] M. Crisfield. Finite element analysis for combined material and geometric nonlinearities. *Nonlinear finite element analysis in structural mechanics*. Springer, 1981, 325–338.

- [17] B. Brank, D. Perić and F. B. Damjanić. On large deformations of thin elasto-plastic shells: Implementation of a finite rotation model for quadrilateral shell element. *International Journal for Numerical Methods in Engineering* 40.4 (1997), 689–726. DOI: [10.1002/\(SICI\)1097-0207\(19970228\)40:4<689::AID-NME85>3.0.CO;2-7](https://doi.org/10.1002/(SICI)1097-0207(19970228)40:4<689::AID-NME85>3.0.CO;2-7).
- [18] M. Ambati, J. Kiendl and L. De Lorenzis. Isogeometric Kirchhoff–Love shell formulation for elasto-plasticity. *Computer Methods in Applied Mechanics and Engineering* 340 (2018), 320–339. DOI: [10.1016/j.cma.2018.05.023](https://doi.org/10.1016/j.cma.2018.05.023).
- [19] A. Ilyushin. Plasticity (in Russian). GITL, Moscow, Leningrad, 1948.
- [20] Bieniek, MP and Funaro, JR. Elasto-plastic behavior of plates and shells. Tech. rep. Weidlinger Associates New York, 1976.
- [21] Q. Zeng, A. Combescure and F. Arnaudeau. An efficient plasticity algorithm for shell elements application to metal forming simulation. *Computers & Structures* 79.16 (2001), 1525–1540. DOI: [10.1016/S0045-7949\(01\)00032-3](https://doi.org/10.1016/S0045-7949(01)00032-3).
- [22] J. Dujc and B. Brank. On stress resultant plasticity and viscoplasticity for metal plates. *Finite Elements in Analysis and Design* 44.4 (2008), 174–185. DOI: [10.1016/j.finel.2007.11.011](https://doi.org/10.1016/j.finel.2007.11.011).
- [23] L. P. Lebedev, M. J. Cloud and V. A. Eremeyev. Tensor Analysis with Applications in Mechanics. WORLD SCIENTIFIC, 2010. DOI: [10.1142/7826](https://doi.org/10.1142/7826).
- [24] Y. Vetyukov. Nonlinear mechanics of thin-walled structures: asymptotics, direct approach and numerical analysis. Springer Science & Business Media, 2014.
- [25] V. Eliseev. Mechanics of deformable solid bodies (in Russian). St. Petersburg: St. Petersburg State Polytechnical University Publishing House, 2006.
- [26] H. Kleemola and M. Nieminen. On the strain-hardening parameters of metals. *Metalurgical transactions* 5.8 (1974), 1863–1866. DOI: [10.1007/BF02644152](https://doi.org/10.1007/BF02644152).
- [27] M. Lindgren. An Improved Model for the Longitudinal Peak Strain in the Flange of a Roll Formed U-Channel developed by FE-Analyses. *Steel Research International* 78.1 (2007), 82–87. DOI: [10.1002/srin.200705863](https://doi.org/10.1002/srin.200705863).
- [28] J. Dujc and B. Brank. Stress resultant plasticity for shells revisited. *Computer Methods in Applied Mechanics and Engineering* 247-248 (2012), 146–165. DOI: [10.1016/j.cma.2012.07.012](https://doi.org/10.1016/j.cma.2012.07.012).
- [29] J. Lubliner. Plasticity theory. Dover Publications, Inc., 2008.
- [30] Q. Hu, X. Li and J. Chen. On the calculation of plastic strain by simple method under non-associated flow rule. *European Journal of Mechanics - A/Solids* 67 (2018), 45–57. DOI: [10.1016/j.euromechsol.2017.08.017](https://doi.org/10.1016/j.euromechsol.2017.08.017).
- [31] J. C. Simo and R. L. Taylor. A return mapping algorithm for plane stress elastoplasticity. *International Journal for Numerical Methods in Engineering* 22.3 (1986), 649–670. DOI: [10.1002/nme.1620220310](https://doi.org/10.1002/nme.1620220310).



## Paper A

*Stress resultant plasticity for plate bending in the context of roll forming of sheet metal*

TU Wien: Emin Kocbay, Yury Vetyukov  
*International Journal for Numerical Methods in Engineering*  
Volume 122, Issue 18 p. 5144-5168  
<https://doi.org/10.1002/nme.6760>

**Keywords:** stress resultant plasticity, elastic-plastic plate, roll forming, finite element analysis

**Abstract:** Modelling of roll forming process of sheet metal requires efficient treatment of plastic deformations of thin shells and plates. We suggest a new general approach towards constructing the governing equations of bending of an elastic-plastic Kirchhoff plate on the structural mechanics level. The generic function of the isotropic hardening law is formulated in terms of variables, which are meaningful for a material surface, namely resultant bending moments and dissipative work. This function is then identified by comparison of the exact solutions for a uni-axial or isotropic bending experiment within the structural model and with the continuum model of a through-the-thickness element. We validate the approach against both the fully three-dimensional simulations as well as the results of the traditional elastic-plastic plate analysis, the latter one featuring the continuum laws of plasticity treated in the integration points along the thickness direction. We considered benchmark problems from the literature as well as a prototype for the roll forming problem. Besides good agreement regarding the shape of plastic zones and force-deflection characteristics, experiments also demonstrate higher computational efficiency of the new stress resultant model.

## References of Paper A

- [1] G. T. Halmos, ed. Roll Forming Handbook. 0th ed. CRC Press, 2005. DOI: [10.1201/9781420030693](https://doi.org/10.1201/9781420030693).
- [2] Y. Crutzen et al. Lagrangian and arbitrary Lagrangian Eulerian simulations of complex roll-forming processes. *Comptes Rendus Mécanique* 344.4-5 (2016), 251–266. DOI: [10.1016/j.crme.2016.02.005](https://doi.org/10.1016/j.crme.2016.02.005).
- [3] Y. Vetyukov et al. Mixed Eulerian-Lagrangian description in materials processing: deformation of a metal sheet in a rolling mill: Mixed Eulerian-Lagrangian description in materials processing: deformation of a metal sheet in a rolling mill. *International Journal for Numerical Methods in Engineering* 109.10 (2017), 1371–1390. DOI: [10.1002/nme.5314](https://doi.org/10.1002/nme.5314).

- [4] Y. Vetyukov, P. G. Gruber and M. Krommer. Nonlinear model of an axially moving plate in a mixed Eulerian–Lagrangian framework. *Acta Mechanica* 227.10 (2016), 2831–2842. DOI: [10.1007/s00707-016-1651-0](https://doi.org/10.1007/s00707-016-1651-0).
- [5] J. Scheidl et al. Mixed Eulerian–Lagrangian shell model for lateral run-off in a steel belt drive and its experimental validation. *International Journal of Mechanical Sciences* 204 (2021), 106572. DOI: [10.1016/j.ijmecsci.2021.106572](https://doi.org/10.1016/j.ijmecsci.2021.106572).
- [6] M. Ambati, J. Kiendl and L. De Lorenzis. Isogeometric Kirchhoff–Love shell formulation for elasto-plasticity. *Computer Methods in Applied Mechanics and Engineering* 340 (2018), 320–339. DOI: [10.1016/j.cma.2018.05.023](https://doi.org/10.1016/j.cma.2018.05.023).
- [7] A. Ilyushin. Plasticity (in Russian). GITL, Moscow, Leningrad, 1948.
- [8] J. Lubliner. Plasticity theory. Dover Publications, Inc., 2008.
- [9] J. Simo and J. Kennedy. On a stress resultant geometrically exact shell model. Part V. Nonlinear plasticity: formulation and integration algorithms. *Computer Methods in Applied Mechanics and Engineering* 96.2 (1992), 133–171. DOI: [10.1016/0045-7825\(92\)90129-8](https://doi.org/10.1016/0045-7825(92)90129-8).
- [10] A. Ibrahimbegović and F. Frey. An efficient implementation of stress resultant plasticity in analysis of Reissner–Mindlin plates. *International Journal for Numerical Methods in Engineering* 36.2 (1993), 303–320. DOI: [10.1002/nme.1620360209](https://doi.org/10.1002/nme.1620360209).
- [11] M. A. Crisfield. Finite Element Analysis for Combined Material and Geometric Non-linearities. *Nonlinear Finite Element Analysis in Structural Mechanics*. Ed. by W. Wunderlich, E. Stein and K.-J. Bathe. Berlin, Heidelberg: Springer Berlin Heidelberg, 1981, 325–338. DOI: [10.1007/978-3-642-81589-8\\_18](https://doi.org/10.1007/978-3-642-81589-8_18).
- [12] J. Dujc and B. Brank. On stress resultant plasticity and viscoplasticity for metal plates. *Finite Elements in Analysis and Design* 44.4 (2008), 174–185. DOI: [10.1016/j.finel.2007.11.011](https://doi.org/10.1016/j.finel.2007.11.011).
- [13] J. Dujc and B. Brank. Stress resultant plasticity for shells revisited. *Computer Methods in Applied Mechanics and Engineering* 247–248 (2012), 146–165. DOI: [10.1016/j.cma.2012.07.012](https://doi.org/10.1016/j.cma.2012.07.012).
- [14] C. H. Chou, J. Pan and S. C. Tang. Analysis of sheet metal forming operations by a stress resultant constitutive law. *International Journal for Numerical Methods in Engineering* 37.5 (1994), 717–735. DOI: [10.1002/nme.1620370502](https://doi.org/10.1002/nme.1620370502).
- [15] M. Wali et al. A simple integration algorithm for a non-associated anisotropic plasticity model for sheet metal forming: A NON-ASSOCIATED ANISOTROPIC PLASTICITY MODEL FOR SHEET METAL FORMING. *International Journal for Numerical Methods in Engineering* 107.3 (2016), 183–204. DOI: [10.1002/nme.5158](https://doi.org/10.1002/nme.5158).
- [16] V. V. Eliseev and Y. M. Vetyukov. Finite deformation of thin shells in the context of analytical mechanics of material surfaces. *Acta Mechanica* 209.1-2 (2010), 43–57. DOI: [10.1007/s00707-009-0154-7](https://doi.org/10.1007/s00707-009-0154-7).

- [17] Y. Vetyukov. *Nonlinear Mechanics of Thin-Walled Structures: Asymptotics, Direct Approach and Numerical Analysis*. Foundations of Engineering Mechanics. Vienna: Springer Vienna, 2014. DOI: [10.1007/978-3-7091-1777-4](https://doi.org/10.1007/978-3-7091-1777-4).
- [18] L. P. Lebedev, M. J. Cloud and V. A. Eremeyev. *Tensor Analysis with Applications in Mechanics*. WORLD SCIENTIFIC, 2010. DOI: [10.1142/7826](https://doi.org/10.1142/7826).
- [19] F. Auricchio and R. L. Taylor. A generalized elastoplastic plate theory and its algorithmic implementation. *International Journal for Numerical Methods in Engineering* 37.15 (1994), 2583–2608. DOI: [10.1002/mme.1620371506](https://doi.org/10.1002/mme.1620371506).
- [20] Y. Vetyukov, A. Kuzin and M. Krommer. Asymptotic splitting in the three-dimensional problem of elasticity for non-homogeneous piezoelectric plates. *International Journal of Solids and Structures* 48.1 (2011), 12–23. DOI: [10.1016/j.ijsolstr.2010.09.001](https://doi.org/10.1016/j.ijsolstr.2010.09.001).
- [21] A. Öchsner. *Elasto-Plasticity of Frame Structure Elements: Modeling and Simulation of Rods and Beams*. Berlin, Heidelberg: Springer Berlin Heidelberg, 2014. DOI: [10.1007/978-3-662-44225-8](https://doi.org/10.1007/978-3-662-44225-8).
- [22] H. J. Kleemola and M. A. Nieminen. On the strain-hardening parameters of metals. *Metallurgical transactions* 5.8 (1974), 1863–1866. DOI: [10.1007/BF02644152](https://doi.org/10.1007/BF02644152).
- [23] F. Heislitz et al. Simulation of roll forming process with the 3-D FEM code PAM-STAMP. *Journal of Materials Processing Technology* 59.1-2 (1996), 59–67. DOI: [10.1016/0924-0136\(96\)02287-X](https://doi.org/10.1016/0924-0136(96)02287-X).
- [24] Y. Vetyukov. Finite element modeling of Kirchhoff-Love shells as smooth material surfaces. *ZAMM - Journal of Applied Mathematics and Mechanics / Zeitschrift für Angewandte Mathematik und Mechanik* 94.1-2 (2014), 150–163. DOI: [10.1002/zamm.201200179](https://doi.org/10.1002/zamm.201200179).
- [25] F. K. Bogner, R. L. Fox and L. A. Schmit. The generation of interelement compatible stiffness and mass matrices by the use of interpolation formulae. *Proc. Conf. Matrix Methods in Struct. Mech., Airforce Inst. Of Tech.* Wright Patterson AF Base, Ohio. 1965.
- [26] J. C. Simo and R. L. Taylor. A return mapping algorithm for plane stress elastoplasticity. *International Journal for Numerical Methods in Engineering* 22.3 (1986), 649–670. DOI: [10.1002/nme.1620220310](https://doi.org/10.1002/nme.1620220310).
- [27] M. Crisfield. *Non-linear Finite Element Analysis of Solids and Structures*. Vol.1. John Wiley & Sons, 1991.
- [28] Y. Vetyukov, J. Gerstmayr and H. Irschik. Plastic multipliers as driving variables of numerical simulation in elastoplasticity. *Mechanics Research Communications* 30.5 (2003), 421–430. DOI: [10.1016/S0093-6413\(03\)00042-9](https://doi.org/10.1016/S0093-6413(03)00042-9).
- [29] R. Hill. *Plasticity: Theory and Application*. A. Mendelson. Collier-Macmillan, London. 360 pp. Illustrated. 120s. *The Aeronautical Journal* 72.694 (1968), 889–889. DOI: [10.1017/S0001924000085298](https://doi.org/10.1017/S0001924000085298).

# Stress resultant plasticity for plate bending in the context of roll forming of sheet metal

Emin Kocbay | Yury Vetyukov<sup>ORCID</sup>Institute of Mechanics and Mechatronics,  
TU Wien, Vienna, Austria**Correspondence**Yury Vetyukov, Institute of Mechanics and  
Mechatronics, TU Wien, Getreidemarkt 9,  
A-1060 Vienna, Austria.  
Email: yury.vetyukov@tuwien.ac.at**Abstract**

Modeling of roll forming process of sheet metal requires efficient treatment of plastic deformations of thin shells and plates. We suggest a new general approach toward constructing the governing equations of bending of an elastic-plastic Kirchhoff plate on the structural mechanics level. The generic function of the isotropic hardening law is formulated in terms of variables, which are meaningful for a material surface, namely resultant bending moments and dissipative work. This function is then identified by comparison of the exact solutions for a uni-axial or isotropic bending experiment within the structural model and with the continuum model of a through-the-thickness element. We validate the approach against both the fully three-dimensional simulations as well as the results of the traditional elastic-plastic plate analysis, the latter one featuring the continuum laws of plasticity treated in the integration points along the thickness direction. We considered benchmark problems from the literature as well as a prototype for the roll forming problem. Besides good agreement regarding the shape of plastic zones and force-deflection characteristics, experiments also demonstrate higher computational efficiency of the new stress resultant model.

**KEYWORDS**

elastic-plastic plate, finite element analysis, roll forming, stress resultant plasticity

## 1 | INTRODUCTION

In the present paper, we introduce a novel approach to modeling plasticity in thin plate- and shell-like structures at bending, which is computationally more efficient than traditional ones. The ultimate aim of our simulations is set on the roll forming of sheet metal, where the proposed model of thin elastic-plastic plates shall play a fundamental role.

Roll forming belongs to the class of cold forming manufacturing processes. The basic idea is that an initially flat sheet metal strip is transformed to the desired product with a different profile (shape of the cross section), see References 1,2. The strip is continuously fed through the consecutively arranged forming passes. Each forming pass consists of a set of contoured rolls, which incrementally contribute to the finally obtained deformation, thus producing the desired shape mainly by bending. Therefore, roll forming is essentially different to rolling: no significant thickness deformations occur, the membrane strains remain small, and the final product shape is acquired by irreversible plastic bending deformations.

This is an open access article under the terms of the Creative Commons Attribution License, which permits use, distribution and reproduction in any medium, provided the original work is properly cited.

© 2021 The Authors. *International Journal for Numerical Methods in Engineering* published by John Wiley & Sons Ltd.

Roll forming is a highly economical manufacturing process for the mass production of high-quality profiles. Their complexity can vary from simple profiles (e.g., U-profiles) to highly sophisticated ones. While being very important for practical applications, predicting the final shape for a given assembly and design of the forming passes is currently an extremely time-consuming computational task, because traditionally continuum models with Lagrangian kinematic formulation of the finite element scheme are put into practice. Because of the axial motion of the deformable structure through a series of contact zones, it is computationally more efficient to use the mixed Eulerian–Lagrangian kinematic description with a nonmaterial finite element formulation as discussed in References 3–5. Previous attempts to apply this approach for roll forming featured solid continuum elements<sup>2</sup> and were not very successful from the point of view of numerical efficiency. Faster simulations are expected with structural mechanics models of plates and shells, which require a consistent and efficient treatment of elastic-plastic behavior at bending dominated deformations.

The proposed stress-resultant model of plasticity allows to reduce the computational complexity of this nonlinear problem to a great extent.

In the present paper we consider static deformation of plates with the focus on the plasticity formulation. A widely utilized approach to treat plasticity in thin bodies avoiding the full three-dimensional analysis are structural models of beams, plates, and shells, in which the continuum mechanics laws of elastoplasticity are treated in chosen points of a through-the-thickness element. The kinematic assumptions of the structural model relate the local strains with the overall strain measures of the structure (e.g., curvature of a beam or of a plate), and the stress resultants (forces and moments) follow by integration. A good correspondence to full three-dimensional solutions is usually observed for thin structures with sufficient number of integration points, see discussion in Reference 6. A further step toward computational efficiency can be taken, if the constitutive relations directly connect the stress resultants to the local strain measures of the structural theory (e.g., a relation between the bending moments and curvature for a beam or for a plate) and thus the through-the-thickness integration becomes obsolete.

In the literature, one finds several attempts to describe the elastic-plastic behavior of plates and shells completely on the level of structural mechanics, mainly in the view of computational aspects. Practically all formulations make use of the associated flow rule and an extended form of the Ilyushin yield criterion.<sup>7</sup> The differences lie in the underlying structural plate model (with or without shear and membrane deformations), in the details of the finite element kinematic approximation and, what is most important, in the formulation of the isotropic and/or kinematic hardening law.<sup>8</sup> Moreover, the choice of the internal hardening variables, which enter the evolution law, is also not unique. Thus, Simo and Kennedy<sup>9</sup> introduced a hardening potential that is quadratic in terms of the hardening variables, which implies linear hardening behavior. Two hardening laws are obtained by using that potential. One for isotropic hardening, where the internal hardening variable takes the form of a dissipative function, which is defined as a generalization of the equivalent plastic work. The other introduced law considers kinematic hardening and is an extension to the Prager–Ziegler kinematic hardening law of the classical  $J_2$ -flow theory. The practical application of these laws requires, however, material parameters such as isotropic and kinematic hardening moduli of the structural mechanics theory to be known. Ibrahimbegović and Frey<sup>10</sup> considered the Ilyushin yield criterion adjusted by an additive hardening term in the form of a product of a constant isotropic hardening modulus and the effective plastic strain as an internal variable within a kinematically simple model of a Reissner–Mindlin plate.

While this yield criterion is simple and perfectly applicable, it does not account for the spreading of the plasticity through the thickness of the plate and is useful only for the analysis of limit loads. Crisfield<sup>11</sup> suggested an evolution law for an additional state variable, which reflects the growth of the plastic zone in a through-the-thickness element. Dujc and Brank implemented this strategy in Reference 12 and demonstrated satisfactory results for several benchmark problems, one of which we also consider in the present work. The same authors further extend the approach toward more complicated shell kinematics in Reference 13 making use of a yield criterion function that corresponds to the Ilyushin–Shapiro multisurface flow criterion in three dimensions. Both isotropic and kinematic hardening are accounted for in the proposed yield criterion. The internal hardening variables of their model feature the plastic strain, another scalar parameter which controls the isotropic hardening mechanism and strain like parameters which control the kinematic hardening mechanism.

A different approach of considering hardening in terms of hardening moduli (which are often constants) is pursued by Chou et al.<sup>14</sup> The Ilyushin yield criterion is again applied; however, upon initiation of plastic flow the yield criterion function takes the value of a normalized equivalent stress resultant  $\bar{\Sigma}$ , which is variable because isotropic hardening is considered.  $\bar{\Sigma}$  is handled as a function of the normalized equivalent generalized plastic strain and is formulated in terms of a power law, where the exponent  $n$  is called hardening exponent, which is viewed as a material parameter and must be known a priori in order to apply the structural model.

In the present paper we focus on the Kirchhoff plate model with the associated flow rule and the Ilyushin yield criterion, which is adjusted in order to account for isotropic hardening; see Reference 15 for a discussion of more general plasticity models in application to sheet metal forming. Similar to Reference 14 we propose, that a through-the-thickness element yields, when the yield criterion function equals a limiting value  $k_M^2$ , with  $k_M$  being the maximal equivalent elastic moment. In contrast to many other approaches, we consider the limiting value  $k_M$  as a function of the dissipative work  $A^P$  in the given point of the plate, which fully determines the isotropic hardening of the structural model. Furthermore we do not assume any particular form (e.g., power law) for  $k_M(A^P)$ , but rather identify the analytic function by solving simple problems like uni-axial bending. The identification relies upon the continuum model of a through-the-thickness element: equations of the three-dimensional elastoplasticity are solved for the points on a line in the thickness direction under the kinematic assumptions of the Kirchhoff plate theory. Integrating the three-dimensional stresses and dissipative work over the thickness, we finally obtain the sought for hardening function of the structural model. We do not consider kinematic hardening and thus are not able to account for the Bauschinger effect.<sup>8</sup> Because reverse plasticity is usually avoided in the practice of roll forming, the present model shall be sufficient for this field of application. In numerical experiments, we observe good agreement regarding the shape of plastic zones and force-deflection characteristics. Moreover, the computational advantage compared to conventional plasticity models is pronounced.

## 2 | GENERAL MODEL OF AN ELASTIC-PLASTIC KIRCHHOFF PLATE

A plate is considered as a material surface in the framework of the so-called *direct approach*.<sup>16,17</sup> The absence of the thickness coordinate makes it very easy to arrive at the complete theory. Formulating the constitutive conditions requires, however, identification by comparison to three-dimensional solutions, which we will accomplish in the subsequent sections.

The single strain measure for a linear Kirchhoff plate is the tensor of curvatures

$$\boldsymbol{\kappa} = \nabla \nabla w, \quad (1)$$

with  $\nabla$  being an in-plane differential operator and  $w$  being the transverse deflection. With Cartesian coordinates  $x, y$  in the plane of the plate and corresponding basis vectors  $\mathbf{e}_x, \mathbf{e}_y$  the invariant differential operator takes the form

$$\nabla = \mathbf{e}_x \frac{\partial}{\partial x} + \mathbf{e}_y \frac{\partial}{\partial y}, \quad (2)$$

such that the symmetric in-plane curvature tensor

$$\boldsymbol{\kappa} = \frac{\partial^2 w}{\partial x^2} \mathbf{e}_x \mathbf{e}_x + \frac{\partial^2 w}{\partial x \partial y} (\mathbf{e}_x \mathbf{e}_y + \mathbf{e}_y \mathbf{e}_x) + \frac{\partial^2 w}{\partial y^2} \mathbf{e}_y \mathbf{e}_y = \kappa_x \mathbf{e}_x \mathbf{e}_x + \kappa_{xy} (\mathbf{e}_x \mathbf{e}_y + \mathbf{e}_y \mathbf{e}_x) + \kappa_y \mathbf{e}_y \mathbf{e}_y, \quad (3)$$

is defined by three components. In the following we use the direct tensor notation with a dyadic product implied when two vectors are written next to each other, thus omitting the symbol  $\otimes$ , which is sometimes used in the literature. This utilized variant of the mathematical notation is common in the theory of elasticity and structural mechanics, see for example, Reference 18.

The elastic law for the isotropic plate is given by

$$\mathbf{M} = D\nu \mathbf{I} \operatorname{tr} \boldsymbol{\kappa}^e + D(1 - \nu) \boldsymbol{\kappa}^e, \quad (4)$$

in which  $\mathbf{M}$  is the plane tensor of moments acting in the plate,  $\mathbf{I}$  is the plane identity tensor,  $\nu$  is the Poisson ratio and  $D$  is the flexural stiffness. Note that  $\mathbf{M}$  shall be considered as one of the stress resultants in the three-dimensional body of a plate. The tensor of elastic curvatures  $\boldsymbol{\kappa}^e$  is identical to the total curvatures  $\boldsymbol{\kappa}$  as long as the deformation is purely elastic. Using the principle of virtual work, one obtains the equilibrium conditions in the form

$$\nabla \cdot \mathbf{M} + \mathbf{Q} = 0, \quad \nabla \cdot \mathbf{Q} + q = 0. \quad (5)$$

Here  $\mathbf{Q}$  is the vector of transverse forces and  $q$  is the external load per unit surface of the plate, which acts in the transverse direction. The equilibrium equations and the corresponding boundary conditions for  $\mathbf{M}$  and  $\mathbf{Q}$  are equivalent

to the variational principle of minimum of total potential energy of the plate, which we use below for the finite element analysis.

We account for inelastic deformations by means of the additive decomposition of the total geometric curvature into the elastic and the plastic parts,

$$\boldsymbol{\kappa} = \boldsymbol{\kappa}^e + \boldsymbol{\kappa}^p. \quad (6)$$

An evolution law for  $\boldsymbol{\kappa}^p$  is required to close the system of equations. Additional relations will need to be introduced for this sake, namely: *yield criterion*, *hardening law*, and *flow rule*. Each of them is formulated in stress resultants which leads to our general model of an elastic-plastic Kirchhoff plate. Furthermore we focus on a plate model with isotropic hardening. Not taking the phenomenon of kinematic hardening into consideration, we will not be able to account for the Bauschinger effect,<sup>8</sup> which is important in case of reverse plasticity. Nevertheless, we decide that the consideration of isotropic hardening is sufficient for our purposes in the field of roll forming, as typically in roll forming, the sheet metal is bend progressively under several, subsequently acting, shaped roll pairs and thus no plastic reverse bending is expected.

We start by introducing the yield criterion function  $f(\mathbf{M})$  and its derivatives. Motivated by the consideration, that the plane stress tensor in the three-dimensional body of the plate is proportional to  $\mathbf{M}$  and making use of the von Mises yield condition, we formulate the yield criterion function as an invariant quadratic form

$$f = \frac{3}{2} \mathbf{M} \cdot \cdot \mathbf{M} - \frac{1}{2} (\text{tr } \mathbf{M})^2, \quad \mathbf{M} \cdot \cdot \mathbf{M} \equiv \text{tr}(\mathbf{M} \cdot \mathbf{M}); \quad (7)$$

the double dot multiplication “ $\cdot \cdot$ ” has a meaning of a full contraction of two tensors, see Reference 18. With Cartesian components of the moment tensor  $M_x$ ,  $M_y$  and  $M_{xy}$  we compute

$$\begin{aligned} \mathbf{M} &= M_x \mathbf{e}_x \mathbf{e}_x + M_y \mathbf{e}_y \mathbf{e}_y + M_{xy} (\mathbf{e}_x \mathbf{e}_y + \mathbf{e}_y \mathbf{e}_x), \\ f &= M_x^2 - M_x M_y + M_y^2 + 3M_{xy}^2, \end{aligned} \quad (8)$$

which corresponds to the definition given by Ilyushin.<sup>7</sup> The above expression differs from the conventional yield criterion function in the three-dimensional plasticity at plane stress<sup>9,10,19</sup> only by substituting the moment components instead of the components of the stress tensor. We note that (7) describes the initial yield surface for the plane stress state, expressed in stress resultant form. The yield surface corresponds to an ellipse. Both at the state of uni-axial bending  $\mathbf{M} = M \mathbf{e}_x \mathbf{e}_x$  as well as at isotropic bending  $\mathbf{M} = M(\mathbf{e}_x \mathbf{e}_x + \mathbf{e}_y \mathbf{e}_y)$  we obtain  $f = M^2$ . The derivative  $\dot{f}$  with respect to time  $t$  follows as

$$\frac{\partial f}{\partial \mathbf{M}} = 3\mathbf{M} - \mathbf{I} \text{tr } \mathbf{M}, \quad \dot{f} = \frac{\partial f}{\partial \mathbf{M}} \cdot \cdot \dot{\mathbf{M}} = 3\mathbf{M} \cdot \cdot \dot{\mathbf{M}} - \text{tr } \mathbf{M} \text{tr } \dot{\mathbf{M}}. \quad (9)$$

In each point, the plate deforms elastically as long as  $f$  does not exceed certain threshold:  $f < k_M^2$ . This boundary is determined by the maximal equivalent moment  $k_M$ , at which plastic flow is initiated such that  $\dot{\boldsymbol{\kappa}}^p \neq 0$ . While the ideal plasticity model with constant yield surface  $k_M = \text{const}$  is perfectly valid in the three-dimensional case, it is inappropriate for beams and plates because the actual plastic zones in a through-the-thickness element will grow as bending progresses, as discussed in the subsequent sections. We describe this phenomenon by means of the isotropic hardening model: the yield surface expands as plastic flow takes place and thus  $k_M$  is a function of an internal hardening variable. The latter we choose as the dissipative work  $A^p$ :  $k_M = k_M(A^p)$ . The time rate of the dissipative work done in a given point of the plate equals the dissipative power

$$\dot{A}^p = \mathbf{M} \cdot \cdot \dot{\boldsymbol{\kappa}}^p. \quad (10)$$

Determining the specific form of the function  $k_M(A^p)$  will be the main goal of the subsequent section.

The evolution law for the plastic curvature  $\boldsymbol{\kappa}^p$ , which is needed to complete the general formulation of the elastic-plastic model, is determined by the postulate of maximum plastic dissipation<sup>8</sup> and is formulated as an associated flow rule in the form

$$\dot{\boldsymbol{\kappa}}^p = \dot{\lambda} \frac{\partial f}{\partial \mathbf{M}} = \dot{\lambda} (3\mathbf{M} - \mathbf{I} \text{tr } \mathbf{M}), \quad (11)$$

such that the flow direction is normal to the yield surface. The nonnegative time derivative of  $\lambda$  (which is sometimes called the plastic consistency parameter) follows from Equations (7) to (11). First we reformulate (10) by using (11) and (7):

$$\dot{A}^P = 2\dot{\lambda}f = \dot{\lambda} (3\mathbf{M} \cdot \dot{\mathbf{M}} - (\text{tr } \mathbf{M})^2). \quad (12)$$

During the active plastic flow process we remain on the yield surface, and the following relations are valid:

$$f = k_M^2(A^P), \quad \dot{f} = 2k_M(A^P)k'_M(A^P)\dot{A}^P. \quad (13)$$

Substituting (7) and (12) into (13) we explicitly find  $\dot{\lambda}$ :

$$\dot{\lambda} = \frac{3\mathbf{M} \cdot \dot{\mathbf{M}} - \text{tr } \mathbf{M} \text{tr } \dot{\mathbf{M}}}{2k_M(A^P)k'_M(A^P)(3\mathbf{M} \cdot \dot{\mathbf{M}} - (\text{tr } \mathbf{M})^2)}. \quad (14)$$

The expression is valid only if it is positive, otherwise the active plastic flow ends immediately and the plate keeps deforming elastically in this point with the reached plastic curvature  $\kappa^P$ .

Assuming the time history of the moment tensor  $\mathbf{M}(t)$  in a given point of the plate to be given, we can now determine the kinematic response of the plate by taking the following steps:

1. We find the plastic work done by dissipative forces  $A^P(t)$  by solving the first-order differential equation, which results after substituting  $\dot{\lambda}$  from (14) into (12). In general, one needs to take the unloading condition into account:  $\dot{\lambda} = 0$  as soon as the right-hand side of (14) becomes negative. Further plastic flow is initiated after an elastic phase as soon as the first equality in (13) is again fulfilled and the yield surface is reached.
2. Now that  $\dot{\lambda}(t)$  is known, we integrate the flow rule (11) over time.
3. The total geometric curvature (6) follows with the elasticity relation (4).

In a practical computation, neither  $\mathbf{M}(t)$  nor the kinematics of deformation are known in advance. Moreover, the problem becomes nonlocal as the moment distribution over the plate at static equilibrium depends both on the external loads as well as on the distribution of plastic curvatures. The time integration scheme applicable in the framework of a finite element simulation will be discussed below in Sect. 5.

### 3 | IDENTIFICATION OF THE ISOTROPIC HARDENING FUNCTION BY COMPARISON TO THREE-DIMENSIONAL SOLUTIONS

We complete the theory and identify the isotropic hardening function  $k_M(A^P)$  by performing simple thought experiments for a continuum model of a through-the-thickness element of a plate with thickness  $h$ , which features integrated three-dimensional equations of elastoplasticity. At doing so, we tacitly assume that integral quantities, such as curvatures, bending moments and dissipative work are equal in both, the structural and the continuum models.

We begin with the case of the *uni-axial bending* with the moment

$$\mathbf{M} = M(t) \mathbf{e}_x \mathbf{e}_x. \quad (15)$$

Now the plate behaves similar to a beam at pure bending and responds with the curvature

$$\boldsymbol{\kappa} = \kappa_x \mathbf{e}_x \mathbf{e}_x + \kappa_y \mathbf{e}_y \mathbf{e}_y; \quad (16)$$

the negative curvature in the transverse direction  $\kappa_y$  appears already during the elastic phase because of the Poisson effect. Our aim is to obtain the moment–curvature characteristic with the structural model and using the continuum solution to identify  $k_M(A^P)$  by comparison. We assume the axial bending moment  $M(t)$  to be monotonously increasing in time, such that no reverse bending occurs, and begin with the *continuum solution* for the three-dimensional body of the plate under the assumptions of Kirchhoff's theory regarding the kinematics of deformation and orders of magnitude of various stress components, see Reference 20 for the asymptotic justification. While the simple theory of elastic-plastic bending of



a beam can be found in the literature (see e.g. Öchsner<sup>21</sup>), here we briefly recall the key points, needed for the subsequent analysis.

The conventional Kirchhoff plate kinematics result into a linear distribution of the axial strain component  $\varepsilon_x$  over the thickness:

$$\varepsilon_x = -\kappa z, \quad (17)$$

here  $z$  is the coordinate in the thickness direction with the origin in the middle of the plate. This linearity is the asymptotic consequence of the three-dimensional equations of compatibility of strains<sup>20</sup> and thus holds independently from the material behavior. In the elastic range this also means a linear distribution of the stress tensor

$$\boldsymbol{\tau} = \sigma(z) \mathbf{e}_x \mathbf{e}_x, \quad \sigma = E\varepsilon_x = -E\kappa z, \quad (18)$$

with  $E$  being Young's modulus. All components of the stress tensor but the axial one vanish because of the plane stress assumption of the plate theory and because the plate is free to bend in the transverse direction. Simple integration relates the bending moment to the stress distribution:

$$\mathbf{M} = -\int_{-h/2}^{h/2} z\boldsymbol{\tau} dz, \quad M = -\int_{-h/2}^{h/2} z\sigma(z) dz. \quad (19)$$

Computing the integral in the elastic range, we find the elastic relation between the moment and the curvature, which also provides us with the flexural stiffness coefficient in (4):

$$M^e(\kappa) = \int_{-h/2}^{h/2} E\kappa z^2 dz = \frac{Eh^3}{12}\kappa, \quad D = \frac{Eh^3}{12(1-\nu^2)}. \quad (20)$$

Plastic flow is initiated at the upper and lower surfaces as soon as the stress reaches the yield stress  $k$  by the absolute value,

$$|\sigma(\pm h/2)| = E\kappa h/2 = k, \quad (21)$$

from which we find the maximal elastic curvature and the maximal elastic moment to be

$$\kappa_* = \frac{2k}{Eh}, \quad M_*^e = M^e \Big|_{\kappa=\kappa_*} = \frac{h^2 k}{6}. \quad (22)$$

Now we let the bending moment grow beyond the elastic limit,  $M(t) > M_*^e$ , when two *plastic zones*  $-h/2 < z < -z^p$  and  $z^p < z < h/2$  begin to develop and the *elastic core*  $-z^p < z < z^p$  starts shrinking, as the boundary between them

$$z^p(t) = \frac{k}{E\kappa}, \quad (23)$$

progresses from  $h/2$  at  $\kappa = \kappa_*$  toward 0 at  $\kappa \rightarrow \infty$ . The expression for  $z^p$  follows from the conditions, that the elastic law (18) holds in the elastic core and that  $|\sigma(z^p)| = k$ , as plasticity is just being initiated in this fiber.

The distribution of  $\sigma(z)$  in the plastic zones follows from the corresponding material characteristic. The analytic derivation below makes use of the assumption of the *ideal elastic-plastic continuum* material behavior, we discuss the implications of more realistic stress-strain curves in the end of this section. Under the stated assumption, the stress equals the yield stress in the plastic zones,  $\sigma = \pm k$ , and the total bending moment in the plastic regime is computed according to (19) as

$$M^p(\kappa) = -2 \int_0^{z^p} z\sigma(z) dz - 2 \int_{z^p}^{h/2} z\sigma(z) dz = 2 \int_0^{z^p} E\kappa z^2 dz + 2 \int_{z^p}^{h/2} zk dz = \frac{h^2 k}{4} - \frac{k^3}{3E^2 \kappa^2}, \quad (24)$$

we used the symmetry of  $\sigma(z)$  and substituted  $z^p$  from (23). The moment-curvature relationship is thus defined piecewise,

$$M(\kappa) = \begin{cases} M^e(\kappa), & \kappa \leq \kappa_* \\ M^p(\kappa), & \kappa > \kappa_*, \end{cases} \quad (25)$$

and it has a horizontal asymptote

$$\lim_{\kappa \rightarrow \infty} M^P = M_*^P = \frac{h^2 k}{4} = \frac{3}{2} M_*^e. \quad (26)$$

While the traditional consideration of the elastic-plastic beam bending usually stops at this point, we keep on computing and find an inverse relation to (25) for the total curvature as a function of the bending moment:

$$\kappa(M) = \begin{cases} \frac{12M}{Eh^3}, & 0 \leq M \leq M_*^e \\ \frac{2k^{\frac{3}{2}}}{\sqrt{3\sqrt{h^2 k E^2 - 4ME^2}}}, & M_*^e < M < M_*^P \end{cases} \quad (27)$$

The total curvature  $\kappa = \kappa^e + \kappa^P$  is a sum of the elastic part  $\kappa^e = 12M/(Eh^3)$  and of the plastic curvature  $\kappa^P$ , see (6) and (4). Further analysis requires  $\kappa^P$  being expressed as a function of the total curvature:

$$\kappa^P(\kappa) = \begin{cases} 0, & \kappa \leq \kappa_* \\ \frac{(hE\kappa - 2k)^2 (hE\kappa + k)}{h^3 E^3 \kappa^2}, & \kappa > \kappa_* \end{cases} \quad (28)$$

Vanishing of  $\kappa^P$  in the elastic range is obvious, and the expression for  $\kappa \geq \kappa_*$  follows after subtracting  $\kappa^e$  from both sides of (27) and further substituting  $M = M^P(\kappa)$  from (24).

Now we proceed to compute the *dissipative work* per unit area of the plate  $A^P$  done in the plastic zones. The dissipative power of the internal forces is the product of the stress tensor with the time rate of the plastic part of the strains. This power equals the time rate of the dissipative work  $A_3^P$  per unit volume:

$$A_3^P = \boldsymbol{\tau} \cdot \dot{\boldsymbol{\epsilon}}^P = \sigma \dot{\epsilon}_x^P = -k \dot{\epsilon}_x^P \Rightarrow A_3^P = -k \dot{\epsilon}_x^P. \quad (29)$$

The computation is simple in the present case of ideal elastoplasticity, as the stress remains constant. For certainty we consider the upper plastic zone  $z^P < z < h/2$  with compression,  $\sigma = -k$ . At known stress and total strain it is easy to find the plastic part using the elastic relation:

$$E(\epsilon_x - \epsilon_x^P) = \sigma = -k \Rightarrow \epsilon_x^P = \epsilon_x + k/E, \quad (30)$$

and with (17) the total dissipative work in a through-the-thickness element follows to

$$A^P = 2 \int_{z^P}^{h/2} A_3^P dz = -2 \int_{z^P}^{h/2} k \left( \frac{k}{E} - \kappa z \right) dz = \frac{k(hE\kappa - 2k)^2}{4E^2 \kappa}. \quad (31)$$

The expression makes only sense in the elastic-plastic region  $\kappa \geq \kappa_*$ . The function  $A^P(\kappa)$  vanishes together with its first derivative at  $\kappa = \kappa_*$  and grows linearly at  $\kappa \rightarrow \infty$ . The inverse relation  $\kappa(A^P)$  is then found to be

$$\kappa(A^P) = \frac{2 \left( hk^2 E + A^P E^2 + \sqrt{A^P E^3 (2hk^2 + A^P E)} \right)}{h^2 k E^2}, \quad \kappa \Big|_{A^P=0} = \kappa_*. \quad (32)$$

Now we switch out attention to the *structural plate model* from Section 2 and evaluate it for the problem of uni-axial bending at hand. Using the same Cartesian coordinate system as before, we write the elasticity law (4) for the bending moment (15), invert it and find the total curvature in the axial direction to

$$\kappa_x = \frac{M}{D(1 - \nu^2)} + \kappa_x^P, \quad (33)$$

the other components are of little interest. As already stated above, the yield criterion function (8) takes now the simple form:

$$f = M^2. \quad (34)$$

The governing differential Equations (11), (12), and (14) result into

$$\begin{aligned} \dot{\kappa}_x^p &= 2M\dot{\lambda}, \quad \dot{\kappa}_{xy}^p = 0, \quad \dot{\kappa}_y^p = -M\dot{\lambda}, \quad \dot{A}^p = 2M^2\dot{\lambda}, \\ \dot{\lambda} &= \frac{2\dot{M} + D(2 - \nu)\dot{\kappa}_x^p - D(1 - 2\nu)\dot{\kappa}_y^p}{M(4k_M(A^p)k'_M(A^p) + D(5 - 4\nu))}. \end{aligned} \quad (35)$$

The component  $\kappa_{xy}^p$  vanishes. We furthermore eliminate  $\dot{\kappa}_y^p$  and solve for  $\kappa_x^p$  and  $\dot{A}^p$ , thus obtaining expressions, which correspond to our expectations in the simple case of beam bending:

$$\kappa_x^p = \frac{\dot{M}}{k_M(A^p)k'_M(A^p)}, \quad \dot{A}^p = \frac{M\dot{M}}{k_M(A^p)k'_M(A^p)}. \quad (36)$$

The denominator in both time derivatives is the same and contains the isotropic hardening function, which we seek to identify. The expression in the denominator can be written more conveniently by introducing a new function

$$\varphi(A^p) = 2k_M(A^p)k'_M(A^p) = (k_M(A^p))^2, \quad (37)$$

which allows us to reformulate (36):

$$\kappa_x^p = \frac{2\dot{M}}{\varphi(A^p)}, \quad \dot{A}^p = \frac{2M\dot{M}}{\varphi(A^p)}. \quad (38)$$

Dividing  $\dot{A}^p$  by  $\kappa_x^p$ , we eliminate the explicit time derivatives and arrive at the differential relation, which will hold in the structural model regardless of the choice of the functions  $k_M$  and  $\varphi$ :

$$\frac{\dot{A}^p}{\kappa_x^p} = \frac{dA^p}{d\kappa_x^p} = M; \quad (39)$$

the relation makes sense only in the elastic-plastic range. Now the question arises whether this relation holds for the continuum model of a through-the-thickness element. Computing the derivatives of  $A^p$  and  $\kappa^p$  with respect to  $\kappa$  according to (31) and (28), we find

$$\frac{dA^p}{d\kappa} \left( \frac{d\kappa^p}{d\kappa} \right)^{-1} = \frac{dA^p}{d\kappa^p} = \frac{h^3 k E \kappa (2k + h E \kappa)}{4(4k^2 + 2hkE\kappa + h^2 E^2 \kappa^2)}, \quad (40)$$

which differs from the expression (24) for the bending moment in the plastic range  $M^p(\kappa)$ . Although this observation means that the exact correspondence of both models cannot be reached, we nevertheless continue the process of identification, such that the most important characteristic of the continuum model, namely the moment–curvature relation, is described by the structural model as accurately as possible. To this end we express the unknown function  $\varphi$  from the first equality in (38):

$$\varphi(A^p) = \frac{2\dot{M}}{\kappa_x^p} = 2 \frac{dM}{d\kappa_x^p}. \quad (41)$$

We evaluate the right-hand side in the elastic-plastic regime of the continuum model to

$$\varphi(A^p) = 2 \frac{dM^p}{d\kappa} \left( \frac{d\kappa^p}{d\kappa} \right)^{-1} \quad (42)$$

according to (24), (28) and substitute  $\kappa = \kappa(A^p)$  from (32), which finally results into the sought for expression

$$\varphi(A^p) = \frac{1}{36} \sqrt{E} \left( \frac{\sqrt{2hk^2 + EA^p}}{\sqrt{A^p}} + \frac{4E\sqrt{A^p}\sqrt{2hk^2 + EA^p}}{3hk^2 + 2EA^p} \right) - \frac{E}{12}. \quad (43)$$

Integrating (43) with respect to  $A^p$  and taking into account the initial yield condition  $k_M^2(0) = (M_*^e)^2$  at the beginning of plastic deformation with  $A^p = 0$ , we obtain the *yield criterion function* to be

$$k_M^2(A^p) = -\frac{1}{36}h^3(3EA^p - 3\sqrt{EA^p}\sqrt{2hk^2 + EA^p} + 2\sqrt{3hk^2} \arctan \frac{\sqrt{EA^p}}{\sqrt{6hk^2 + 3EA^p}}) + \frac{h^4k^2}{36}. \quad (44)$$

The obtained functions  $\varphi$  and  $k_M$  determine the evolution of the yield surface and thus the growth of the values of the yield criterion function  $f$ , see (8), (13), this corresponds to the isotropic hardening effect. As discussed earlier, the continuum and the structural mechanics models cannot be identical, and the accuracy of the approximation depends on the question, how well the differential equation for  $A^p$  is fulfilled. Before we answer this question in the subsequent section with the help of simple numerical simulations, we shortly discuss the second option to identify the hardening behavior based on the thought experiment of *isotropic plate bending*.

We follow the same methodology as above, but the tensor of bending moments and the curvature tensor take now the form

$$\mathbf{M} = M(t)(\mathbf{e}_x\mathbf{e}_x + \mathbf{e}_y\mathbf{e}_y), \quad \boldsymbol{\kappa} = \kappa (\mathbf{e}_x\mathbf{e}_x + \mathbf{e}_y\mathbf{e}_y), \quad \kappa = \kappa^e + \kappa^p; \quad (45)$$

the same variables obtain a new meaning now. The plane parts of the stress and the strain tensors in the *continuum model* are isotropic,

$$\boldsymbol{\tau} = \sigma (\mathbf{e}_x\mathbf{e}_x + \mathbf{e}_y\mathbf{e}_y), \quad \boldsymbol{\varepsilon} = \varepsilon (\mathbf{e}_x\mathbf{e}_x + \mathbf{e}_y\mathbf{e}_y) + \varepsilon_z\mathbf{e}_z\mathbf{e}_z, \quad \varepsilon = -E\kappa z. \quad (46)$$

In the elastic range holds

$$\sigma = \frac{E\varepsilon}{1-\nu}. \quad (47)$$

The yield condition at general plane stress is known to be<sup>7</sup>

$$\sigma_x^2 - \sigma_x\sigma_y + \sigma_y^2 + 3\tau_{xy}^2 = k^2, \quad (48)$$

which in our case  $\sigma_x = \sigma_y = \sigma$ ,  $\tau_{xy} = 0$  reduces to the same relation as above:

$$|\sigma| = k. \quad (49)$$

The maximal elastic curvature and the height of the boundary between the elastic core and the plastic zone, after plasticity is initiated, follow to

$$\kappa_* = \frac{2k(1-\nu)}{hE}, \quad z^p = \frac{k(1-\nu)}{E\kappa}. \quad (50)$$

The total bending moment again follows as (19). Knowing the stress distribution in the elastic core (47) and in the plastic zones (49), we compute the integral and find

$$M(\kappa) = \begin{cases} \frac{Eh^3\kappa}{12(1-\nu)}, & 0 \leq \kappa \leq \kappa_* \\ \frac{h^2k}{4} + \frac{k^3(1-\nu)^2}{3E^2\kappa^2}, & \kappa \geq \kappa_* \end{cases} \quad (51)$$

The maximal elastic moment  $M_*^e$  and the plastic one  $M_*^p$  are the same as above in the uni-axial case. The plastic curvature as a function of the total one  $\kappa^p(\kappa)$  follows by inverting (51) and subtracting the elastic curvature  $\kappa^e = 12(1-\nu)^2M/(Eh^3)$ .

To compute the dissipative work in a through-the-thickness element  $A^P$ , we again begin with the dissipative work per unit volume  $A_3^P$ . According to the first equality in (29), it takes now the form

$$A_3^P = -2k\varepsilon^P, \quad (52)$$

because both the stress tensor and the tensor of plastic strains have two identical components in the plane of the plate, and  $\sigma = -k$  as we again focus on the upper plastic zone with uniform compression. The plastic strain follows from the elastic relation (47), in which we now replace the total strain by its elastic part:

$$-k = \frac{E(\varepsilon - \varepsilon^P)}{1 - \nu} \Rightarrow \varepsilon^P = \varepsilon + \frac{k(1 - \nu)}{E}. \quad (53)$$

Acting further as when deriving (31) and (32), we first find  $A^P(\kappa)$  by integration over the upper plastic zone  $z^P \leq z \leq h/2$ , and then invert the relation to obtain the curvature as a function of the dissipative work  $\kappa(A^P)$ .

Proceeding, we treat the *structural plate model* in a full analogy to the above derivation of (33)–(36). The yield criterion function  $f$  retains its form as in the uni-axial case, the differential relations for the plastic curvature and the dissipative work look now

$$\dot{\kappa}^P = \frac{\dot{M}}{\varphi(A^P)}, \quad \dot{A}^P = \frac{2M\dot{M}}{\varphi(A^P)}. \quad (54)$$

Again, either the first relation or the second one may be made compatible with the continuum model by the appropriate choice of  $\varphi(A^P)$ . We choose the differential relation for  $\kappa^P$  and express

$$\begin{aligned} \varphi(A^P) &= \frac{dM}{d\kappa^P} = \frac{dM^P}{d\kappa} \left( \frac{d\kappa^P}{d\kappa} \right)^{-1} = \\ &= \frac{k^3(1 - \nu)^2 \left( A^P E + \sqrt{A^P E (A^P E + 4hk^2(1 - \nu))} + 2hk^2(1 - \nu) \right)^2}{3E^2\kappa^3 \left( A^P E + \sqrt{A^P E (A^P E + 4hk^2(1 - \nu))} \right) (A^P E + 3hk^2(1 - \nu))}. \end{aligned} \quad (55)$$

The analytic integration with respect to  $A^P$  is again possible. Accounting for the initial yield condition, we find a lengthy expression for the square of the hardening function  $k_M^2(A^P)$ . It is natural to expect, that the accuracy of solutions of the structural plate model with each of the two hardening functions, identified, respectively, for the cases of uni-axial and isotropic plate bending, shall depend on whether the actual bending state is closer to the uni-axial or to the isotropic one.

Finally, we emphasize the fact, that the previously followed procedure to identify  $k_M(A^P)$  is not restricted to ideal elastic-plastic continuum. Generally, empirically estimated isotropic hardening laws (see Reference 22) find use in roll forming simulations (thus, the isotropic hardening law of Swift is applied in Reference 23). *Hardening behavior of the stress-strain characteristic of the material of the plate* can also be incorporated in our model by virtue of certain modifications of the above procedure, which we now consider for the case of uni-axial bending. The stress tensor again takes the simple form of (18). Subsequently we introduce an isotropic hardening law, for example a power law according to Swift:

$$\sigma(z) = \begin{cases} -E\kappa z, & 0 \leq z \leq z^P \\ -k \left( \frac{E\kappa z}{k} \right)^n, & z^P < z \leq \frac{h}{2} \end{cases}, \quad (56)$$

where  $n$  is a material parameter named strain hardening exponent, which is physically limited to only assume values in the range of  $0 \leq n \leq 1$ . The limiting case  $n = 0$  corresponds to the ideal elastic-plastic material behavior, whereas  $n = 1$  corresponds to purely elastic behavior. The moment–curvature relation of the continuum model follows with the same procedure as before, simply by integration of the stress distribution along the thickness. In the general relation (25) we thus find a new expression for the moment in the plastic range:

$$M^P(\kappa) = -2 \int_0^{h/2} z\sigma(z) dz = 2 \int_0^{z^P} E\kappa z^2 dz + 2 \int_{z^P}^{h/2} zk \left( \frac{E\kappa z}{k} \right)^n dz = \frac{k \left( 2^{-n} h^2 \left( \frac{hE\kappa}{k} \right)^n - \frac{4k^2(1-n)}{3E^2\kappa^2} \right)}{2(2+n)}. \quad (57)$$

The expressions for the maximal elastic curvature  $\kappa_*$  and for the boundary between elastic and plastic region  $z^p$  are identical to the uni-axial case without hardening. Furthermore it is easy to verify that for the case of  $n = 0$  all other expressions will also be identical to the expressions above. At  $n > 0$ , however, closed form expressions for the sought for functions  $k_M(A^p)$  and  $\varphi(A^p)$  are no longer available, because the moment-curvature relation (57) is not solvable analytically. Nevertheless it is still possible to find the plastic curvature and the dissipative work as functions of the total curvature:

$$\kappa^p(\kappa) = \begin{cases} 0, & \kappa \leq \kappa_* \\ \frac{8k^3(1-n)-3k^3 2^{1-n} \left(\frac{Eh\kappa}{k}\right)^{n+2}}{E^3 h^3 \kappa^2 (n+2)} + \kappa, & \kappa > \kappa_* \end{cases} \quad (58)$$

$$\begin{aligned} A^p &= 2 \int_{z^p}^{h/2} A_3^p dz = 2 \int_{z^p}^{h/2} \frac{k(E\kappa z - k) \left(\frac{E\kappa z}{k}\right)^n}{E} dz = \\ &= \frac{2^{-n-1} \left(Eh\kappa k(Eh\kappa(n+1) - 2k(n+2)) \left(\frac{Eh\kappa}{k}\right)^n + k^3 2^{n+2}\right)}{E^2 \kappa (n+1)(n+2)}. \end{aligned} \quad (59)$$

Equations of the general structural plate model remain unchanged. We again identify the function  $\varphi$  according to (41), which is available in dependence on the total curvature:

$$\varphi(\kappa) = \frac{Eh^3 k \left(3k^2 n \left(\frac{Eh\kappa}{k}\right)^{n+2} + k^2 2^{n+3} (1-n)\right)}{3 \left(E^3 h^3 \kappa^3 2^n (n+2) - 6k^3 n \left(\frac{Eh\kappa}{k}\right)^{n+2} - k^3 2^{n+4} (1-n)\right)}. \quad (60)$$

As our implementation rests upon the dissipative work  $A^p$  being the internal hardening variable, we deal with this problem by first numerically solving the Equation (59) for  $\kappa$  and then substituting this numerically obtained characteristic in (60), such that  $\varphi(A^p)$  can be evaluated. The necessary isotropic hardening function  $k_M(A^p)$  follows by integration, which is now only numerically possible. However, as  $\varphi(A^p)$  is singular in the vicinity of the initial state  $A^p = 0$ , numerical integration proves to be challenging. We approach this issue by introducing the function  $\frac{d(k_M^2)}{d\kappa}$ , which is available analytically:

$$\frac{d(k_M^2)}{d\kappa} = \varphi \frac{dA^p}{d\kappa}, \quad (61)$$

see (37). Subsequently, by the use of (59) and (60) it is possible to analytically derive the lengthy expression for the derivative (61). The thus gained function is valid for  $\kappa \geq \kappa_*$  and is no longer singular. Therefore, numerical integration can be carried out very easily and provides us with  $k_M(\kappa)$ . The sought for dependence  $k_M(A^p)$  follows with the use of the numerical characteristic  $\kappa(A^p)$ .

#### 4 | ELASTIC-PLASTIC RESPONSE OF A THROUGH-THE-THICKNESS ELEMENT

Prior to proceeding to finite-element simulations for a whole plate, we validate the derived local constitutive relations by comparing curvature-moment characteristics of a through-the-thickness element, computed for a particular parameter set using both the structural mechanics equations as well as continuum mechanics solutions. The latter continuum mechanics solutions are available analytically for simple cases of uni-axial and isotropic bending, but they result from numerical integration of systems of differential equations when the direction of the bending moment is changing in time. The used set of parameters for all subsequent comparisons is provided in Table 1; SI system of units will be used throughout the paper.

We begin with a *uni-axial bending experiment* and use the previously derived continuum solution of (25). A solution for the structural plate model follows after the integration of the system of ordinary differential Equations (36).

A moment-driven simulation is considered, such that the bending moment  $M(t)$  is known and monotonously increasing in time. Remaining with the assumption of ideal elastic-plastic continuum, we test both previously identified hardening functions, derived respectively for uni-axial and isotropic bending. Subsequently we solve the system of differential equations numerically and obtain  $\kappa_x^p(t)$  and  $A^p(t)$ . Thus, by inverting the relation, and by considering the elastic range by means of the elastic law, given in (4), we acquire the complete moment-curvature characteristic. Finally, all three moment-curvature characteristics are depicted in Figure 1. Besides the general good correspondence of both structural models to the continuum one, we also note that the solution with the hardening function, identified for the uni-axial bending problem, expectedly shows slightly better correspondence, in particular in the beginning of the plastic stage.

We also perform a similar experiment for the case of *isotropic bending*. The continuum solution for the moment-curvature characteristic is given by (51). And for the structural plate solution we need to solve the previously introduced system of ordinary differential equations (54) under consideration of (37). The three moment-curvature characteristics are plotted in Figure 2.

We again observe, that the solution with the corresponding hardening function, obtained for the isotropic bending case, longer remains very close to the reference continuum solution.

To further support the conclusion, that the introduced structural plate model shows very satisfying results, we consider a more complicated loading scenario. The loading is applied quasi-statically, the bending moment is now not only

TABLE 1 Sample model parameters in SI system of units

Parameter	$E$	$\nu$	$k$	$h$
Value	$2.1 \cdot 10^{11}$	0.3	$250 \cdot 10^6$	0.01

FIGURE 1 Comparison of moment-curvature characteristics for uni-axial bending

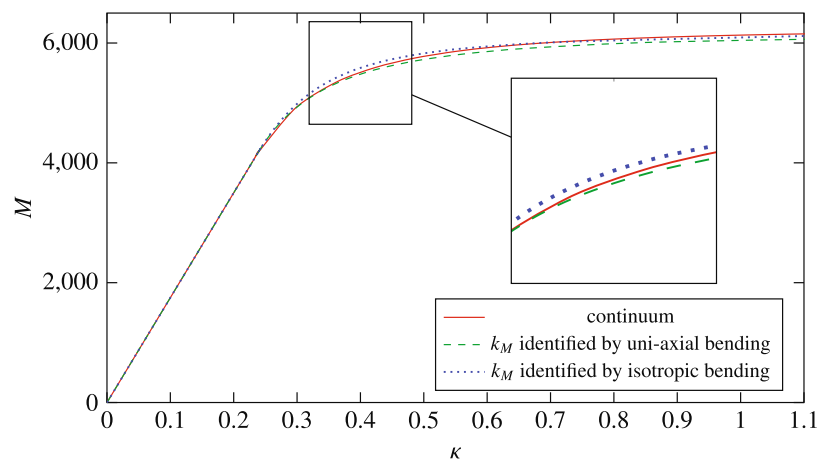
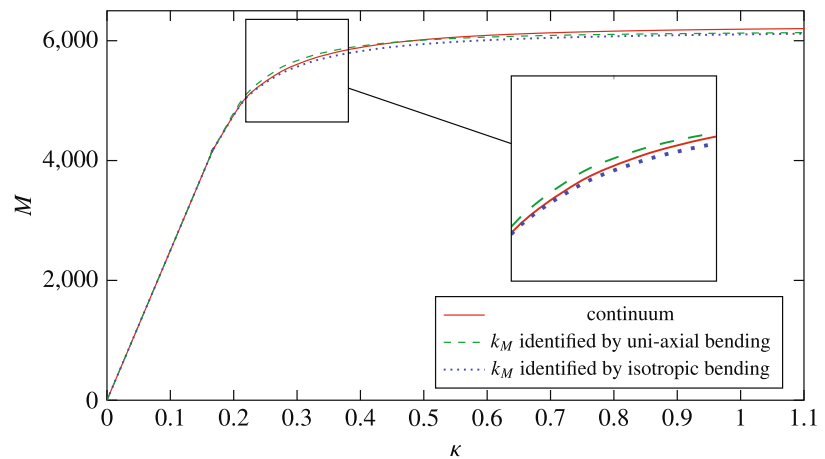


FIGURE 2 Comparison of moment-curvature characteristics for isotropic bending



increasing monotonously in time, but its *direction is rotating*, such that the assumption of proportional loading no longer holds and the continuum solution is not directly available. The tensor of bending moment changes now in time according to the law

$$\mathbf{M}(t) = M(t)(\cos^2\theta(t)\mathbf{e}_x\mathbf{e}_x + \cos\theta(t)\sin\theta(t)(\mathbf{e}_x\mathbf{e}_y + \mathbf{e}_y\mathbf{e}_x) + \sin^2\theta(t)\mathbf{e}_y\mathbf{e}_y), \quad (62)$$

with the magnitude of the bending moment  $M$  and its rotation angle  $\theta$  varying linear in time:

$$M(t) = M_*^e + (0.95M_*^p - M_*^e)t, \quad \theta(t) = \frac{\pi}{2}t, \quad (63)$$

the dimensionless time variable changes from 0 to 1. Plasticity starts with the bending moment  $M_*^e$  in  $x$  direction, and in the end of the simulation we reach 95% of the maximal possible bending moment  $M_*^p$  in  $y$  direction.

We begin the analysis with the structural model. Equilibrating the externally imposed moments (62) with the elastic response (4) and furthermore considering the additive decomposition of the total curvature (6), we obtain the components of the tensor of total curvatures:

$$\begin{aligned} \kappa_x &= \frac{12M(\cos^2\theta - \nu\sin^2\theta)}{h^3E} + \kappa_x^p, \\ \kappa_{xy} &= \frac{6(1+\nu)M\sin 2\theta}{h^3E} + \kappa_{xy}^p, \\ \kappa_y &= \frac{6(1-\nu - (1+\nu)\cos 2\theta)M}{h^3E} + \kappa_y^p. \end{aligned} \quad (64)$$

We substitute these relations in the governing differential Equations (11), (12), and (14). The differential equations for the plastic curvature components and the dissipative work follow after elimination of the plastic consistency parameter  $\lambda$ :

$$\begin{aligned} \dot{\kappa}_x^p &= \frac{1 + 3\cos 2\theta}{2\varphi(A^p)}\dot{M}, & \dot{\kappa}_{xy}^p &= \frac{3\cos\theta\sin\theta}{\varphi(A^p)}\dot{M}, \\ \dot{\kappa}_y^p &= \frac{1 - 3\cos 2\theta}{2\varphi(A^p)}\dot{M}, & A^p &= \frac{2M}{\varphi(A^p)}\dot{M}. \end{aligned} \quad (65)$$

We restrict the consideration to the hardening function (43), identified for the case of uni-axial bending, and numerically integrate the obtained system of differential equations. Using (64), we find the time histories of the components of the total curvature tensor, which are plotted in Figure 3 in comparison to the purely uni-axial case  $\theta = \pi/2$ , that is, when the bending moments acts along the  $y$ -axis all the time:  $\mathbf{M} = M(t)\mathbf{e}_y\mathbf{e}_y$ .

The final values at  $t = 1$  with  $\theta = \pi/2$ , which correspond to the same bending moment  $\mathbf{M} = 0.95M_*^p\mathbf{e}_y\mathbf{e}_y$ , are clearly different. From these results we see, that the time history of the applied bending moment affects the current elastic-plastic

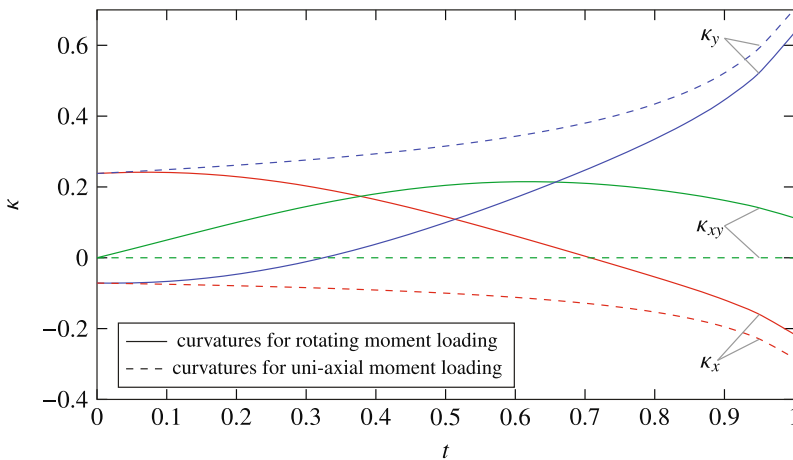


**FIGURE 3** Comparison of time histories of curvature components for rotating bending moment versus uni-axial moment



response of the plate. A few other observations can be made. In the very beginning at  $t = 0$  both solutions are yet purely elastic and rotated with respect to each other, in the same way as the applied moments. Here we also notice that the ratio between both diagonal components of the elastic curvature is exactly  $\nu$ . The non-diagonal curvature component  $\kappa_{xy}$  becomes nonzero only when the moment is rotating.

Ultimately, we seek to validate the results against the continuum model for the case of rotating moment. In the absence of an analytical solution, we need to replace the integral for the total bending moment (19) by a sum using a quadrature formula with discrete integration points. Each of the points contributes to  $\mathbf{M}$ , and the local strain components in the plane of the plate are determined by the total curvature similar to (17). This makes the moment-driven problem formulation complicated, because the elastic-plastic deformation processes in all the integration points are coupled. We simplify our task and use the previously obtained time history  $\kappa(t)$  from the solution with the structural theory as an input for the continuum model, which makes the computation straightforward. The plate kinematics provides us with the plane part of the three-dimensional strain tensor  $-\kappa z$ . Presuming the plane stress state in the entire through-the-thickness element and using the yield condition in the form (48), we integrate the local stress-strain relation over time in each integration point, find stresses  $\tau(z, t)$  and then compute the time history of the resulting moments  $\mathbf{M}(t)$  by integration of (19) using five equidistant integration points in the upper half of the through-the-thickness element  $0 \leq z \leq h/2$ . Time histories of the components of the computed moment tensor are compared against the originally imposed one (62) in Figure 4. The observed correspondence convinces us, that the developed structural theory consistently describes the constitutive behavior of the significantly more complicated continuum plate model in the broad range of loading conditions.

### 5 | STRUCTURAL PLASTICITY MODEL IN A FINITE ELEMENT SIMULATION

We approximate the deflection field  $w(x, y)$  using  $C^1$ -continuous four-node Bogner-Fox-Schmitt finite elements with bi-cubic Hermitian shape functions.<sup>24,25</sup> The functional of the elastic strain energy of the isotropic Kirchhoff plate

$$U^{\text{strain}}[w(x, y)] = \int_{\Omega} U \, d\Omega, \quad U = \frac{1}{2} (D\nu(\text{tr } \kappa^e)^2 + D(1 - \nu)\kappa^e \cdot \kappa^e), \tag{66}$$

which comprises the contribution of each finite element with the area  $\Omega_{\text{el}}$ ,

$$U^{\text{strain}} = \sum U_{\text{el}}^{\text{strain}}, \quad U_{\text{el}}^{\text{strain}} = \int_{\Omega_{\text{el}}} U \, d\Omega_{\text{el}}, \tag{67}$$

becomes thus a function of the entire vector of nodal variables  $W$ . In each node  $i$  we have four degrees of freedom, namely the deflection  $w_i$ , its first derivatives  $(\partial_1 w)_i, (\partial_2 w)_i$  as well as the mixed second-order derivatives  $(\partial_1 \partial_2 w)_i$ , in which  $\partial_\alpha$

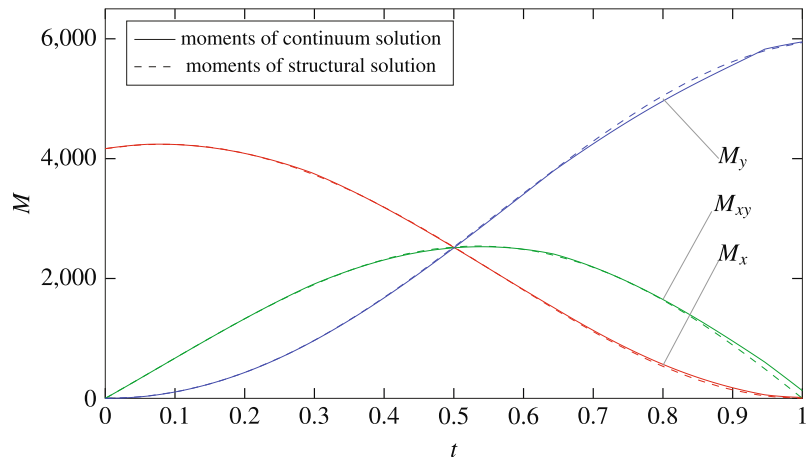


FIGURE 4 Comparison of time histories of moment components of continuum versus structural theory

stands for the derivative with respect to the local coordinate on the element  $q_\alpha$ ,  $\alpha = 1, 2$ . Rectangular elements are used in the following, such that the Cartesian coordinate  $x$  depends only on the local coordinate  $q_1$ , and  $y$  only on  $q_2$ . The variable element size in the below considered examples and the requirement regarding continuity of the deflection gradient  $\nabla w$  imply, however, that the function  $x(q_1)$  is nonlinear, such that the geometry is also smoothly approximated across the element boundaries.

We seek the state of equilibrium by minimizing the total energy of the system

$$U^\Sigma = U^{\text{strain}} + U^{\text{ext}} \rightarrow \min, \quad (68)$$

with the potential energy of external distributed forces

$$U^{\text{ext}} = - \int_{\Omega} \gamma q(x, y) w(x, y) \, d\Omega; \quad (69)$$

the load factor  $\gamma$  grows incrementally from 0 to 1. In the considered geometrically linear setting the energy  $U^\Sigma$  is quadratic in the kinematic variables  $W$ . For a given distribution of plastic curvatures  $\kappa^p(x, y)$ , the energy is minimized by solving a system of linear equations for  $W$ :

$$U^{\text{strain}} = \frac{1}{2} W^T K W - W^T F^p, \quad U^{\text{ext}} = -\gamma W^T F^e \quad \Rightarrow \quad K W = (F^p + \gamma F^e). \quad (70)$$

Here  $K$  is the stiffness matrix of the elastic plate, the force vector  $F^e$  is determined by the externally applied loading, and the vector  $F^p$  depends on the distribution of the plastic curvature, because of  $\kappa^e = \kappa - \kappa^p$  in (66). The integrals (67) are evaluated numerically using  $3 \times 3$  Gaussian quadrature rule. Plastic curvature values need to be available in each integration point of the model.

As soon as the yield criterion

$$f(\mathbf{M}) \leq k_M^2(A^p), \quad (71)$$

is violated in at least one of the integration points, the rate Equations (11)–(14) need to be integrated over time. For sufficiently small increments of the load factor  $\gamma$ , the yield criterion function of the new moment tensor  $f(\mathbf{M})$  exceeds the current value of  $k_M^2$  by just a small value, and we shall use linearized approximation of both terms in order to accurately integrate the evolution law over time. The update of the local plastic variables  $\kappa^p$  and  $A^p$  within a load increment is performed such, that both sides of the consistency condition (71) become equal for the new values. The flow rule (11) closes the problem, making the solution for the local increments  $\Delta \kappa^p$  and  $\Delta A^p$  unique. This leads us to the following formulation of the classical *elastic predictor - plastic corrector* return mapping algorithm<sup>26,27</sup> for the structural plasticity model.

From the differential relation for the dissipative work (12) we find

$$\Delta A^p = 2f \, \Delta \lambda, \quad \Delta k_M^2 = 2k_M k_M' \, \Delta A^p = 2\varphi f \, \Delta \lambda. \quad (72)$$

Demanding the consistency condition  $f + \Delta f = k_M^2 + \Delta k_M^2$  to be fulfilled after the update, we write

$$f + \frac{\partial f}{\partial \lambda} \Delta \lambda = k_M^2 + 2\varphi f \, \Delta \lambda \quad \Rightarrow \quad \Delta \lambda = \frac{f - k_M^2}{2\varphi f - \frac{\partial f}{\partial \lambda}}. \quad (73)$$

Here the value of  $f$  is to be evaluated for the new deformed state with updated kinematic degrees of freedom  $W$ . Its derivative with respect to the consistency parameter  $\lambda$  follows by first substituting the flow rule (11) into the additive decomposition of the curvature tensor (6) considering the total curvature  $\kappa = \text{const}$ , then finding the time derivative of the moment tensor  $\mathbf{M}$  from the elastic law (4), and finally substituting the result into (9) and dividing by  $\dot{\lambda}$ . In Cartesian components the result of this computation reads

$$\frac{\partial f}{\partial \lambda} = -D\nu(M_x + M_y)^2 - D(1 - \nu)(5M_x^2 + 18M_{xy}^2 - 8M_x M_y + 5M_y^2). \quad (74)$$

Having computed  $\Delta\lambda$ , we immediately obtain the increment of the dissipative work from (72) and that of the plastic curvature from

$$\Delta\mathbf{\kappa}^p = \frac{\partial f}{\partial \mathbf{M}} \Delta\lambda = (3\mathbf{M} - \mathbf{I} \operatorname{tr} \mathbf{M}) \Delta\lambda. \quad (75)$$

Clearly, the update of the plastic variables changes the internal moments in the plate and results in the violation of the equilibrium equation. Updating the kinematic degrees of freedom and thus the deformations according to (70) once more, we again need to adjust the plastic variables, which results into a kind of fixed-point iterations, see Reference 28. The iterations will in most cases converge to a state, in which all conditions are fulfilled and which is thus the solution of the problem for the current value of the load factor  $\gamma$ . The next load increment shall be processed.

The algorithm is simple and each iteration is efficient, as the constant elastic stiffness matrix  $K$  can be decomposed in advance. This advantage is, however, outweighed by the slow (linear) convergence rate of the iterations. The asymptotic quadratic rate of convergence of the Newton method is achieved by using the *elastoplastic tangent stiffness matrix*  $K^t$ , which is no longer a matrix of the quadratic form of the strain energy, but rather originates from the equilibrium condition in form of the principle of virtual work. Thus, the virtual work of external forces is a linear form

$$\delta A^e = \int_{\Omega} \gamma q \delta w \, d\Omega = \delta W^T \gamma F^e, \quad (76)$$

the virtual work of internal forces reads

$$\delta A^i = - \int_{\Omega} \mathbf{M} \cdot \delta \mathbf{\kappa} \, d\Omega = \delta W^T F^i, \quad (77)$$

and the principle of virtual work  $\delta A^e + \delta A^i = 0$  leads to the equilibrium equation

$$\gamma F^e + F^i = 0. \quad (78)$$

The variations of the nodal variables  $\delta W$  determine the virtual deflections  $\delta w$  and variations of total curvatures  $\delta \mathbf{\kappa}$  via the finite element kinematics. The coefficients of the linear form of the virtual work of internal forces are

$$F_j^i = - \int_{\Omega} \mathbf{M} \cdot \frac{\partial \mathbf{\kappa}}{\partial W_j} \, d\Omega. \quad (79)$$

Here the derivative of the curvature tensor with respect to the degree of freedom  $W_j$  follows directly from the kinematics and does not depend on  $W$  in the geometrically linear model. In the absence of active plastic flow we obtain  $F^i = F^p - KW$  and further again (70). The Newton method for the equilibrium Equation (78) features increments of nodal variables  $\Delta W$ , which result from the linear system of equations

$$K^t \Delta W = \gamma F^e + F^i, \quad (80)$$

with the system matrix being

$$K^t = - \frac{\partial F^i}{\partial W}; \quad (81)$$

the external forces are constant. Using (79), we compute the components of the tangent stiffness matrix:

$$K_{ij}^t = \int_{\Omega} \frac{\partial \mathbf{M}}{\partial W_i} \cdot \frac{\partial \mathbf{\kappa}}{\partial W_j} \, d\Omega. \quad (82)$$

Finding the derivative of the tensor of moments is easy in the elastic zones,

$$\frac{\partial \mathbf{M}}{\partial W_i} = \frac{\partial \mathbf{M}}{\partial \mathbf{\kappa}^e} \cdot \frac{\partial \mathbf{\kappa}}{\partial W_i}, \quad (83)$$

because here the rates of the total curvature and of the elastic curvature are equal. The symmetric fourth rank tensor of the derivative of the moment with respect to  $\kappa^e$  follows directly from the elasticity law (4). In the points with active plastic flow, the derivative of the moment tensor in (82) must take into account the nonvanishing rate of plastic curvature, such that  $d\kappa^e = d\kappa - d\kappa^p$ , and

$$\frac{\partial \mathbf{M}}{\partial W_i} = \frac{\partial \mathbf{M}}{\partial \kappa^e} \cdot \left( \frac{\partial \kappa}{\partial W_i} - \frac{\partial \kappa^p}{\partial W_i} \right). \quad (84)$$

Similar to the incremental form (73) and (75) we write

$$\frac{\partial \kappa^p}{\partial W_i} = \frac{\partial f}{\partial \mathbf{M}} \frac{\partial \lambda}{\partial W_i}, \quad \frac{\partial \lambda}{\partial W_i} = \frac{1}{2\varphi f - \frac{\partial f}{\partial \lambda}} \frac{\partial f}{\partial W_i}, \quad \frac{\partial f}{\partial W_i} = \frac{\partial f}{\partial \mathbf{M}} \cdot \frac{\partial \mathbf{M}}{\partial \kappa^e} \cdot \frac{\partial \kappa}{\partial W_i}. \quad (85)$$

Note that the derivative of the yield criterion function  $\frac{\partial f}{\partial W_i}$  is computed for constant plastic curvature  $\kappa^p$ . As it is always the case when the associated flow rule is used, the tangent stiffness matrix is symmetric:  $K_{ij}^t = K_{ji}^t$ , which greatly simplifies the implementation. This symmetry follows directly from the definition (82) and formulas (84), (85). In the numerical experiments below, the Newton iterations with the updated matrix  $K^t$  converge rapidly as soon as the set of integration points with active plastic flow is no longer changing significantly between the iterations.

The discussed backward time integration scheme produces accurate results for small load increments. In the numerical examples below we applied an adaptive refinement scheme. The load increments  $\Delta \gamma$  are reduced, if in the course of Newton iterations the intermediate value of  $f$  in (73) exceeded the current level of  $k_M^2$  by more than 50%, which guarantees accurate solution. From the point of view of implementation, it is efficient to store in each integration point the current values of  $\varphi$  and  $k_M$  along with the primary plastic variables and to keep them constant during the Newton iterations for a given load increment. This greatly reduces the number of calls to the computationally expensive numerical solver for the Equation (59), which is relevant if material hardening is taken into account.

For the sake of comparison, in the following we also present results of computations with the continuum plasticity model, which features five equidistant integration points in the upper half of the plate  $0 \leq z \leq h/2$ . In each integration point the plane stress plasticity equations are integrated using the conventional return mapping algorithm with the tangent stiffness matrix according to Reference 26.

## 6 | BENCHMARK RESULTS FOR A SQUARE PLATE

We begin by considering the conventional numerical example of a simply supported square plate under uniformly distributed loading  $q = \text{const}$ , without material hardening (see Reference 10). Upon incrementally increasing the load, we observe that the plastic deformation first appears in the corners of the plate. Because the bending moment tensor near the edges of the plate cannot be isotropic we expect the hardening function  $k_M$ , which is identified by uni-axial bending experiment, to be more appropriate in this case. Motivated by this consideration, we used the expression (44) for the below simulations with the structural plate model. The model parameters are according to Reference 10 and are provided in Table 2;  $\ell = b$  is the length and the width of the plate.

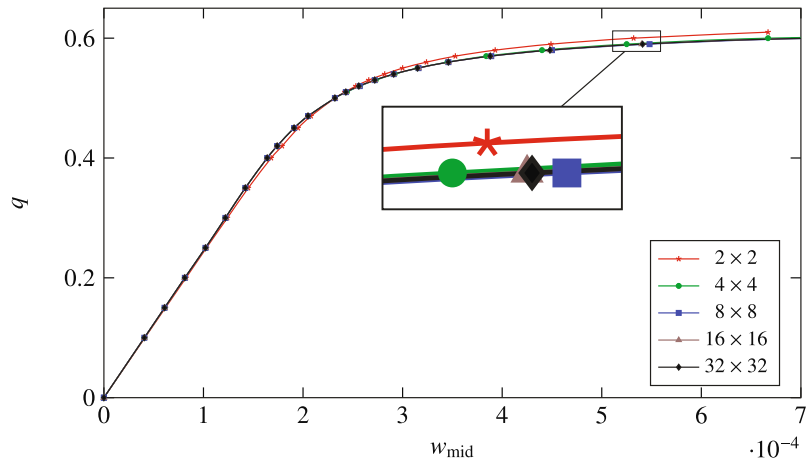
Prior to comparing the results of the general structural plate model to the other simulation, we conduct a convergence study by virtue of computing the inelastic response in form of the displacement of the center point of the plate  $w_{\text{mid}}$  for growing load values  $q$ . The results are provided in Figure 5 for various meshes.

Each marker in this load-displacement diagram corresponds to a certain load level  $q$ ; note the uneven distribution of load increments, which results from the limitation of the maximal plastic flow for the sake of accuracy of the numerical integration. We observe that the deflections for the same load levels become barely distinguishable for the two finer finite element discretization levels even in the higher range of  $q$  when the structure approaches the plastic collapse. Therefore,

Parameter	$\ell$	$b$	$E$	$\nu$	$k$	$h$
Value	10	10	$10.92 \cdot 10^8$	0.3	1000	0.1

TABLE 2 Simulation parameters for the simply supported square plate in SI system of units

FIGURE 5 Uniform loading-center displacement diagram for the middle point of the plate at different meshes



we consider results for the  $32 \times 32$  uniform mesh as converged and use this mesh for further simulations regarding the square plate.

We proceed by comparing the obtained load-displacement diagram to a full continuum solution with a solid model of the three-dimensional body of the plate computed in ABAQUS and to a continuum plasticity model of the plate, which features five equidistant integration points in the upper half of the plate  $0 \leq z \leq h/2$  and is handled by the classical plasticity formulation with the return mapping algorithm according to Reference 26. Since the latter model is handled within the same finite element discretization which is used for the structural plate model, the mesh and the type of the elements are identical. As for the full continuum ABAQUS model, a uniform mesh of  $100 \times 100$  C3D20 (20-noded quadratic brick) elements in the plane and four elements over the thickness is used.

In Figure 6, very good compliance between the new general structural plate model and classical continuum approaches is seen. Comparing to the solution results available in Reference 10 (dots in Figure 6), we notice certain differences, although both solutions are obtained without the consideration of material hardening. Despite the use of the shear-deformable Reissner–Mindlin plate theory by the authors of Reference 10 and the relatively high thickness of the plate, the successful comparison against the full three-dimensional solution convinces us that the new structural plate model is indeed sufficiently accurate. The observed lower accuracy of the results of Reference 10 is explained by the fact, that this model does not take into account the spreading of plasticity through the thickness. Nevertheless, it is capable of predicting the limit loads. The lower and upper bounds for the estimation of the limit load parameter (plastic collapse) are analytically computed in Reference 10 according to the results of a limit analysis by the application of the yield-line theory, see Lubliner.<sup>8</sup>

$$q_L = \frac{8M_*^p}{\ell b} \left( \frac{\ell}{b} + \frac{b}{\ell} + \frac{1}{\sqrt{3}} \right) = 0.515, \quad q_U = \frac{24M_*^p}{\ell b \sqrt{3}} \left( \frac{\ell}{b} + \frac{b}{\ell} \right) = 0.693. \quad (86)$$

Here  $\ell = b$  for the square plate (see Table 2) and  $M_*^p$  follows from (26). From Figure 6 we conclude that like in Reference 10 our limit load (around  $q = 0.61$ ) also falls within the given analytically estimated interval as it should.

In Figure 7 we demonstrate the results of a simple convergence study regarding the effect of the number of integration points over the thickness in the continuum model. It justifies the necessity to use five equidistant integration points over the upper half of the plate. The computationally cheaper models with just 2 or 3 integration points result into a considerably less-accurate load-displacement diagram, which underlines the relevance of the present study.

The actual gain in the efficiency of the structural model is demonstrated by the comparison of computation times, needed to obtain the results of Figure 6. From Table 3 we see, that the stress resultant model is almost twice as efficient as the traditional continuum one. Similar relation of the efficiency was observed for further benchmark examples as well.

We proceed with the comparison of the growth of the plastic zones between the structural plate model and the continuum plate model.

In Figure 8 the used uniform mesh and the boundaries of the developed plastic zones for three different load levels, namely  $q = 0.40$ ,  $q = 0.45$ , and  $q = 0.55$  are shown. The closed boundary curves (dashed for continuum plate and solid

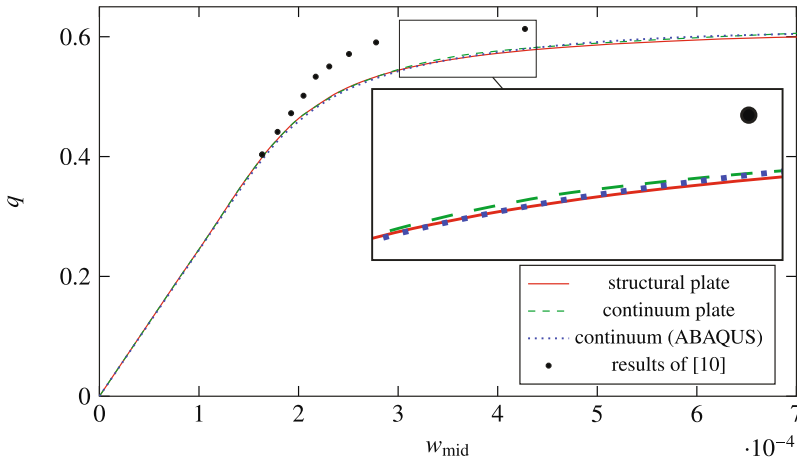


**FIGURE 6** Uniform loading-displacement diagram: structural plate versus continuum plate versus full continuum

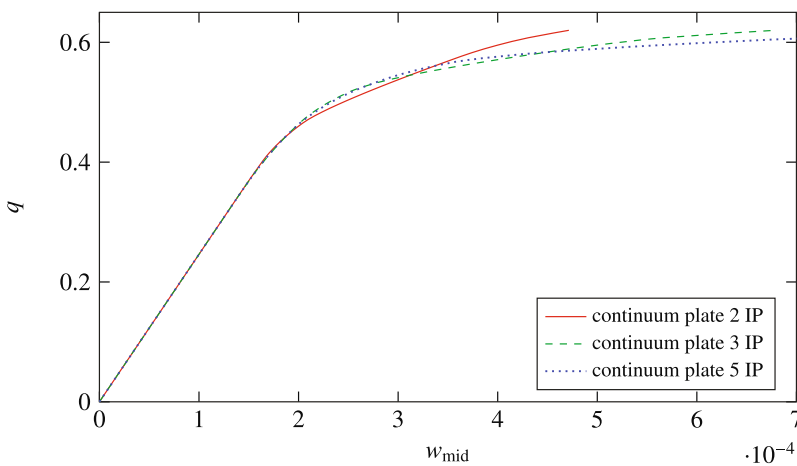


**FIGURE 7** Convergence study: influence of the number of integration points (IP) in the upper half of the continuum plate on the load-displacement diagram

Model	Structural plate model	Continuum plate model
Used CPU time in seconds	46	86

**TABLE 3** Comparison of CPU times: structural plate model versus continuum model with five integration points in the upper half of the plate

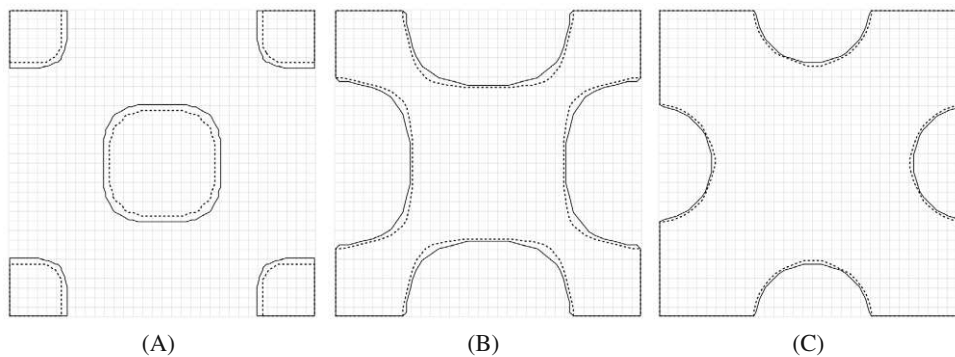


**FIGURE 8** Comparison of plastic zones of structural plate (solid line) versus continuum plate (dashed line). (A)  $q = 0.40$ ; (B)  $q = 0.45$ ; (C)  $q = 0.55$

lines for structural plate) enclose areas with nontrivial plastic strains in the integration points. We observe that a fifth plastic zone appears in the center of the plate as  $q$  is growing in addition to the four initiated in the corners. At some load levels they all merge into a single large plastic zone. Again, good agreement between the structural mechanics and the continuum plasticity models is observed.

We conclude this section by analyzing a loading—reverse loading—loading scenario for the here considered simply supported square plate under uniformly distributed loading. Although it is theoretically clear, that the presented structural model cannot accurately reflect reverse plasticity because of the purely isotropic hardening, the experimental demonstration sheds more light onto the issue. In Figure 9 we compare load-displacement diagrams with nonmonotonous loading history for the continuum and the structural mechanics models.

Both solutions are very close during the initial loading. The maximal force levels in both models are slightly different and chosen such, that the middle point deflections in the end of the initial loading stage are the same and equal  $w_{\text{mid}} = 5 \cdot 10^{-4}$ . Such displacement-controlled loading results in a more informative diagram.

During the reverse loading we steadily change the direction of the distributed force, while its magnitude in the end of this stage is the same. The observed differences are explained by the Bauschinger effect in the continuum plate model, in which yielding occurs earlier than in the structural plate model with just the isotropic hardening. The symmetric hysteresis loop of the continuum model does better correspond to the theoretical expectations.<sup>8,29</sup> Nevertheless, results presented in Figure 4 support the conclusion, that the range of applicability of the structural model reaches far beyond the purely proportional and monotonous loading scenarios.

## 7 | BENCHMARK RESULTS FOR A RECTANGULAR PLATE

Another appropriate benchmark problem with simulation results available in the open literature is a rectangular plate under uniformly distributed loading with ideal elastic-plastic material, considered by Dujc and Brank<sup>12</sup> with the account of gradual spreading of plasticity through the thickness. The model used in Reference 12 features an adapted Ilyushin yield criterion with the time-varying yield moment  $m_0^*(\alpha) = \alpha(t)m_0$  as proposed earlier by Crisfield.<sup>11</sup> The time evolution law for the field variable  $\alpha(t)$  is designed such, that it matches the uni-axial bending experiment. This allows capturing the mentioned effect of the development of plastic zones in a through-the-thickness element and results in a good correspondence with continuum mechanics solutions. The degree of this agreement depends, however, on the boundary conditions, as their choice determines the locations and shapes of the plastic zones in the plate. Therefore we chose the case with simply supported edges, as it results into a slightly worse agreement between the stress resultant and ABAQUS solutions in Reference 12. The parameters of the benchmark example are summarized in Table 4.

We discretized the domain with  $60 \times 40$  finite elements, which formally corresponds to the discretization used in Reference 12—although with different shape functions. In Figure 10 we compare the results of our structural mechanics model to the one from Reference 12 (obtained by sampling the graphical data of the published paper). We also plot the

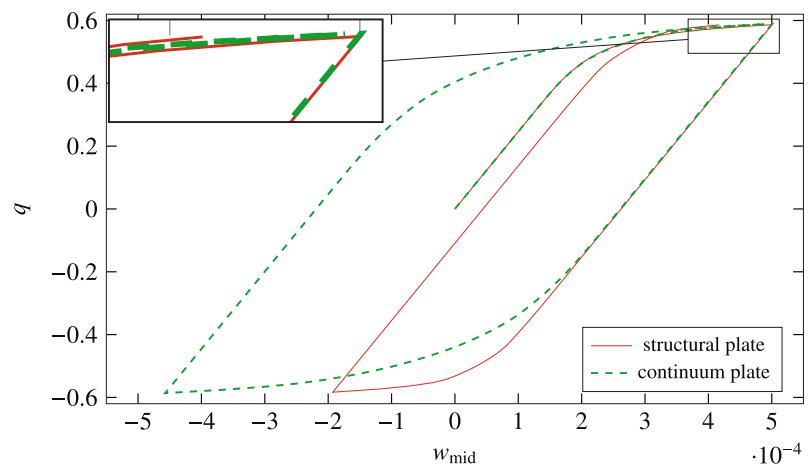


**FIGURE 9** Uniform loading-displacement for the loading—reverse loading—loading scenario: structural plate versus continuum plate

solution of the plate model with  $60 \times 40$  S4R (quadrilateral shell) elements with 10 integration points over thickness, computed in ABAQUS for the sake of reference.

We see, that the stress resultant plate model of Reference 12 tends to overestimate the deformation in the earlier plastic phase and to underestimate it in the latter plastic state. The slight nonsmoothness of the respective curve is due to the time integration strategy for the parameter  $\alpha(t)$ , which is considered constant within a time step. While the model<sup>12</sup> shows much better correspondence to the reference ABAQUS solution for a clamped plate, the accuracy of the present approach appears to be essentially less affected by the particular choice of the boundary conditions and loading.

## 8 | BENCHMARK RESULTS FOR AN ELONGATED PLATE WITH SELF-EQUILIBRATED LINE LOADING

In the last example problem we address an elongated rectangular plate ( $\ell > b$ ) with loading, which resembles the force distribution occurring during the roll forming process. The left boundary of the cantilever plate is clamped and all other boundaries are free. The self-equilibrated loading is distributed along the line in the width direction in the middle of the plate:  $q(x, y) = P(y)\delta(x - \ell/2)$  with  $\delta$  being the Dirac impulse and the load intensity per unit length of the line is

$$P(y) = p \left( \frac{4|y|}{b} - 1 \right), \text{ for } -\frac{b}{2} \leq y \leq \frac{b}{2}; \quad (87)$$

$p$  is the amplitude of the load. Simulation parameters are provided in Table 5 and the distribution of the load along the width of the plate is depicted in Figure 11.

Due to the fact that the considered plate problem shows similarity to a cantilever beam, again the hardening function in the form (44), which is identified for uni-axial bending, is used for the structural plate model.

In the simulations we consider a mesh with 20 elements over the width, while the element size in the length direction is variable, such that finer discretization is reached in the middle of the plate, where the load is acting, see Figure

Parameter	$\ell$	$b$	$E$	$\nu$	$k$	$h$
Value	1.5	1.0	$2.1 \cdot 10^{11}$	0.3	$400 \cdot 10^6$	$5 \cdot 10^{-3}$

TABLE 4 Simulation parameters for the simply supported rectangular plate in SI system of units

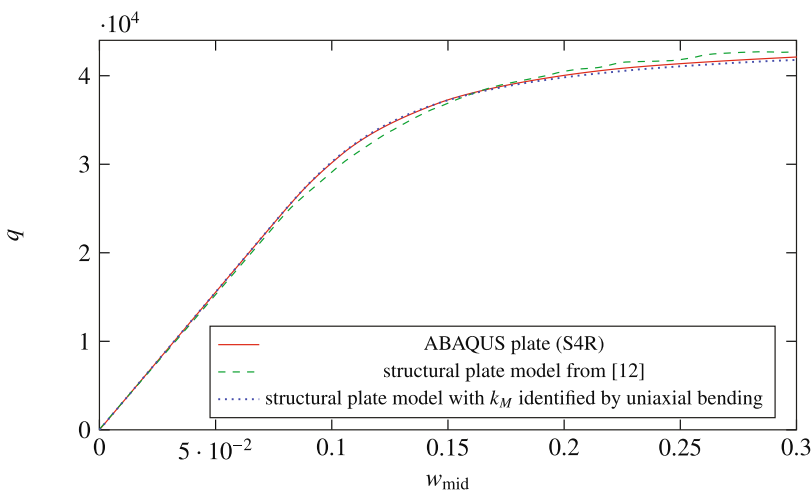


FIGURE 10 Uniform loading-displacement diagram: two structural plate models versus ABAQUS plate

Parameter	$\ell$	$b$	$E$	$\nu$	$k$	$h$	$p$
Value	0.3	0.04	$1.9 \cdot 10^{11}$	0.3	$160 \cdot 10^6$	$6 \cdot 10^{-4}$	12,000

TABLE 5 Simulation parameters for the elongated plate in SI system of units



15. We increased the loading factor in the model, until the specified load amplitude from Table 5 is reached. Afterwards we fully unload the plate, in order to evaluate its new shape as a result of the residual plastic strains. The corresponding deformed shapes of the structural plate model and of the classical continuum plasticity model are shown in Figure 12.

At the edge  $x = 0$  the plate is clamped and no deformation is visible there. The plotted configuration with the larger deflection downwards at the right end corresponds to the residual deformation of the structural plate. This slight difference in the residual deflections far away from the location of the loading should be regarded as insignificant owing to the two reasons:

- it is the shape of the residual deformation of the plate, at the location of action of the rolling forces, which is of actual practical importance for modeling the rolling process and
- minimal differences in the deformed state in the middle of the plate, where plastic deformations are essential, would result into noticeable change of the deflection of its right end because of the long lever arm.

The comparison of both solutions is better visible from the distributions of the deflection in the length direction  $w(x, 0)$  provided in Figure 13 and in the width direction in the middle of the plate  $w(\ell/2, y)$  plotted in Figure 14, which further underlines the similarity between the computed deformed shapes within the middle cross-section as a result of the rolling action.

Furthermore, we again highlight the development of the plastic zones, whose configurations for three levels of the load amplitude  $p$  are depicted in Figure 15.

Three plastic zones are observable at lower values of  $p$ , while they later merge into a single one with two small elastic “islands” at the middle transverse line near the points, where the line load intensity  $P(y)$  vanishes.

We conclude the analysis by discussing the results of the structural plasticity model with the account for material hardening, which is important to consider in metal forming processes. Making use of the Swift law (56) with the strain hardening exponent value  $n = 0.26$ , we obtain deflections, plotted by dotted lines in Figures 13 and 14. While the solution

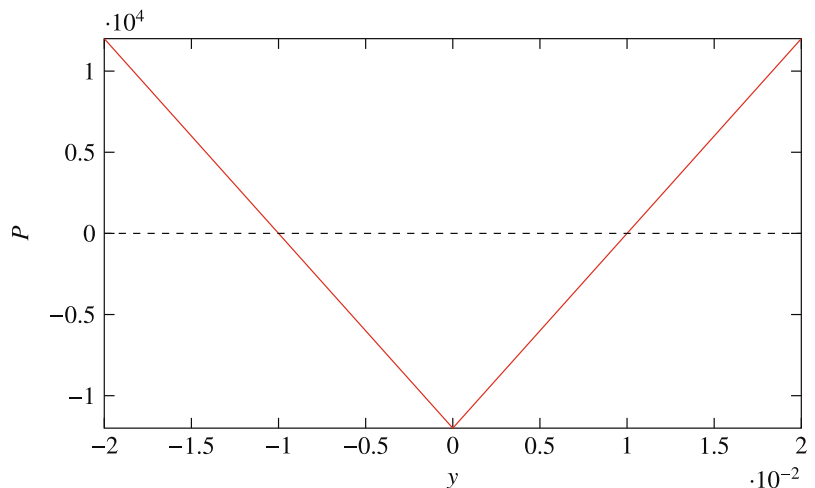


**FIGURE 11** Self-equilibrated line load, which acts along the width, at the center of the plate

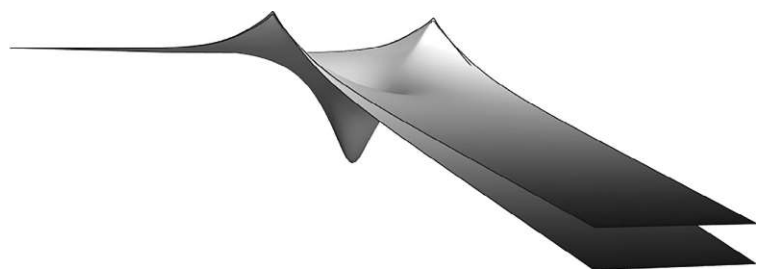


**FIGURE 12** Residual deformation of the structural plasticity and of the continuum plasticity plate models; note the scaling of the deflections by the factor of  $2 \cdot 10^3$ , for the sake of better visualization

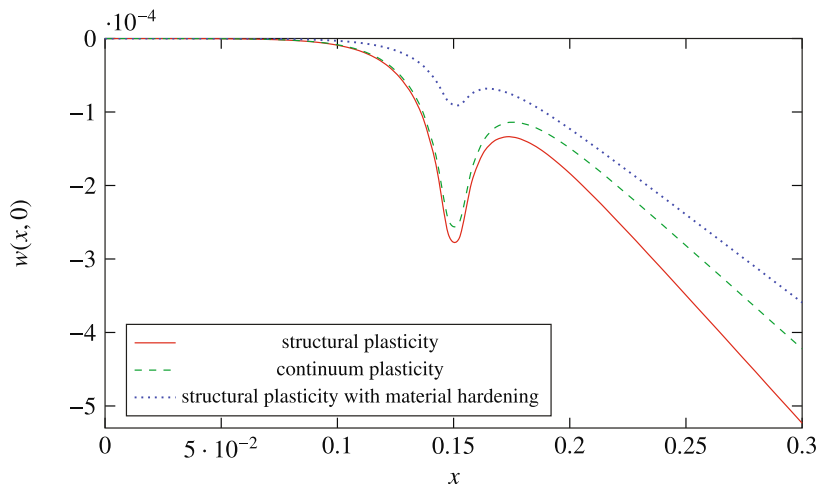


**FIGURE 13** Distribution of the residual transverse deflection  $w(x, 0)$  along the center line of the plate in the length direction, computed for three models of plastic behavior

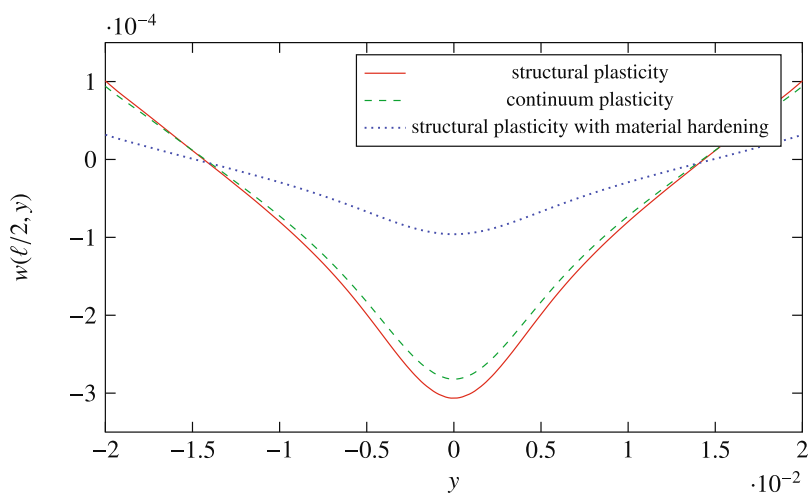


**FIGURE 14** Distribution of the residual transverse deflection  $w(\ell/2, y)$  along the middle transverse line of the plate in the width direction, computed for three models of plastic behavior

does not change qualitatively, the magnitude of the residual deformations expectedly becomes smaller. The shapes of the plastic zones for the same load values change slightly.

## 9 | CONCLUSIONS

Presently, simulations of elastic-plastic response of structural members mostly make use of three-dimensional continuum plasticity laws. Already published attempts to handle plasticity solely on the structural mechanics level and thus to obtain a formulation based on stress resultants only, did not really make it into computational practice because of the issues with reliability, convenience of use, and uncertainties regarding the parameters of the model. In this paper we introduce a novel approach, which we expect to be convenient and efficient for practical applications because of its simplicity, consistency and sound theoretical basis. Thereby, the treatment of the classical inelastic constitutive relations of continuum mechanics in several integration points along the thickness becomes obsolete. This has a remarkable positive impact on the computational efficiency of the simulation. Thus, the computations for above benchmark tests took approximately half the CPU time with the new structural mechanics formulation. We expect the proposed model to be particularly efficient in the field of roll forming simulations, which in their own turn need to be fast for the practically relevant purposes of efficient development of the production process as well as of model-based controller design.

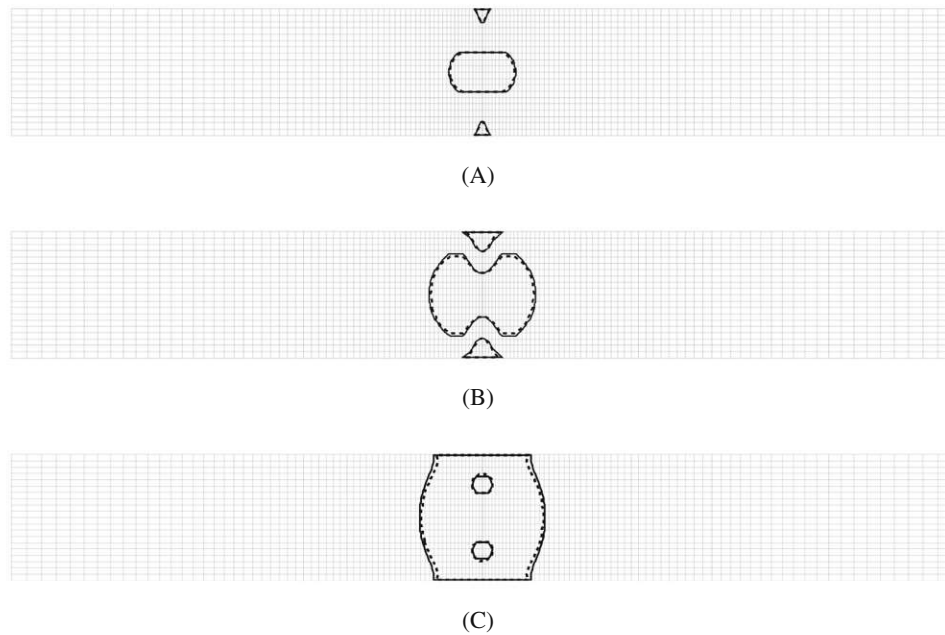



**FIGURE 15** Comparison of plastic zones of structural plate (solid line) versus continuum plate (dashed line). (A)  $p = 8,400$ ; (B)  $p = 10,800$ ; (C)  $p = 12,000$

The basic idea of the proposed structural mechanics plasticity model rests on the identification of a hardening function in the equations featuring curvatures and bending moments. We perform this identification using available analytic solutions for simple loading cases, such as uni-axial or isotropic bending. We restrict the consideration to the isotropic hardening law, because reverse plasticity is not common in roll forming processes. The formulation is presented for both the ideal elastic-plastic material behavior, as well as for isotropic material hardening according to a power law, which is conventionally used in the field of material forming. The finite element structural mechanics model is implemented in the classical form of a return mapping algorithm with tangent stiffness matrix. The proposed approach is validated by comparison against both the full three-dimensional solutions of a benchmark problem as well as against solutions, obtained with the plate theory using integration over the thickness. The comparison results show good accuracy for the considered class of benchmark examples. For future research, we aim at further extending the formulation towards a geometrically nonlinear setting with nonmaterial Eulerian–Lagrangian kinematic description in the spirit of References 4,5. Along with the account for contact conditions, this would allow for realistic simulations of the roll forming process.

#### DATA AVAILABILITY STATEMENT

The data that support the findings of this study are available from the corresponding author upon reasonable request.

#### ORCID

Yury Vetyukov  <https://orcid.org/0000-0001-6931-0099>

#### REFERENCES

1. Halmos GT. *Roll Forming Handbook*. Boca Raton, FL: CRC Press; 2005.
2. Crutzen Y, Boman R, Papeleux L, Ponhot JP. Lagrangian and arbitrary Lagrangian Eulerian simulations of complex roll-forming processes. *Comptes Rendus Mecanique*. 2016;344(4-5):251-266.
3. Vetyukov Y, Gruber P, Krommer M, Gerstmayr J, Gafur I, Winter G. Mixed Eulerian-Lagrangian description in materials processing: deformation of a metal sheet in a rolling mill. *Int J Numer Methods Eng*. 2017;109:1371-1390.
4. Vetyukov Y, Gruber P, Krommer M. Nonlinear model of an axially moving plate in a mixed Eulerian-Lagrangian framework. *Acta Mech*. 2016;227:2831-2842.

5. Scheidl J, Vetyukov Y, Schmidrathner C, Schulmeister K, Proschek M. Mixed Eulerian-Lagrangian shell model for lateral run-off in a steel belt drive and its experimental validation. *Int J Mech Sci.* submitted. <https://doi.org/10.1016/j.ijmecsci.2021.106572>.
6. Ambati M, Kiendl J, De Lorenzis L. Isogeometric Kirchhoff–Love shell formulation for elasto-plasticity. *Comput Methods Appl Mech Eng.* 2018;340:320–339.
7. Ilyushin A. *Plasticity (in Russian)*. Moscow, Leningrad: GITL; 1948.
8. Lubliner J. *Plasticity Theory*. New York, NY: Dover Publications, Inc; 2008.
9. Simo JC, Kennedy JG. On a stress resultant geometrically exact shell model. Part V. nonlinear plasticity: formulation and integration algorithms. *Comput Methods Appl Mech Eng.* 1992;96(2):133–171.
10. Ibrahimbegović A, Frey F. An efficient implementation of stress resultant plasticity in analysis of Reissner-Mindlin plates. *Int J Numer Methods Eng.* 1993;36(2):303–320.
11. Crisfield M. Finite element analysis for combined material and geometric nonlinearities. *Nonlinear Finite Element Analysis in Structural Mechanics*. New York, NY: Springer; 1981:325–338.
12. Dujc J, Brank B. On stress resultant plasticity and viscoplasticity for metal plates. *Finite Elem Anal Des.* 2008;44(4):174–185.
13. Dujc J, Brank B. Stress resultant plasticity for shells revisited. *Comput Methods Appl Mech Eng.* 2012;247:146–165.
14. Chou C, Pan J, Tang SC. Analysis of sheet metal forming operations by a stress resultant constitutive law. *Int J Numer Methods Eng.* 1994;37(5):717–735.
15. Wali M, Autay R, Mars J, Dammak F. A simple integration algorithm for a non-associated anisotropic plasticity model for sheet metal forming. *Int J Numer Methods Eng.* 2016;107(3):183–204.
16. Eliseev VV, Vetyukov YM. Finite deformation of thin shells in the context of analytical mechanics of material surfaces. *Acta Mech.* 2010;209(1–2):43.
17. Vetyukov Y. *Nonlinear Mechanics of Thin-Walled Structures: Asymptotics, Direct Approach and Numerical Analysis*. Berlin, Germany: Springer Science & Business Media; 2014.
18. Lebedev LP, Cloud MJ, Eremeyev VA. *Tensor Analysis with Applications in Mechanics*. Singapore: World Scientific; 2010.
19. Auricchio F, Taylor RL. A generalized elastoplastic plate theory and its algorithmic implementation. *Int J Numer Methods Eng.* 1994;37(15):2583–2608.
20. Vetyukov Y, Kuzin A, Krommer M. Asymptotic splitting in the three-dimensional problem of elasticity for non-homogeneous piezoelectric plates. *Int J Solids Struct.* 2011;48(1):12–23.
21. Ōchsner A. *Elasto-Plasticity of Frame Structure Elements*. New York, NY: Springer; 2016.
22. Kleemola H, Nieminen M. On the strain-hardening parameters of metals. *Metall Trans A.* 1974;5(8):1863–1866.
23. Heislitz F, Livatyali H, Ahmetoglu MA, Kinzel GL, Altan T. Simulation of roll forming process with the 3-D FEM code PAM-STAMP. *J Mater Process Technol.* 1996;59(1–2):59–67.
24. Vetyukov Y. Finite element modeling of Kirchhoff–Love shells as smooth material surfaces. *ZAMM.* 2014;94(1–2):150–163.
25. Bogner F. The generation of interelement-compatible stiffness and mass matrices by the use of interpolation formulas. Paper presented at: Proceedings of the Conference Matrix Methods Structural Engineering Mechanics; 1965:397–443; Wright-Patterson AFB.
26. Simo J, Taylor R. A return mapping algorithm for plane stress elastoplasticity. *Int J Numer Methods Eng.* 1986;22(3):649–670.
27. Crisfield M. *Non-linear Finite Element Analysis of Solids and Structures*. Vol 1. Hoboken, NJ: John Wiley & Sons; 1991.
28. Vetyukov Y, Gerstmayr J, Irschik H. Plastic multipliers as driving variables of numerical simulation in elastoplasticity. *Mech Res Commun.* 2003;30(5):421–430.
29. Mendelson A. *Plasticity, Theory and Application*. New York, NY: MacMillan; 1968.

**How to cite this article:** Kocbay E, Vetyukov Y. Stress resultant plasticity for plate bending in the context of roll forming of sheet metal. *Int J Numer Methods Eng.* 2021;122:5144–5168. <https://doi.org/10.1002/nme.6760>

## Paper B

### *Mixed Eulerian–Lagrangian modeling of sheet metal roll forming*

TU Wien: Emin Kocbay, Jakob Scheidl, Fabian Riegler, Martin Leonhartsberger, Matthias Lamprecht, Yury Vetyukov

*Thin-Walled Structures* Volume 186, May 2023, 110662

<https://doi.org/10.1016/j.tws.2023.110662>

**Keywords:** Mixed Eulerian–Lagrangian description, Kirchhoff–Love shell, Finite element analysis, Metal plasticity, Roll forming

**Abstract:** We propose a nonlinear shell finite element model to simulate sheet metal roll forming, a continuous forming process to produce endless metal profiles. A mixed Eulerian–Lagrangian kinematic description is employed to overcome the drawbacks of the common Lagrangian parametrization. The finite element mesh is detached from the particle motion in axial direction and, thus, facilitates a two-step solution procedure to capture the continuous forming process: First, an equilibrium is sought with the account for contact and plastic flow. Secondly, the material transport is taken into account, which amounts to the integration of an advection problem for the plastic variables. The continuum plasticity model with through-the-thickness integration for the stress resultants guarantees a precise resolution of the forming process in each cross section of the Kirchhoff–Love shell. A series of simulations is carried out to ascertain the convergence of the numerical scheme, to highlight the impact of characteristic parameters and to establish a correspondence to a reference computation with the commercial software Abaqus in a simplified static setting. A physical experiment is devised on an actual roll forming mill to assess the quality of the current computational model.

## References of Paper B

- [1] G. T. Halmos, ed. *Roll Forming Handbook*. 0th ed. CRC Press, 2005. DOI: [10.1201/9781420030693](https://doi.org/10.1201/9781420030693).
- [2] Y. Crutzen et al. Lagrangian and arbitrary Lagrangian Eulerian simulations of complex roll-forming processes. *Comptes Rendus Mécanique* 344.4-5 (2016), 251–266. DOI: [10.1016/j.crme.2016.02.005](https://doi.org/10.1016/j.crme.2016.02.005).
- [3] M. S. Tehrani et al. Localised edge buckling in cold roll-forming of symmetric channel section. *Thin-Walled Structures* 44.2 (2006), 184–196. DOI: [10.1016/j.tws.2006.01.008](https://doi.org/10.1016/j.tws.2006.01.008).
- [4] F. Heislitz et al. Simulation of roll forming process with the 3-D FEM code PAM-STAMP. *Journal of Materials Processing Technology* 59.1-2 (1996), 59–67. DOI: [10.1016/0924-0136\(96\)02287-X](https://doi.org/10.1016/0924-0136(96)02287-X).

- [5] Q. Bui and J. Ponthot. Numerical simulation of cold roll-forming processes. *Journal of Materials Processing Technology* 202.1-3 (2008), 275–282. DOI: [10.1016/j.jmatprotec.2007.08.073](https://doi.org/10.1016/j.jmatprotec.2007.08.073).
- [6] J. Cheng et al. The flower pattern and rolls design for ERW pipes with the different specification in the flexible roll forming process. *Thin-Walled Structures* 154 (2020), 106809. DOI: [10.1016/j.tws.2020.106809](https://doi.org/10.1016/j.tws.2020.106809).
- [7] E. Oborin, Y. Vetyukov and I. Steinbrecher. Eulerian description of non-stationary motion of an idealized belt-pulley system with dry friction. *International Journal of Solids and Structures* 147 (2018), 40–51. DOI: [10.1016/j.ijsolstr.2018.04.007](https://doi.org/10.1016/j.ijsolstr.2018.04.007).
- [8] J. Donea et al. Arbitrary Lagrangian-Eulerian Methods. *Encyclopedia of Computational Mechanics*. Ed. by E. Stein, R. De Borst and T. J. R. Hughes. Chichester, UK: John Wiley & Sons, Ltd, 2004, ecm009. DOI: [10.1002/0470091355.ecm009](https://doi.org/10.1002/0470091355.ecm009).
- [9] V. Longva and S. Sævik. A Lagrangian–Eulerian formulation for reeling analysis of history-dependent multilayered beams. *Computers & Structures* 146 (2015), 44–58. DOI: [10.1016/j.compstruc.2014.09.002](https://doi.org/10.1016/j.compstruc.2014.09.002).
- [10] E. Kuhl, H. Askes and P. Steinmann. An ALE formulation based on spatial and material settings of continuum mechanics. Part 1: Generic hyperelastic formulation. *Computer Methods in Applied Mechanics and Engineering* 193.39-41 (2004), 4207–4222. DOI: [10.1016/j.cma.2003.09.030](https://doi.org/10.1016/j.cma.2003.09.030).
- [11] A. Humer, I. Steinbrecher and L. Vu-Quoc. General sliding-beam formulation: A non-material description for analysis of sliding structures and axially moving beams. *Journal of Sound and Vibration* 480 (2020), 115341. DOI: [10.1016/j.jsv.2020.115341](https://doi.org/10.1016/j.jsv.2020.115341).
- [12] Y. Vetyukov, P. G. Gruber and M. Krommer. Nonlinear model of an axially moving plate in a mixed Eulerian–Lagrangian framework. *Acta Mechanica* 227.10 (2016), 2831–2842. DOI: [10.1007/s00707-016-1651-0](https://doi.org/10.1007/s00707-016-1651-0).
- [13] Y. Vetyukov et al. Mixed Eulerian-Lagrangian description in materials processing: deformation of a metal sheet in a rolling mill: Mixed Eulerian-Lagrangian description in materials processing: deformation of a metal sheet in a rolling mill. *International Journal for Numerical Methods in Engineering* 109.10 (2017), 1371–1390. DOI: [10.1002/nme.5314](https://doi.org/10.1002/nme.5314).
- [14] J. Scheidl et al. Mixed Eulerian–Lagrangian shell model for lateral run-off in a steel belt drive and its experimental validation. *International Journal of Mechanical Sciences* 204 (2021), 106572. DOI: [10.1016/j.ijmecsci.2021.106572](https://doi.org/10.1016/j.ijmecsci.2021.106572).
- [15] V. V. Eliseev and Y. M. Vetyukov. Finite deformation of thin shells in the context of analytical mechanics of material surfaces. *Acta Mechanica* 209.1-2 (2010), 43–57. DOI: [10.1007/s00707-009-0154-7](https://doi.org/10.1007/s00707-009-0154-7).
- [16] Y. Vetyukov. *Nonlinear Mechanics of Thin-Walled Structures: Asymptotics, Direct Approach and Numerical Analysis*. Foundations of Engineering Mechanics. Vienna: Springer Vienna, 2014. DOI: [10.1007/978-3-7091-1777-4](https://doi.org/10.1007/978-3-7091-1777-4).

- [17] F. K. Bogner, R. L. Fox and L. A. Schmit. The generation of interelement compatible stiffness and mass matrices by the use of interpolation formulae. *Proc. Conf. Matrix Methods in Struct. Mech., Airforce Inst. Of Tech.* Wright Patterson AF Base, Ohio. 1965.
- [18] Y. Vetyukov. Finite element modeling of Kirchhoff-Love shells as smooth material surfaces. *ZAMM - Journal of Applied Mathematics and Mechanics / Zeitschrift für Angewandte Mathematik und Mechanik* 94.1-2 (2014), 150–163. DOI: [10.1002/zamm.201200179](https://doi.org/10.1002/zamm.201200179).
- [19] S. Kaczmarczyk. The Dynamic Interactions and Control of Long Slender Continua and Discrete Inertial Components in Vertical Transportation Systems. *Nonlinear Dynamics of Discrete and Continuous Systems*. Ed. by A. K. Abramian, I. V. Andrianov and V. A. Gaiko. Vol. 139. Cham: Springer International Publishing, 2021, 117–128. DOI: [10.1007/978-3-030-53006-8\\_8](https://doi.org/10.1007/978-3-030-53006-8_8).
- [20] K. Marynowski. Free vibration analysis of an axially moving multiscale composite plate including thermal effect. *International Journal of Mechanical Sciences* 120 (2017), 62–69. DOI: [10.1016/j.ijmecsci.2016.11.013](https://doi.org/10.1016/j.ijmecsci.2016.11.013).
- [21] C. Mueller et al. Influence of Friction on the Loads in a Roll Forming Simulation with Compliant Rolls. *Key Engineering Materials* 611-612 (2014), 436–443. DOI: [10.4028/www.scientific.net/KEM.611-612.436](https://doi.org/10.4028/www.scientific.net/KEM.611-612.436).
- [22] R. Safdarian and H. Moslemi Naeni. The effects of forming parameters on the cold roll forming of channel section. *Thin-Walled Structures* 92 (2015), 130–136. DOI: [10.1016/j.tws.2015.03.002](https://doi.org/10.1016/j.tws.2015.03.002).
- [23] H. Hetzler. On moving continua with contacts and sliding friction: Modeling, general properties and examples. *International Journal of Solids and Structures* 46.13 (2009), 2556–2570. DOI: [10.1016/j.ijsolstr.2009.01.037](https://doi.org/10.1016/j.ijsolstr.2009.01.037).
- [24] M. Crisfield. Finite element analysis for combined material and geometric nonlinearities. *Nonlinear Finite Element Analysis in Structural Mechanics: Proceedings of the Europe-US Workshop Ruhr-Universität Bochum, Germany, July 28–31, 1980*. Springer. 1981, 325–338.
- [25] J. Lubliner. *Plasticity theory*. Dover Publications, Inc., 2008.
- [26] M. Bieniek and J. Funaro. Elasto-plastic behaviour of plates and shells. *Techn. Rep. DNA 3954* (1976), 261–2.
- [27] A. Ibrahimbegović and F. Frey. An efficient implementation of stress resultant plasticity in analysis of Reissner-Mindlin plates. *International Journal for Numerical Methods in Engineering* 36.2 (1993), 303–320. DOI: [10.1002/nme.1620360209](https://doi.org/10.1002/nme.1620360209).
- [28] B. Skallerud, L. Myklebust and B. Haugen. Nonlinear response of shell structures: effects of plasticity modelling and large rotations. *Thin-Walled Structures* 39.6 (2001), 463–482. DOI: [10.1016/S0263-8231\(01\)00014-3](https://doi.org/10.1016/S0263-8231(01)00014-3).

- [29] J. Dujc and B. Brank. On stress resultant plasticity and viscoplasticity for metal plates. *Finite Elements in Analysis and Design* 44.4 (2008), 174–185. DOI: [10.1016/j.finel.2007.11.011](https://doi.org/10.1016/j.finel.2007.11.011).
- [30] J. Dujc and B. Brank. Stress resultant plasticity for shells revisited. *Computer Methods in Applied Mechanics and Engineering* 247-248 (2012), 146–165. DOI: [10.1016/j.cma.2012.07.012](https://doi.org/10.1016/j.cma.2012.07.012).
- [31] E. Kocbay and Y. Vetyukov. Stress resultant plasticity for plate bending in the context of roll forming of sheet metal. *International Journal for Numerical Methods in Engineering* 122.18 (2021), 5144–5168. DOI: [10.1002/nme.6760](https://doi.org/10.1002/nme.6760).
- [32] M. Ambati, J. Kiendl and L. De Lorenzis. Isogeometric Kirchhoff–Love shell formulation for elasto-plasticity. *Computer Methods in Applied Mechanics and Engineering* 340 (2018), 320–339. DOI: [10.1016/j.cma.2018.05.023](https://doi.org/10.1016/j.cma.2018.05.023).
- [33] J. C. Simo and R. L. Taylor. A return mapping algorithm for plane stress elastoplasticity. *International Journal for Numerical Methods in Engineering* 22.3 (1986), 649–670. DOI: [10.1002/nme.1620220310](https://doi.org/10.1002/nme.1620220310).
- [34] M. Crisfield, J. Remmers and C. Verhoosel. Non-linear finite element analysis of solids and structures. 1991.
- [35] V. Eliseev. Mechanics of deformable solid bodies. *St. Petersburg State Polytechnical University Publishing House, St. Petersburg* (2006).
- [36] S. Eisenträger et al. Stability analysis of plates using cut Bogner-Fox-Schmit elements. *Computers & Structures* 270 (2022), 106854. DOI: [10.1016/j.compstruc.2022.106854](https://doi.org/10.1016/j.compstruc.2022.106854).
- [37] P. G. Ciarlet. An Introduction to Differential Geometry with Applications to Elasticity. *Journal of Elasticity* 78-79.1-3 (2005), 1–215. DOI: [10.1007/s10659-005-4738-8](https://doi.org/10.1007/s10659-005-4738-8).
- [38] L. P. Lebedev, M. J. Cloud and V. A. Eremeyev. Tensor Analysis with Applications in Mechanics. WORLD SCIENTIFIC, 2010. DOI: [10.1142/7826](https://doi.org/10.1142/7826).
- [39] Y. Vetyukov, A. Kuzin and M. Krommer. Asymptotic splitting in the three-dimensional problem of elasticity for non-homogeneous piezoelectric plates. *International Journal of Solids and Structures* 48.1 (2011), 12–23. DOI: [10.1016/j.ijsolstr.2010.09.001](https://doi.org/10.1016/j.ijsolstr.2010.09.001).
- [40] Q. Hu, X. Li and J. Chen. On the calculation of plastic strain by simple method under non-associated flow rule. *European Journal of Mechanics - A/Solids* 67 (2018), 45–57. DOI: [10.1016/j.euromechsol.2017.08.017](https://doi.org/10.1016/j.euromechsol.2017.08.017).
- [41] H. J. Kleemola and M. A. Nieminen. On the strain-hardening parameters of metals. *Metallurgical transactions* 5.8 (1974), 1863–1866. DOI: [10.1007/BF02644152](https://doi.org/10.1007/BF02644152).
- [42] M. C. Butuc et al. Analysis of sheet metal formability through isotropic and kinematic hardening models. *European Journal of Mechanics - A/Solids* 30.4 (2011), 532–546. DOI: [10.1016/j.euromechsol.2011.03.005](https://doi.org/10.1016/j.euromechsol.2011.03.005).
- [43] V. Eliseev and Y. Vetyukov. Effects of deformation in the dynamics of belt drive. *Acta Mechanica* 223.8 (2012), 1657–1667. DOI: [10.1007/s00707-012-0675-3](https://doi.org/10.1007/s00707-012-0675-3).



- [44] U. Nackenhorst. The ALE-formulation of bodies in rolling contact. *Computer Methods in Applied Mechanics and Engineering* 193.39-41 (2004), 4299–4322. DOI: [10.1016/j.cma.2004.01.033](https://doi.org/10.1016/j.cma.2004.01.033).
- [45] J. Simo and R. Taylor. Consistent tangent operators for rate-independent elastoplasticity. *Computer Methods in Applied Mechanics and Engineering* 48.1 (1985), 101–118. DOI: [10.1016/0045-7825\(85\)90070-2](https://doi.org/10.1016/0045-7825(85)90070-2).
- [46] J. Scheidl and Y. Vetyukov. Steady Motion of a Slack Belt Drive: Dynamics of a Beam in Frictional Contact With Rotating Pulleys. *Journal of Applied Mechanics* 87.12 (2020), 121011. DOI: [10.1115/1.4048317](https://doi.org/10.1115/1.4048317).
- [47] D. Bhattacharyya et al. The prediction of deformation length in cold roll-forming. *Journal of Mechanical Working Technology* 9.2 (1984), 181–191. DOI: [10.1016/0378-3804\(84\)90004-4](https://doi.org/10.1016/0378-3804(84)90004-4).
- [48] M. Lindgren. An Improved Model for the Longitudinal Peak Strain in the Flange of a Roll Formed U-Channel developed by FE-Analyses. *steel research international* 78.1 (2007), 82–87. DOI: [10.1002/srin.200705863](https://doi.org/10.1002/srin.200705863).



Contents lists available at ScienceDirect

## Thin-Walled Structures

journal homepage: [www.elsevier.com/locate/tws](http://www.elsevier.com/locate/tws)

Full length article

## Mixed Eulerian–Lagrangian modeling of sheet metal roll forming

Emin Kocbay <sup>a</sup>, Jakob Scheidl <sup>a</sup>, Fabian Riegler <sup>a</sup>, Martin Leonhartsberger <sup>b</sup>,  
Matthias Lamprecht <sup>b</sup>, Yury Vetyukov <sup>a,\*</sup><sup>a</sup> Institute of Mechanics and Mechatronics, TU Wien, Getreidemarkt 9, 1060 Vienna, Austria<sup>b</sup> IFT - Institute of Production Engineering and Photonic Technologies, TU Wien, Getreidemarkt 9, 1060 Vienna, Austria

## ARTICLE INFO

## Keywords:

Mixed Eulerian–Lagrangian description  
Kirchhoff–Love shell  
Finite element analysis  
Metal plasticity  
Roll forming

## ABSTRACT

We propose a nonlinear shell finite element model to simulate sheet metal roll forming, a continuous forming process to produce endless metal profiles. A mixed Eulerian–Lagrangian kinematic description is employed to overcome the drawbacks of the common Lagrangian parametrization. The finite element mesh is detached from the particle motion in axial direction and, thus, facilitates a two-step solution procedure to capture the continuous forming process: First, an equilibrium is sought with the account for contact and plastic flow. Secondly, the material transport is taken into account, which amounts to the integration of an advection problem for the plastic variables. The continuum plasticity model with through-the-thickness integration for the stress resultants guarantees a precise resolution of the forming process in each cross section of the Kirchhoff–Love shell. A series of simulations is carried out to ascertain the convergence of the numerical scheme, to highlight the impact of characteristic parameters and to establish a correspondence to a reference computation with the commercial software Abaqus in a simplified static setting. A physical experiment is devised on an actual roll forming mill to assess the quality of the current computational model.

## 1. Introduction

Roll forming is a highly efficient continuous production process for steel profiles of various cross-sectional shapes. An initially flat, thin metal sheet receives incremental bends at subsequent roll stands as it travels through the rolling line, see [1,2]. Each stand typically consists of a couple of profiled rolls, which form a complex-shaped roll gap. Plastic deformations are accumulated at the individual roll stands such that the desired shape of the profile is reached in the end. The process is deliberately designed to be bending dominant, because thickness deformations and residual membrane strains pose the risk to deteriorate the final product with respect to its load capacity and shape accuracy (straightness, local waviness). Thus, Tehrani et al. [3] investigated the local edge buckling phenomena in cold roll-forming of symmetric channel sections.

The accurate yet computationally efficient numerical simulation of the roll forming process is a challenging task. Applied finite element schemes are reported by Heislitz et al. [4] and Bui and Ponthot [5] and implemented in the commercial software COPRA,<sup>1</sup> see [6] for a use case. These approaches still rely on the conventional Lagrangian description despite its deficiencies owing to the strict coupling of material particles with finite element nodes. As a consequence, such models are computationally expensive, due to the inability to use refined meshes

over longer simulation times, and susceptible to spurious numerical oscillations, due to material nodes entering or leaving the contact zones repeatedly, see [7].

An effective alternative would be the application of the Arbitrary Lagrangian Eulerian (ALE) formalism, see [2] for an extensive presentation of a 3D volumetric non-material finite element scheme. The latter approach belongs to the class of traditional ALE schemes with a Lagrangian step and a Eulerian step comprising a single time increment [8]. The necessity of transferring all mechanical fields, including material density and stresses, to a new mesh during the Eulerian step makes the approach complicated and increases the risk of accuracy loss during the time integration. Different methods to remediate these drawbacks are reported in the literature on modern ALE variants, see [9,10] or Humer et al. [11], who propose a kinematic description featuring a stretched coordinate to model axially moving one-dimensional continua of variable length. In the present paper we introduce a computational scheme for the roll forming process with two novel features:

1. The mixed Eulerian–Lagrangian (MEL) kinematic description [12–14], belonging generally to the broad class of ALE methods, alleviates the necessity to transfer the conventional mechanical fields during the Eulerian step with the help of an appropriate variable transformation. It improves the accuracy of the time

\* Corresponding author.

E-mail address: [yury.vetyukov@tuwien.ac.at](mailto:yury.vetyukov@tuwien.ac.at) (Y. Vetyukov).<sup>1</sup> <https://www.datam.de/en/products/software-division/fea-simulation><https://doi.org/10.1016/j.tws.2023.110662>

Received 7 December 2022; Accepted 24 February 2023

Available online 14 March 2023

0263-8231/© 2023 The Author(s). Published by Elsevier Ltd. This is an open access article under the CC BY license

<http://creativecommons.org/licenses/by/4.0/>.

**Nomenclature****Geometry, material and numerical parameters**

$L, w, h$	length, width and thickness of the metal sheet
$E, \nu$	elastic modulus and Poisson ratio of the metal sheet
$\sigma_0, k, n$	nominal & actual yield strength and strain hardening exponent
$P, \gamma$	contact penalty factor and penetration depth

**Coordinates, kinematic description, differential operators and strain measures**

$x, y, z$	global Cartesian coordinates of the actual configuration
$i, j, k$	global Cartesian basis
$\hat{x}, \hat{y}$	material coordinates of the reference configuration of the shell model
$\zeta$	material thickness coordinate in the 3D body of the shell
$\hat{p}, \bar{r}, r$	position vector of the reference, the intermediate and the actual configuration
$u, u_x, u_y, u_z$	displacement vector and its Cartesian components
$v, \dot{u}_x$	axial material transport rate and axial material velocity
$\hat{\nabla}, \bar{\nabla}, \nabla$	differential operators of the reference, the intermediate and the actual configuration
$\hat{\mathbf{F}}, \mathbf{F}$	deformation gradient tensors between the reference configuration and the intermediate configuration or the actual configuration
$\epsilon_{\perp}, \epsilon_{\perp}^e, \epsilon_{\perp}^p$	in-plane parts of the total strain tensor, elastic strain tensor and plastic strain tensor in the 3D body of the shell
$\mathbf{E}, \mathbf{K}$	membrane and bending strain tensor of the shell

**Forming parameters and measures of the forming process**

$\rho, \Delta z, \varphi$	roll-gap-reduction, vertical offset and bending angle of the profile
$g, \hat{\varphi}$	roll gap and profile opening angle (physical experiment)
$F_1, F_1$	roll forces on lower and upper rolls
$F_1, F_2$	mean forces measured at lower rolls at first and second roll stand (physical experiment)
$A^p, \dot{A}^p$	densities of plastic dissipation work and dissipation power

integration and reduces the complexity of the model. Just the inelastic (plastic) variables need to be transported.

2. The treatment of the inelastic constitutive laws within the shell finite element model reduces the number of degrees of freedom in comparison to a 3D volumetric analysis, which, in turn, decreases the computational cost and accelerates the simulation.

Three sources of nonlinearity exist in the model: the geometric nonlinearity because of large deformations, the contact between rolls and metal sheet and the inelastic material behavior. In terms of the first, the thin metal sheet is modeled as a material surface using

the Kirchhoff–Love shell theory in the form, proposed by Eliseev and Vetyukov [15], Vetyukov [16]. This choice is justified by the observation, that the thickness remains practically unchanged during the roll forming process, see [5]. A regular mesh of rectangular  $C^1$ -continuous four-node shell finite elements constitutes the numerical model. These elements are essentially an extension of the Bogner–Fox–Schmit plate finite elements with bi-cubic Hermitian shape functions [17,18].

In general, the imposed axial travel gives rise to inertia terms owing to the motion of the structure’s material particles. These contributions, though essential, e.g., for the dynamics of high-rise elevators or the production of paper webs [19,20], are negligible in the present context of the comparatively slow roll forming process. Hence, the simulation procedure follows a quasistatic time-stepping scheme, where the minimization of the total potential energy is followed by the convective transport of plastic variables along the streamlines of material flow.

Regarding the contact interaction at a roll stand, we employ the usual simplifying assumptions that the rolls are rigid and that the contact is frictionless [21,22]; see [23] with regard to the modeling of frictional contact in problems of moving continua. These prerequisites are necessary, because no reliable information on the elastic compliance of the roll stand nor on the frictional conditions is available; under production conditions, rolls are typically lubricated to minimize tool wear. Doubtlessly, these simplifying assumptions may impede the capability of the computational model to accurately mimic an actual roll forming process, the comparison against physical experiments in Section 9.5 shall highlight to what extent.

Elastic–plastic behavior of plates and shells is a classical topic in the literature [24,25]. Past attempts to treat the plastic laws on the level of structural mechanics in the form of the so-called stress resultant theories, where plastic curvatures replace the distribution of plastic strains over the thickness of the shell [26–30] are not sufficiently mature and thus inapplicable in the present context. The stress resultant plasticity model recently proposed by Kocbay and Vetyukov [31] is computationally efficient but limited to pure bending deformations. In comparison to the primarily applied continuum plasticity model it is found, that even if bending deformations are predominant, as is the case for roll forming, the applicability of this stress resultant model quickly diminishes, see simulation results in Section 9.2. In contrast, the continuum plasticity model evaluates the well-established relations of plane-stress plasticity in chosen integration points through the thickness coordinate, see e.g. [32]. It allows for an accurate resolution of the 3D plastic state, albeit at a significantly increased computational effort.

In what follows, we discuss the important features of the model and the numerical algorithm, present results of parameter studies and establish convergence of the proposed scheme with respect to the primary numerical parameters. The finite element model is further compared against a reference computation with Abaqus<sup>2</sup> in a simplified static setting and validated against physical experiments conducted on an actual roll forming mill.

**2. Mechanical simulation model for the process of roll forming**

A schematic sketch of the simulation setup in the spatially fixed *control domain* is depicted in Fig. 1. The part of the metal sheet currently inside the control domain is called *active material volume*. The origin of the Cartesian reference frame is situated at the center of the left edge, where material enters the control domain at a constant rate. The metal sheet is modeled as a nonlinear Kirchhoff–Love shell and discretized with a regular mesh of rectangular four-node shell elements. Bi-cubic Hermitian shape functions are used to achieve a  $C^1$ -continuous approximation of the displacement field. The axial mesh refinement visualized in the sketch is made possible by the MEL kinematic formulation. Theoretically speaking, an arbitrary number of forming stands, each comprising a pair of rolls, can be incorporated in the simulation

<sup>2</sup> <https://www.3ds.com/products-services/simulia/products/abaqus/>

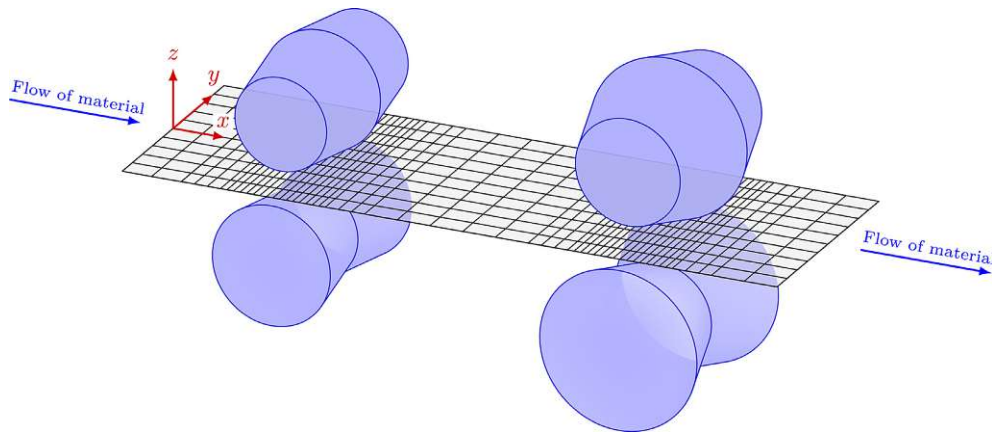


Fig. 1. Schematic sketch of the roll forming simulation topology.

model. The rolls are modeled as rigid bodies and the contact between them and the metal sheet is assumed to be frictionless. Forming takes place if the rolls of each stand are pushed against the metal sheet by means of an appropriate vertical adjustment of the axes of the rolls. Naturally, the outcome of the process largely depends on the vertical positioning of the rolls with respect to the reference plane  $z = 0$  of the flat metal sheet. During a simulation the impenetrability condition of normal contact is enforced at the integration points of the shell finite elements via the penalty regularization method.

The transient quasistatic evolution of the forming process is viewed as a sequence of statically and plastically admissible equilibrium states, which are computed with the help of a variant of the return mapping algorithm [33,34]. The intermediate transport of plastic variables between two equilibrium iterations in account for the axial motion of particles may be regarded as a “load-increment” that is needed to sustain the simulation. Given enough simulation time a stationary state is reached, whose outside appearance remains unchanged from the perspective of a spatially fixed observer. Internally, the local time rates of the plastic variables due to plastic flow and convective transport compensate each other. This steady state possesses particular practical relevance, because it directly corresponds to the operating conditions of the continuous roll forming process. Such a stationary solution cannot be reached within a conventional Lagrangian finite element simulation because the elements would enter and leave the contact zones — in contrast to the MEL approach.

### 3. Mixed Eulerian–Lagrangian description of axially moving Kirchhoff–Love shells

The non-material model of an elastic shell, whose particles are moving across the finite element mesh in the axial direction, has been introduced and validated by Vetyukov et al. [12]. The same kinematic description is used in the present research. Here, we recap the basic features of the model. The key idea is that the nodes of the finite element mesh do not move in the axial direction, but follow the deformation of the structure in the lateral (horizontal) and the transverse (vertical) directions. This allows to speak about the axial coordinate  $x$  as the Eulerian one, whereas the other coordinates  $y$  and  $z$  remain Lagrangian.

The mathematical description exploits an infinitely long reference configuration, which corresponds to the initially flat metal sheet. The particles are identified by the material coordinates  $\hat{x}$  and  $\hat{y}$ . With  $i, j$  and  $k$  being the Cartesian unit base vectors, the position vector of the reference configuration reads:

$$\hat{r} = \hat{x}i + \hat{y}j, \quad -w/2 \leq \hat{y} \leq w/2. \quad (1)$$

In the actual state the particle is located at the position

$$r = xi + yj + zk \quad \text{with} \quad x = \hat{x} + u_x, \quad y = \hat{y} + u_y, \quad z = u_z. \quad (2)$$

In the simulation, we treat the part of the sheet in the control domain  $0 \leq x \leq L$ , whose pre-image in the reference configuration forms the active material volume. The latter is changing in time, as new particles enter the control domain and leave it because of the axial motion of the metal sheet.

Conventional shell theory [15,35] is based upon a mapping  $r = r(\hat{r})$ , which corresponds to the Lagrangian description and is inefficient in the present case because of the axial motion. We overcome the issue by introducing a spatially fixed intermediate configuration, which occupies a planar rectangular domain

$$\bar{r} = \bar{x}i + \bar{y}j, \quad 0 \leq \bar{x} \leq L, \quad -w/2 \leq \bar{y} \leq w/2. \quad (3)$$

The entire deformation is thus split into two steps, see Fig. 2. First, the axial displacement  $u_x$  transforms the reference state into the intermediate one,

$$\bar{r} = \hat{r} + u_x i, \quad \bar{x} = \hat{x} + u_x, \quad \bar{y} = \hat{y}. \quad (4)$$

Secondly, the two additional displacement components result into the actual state with in-plane deformations and bending:

$$r = \bar{r} + u_y j + u_z k, \quad x = \bar{x}, \quad y = \bar{y} + u_y, \quad z = u_z. \quad (5)$$

The key idea of the MEL-description is that all mechanical fields are considered as functions of the coordinates in the intermediate configuration, and also the mapping from the reference configuration to the actual state is defined implicitly as

$$\hat{r} = \hat{r}(\bar{r}), \quad r = r(\bar{r}). \quad (6)$$

In the numerical procedure, we introduce a finite element mesh in the intermediate state and discretize the three displacement components as functions

$$u_{x,y,z} = u_{x,y,z}(\bar{x}, \bar{y}), \quad (7)$$

i.e.  $u = u(\bar{r})$ . The necessary  $C^1$ -continuity condition, which guarantees the smoothness of the deformed surface as required by the Kirchhoff–Love shell theory, is easily achieved with the help of the bi-cubic approximation of all three displacement components. The respective Bogner–Fox–Schmit-like four-node finite element was presented in detail by Vetyukov [18] in the context of geometrically nonlinear theory of shells; for the non-material shell finite elements this approximation technique found use in [12,14]; see also [36] for the application in the context of a fictitious domain approach. Each node  $i$  thus features 12 degrees of freedom, namely the deflection  $u^{(i)}$ , the derivatives  $(\partial_i u)^{(i)}$ ,

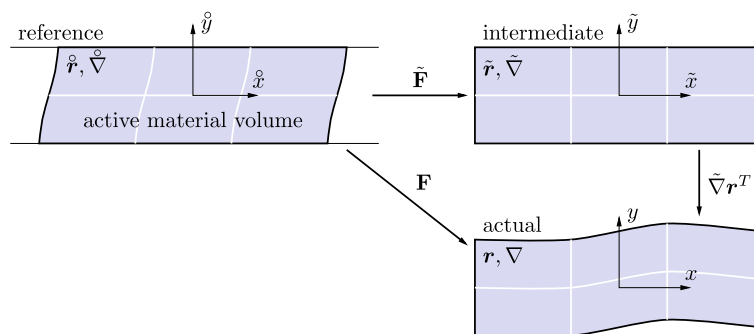


Fig. 2. Three configurations used for the mixed Eulerian–Lagrangian kinematic description of the deformation of the metal sheet and multiplicative decomposition of the deformation gradient tensor  $\mathbf{F}$ .

$(\partial_2 \mathbf{u})^{(i)}$  with respect to the local element coordinates  $q^1, q^2$  as well as the mixed second-order derivative  $(\partial_1 \partial_2 \mathbf{u})^{(i)}$ . The geometry of the finite element  $\tilde{\mathbf{r}}(q^1, q^2)$  needs to be approximated smoothly as well. The simulations below feature a regular mesh with  $\tilde{x} = \tilde{x}(q^1)$  being a cubic polynomial on each finite element with  $C^1$  interelement continuity, which is necessary to enable a local mesh refinement in the vicinity of the roll stands. The mapping in the lateral direction  $\tilde{y} = \tilde{y}(q^2)$  is a linear one, because all elements retain the same material width.

As shear is kinematically suppressed, the local deformed state of the shell is determined by the membrane strain measure  $\mathbf{E}$  and by the bending strain measure  $\mathbf{K}$ :

$$\mathbf{E} = \frac{1}{2} (\mathbf{F}^T \cdot \mathbf{F} - \mathbf{I}_\perp), \quad \mathbf{K} = \mathbf{F}^T \cdot \mathbf{b} \cdot \mathbf{F}. \quad (8)$$

Here  $\mathbf{I}_\perp = \mathbf{ii} + \mathbf{jj}$  is the in-plane unit tensor. The deformation gradient tensor follows with

$$\mathbf{F} = \overset{\circ}{\nabla} \tilde{\mathbf{r}}^T, \quad \overset{\circ}{\nabla} = i \frac{\partial}{\partial \tilde{x}} + j \frac{\partial}{\partial \tilde{y}} \equiv i \partial_{\tilde{x}} + j \partial_{\tilde{y}}, \quad (9)$$

and the curvature tensor is the negative gradient of the unit normal vector to the actual surface  $\mathbf{n}$ :

$$\mathbf{b} = -\nabla \mathbf{n}, \quad \nabla = i \partial_x + j \partial_y, \quad (10)$$

see [37].

With the finite element approximation bound to the intermediate configuration, the derivatives  $\overset{\circ}{\nabla} = i \partial_{\tilde{x}} + j \partial_{\tilde{y}}$  are readily available. Because the above definitions feature the differential operators  $\overset{\circ}{\nabla}$  and  $\nabla$ , certain mathematical transformations need to be taken (see again [12]), which result into the following multiplicative decomposition of the total deformation gradient:

$$\mathbf{F} = \tilde{\nabla} \tilde{\mathbf{r}}^T \cdot \tilde{\mathbf{F}}, \quad \tilde{\mathbf{F}} = \overset{\circ}{\nabla} \tilde{\mathbf{r}}^T = (\mathbf{I}_\perp - i \tilde{\nabla} u_x)^{-1}. \quad (11)$$

The membrane strain measure  $\mathbf{E}$  from Eq. (8) can now be directly computed. Additional derivations provide us with the expression for the bending strain measure:

$$\mathbf{K} = \tilde{\mathbf{F}}^T \cdot (\tilde{\nabla} \tilde{\nabla} \tilde{\mathbf{r}} \cdot \mathbf{n}) \cdot \tilde{\mathbf{F}}, \quad \mathbf{n} = \frac{\partial_{\tilde{x}} \tilde{\mathbf{r}} \times \partial_{\tilde{y}} \tilde{\mathbf{r}}}{|\partial_{\tilde{x}} \tilde{\mathbf{r}} \times \partial_{\tilde{y}} \tilde{\mathbf{r}}|}. \quad (12)$$

With given values of the nodal degrees of freedom of the entire model  $q$ , which determine the approximation of the displacement components Eq. (7), the local strain measures of the shell can now be directly evaluated in a given integration point within the intermediate configuration  $\tilde{\mathbf{r}}$ .

The equilibrium would be obtained by minimizing the total strain energy of the model  $U^2$  under the inequality constraints imposed by the kinematic contact conditions. In a purely elastic case, the distributed strain energy per unit material area reads

$$U = \frac{1}{2} (A \nu (\text{tr } \mathbf{E})^2 + A(1 - \nu) \mathbf{E} \cdot \mathbf{E} + D \nu (\text{tr } \mathbf{K})^2 + D(1 - \nu) \mathbf{K} \cdot \mathbf{K}), \quad (13)$$

with  $A = Eh/(1 - \nu^2)$  being the plane stress membrane stiffness,  $E$  the Young modulus,  $\nu$  the Poisson ratio,  $h$  the thickness of the plate and

$D = h^2 A / 12$  its bending stiffness. The double dot multiplication “ $\cdot$ ” has a meaning of a double contraction of two tensors:  $\mathbf{A} \cdot \mathbf{B} = \text{tr}(\mathbf{A} \cdot \mathbf{B})$ , see [38]. Now,  $U^\Sigma$  is the integral over the active material volume in the reference configuration with the elementary surface area

$$d\tilde{x} d\tilde{y} = (\det \tilde{\mathbf{F}})^{-1} d\tilde{x} d\tilde{y}, \quad (\det \tilde{\mathbf{F}})^{-1} = 1 - \partial_{\tilde{x}} u_x, \quad (14)$$

and thus we arrive at the integral over the intermediate configuration

$$U^\Sigma = \int_0^L d\tilde{x} \int_{-w/2}^{w/2} (1 - \partial_{\tilde{x}} u_x) U d\tilde{y}, \quad (15)$$

which is directly available for the given finite element discretization using a  $3 \times 3$  Gaussian quadrature rule per element. The Newton method for minimizing the energy requires first and second order derivatives of the strain measures  $\mathbf{K}$  and  $\mathbf{E}$  with respect to the nodal degrees of freedom  $q$ . The respective expressions were derived using the computer algebra system Wolfram Mathematica<sup>3</sup> and then exported into the simulation software in the form of auto-generated code.

#### 4. Contact with rolls

The frictionless contact between deformable shell and rigid rolls is governed by the penalty potential

$$V^\Sigma = \int_0^L d\tilde{x} \int_{-w/2}^{w/2} (1 - \partial_{\tilde{x}} u_x) V d\tilde{y}, \quad (16)$$

where the density  $V$  per unit reference area is a quadratic form in the penetration depth  $\gamma$ :

$$V = \frac{1}{2} P \gamma^2. \quad (17)$$

Any penetration  $\gamma$  of the deformable solid into the rigid counterpart is penalized with a large factor  $P$  such that the impenetrability condition is met exactly in the limiting case of  $P \rightarrow \infty$ .

Integration of the contact potential is done with a standard  $3 \times 3$  Gaussian quadrature rule. This requires the processing of the contact kinematics for each integration point as illustrated in Fig. 3. The actual penetration depth  $\gamma$  is exaggerated strongly in the picture for the sake of visualization. It is computed from the difference of the profile radius  $R(y)$  and the radial distance of the current integration point. Taking the component in direction of the normal vector to the roll surface  $\mathbf{e}_\gamma$ , we obtain:

$$\gamma = \max \left\{ 0, \frac{R(y) - |\mathbf{d}|}{\sqrt{1 + R'(y)^2}} \right\}, \quad \mathbf{d} = \mathbf{r} - \mathbf{r}_0 - \mathbf{r} \cdot \mathbf{jj}, \quad (18)$$

where  $\mathbf{r}$  and  $\mathbf{r}_0$  denote the position vector Eq. (5) and the vector to the center of the roll axis at  $y = 0$ , respectively. The square root in the denominator accounts for the cosine of the inclination angle of the roll

<sup>3</sup> <https://www.wolfram.com/mathematica/>

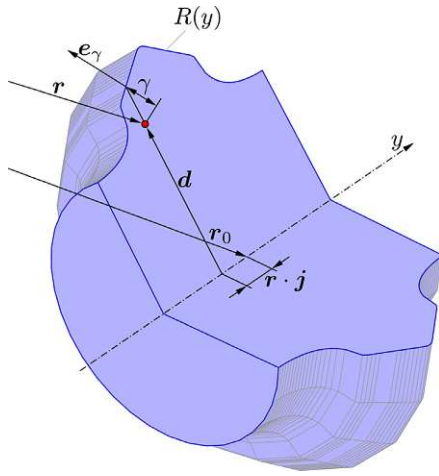


Fig. 3. Evaluation of the current penetration depth  $\gamma$  at an integration point and the surface normal vector  $e_\gamma$  that determine the normal contact response in the penalty model; the radial profile  $R(y)$  describes the roll geometry.

profile  $R(y)$ . If there is no penetration,  $\gamma$  is simply set to zero, which prevents unphysical pulling forces. In case of established contact, the variation of  $\gamma$  is determined by the virtual displacement in direction of the normal vector  $e_\gamma$ :

$$\delta\gamma = -e_\gamma \cdot \delta r = -e_\gamma \cdot (\delta u_y j + \delta u_z k), \quad e_\gamma = \frac{(d/|d| - R'(y)j)}{|d/|d| - R'(y)j|}, \quad (19)$$

which does not feature a variation of the axial displacement  $u_x$  owing to the mixed kinematic framework (integration points do not move in axial direction).

To implement the specific geometry of a given roll as a 3D body of revolution, the radial profile  $R(y)$  is provided as a sequence of cubic polynomials:

$$R(y) = p_i(y), \quad y_i \leq y < y_{i+1}. \quad (20)$$

At their boundaries these polynomials obey the transition conditions

$$\{p_i(y_i), p'_i(y_i), p_i(y_{i+1}), p'_i(y_{i+1})\} = \{R_i, R'_i, R_{i+1}, R'_{i+1}\}. \quad (21)$$

The radii and inclinations  $R_i$  and  $R'_i$  are defined on an equidistant mesh

$$y_i = -l/2 + i \Delta y, \quad \Delta y = \frac{l}{N}, \quad 0 \leq i \leq N, \quad (22)$$

where  $l$  and  $N$  denote the length of the roll axis and the total number of cubic polynomials, respectively. The information concerning the geometry of the rolls, in particular the sequence  $\{R_i, R'_i\}$ , is passed to the program with one text file each. The files used for the simulations presented in Section 9 are made available as supplementary material.

### 5. Elastic-plastic material behavior at bending of shells

The standard way to treat elastic-plastic behavior of shells is to formulate the constitutive relations by means of the *through-the-thickness* approach, see e.g. [32] for one variant of implementation. The basic idea is to recover the in-plane part of the strain tensor  $\epsilon_\perp$  of the 3D continuum by means of a proper evaluation of the shell kinematics. In the Kirchhoff-Love theory specifically, the membrane and bending strain tensors  $\mathbf{E}$  and  $\mathbf{K}$  of the shell result in a linear variation of  $\epsilon_\perp$  in the thickness direction  $\zeta$ . The corresponding stresses  $\sigma$  follow from the material constitutive law by solving the respective differential equations of the 3D theory of plasticity;  $\sigma$  is a planar tensor, as the plane stress hypothesis holds regardless of the constitutive model [39].

Upon numerical integration through the thickness  $h$ , one finally obtains the stress resultants of the shell model, namely the bending moments  $\mathbf{M}$  and the membrane forces  $\mathbf{N}$ :

$$\mathbf{N} = \int_{-h/2}^{h/2} \sigma \, d\zeta, \quad \mathbf{M} = - \int_{-h/2}^{h/2} \zeta \sigma \, d\zeta. \quad (23)$$

While this approach is straightforward and simple, the through-the-thickness integration is computationally quite expensive. There are attempts in the open literature [24,26–30] to resolve this issue and to gain a computationally more efficient method by introducing a pure *stress resultant* formulation. This requires the yield surface and the flow rule to be expressed in terms of stress resultants of the shell model, thus providing the time rates of plastic membrane and bending strains. The mentioned approaches feature shear-deformable shell kinematics and are thus hardly transferable to the model at hand. Moreover, it would be difficult to adapt these models to a specific material hardening law. A more appropriate model was developed by Kocbay and Vetyukov [31] for the geometrically linear bending of plates using special case solutions of three-dimensional equations as a reference. This computationally efficient numerical scheme has successfully been validated against reference 3D continuum solutions and is adaptable to any form of isotropic material hardening law. It does, however, not account for the coupling between membrane and bending deformations in the elastic-plastic constitutive relations. Regarding the process of roll forming, membrane stresses must remain small to prevent the metal sheet from sustaining irreversible changes of the in-plane metric, which can deteriorate the quality of the final product. For this reason, we employ the proposed stress resultant model as well to judge its applicability in comparison to the default continuum model.

In the following we elaborate on the latter and discuss the implementation of the through-the-thickness integration approach in the simulation tool. The asymptotic consequence of the 3D condition of compatibility of strains [39] is that the leading order term of the in-plane part of the strain tensor  $\epsilon_\perp$  is distributed linearly along the thickness coordinate of the continuum of the shell independent of the material behavior:

$$\epsilon_\perp = \mathbf{E} - \zeta \mathbf{K}. \quad (24)$$

The membrane strains of the shell  $\mathbf{E}$  remain small and the thickness coordinate  $\zeta$  varies in the narrow range  $-h/2 \leq \zeta \leq h/2$ . This justifies the use of the relations of the geometrically linear theory of elastoplasticity. We decompose the total in-plane strain into the elastic and plastic parts in the usual manner:

$$\epsilon_\perp = \epsilon_\perp^e + \epsilon_\perp^p. \quad (25)$$

The von Mises yield criterion function under plane stress conditions reads:

$$f = \frac{3}{2} \sigma \cdot \sigma - \frac{1}{2} (\text{tr } \sigma)^2, \quad (26)$$

and the elastic law for isotropic bodies is given as:

$$\sigma = \frac{E}{1+\nu} \epsilon_\perp^e + \frac{E\nu}{1-\nu^2} \mathbf{I}_\perp \text{tr } \epsilon_\perp^e = {}^4\mathbf{C} \cdot \epsilon_\perp^e, \quad (27)$$

where  ${}^4\mathbf{C}$  denotes the fourth rank plane stress elasticity tensor. Strictly speaking, the Cauchy stress tensor  $\sigma$ , which determines the stress resultants Eq. (23), rotates together with the particle of the shell in the geometrically nonlinear theory. We ignore this formal distinction and proceed with the Cauchy stress tensor written in the basis of the reference configuration:

$$\sigma = \sigma_x i i + \sigma_y j j + \sigma_{xy} (i j + j i), \quad (28)$$

This “pull-back” may be interpreted as the transition to the Piola stress tensor, when the deformation gradient is approximated as a pure rotation, which is justified by the smallness of  $\epsilon_\perp$ . The yield criterion function becomes:

$$f = \sigma_x^2 - \sigma_x \sigma_y + \sigma_y^2 + 3\sigma_{xy}^2. \quad (29)$$

The deformation remains purely elastic and no change in plastic variables occurs,  $\dot{\epsilon}_1^p = 0$ , as long as the stresses remain within the yield surface:  $f < k^2(A^p)$ . The yield strength value  $k$ , which determines the boundary of the yield surface at the uniaxial stressed state, grows monotonously with the locally performed dissipative work  $A^p$ . Alongside the three plastic strain components  $\epsilon_x^p$ ,  $\epsilon_{xy}^p$  and  $\epsilon_y^p$ ,  $A^p$  belongs to the set of material state variables, or plastic variables. This isotropic hardening model, in which the yield surface expands concentrically, is suitable for the roll forming process, because neither cyclic loading nor significant changes in the direction of the plastic flow are expected.

At yield the equality

$$f = k^2(A^p) \quad (30)$$

holds and the plastic variables change in time, irreversible plastic strains are accumulated. Therefore, during the active plastic flow process we remain on the yield surface, and

$$\dot{f} = 2k(A^p)k'(A^p)\dot{A}^p. \quad (31)$$

in which  $\dot{f}$  is the derivative of  $f$  with respect to time  $t$ . The rate equation for the dissipative work in a given point follows the definition of the dissipation power as:

$$\dot{A}^p = \boldsymbol{\sigma} \cdot \dot{\boldsymbol{\epsilon}}_1^p. \quad (32)$$

The system of rate equations is closed by the associated flow rule:

$$\dot{\boldsymbol{\epsilon}}_1^p = \lambda \frac{\partial f}{\partial \boldsymbol{\sigma}}, \quad \frac{\partial f}{\partial \boldsymbol{\sigma}} = 3\boldsymbol{\sigma} - \mathbf{I}_1 \text{tr } \boldsymbol{\sigma}. \quad (33)$$

This time rate equation for the plastic strains is a consequence of the postulate of maximum plastic dissipation, see [25]. The non-negative factor  $\lambda$  follows from the consistency condition, i.e. the time derivative  $\dot{f}$  in Eq. (31) must be equal to the time rate derived from Eq. (26):

$$\dot{f} = \frac{\partial f}{\partial \boldsymbol{\sigma}} \cdot \dot{\boldsymbol{\sigma}} = 3\boldsymbol{\sigma} \cdot \dot{\boldsymbol{\sigma}} - \text{tr } \boldsymbol{\sigma} \text{tr } \dot{\boldsymbol{\sigma}}. \quad (34)$$

Computing the time derivative of the stress tensor from the elastic law Eq. (27) and accounting for the flow rule Eq. (33), we obtain:

$$\dot{\boldsymbol{\sigma}} = {}^4\mathbb{C} \cdot (\dot{\boldsymbol{\epsilon}}_1 - \dot{\boldsymbol{\epsilon}}_1^p) = {}^4\mathbb{C} \cdot \left( \dot{\boldsymbol{\epsilon}}_1 - \lambda \frac{\partial f}{\partial \boldsymbol{\sigma}} \right). \quad (35)$$

Finally, equating Eq. (31) and Eq. (34) in their appropriately expanded forms yields a rate equation for the consistency parameter:

$$\lambda = \frac{\frac{\partial f}{\partial \boldsymbol{\sigma}} \cdot {}^4\mathbb{C} \cdot \dot{\boldsymbol{\epsilon}}_1}{2k(A^p)k'(A^p)\boldsymbol{\sigma} \cdot \frac{\partial f}{\partial \boldsymbol{\sigma}} + \frac{\partial f}{\partial \boldsymbol{\sigma}} \cdot {}^4\mathbb{C} \cdot \frac{\partial f}{\partial \boldsymbol{\sigma}}}. \quad (36)$$

This expression holds only if positive, otherwise the material is deforming elastically and the plastic variables remain unchanged. Backward substitution in Eq. (35) yields the incremental stress–strain relation of the elastic–plastic state:

$$\dot{\boldsymbol{\sigma}} = \left( {}^4\mathbb{C} - \frac{{}^4\mathbb{C} \cdot \frac{\partial f}{\partial \boldsymbol{\sigma}} \frac{\partial f}{\partial \boldsymbol{\sigma}} \cdot {}^4\mathbb{C}}{2k(A^p)k'(A^p)\boldsymbol{\sigma} \cdot \frac{\partial f}{\partial \boldsymbol{\sigma}} + \frac{\partial f}{\partial \boldsymbol{\sigma}} \cdot {}^4\mathbb{C} \cdot \frac{\partial f}{\partial \boldsymbol{\sigma}}} \right) \cdot \dot{\boldsymbol{\epsilon}}_1, \quad (37)$$

with the term in brackets representing the elastic–plastic tangent stiffness tensor. Both this fourth rank tensor as well as the closely related tangent stiffness matrix of the finite element scheme are symmetric owing to the associated flow rule, see [40] for further discussion.

In metal forming simulations, *material hardening* is typically considered by a strain hardening power law, see [41,42], which is conventionally formulated in the uniaxial form:

$$\sigma_x(\epsilon_x) = \begin{cases} E\epsilon_x, & 0 \leq \sigma_x \leq \sigma_0 \\ k, & \sigma_x \geq \sigma_0, \end{cases} \quad k = \sigma_0 \left( \frac{E\epsilon_x}{\sigma_0} \right)^n. \quad (38)$$

Here,  $\sigma_x(\epsilon_x)$  is the uniaxial stress at monotonous loading,  $\epsilon_x$  is the corresponding axial strain component,  $n$  is the strain hardening exponent and  $\sigma_0$  is the nominal yield strength, which corresponds to the actual yield strength  $k$  only for the elastic-ideal plastic case ( $n = 0$ ). As long as  $0 \leq \sigma_x \leq \sigma_0$  the material behaves purely elastic. To generalize this one

dimensional law for plane stress plasticity in terms of  $k(A^p)$ , we first invert Eq. (38) in the elastic–plastic regime:

$$\epsilon_x(k) = \frac{\sigma_0 \left( \frac{k}{\sigma_0} \right)^{\frac{1}{n}}}{E}, \quad (39)$$

and use it together with  $\epsilon_x^p = \epsilon_x - \epsilon_x^e$  and Hooke's law  $\epsilon_x^e = k/E$ , to evaluate the plastic dissipative work as  $A^p(k) = k\epsilon_x^p$  in the simple uniaxial case:

$$A^p(k) = \frac{k}{E} \left( \sigma_0 \left( \frac{k}{\sigma_0} \right)^{\frac{1}{n}} - k \right). \quad (40)$$

Naturally, plastic work requires plastic flow and evaluates to zero otherwise. For a given value of  $A^p$  the above nonlinear equation is solved numerically for  $k(A^p)$ , which in a second step is used to evaluate the derivative:

$$k'(A^p) = \left( \frac{dA^p}{dk} \right)^{-1} = \left( \frac{\sigma_0(1+n) \left( \frac{k}{\sigma_0} \right)^{\frac{1}{n}} - 2kn}{nE} \right)^{-1}. \quad (41)$$

With  $k(A^p)$  and  $k'(A^p)$  made available, the consistency parameter  $\lambda$  can now be calculated according to Eq. (36).

The just established elastic–plastic constitutive relations allow us to formulate the required update routines for the internal plastic variables. In terms of the finite element scheme, the deformed configuration of the shell model is defined by the nodal degrees of freedom, stored in the matrix  $\boldsymbol{q}$ . The plastic state on the other hand is stored in the matrix  $\boldsymbol{p}$ , which contains the components of the plastic strain tensor  $\boldsymbol{\epsilon}_1^p$  as well as the accumulated plastic work  $A^p$  for each integration point in the continuum plasticity model. Together,  $\boldsymbol{q}$  and  $\boldsymbol{p}$  fully specify the current state. With them at hand we are able to evaluate the strain energy density per unit reference area:

$$U = \int_{-h/2}^{h/2} \frac{1}{2} \boldsymbol{\epsilon}_1^e \cdot {}^4\mathbb{C} \cdot \boldsymbol{\epsilon}_1^e \, d\zeta, \quad \boldsymbol{\epsilon}_1^e = \boldsymbol{\epsilon}_1 - \boldsymbol{\epsilon}_1^p, \quad (42)$$

which is the elastic–plastic extension of Eq. (13). The thickness integration is performed by means of an evaluation at several (usually 8) integration points  $\zeta_i$  according to the Gaussian quadrature rule. The total strain energy, as obtained through a second integration step of the above density according to Eq. (15), and its derivatives up to second order with respect to the nodal degrees of freedom  $\boldsymbol{q}$  enter the assembly of the linear system for the equilibrium iterations within the Newton solver. We account for the possible variation of the plastic strains  $\boldsymbol{\epsilon}_1^p$  as the nodal degrees of freedom change because of the plastic flow by replacing the elastic stiffness tensor  ${}^4\mathbb{C}$  with the tangent stiffness tensor from Eq. (37), which relates the increment of the stress to the increment of the total strain in the inelastic regime. The proposed variant of the return mapping algorithm to reach a statically and plastically admissible state, to be explained below in Section 7.2, facilitates a simplified (linearized) update of the plastic variables  $\boldsymbol{p}$  as it requires the trial stress state of the predictor step to remain in close proximity to the yield surface. Consequently, an explicit plastic corrector step suffices that does not require an iterative solution itself, see [31] for further details.

## 6. Transport of inelastic variables for axially moving shells

As we apply the mixed Eulerian–Lagrangian kinematic formulation, the mesh remains axially fixed, while material particles keep entering and leaving the control domain, see Fig. 1. Therefore, in each time step the necessity arises to update the inelastic variables, which are stored in the integration points of the finite elements with  $\bar{r} = \text{const}$ , but which should be considered as functions of the material coordinates  $\bar{r}$ . For this purpose, a 1D advection equation is solved at the concluding stage of each time increment, which is similar to the Eulerian step in the general

ALE formulation [8]. The algorithm described below was successfully applied in the simplified setting of a plane problem by Vetyukov et al. [13].

We begin by computing the material velocity of a particle in the axial direction  $\dot{x}$  according to

$$x = \hat{x} + u_x \Rightarrow \dot{x} = \dot{u}_x. \quad (43)$$

Here  $\hat{x}$  is the material coordinate and  $u_x$  is the axial displacement component, see Eqs. (4) and (5). A dot denotes a total (material) time derivative, computed in a moving material particle, while the notation  $\partial_t$  will be used for the local time derivative from the perspective of a spatially fixed observer:

$$(\dots)' = \left. \frac{\partial(\dots)}{\partial t} \right|_{\hat{x}=\text{const}}, \quad \partial_t(\dots) = \left. \frac{\partial(\dots)}{\partial t} \right|_{x=\text{const}}. \quad (44)$$

The local time derivative coincides with the time rate of a variable, observed in a given integration point of a finite element, which is fixed in the intermediate configuration. The material time derivative of any field variable  $\varphi(\vec{r}, t)$  thus results into a sum of the local time rate and the convective term:

$$\dot{\varphi} = \partial_t \varphi + \dot{u}_x \partial_x \varphi. \quad (45)$$

This also holds for  $\varphi = u_x$ , which allows to compute the axial component of the material velocity of a particle in terms of the nodal degrees of freedom:

$$\dot{u}_x = \partial_t u_x + \dot{u}_x \partial_x u_x \Rightarrow \dot{u}_x = \partial_t u_x (1 - \partial_x u_x)^{-1}. \quad (46)$$

The local time derivative of  $u_x$  determines the ‘‘amount’’ of material particles, which flow across a given spatial point per unit time and is thus called the *material transport rate*  $v = \partial_t u_x$ . It is clear, that the transport rate must remain constant in the entire model at stationary motion, when neither the deformation nor the plastic variables change from the perspective of a spatially fixed observer — because otherwise the particles would move across the control volume with different speeds and strains would accumulate, see [43] for further discussion. Seeking the stationary motion of the kind

$$u_x = \tilde{u}_x(\vec{r}) + vt, \quad u_y = u_y(\vec{r}), \quad u_z = u_z(\vec{r}), \quad \epsilon_{\perp}^p = \epsilon_{\perp}^p(\vec{r}, \zeta), \quad A^p = A^p(\vec{r}, \zeta), \quad (47)$$

which also implies the linear time dependence of the nodal variables  $q$  and the constancy of the plastic variables  $p$ , is the main aim of the simulation. Therefore we allow for a minor inaccuracy in resolving the transient stage and assume  $\partial_t u_x = v = \text{const}$  with  $v$  being a model parameter, which effectively scales the time variable  $t$  to the length dimension of the part of the metal sheet, which entered the control domain (sometimes called running meter). As a consequence of the geometric nonlinearity, the material velocity of particles remains deformation dependent because of the inverse of the expression in brackets in Eq. (46).

The total time rates of inelastic variables in a moving material particle are determined by the plastic flow terms, discussed in Section 5. However, local time rates define the increments in the integration points and thus the values in  $p$  in the end of a specific time step. From Eq. (45) follows

$$\partial_t \epsilon_{\perp}^p = \dot{\epsilon}_{\perp}^p - v(1 - \partial_x u_x)^{-1} \partial_x \epsilon_{\perp}^p, \quad \partial_t A^p = \dot{A}^p - v(1 - \partial_x u_x)^{-1} \partial_x A^p. \quad (48)$$

We proceed to the incremental form and multiply the equations by the time increment  $\Delta t$ . The material increments  $\Delta \epsilon_{\perp}^p = \dot{\epsilon}_{\perp}^p \Delta t$  and  $\Delta A^p = \dot{A}^p \Delta t$ , obtained from the converged Newton equilibrium iterations need to be augmented by additional terms to find the local changes in the plastic variables  $\partial_t \epsilon_{\perp}^p \Delta t$  and  $\partial_t A^p \Delta t$ . These additional ‘‘transport’’ terms are computed and applied in the concluding part of the time increment (Eulerian step), which reminds us of a single time step of the 1D advection equation. During stationary motion, the local time derivatives vanish, such that the increments because of the active plastic flow should be exactly compensated by the ‘‘transport’’ terms.

The Eulerian step is completed using a set of so called streamlines [44], which comprise all integration points along the axial coordinate with the same lateral coordinate  $\hat{y}$  and thickness coordinate  $\zeta$ . The total number of streamlines is thus a product of the number of elements in the lateral direction times the number of element integration points in one direction (equals 3) times the number of through-the-thickness integration points. The single explicit time step of the advection equation is performed for each transport line on the irregular 1D grid of the axial coordinates  $x_i$  using the backward-space finite difference scheme for the approximation of  $\partial_x \epsilon_{\perp}^p$  and  $\partial_x A^p$ , which ensures the stability of the time integration and accurate resolution of the stationary regime. The local values  $\partial_x u_x$  are directly available from the finite element approximation.

## 7. Simulation setup and time stepping procedures

In this section we shall first discuss the primary properties that determine the roll forming solution and later touch on the algorithmic steps involved in a simulation run.

### 7.1. Simulation setup and primary input/output-variables

The simulation setup for the upcoming Section 9 is depicted in Fig. 4. Material particles are transported with constant rate  $v$  through the control domain, entering at the left, clamped edge and exiting at the right, free edge. In this regard ‘‘clamping’’ means that the transverse deflections and their first derivatives must vanish. The roll-stand in the middle forms the planar sheet into a symmetric V-shaped profile. We actively enforce this symmetry by prohibiting lateral deflections  $u_y$  at the center fiber  $\hat{y} = 0$ , which effectively resolves stability issues due to under-constraining owing to the assumption of frictionless contact. This measure requires an element edge at the middle fiber and, thus, an even number of elements in lateral direction. All kinematic constraints are implemented via simple penalization of the corresponding nodal degrees of freedom.

Three distinct factors determine the result of the forming process for a given metal sheet, namely: the geometry of the roll pairings (i.e.: the roll profiles), the size of the roll gap and its position with respect to the reference height  $z = 0$  of the planar sheet. As for the roll profiles, we simply duplicate the actual profiles used during the physical experiments. We provide the corresponding files as supplementary material and visualize the geometry in Fig. 5. It depicts the roll-stand in its reference and actual configuration, as adjusted by means of the ‘‘roll-gap-reduction’’  $\rho$  and the vertical offset  $\Delta z$ . The former decreases the distance of the roll axes and, thus, determines the roll gap, while the latter applies a common vertical shift to both roll axes in order to lower or raise them with respect to the reference height  $z = 0$ . Initially, at  $\rho = \Delta z = 0$  the sheet barely passes through the roll stand without forming.

For an actual roll-forming mill, the forming forces between rolls and metal sheet are typically measured by load cells at the support positions, see Section 8. These forces act predominantly in vertical direction and are statically equivalent to the integrated normal contact forces in the corresponding regions at the lower and upper roll. We visualize them as external forces acting on the rolls in Fig. 5 and denote them as  $F_1$  for the upper roll and  $F_2$  for the lower roll. In case of the here considered simple V-shaped profile, the bending angle  $\varphi$  at the free end, see Fig. 4, is used to measure the outcome of the roll-forming process.

### 7.2. Algorithmic structure of a roll-forming simulation

The employed time-stepping procedure gradually approaches a steady state as described in Section 6. In the simulations, we consider a state to be quasi-stationary once the variations of the main postprocessing variables  $F_1$ ,  $F_2$  and  $\varphi$  become insignificant.



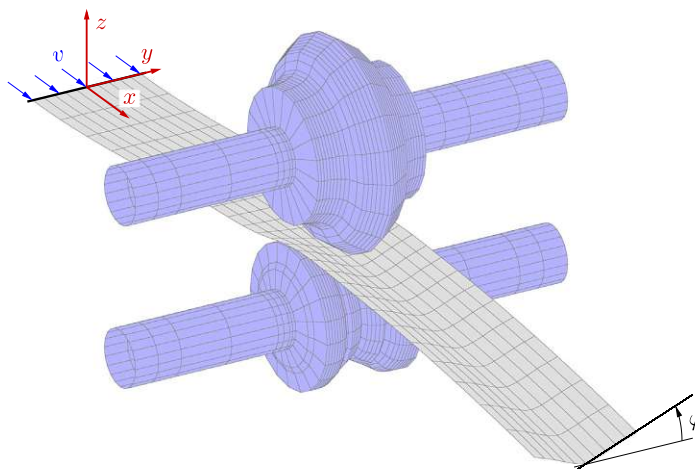


Fig. 4. Roll-forming simulation: As it passes through a single roll-stand, the flat sheet is bent into a symmetric V-shaped profile. The sheet is assumed to be clamped (no inclination, no transverse deflections) at  $x = 0$ , where particles enter the domain with the constant transport rate  $v$ . The bending angle  $\varphi$  is measured at the opposite free end.

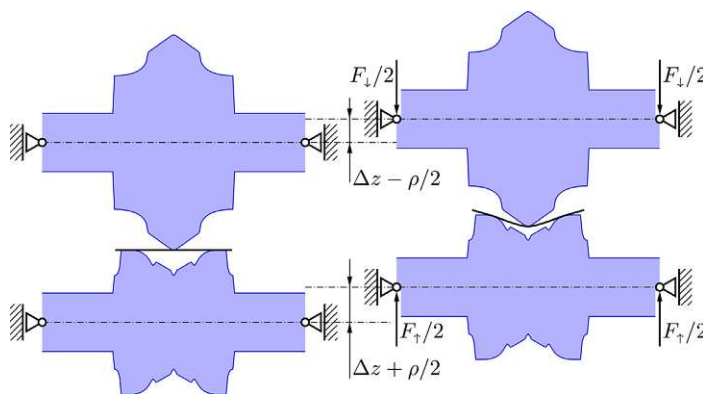


Fig. 5. Transverse cut through the roll stand for two configurations; left: the rolls are just touching the metal sheet and no forming happens (reference configuration); right: the distance between the rolls is reduced by  $\rho$  and their axes are further offset in vertical direction by  $\Delta z$  - actual forming requires roll forces  $F_i$  and  $F_t$ .

We provide a flowchart in Fig. 6 to illustrate the proposed algorithm. At  $t = 0$ , the metal sheet is in its planar reference state ( $q_0 = 0, p_0 = 0$ ) and the rolls are already at their final positions as described by  $\rho$  and  $\Delta z$ , see Fig. 5. This leads to a severe penetration of the contacting parts, which is alleviated by a corresponding time-incrementation of the contact penalty factor  $P$  following the interpolation:

$$P(t) = \begin{cases} P_{\max} \frac{\exp(\frac{bt}{t_1}) - 1}{\exp(b) - 1} & 0 \leq t < t_1 \\ P_{\max} & t_1 \leq t \end{cases} \quad (49)$$

Thus, the penalty vanishes initially, increases according to an exponential law with bias  $b$  up to some point in time  $t_1$  and is then held constant at its maximum value  $P_{\max}$ . The nonlinear growth promotes convergence in the early phase of the simulation. This time-incrementation of the penalty is a simple alternative to the kinematic loading by means of an adjustment of the roll gap; the system approaches the same stationary state regardless of the applied loading scheme.

The actual solution procedure for a given time step, again see Fig. 6, is entered after the actual penalty has been calculated. At heart, it contains a return-mapping scheme that features an elastic predictor-step to update the deformed state  $q$  followed by a corrector-step to update the plastic variables  $p$ . Unlike standard procedures, see [33], which perform the plastic correction only after the Newton solver has obtained a statically admissible state, we employ a common

single Newton loop that features plastic updates already at the level of equilibrium iterations. Although certain doubts were expressed in the literature regarding the compliance of this procedure with the path-dependent nature of the plastic material behavior, see remark 3.3 on page 107 of [45], it has proven to be numerically robust, computationally efficient and sufficiently accurate for the present needs. The measure undertaken to minimize the inconsistencies of the iterative plastic update within a time step amounts to the monitoring of the trial stress state  $\sigma_{\text{trial}}$  of the elastic predictor step with respect to its plastic admissibility:

$$\epsilon_{\text{flow}} = \frac{f(\sigma_{\text{trial}})}{k^2} - 1, \quad (50)$$

which features a comparison of the equivalent yield stress  $f$ , see Eq. (26), with the current yield strength  $k$ . The state at a particular point is plastically inadmissible if the above measure is positive ( $\epsilon_{\text{flow}} > 0$ ) and we make sure that this error remains small during the Newton loop. As remarked earlier at the end of Section 5, one benefit of this strategy is that all plastic states encountered while iterating are confined to the close proximity of the actual yield surface, which facilitates the linearization of the update procedure for plastic states and, thus, contributes to the accuracy of the solution of the path-dependent problem. The numerical convergence study with respect to the time step size, as presented in Table 6, as well as the successful validation against reference computations with the commercial software Abaqus

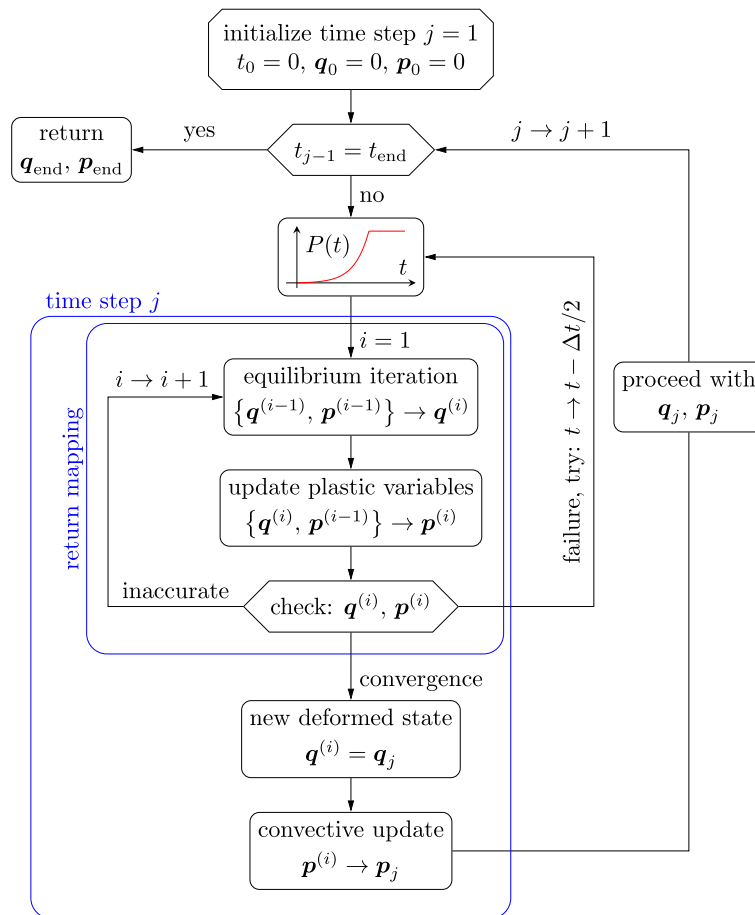


Fig. 6. Flowchart of the program to simulate the roll forming process: It features a return mapping scheme to obtain increments of the deformed state  $q$  and plastic variables  $p$ . The latter are further transported in accordance with the axial motion of the metal sheet. The forming forces are applied in an artificial manner by means of a time-incrementation of the contact penalty  $P$ .

in Section 9.1, dispel any doubt on the capability of the proposed scheme.

The return mapping iteration proceeds until a both statically and plastically admissible state is reached, which is judged by the maximum absolute values detected for the residual vector of the Newton scheme and the plastic error measure Eq. (50), respectively. Failure due to divergence, non-convergence after a maximum number of iteration steps or excessive plastic flow, when the plastic error measure  $\epsilon_{\text{flow}}$  exceeds a certain threshold, is addressed by restarting the solution increment with a halved time step.

Once a converged solution is obtained, the time step continues with the convective update of plastic variables in account of the axial transport of particles, as described in Section 6. At this stage, the accumulated plastic variables attached to the material particles are simply transported in axial direction. The convective update concludes the current time step. At constant penalty  $P$  only the axial transport of plastic variables  $p$  persists as “source of loading”. It effectively sustains the simulation, disposes of possibly non-physical artefacts of the load history along the way and ensures that the solution approaches a steady-state.

### 7.3. Static simulation case without transport

In order to validate the here proposed scheme against reference computations with conventional Lagrangian finite elements available

in the commercial software Abaqus, we also consider a static solution case with no axial motion of particles ( $v = 0$ ). This absence of material transport requires some adaptations to the simulation scheme presented in the flowchart of Fig. 6, because the just mentioned independence of simulation results from the load history is lost. In particular, the unphysical artefacts of the loading via incrementation of the penalty factor  $P$  will no longer be carried past the domain boundaries. The modified scheme for these static simulations features two separate stages:

1. Kinematic loading: With the contact penalty already at its maximum  $P_{\text{max}}$  increase the roll-gap-reduction  $\rho$  linearly from zero to its final value.
2. Unloading: Keep  $\rho$  and decrease the contact penalty from  $P_{\text{max}}$  to zero.

A vertical offset of the roll axes is not considered for this kind of simulation ( $\Delta z = 0$ ). The kinematic type of loading complies with the procedure implemented in Abaqus, but the penalty-controlled unloading does not. This does however not impede the comparability of results, as long as the unloading is primarily elastic. In conclusion, to adapt Fig. 6 for the static solution case, the convective update of plastic variables needs to be skipped and the load-scheme needs to be replaced with the just described two-stage procedure.

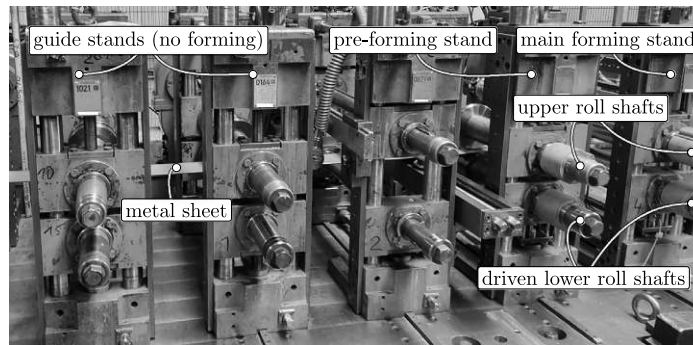


Fig. 7. Experimental setup to validate the simulation results; Roll forming mill — sideview.

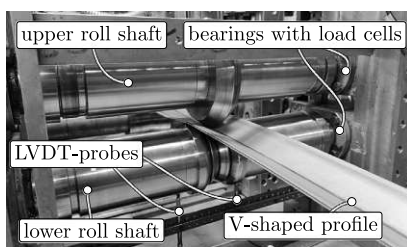


Fig. 8. Main roll forming pass during an experiment.

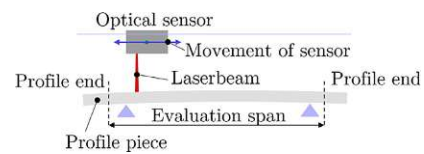


Fig. 9. Optical measurement unit to scan the profile geometry.

Table 1  
Measurement results of the physical experiments conducted for two different roll gaps.

ID	$F_1$ [N]	$F_2$ [N]	$g$ [mm]	$\rho$ [mm]	$\varphi$ [°]
a	11 876	11 654	7.719	10.622	17.9
b	11 892	12 544	5.547	12.794	20.9

### 8. Setup of physical experiments

For the sake of a validation of the simulation program a physical experiment was carried out on an actual roll forming mill, see Fig. 7. The metal sheet, continuously supplied by an uncoiler, is transported continuously through the mill from left to right through a series of roll forming passes. The first two stands serve as guides for the planar metal sheet to center it laterally, the third is inactive and the actual forming is performed at the last two stands. In this case pre-forming means, that an initial bending is applied to the metal sheet to guarantee a stable process. Nevertheless, the primary angle-change is caused by the main pass, as depicted in Fig. 8. The roll profiles of this stand correspond to those depicted in Fig. 5. In the experiment, the lower shafts of the two forming passes are driven to transport the sheet in axial direction and the forming process is carried out without lubrication at a low feed speed of 2.13 m/min. The primary variables of measurement are the roll force, the actual roll gap as well as the opening angle of the profile after forming. The mean of each measured parameter over the minimum produced profile length (6 m) per experiment under quasi static process conditions is used to characterize the individual experiments. To be able to make reliable statements, the experiments were repeated several times. The roll force acting on the lower rolls is measured by piezo-based load cells situated in the forming stands. Due to its correspondence to the distance of the upper and lower rolls, the roll gap can be accurately monitored by means of LVDT-based (Linear Variable Differential Transformer) measuring probes. A couple of these sensors are connected to the rotating surface of each roll; the ones in touch with the lower shaft are visible in Fig. 8. The forming angle was measured optically by a profile scanner every 10 mm on the cut pieces of 2 m length, with a distance to the profile ends of 300 mm to prevent the influence of end flare and deformations induced by the cutting process, see Fig. 9.

Two experiments (with ID “a” and “b”) for different roll gap sizes were conducted so far, which, nonetheless, should suffice to conclude on the general applicability of the simulation model and aid in the ongoing development of both the computational scheme as well as the

experimental setup. The results of these measurements are collected in Table 1, where  $F_1$  and  $F_2$  denote the measured mean roll forces at the first pre-forming stand and the second main forming stand, respectively.

For convenience, the optically measured opening angle of the profile is presented in terms of the equivalent bending angle  $\varphi$ . Likewise, the equivalent roll-gap-reduction  $\rho$  is provided alongside the actually measured value of the roll gap  $g$  for the sake of comparison against the simulation results. Both quantities are connected linearly through the conversion formula:

$$\rho = -g + h + \rho_*, \quad \text{with } \rho_* = 15.34 \text{ mm}, \quad (51)$$

which relates to the limiting situation of a minimal roll gap, where the minimum distance of the rolls at the main forming stand equals the thickness of the metal sheet  $h = 3 \text{ mm}$ ; the corresponding value  $\rho = \rho_*$  for this case was estimated geometrically based on the given radial roll profiles, see Fig. 5. It is important to note that Eq. (51) rests upon a simplification regarding the kinematic description of the contact interaction, where the thickness  $h$  of the metal sheet is disregarded; i.e. the contact is resolved as if the metal sheet had thickness zero. The thickness  $h$  of the metal sheet is not yet accounted for in the kinematic description of the contact interaction (as if the shell had zero thickness). In reality, this prerequisite will be violated; to what extent shall be revealed by the comparison of measured and simulated values for  $\rho$ .

### 9. Simulation results and validation

The formerly declared variables  $F_1$ ,  $F_2$  and  $\varphi$  shall serve as primary measures to judge the accuracy or convergence for the numerical studies ahead. For the sake of comparison, we introduce corresponding relative error measures for each parameter:

$$\epsilon_{F_{1,i}} = \frac{F_{1,i}}{F_{1,\text{ref}}} - 1, \quad \epsilon_{F_{2,i}} = \frac{F_{2,i}}{F_{2,\text{ref}}} - 1, \quad \epsilon_{\varphi,i} = \frac{\varphi_i}{\varphi_{\text{ref}}} - 1, \quad (52)$$

which relate the individual values to an entitled reference solution.

**Table 2**

The default parameters of the simulation model are provided in the SI-system of units.

Geometry			Material				
$L$	$w$	$h$	$E$	$\nu$	$\sigma_0$	$n$	
0.8	0.1	0.003	$2.08 \times 10^{11}$	0.3	$362 \times 10^6$	0.012	
Forming		Transport		Numerical			
$\rho$	$\Delta z$	$v$	$\Delta t$	$N_x$	$N_y$	$N_z$	$P$
0.01	0	0.8	0.005	26	10	8	$1 \times 10^{13}$

In what follows, we shall first ascertain the convergence of the finite element scheme itself, compare it briefly against reference computations with Abaqus for the static simulation case of Section 7.3, highlight the limitations of the stress resultant plasticity model, present the results of parameter studies and conclude with a first validation against physical experiments. The corresponding studies emanate from the set of default parameters presented in Table 2. The material parameters  $\sigma_0$  and  $n$  were experimentally identified by means of tension tests. The newly introduced parameters  $N_x$  and  $N_y$  denote the number of finite elements in axial and width direction, respectively, while  $N_z$  stands for the number of Gauss-points for the thickness integration of plastic states. The mesh is refined in axial direction such that the largest elements at the outmost ends are 2.5-times larger than the finest, which occupy the contact region. For the studies ahead the geometric and material properties remain unchanged, but we will vary both the numerical and the forming parameters.

### 9.1. Static comparison against abaqus

We consider the static simulation case as described in Section 7.3 and compare the simulation results of the proposed finite element scheme with reference computations conducted with the commercial software Abaqus. The default parameter set of Table 2 still applies, but the material transport rate vanishes ( $v = 0$ ) and the evolution of solutions is studied by means of an incrementation of the roll-gap-reduction  $\rho$ . In addition, we consider the elastic-ideal plastic case  $n = 0$  for simplicity.

The reference computations in Abaqus feature a very fine mesh with 5640 elements of the S4 type. The roll geometry needed to model the solid-to-rigid contact interaction is imported using piecewise interpolation in a similar manner as explained in Section 4. The corresponding Abaqus input file for the smallest roll gap is made available as supplementary material.

Since the bending angle  $\varphi$  at the free end, see Fig. 4, has little meaning in the context of the static simulation, we instead compare the persistent deformations after unloading by means of an angle  $\varphi_{\text{static}}$ , which is constructed in the same way but measured directly at the roll gap along the center line of the rolls in the lateral direction. Its plot with respect to the roll gap reduction  $\rho$  is accompanied by a corresponding graph of the roll force  $F_1$  in Fig. 10. The left plot covers the evolution of the lower roll force as  $\rho$  increases from zero to its final value (kinematic loading). The right graphic, on the other hand, depicts the resultant forming angle  $\varphi_{\text{static}}$  reached after unloading from particular values of  $\rho$ , that is to say: after elastic spring-back.

A kink is observed in the curve of  $F_1$  at  $\rho = 0.01834$  m. This corresponds to the minimal roll gap according to Eq. (51), as  $\rho(g = 0) = h + \rho_s = 0.01834$  m. The fact that the plotted curve after the kink is not perfectly vertical and even involves regions beyond  $\rho = 0.01834$  m is a consequence of the penalty contact formulation, which merely approximates the impenetrability condition of perfectly rigid rolls. However, the fact that the curve starts off in almost vertical direction after the kink, indicates that the chosen contact penalty is sufficiently large. The offset in the positions of the kinks and the somewhat “wavy” characteristic of the curve of  $F_1$  for the standard model relates to the discrete resolution of the contact zone expansion; a dense placement of integration points captures this continuous process

**Table 3**

Comparison of simulation results obtained for the stress resultant plasticity model against a reference computation with the default continuum plasticity approach; parameters according to Table 2.

Plasticity model	$F_1$ [N]	$\epsilon_{F_1}$ [%]	$F_1$ [N]	$\epsilon_{F_1}$ [%]	$\varphi$ [°]	$\epsilon_\varphi$ [%]
stress resultant	13 585	13.67	13 413	12.89	21.72	3.16
continuum	11 951	–	11 881	–	21.06	–

more accurately. Correspondence of  $\varphi_{\text{static}}$  between the two models is good and the persistent discrepancies in  $F_1$  obtained for the default model clearly diminish for the second, refined mesh. Furthermore, we note the development of a plateau in the curves of  $\varphi_{\text{static}}$ , after the minimal roll gap at  $\rho = 0.01834$  m is reached. This observation is according to expectation, as the maximum forming angle (in the loaded and therefore also in the unloaded state) is limited by what is kinematically prescribed by the roll profiles at the minimal roll gap.

### 9.2. Continuum vs. Stress resultant model

Here, we compare results of the continuum model which features the classical continuum plasticity treatment with integration points along the thickness against the stress resultant model introduced by Kocbay and Vetyukov [31]. The parameters and also the mesh are identical and correspond to Table 2; the number of thickness integration points  $N_z$  is meaningless for the stress resultant model, as it avoids the computationally costly thickness integration of plastic variables. We view the continuum model solution as the reference solution and collect the results in Table 3. The plate is moving with the transport rate  $v$ ; the presented values correspond to the quasi-steady state solution.

The bending angle agrees significantly better than the roll forces, which exhibit an error of about 13%. This indicates that the roll forming process is, as expected, bending-dominant meaning that the sustained plastic deformations mostly relate to a pure bending of the structure. However, the complete neglect of the membrane forces in the elastic–plastic constitutive relations of the stress resultant model, originally proposed for pure plate bending, leads to a pronounced over-estimation of the required forming forces. Based on the through-the-thickness resolution of plane-stress plasticity, the continuum model takes the coupling of bending and membrane effects into account and, consequently, achieves a similar persistent deformation at a lower force level. Hence, in its current form, the stress resultant model is not sufficiently accurate to resolve elastic–plastic bending of geometrically nonlinear shells. Nevertheless, from a practical point of view, a further development is worthwhile for the gain of computational efficiency, as the stress resultant model needs approximately seven times less computation time than the continuum model.<sup>4</sup>

### 9.3. Convergence of the finite element scheme

To verify the convergence of the proposed finite element scheme, we present parameter studies for the purely numerical parameters, namely: mesh discretization ( $N_x \times N_y$ ), time step  $\Delta t$ , thickness integration points  $N_z$  and contact penalty  $P$ . We treat each parameter individually, each time using the last (finest) simulation conducted for the particular sequence as a reference for the evaluation of the error measures Eq. (52). In every sequence we merely alter a single parameter of the default set of Table 2.

The finite element mesh is regular in lateral direction, but refined in axial direction  $x$  with the finest elements at the roll gap. Hence,

<sup>4</sup> Reaching a quasi-steady state solution for the default parameter set from Table 2 takes about 1 week for the continuum model vs. 1 day for the stress resultant model on a 16-core Intel(R) Xeon(R) CPU E5-2640 v3 at 2.60 GHz.

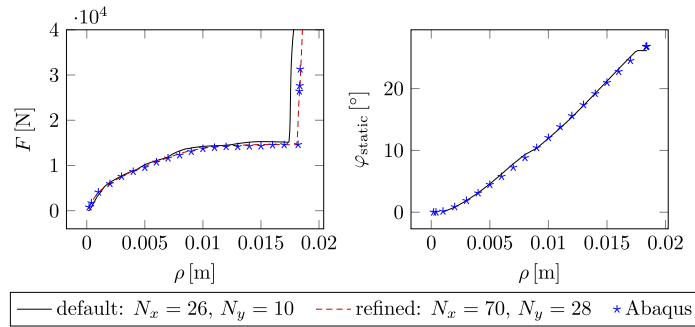


Fig. 10. Comparison of simulation results against reference computations with the commercial software Abaqus for the static analysis case as specified in Section 7.3; evolution of the roll force  $F_i$  for kinematic loading with  $\rho$ ; final forming angle  $\varphi_{\text{static}}$  after unloading from a state with roll-gap-reduction  $\rho$ .

**Table 4**  
Convergence of finite element results with respect to the number of elements in axial direction  $N_x$ .

$N_x$	$F_i$ [N]	$\epsilon_{F_i}$ [%]	$F_i$ [N]	$\epsilon_{F_i}$ [%]	$\varphi$ [°]	$\epsilon_\varphi$ [%]
14	12 471	9.64	12 433	9.66	23.58	15.39
18	12 092	6.31	12 073	6.48	22.39	9.55
26	11 951	5.06	11 881	4.79	21.06	3.06
36	11 514	1.22	11 476	1.22	21.36	4.53
50	11 375	-	11 338	-	20.43	-

**Table 5**  
Convergence of finite element results with respect to the number of elements in width direction  $N_y$ .

$N_y$	$F_i$ [N]	$\epsilon_{F_i}$ [%]	$F_i$ [N]	$\epsilon_{F_i}$ [%]	$\varphi$ [°]	$\epsilon_\varphi$ [%]
6	12 285	6.34	12 219	6.41	21.20	0.5
8	12 118	4.9	12 049	4.92	21.46	1.71
10	11 951	3.45	11 881	3.46	21.06	-0.17
14	11 641	0.76	11 570	0.76	21.45	1.67
20	11 552	-	11 483	-	21.10	-

**Table 6**  
Convergence of finite element results with respect to the time step size  $\Delta t$ .

$\Delta t$ [s]	$F_i$ [N]	$\epsilon_{F_i}$ [%]	$F_i$ [N]	$\epsilon_{F_i}$ [%]	$\varphi$ [°]	$\epsilon_\varphi$ [%]
$2.5e^{-2}$	11 951	-0.17	11 881	-0.18	21.06	0.31
$5.0e^{-3}$	11 951	-0.17	11 881	-0.18	21.06	0.31
$2.0e^{-3}$	11 971	$1.52e^{-3}$	11 902	$1.52e^{-3}$	20.99	$7.44e^{-4}$
$1.0e^{-3}$	11 971	$1.86e^{-3}$	11 902	$1.85e^{-3}$	20.99	$5.27e^{-4}$
$5.0e^{-4}$	11 971	-	11 902	-	20.99	-

**Table 7**  
Convergence of finite element results with respect to the number of Gauss-points for the thickness integration  $N_\zeta$ .

$N$	$F_i$ [N]	$\epsilon_{F_i}$ [%]	$F_i$ [N]	$\epsilon_{F_i}$ [%]	$\varphi$ [°]	$\epsilon_\varphi$ [%]
4	11 916	-0.25	11 848	-0.25	20.95	-0.37
6	11 942	$-3.23e^{-2}$	11 869	$-7.79e^{-2}$	21.14	0.51
8	11 951	$4.20e^{-2}$	11 881	$2.50e^{-2}$	21.06	0.14
10	11 947	$7.43e^{-3}$	11 879	$1.10e^{-2}$	21.02	$-5.23e^{-2}$
14	11 945	$-5.60e^{-3}$	11 877	$-5.20e^{-3}$	21.04	$3.79e^{-2}$
18	11 946	-	11 878	-	21.03	-

**Table 8**  
Convergence of finite element results with respect to penalty factor for the contact model  $P$ .

$P$ [N/m <sup>3</sup> ]	$F_i$ [N]	$\epsilon_{F_i}$ [%]	$F_i$ [N]	$\epsilon_{F_i}$ [%]	$\varphi$ [°]	$\epsilon_\varphi$ [%]
$1e^{12}$	11 995	0.25	11 933	0.35	20.46	-3.09
$1e^{13}$	11 951	-0.11	11 881	$-8.80e^{-2}$	21.06	-0.27
$1e^{14}$	11 964	$-5.97e^{-3}$	11 891	$-3.87e^{-3}$	21.11	$-1.80e^{-2}$
$1e^{15}$	11 964	-	11 891	-	21.12	-

the number of elements in axial direction  $N_x$  is actually an incomplete measure of mesh quality, but it remains adequate as long as the actual refinement strategy is not altered. We collect the results of the simulation sequences for  $N_x$  and  $N_y$  in Tables 4 and 5, respectively. Element numbers are increased or decreased by scaling the standard parameters of Table 2 with positive or negative powers of  $\sqrt{2}$ . However,  $N_x$  scales only roughly with this factor, as we actually modify internal mesh parameters that relate to the element lengths at the left end, the right end and the middle, where the roll-stand is situated. Furthermore, the fulfillment of the symmetry constraint, see Section 7.1, requires the scaled result for  $N_y$  to be rounded to the next even number.

The maximum number of elements for the last simulation is  $N_x \times N_y = 1000$ . With a maximum relative error of  $\approx 5\%$  and only 260 elements, the default parameter set yields sufficient accuracy for a first validation at reasonable computational cost. In both studies, convergence of the error measures is clearly visible, but non-monotonous in case of  $\epsilon_\varphi$ . This kind of somewhat erratic convergence behavior is common in problems of contact of structures, see [46]. Evidently, the discretization and, thus, the actual integration point placement for contact and plastic variables in relation to the roll geometry has a significant impact on the quality of a particular simulation.

Table 6 covers the convergence study for the time-step size  $\Delta t$ ; the actual step sizes are halved sequentially. Owing to the accompanying backward finite difference integration for the advection problem of plastic variables, see Section 6, the maximum admissible time-step is bounded. This upper limit depends on the transport velocity as well as the discretization level in axial direction, because the finite differences

are evaluated at sequential finite element integration points. In other words: the traveled distance of a material particle per time step shall not surpass the distance between two successive integration points. Consequently, a finer discretization in axial direction also requires finer time-steps; in the present case  $\Delta t = 0.025$  is close to this limit. Emanating from this step size, the solution converges rapidly, which demonstrates the robustness of the time integration scheme.

For the sake of completeness, we further consider the number of thickness integration points  $N_\zeta$  and the penalty factor  $P$  in Tables 7 and 8, respectively. While  $N_\zeta$  determines the resolution of the inner variables in the thickness direction of the proposed continuum plasticity model, the penalty factor  $P$  should ensure a sufficient approximation of the impenetrability condition of the solid-to-rigid contact model.

Convergence with respect to both parameters is rapid and monotonous. Theoretically, the number of thickness integration points could

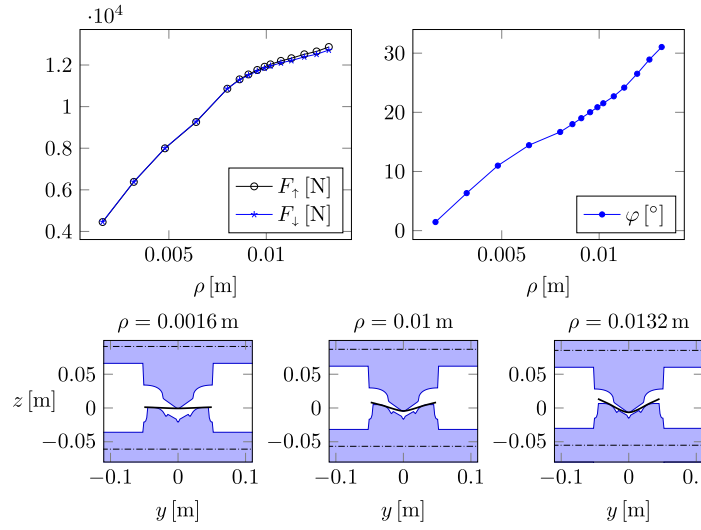


Fig. 11. Evolution of the roll forces ( $F_t, F_b$ ) and forming angle ( $\varphi$ ) with respect to the roll-gap-reduction; the three small graphics depict the situation in the roll gap for: the maximal, an intermediate and the minimal roll gap.

be increased further, albeit at diminishing gain and excessive computational cost. The maximum admissible penalty factor on the other hand is bounded by numerical ill-conditioning of the system of equations.

#### 9.4. Parameter studies

The roll-gap-reduction  $\rho$  is the most influential parameter to determine the resultant profile of the metal sheet. The degree of roll forming, measured in terms of the angle  $\varphi$ , as well as the roll forces  $F_t$  and  $F_b$  increase as the roll gap is reduced. Naturally, the actual evolution of these variables with respect to  $\rho$  strongly depends on the roll geometry; Fig. 11 depicts the corresponding graphs for the default parameter set and roll profiles, see Table 2 and Fig. 5, respectively. The accompanying small graphics illustrate the forming process in the roll gap for three sample values of  $\rho$ . The initial almost linear growth of the variables becomes degressive for the roll forces and progressive for the forming angle for ever-increasing values of  $\rho$ . Since the forming process in the roll gap is reminiscent of three-point-bending, this gradual loss of load bearing capacity relates to the establishment of a kind of plastic joint in the center, which cannot be compensated by the small parameter of isotropic hardening.

If  $\rho$  was increased even further, the upper and lower rolls would eventually touch each other through the metal sheet, a situation not accounted for in the program so far. Moreover, owing to the assumption of rigid rolls, the reliability of simulation results diminishes as the actual magnitude of elastic deformations of the rolls approaches the size of the persistent roll gap.

To further illustrate the forming-process and visualize the regions of plastic forming, Fig. 12 features a color-mapping of the plastic dissipation power per unit surface area, which we denote as  $\dot{A}_1^p$ . To compute it, we refer to Eq. (48) and make use of the fact that the local time derivative  $\partial_t A^p$  tends to zero and only the convective part persists as the simulation approaches a stationary state. Hence, we merely need to integrate Eq. (48) for  $\partial_t A^p = 0$  with respect to the thickness coordinate:

$$\dot{A}_1^p = \int_{-h/2}^{h/2} (v(1 - \partial_x u_x)^{-1} \partial_x A^p) d\zeta. \quad (53)$$

The color-mapping is overlaid on a plot of a part of the deformed structure; black lines depict the edges of the axially refined Eulerian-Lagrangian finite element mesh. As expected, most of the plastic work

is done at the center of the roll gap, where the sheet receives its primary bend. The minor peaks on either side correspond to the contact with the shoulders of the lower profile, which induces some counter-bending, see Fig. 11 for comparison. Though most of the forming happens in the contact region, plastic deformations also occur before contact with the rolls is established, an observation well founded in engineering practice, see [47,48].

We maintain all other parameters from Table 2 and focus the second parameter study on the vertical offset  $\Delta z$  of the roll gap. We vary the parameter in the interval  $\Delta z = \pm 0.05$  m and analyze its impact on the roll forces and the forming angle in Fig. 13. The accompanying small plots show the geometric proportions in the roll gap for three particular cases. The offset induces a vertical bending of the sheet, which alters the contact force distribution. Consequently, the roll forces, which were almost indistinguishable earlier on in Fig. 11, separate from each other. The effect of a vertical shift on the forming angle  $\varphi$ , which relates to the coupling of bending deformations in the geometrically nonlinear theory, is minimal at first and pronounced at higher magnitudes of  $\Delta z$ . Interestingly, since the mean of the two roll forces increases monotonously with  $\Delta z$  (except for the leftmost point), higher degrees of forming may be reached at reduced force levels.

It is worth mentioning that the actual effect of the vertical offset depends on the global boundary conditions, which is important in prospect of a future comparison against physical experiments. At present the sheet is clamped at the left boundary (except for the axial motion) and free to move at the right boundary.

Another outcome of the plastic forming process with vertical offset  $\Delta z$ , which is known to occur in practice and reproducible in our simulations, is a pronounced bending deformation of the structure in the  $xz$ -plane after rolling, see Fig. 14. To better visualize the resultant curvature, the center fiber  $\hat{y} = 0$  is highlighted in the 3D picture and plotted in Fig. 15, which features corresponding graphs for three different values of the offset  $\Delta z$ . The curvature of the elastic bending deformation changes its sign due to plastic deformations at the roll stand. As illustrated in the picture, the persistent deformations of the fiber past the roll gap may be approximated by quadratic parabolas. For various values of  $\Delta z$  the resultant curvatures of these fitting parabolas, computed as second order derivatives with respect to  $x$ , are connected in Fig. 16. The zero-point of this curve at  $\Delta z \approx -7.76 \times 10^{-3}$  m marks the optimal offset to obtain a straight profile after roll forming.

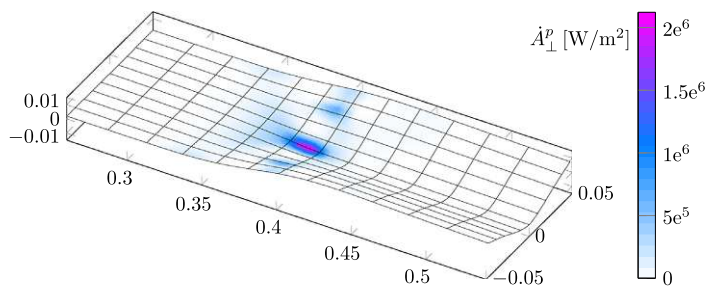


Fig. 12. Dissipation power per unit of area  $\dot{A}_\perp^p$  mapped over the deformed structure; black lines correspond to the axially refined finite element mesh.

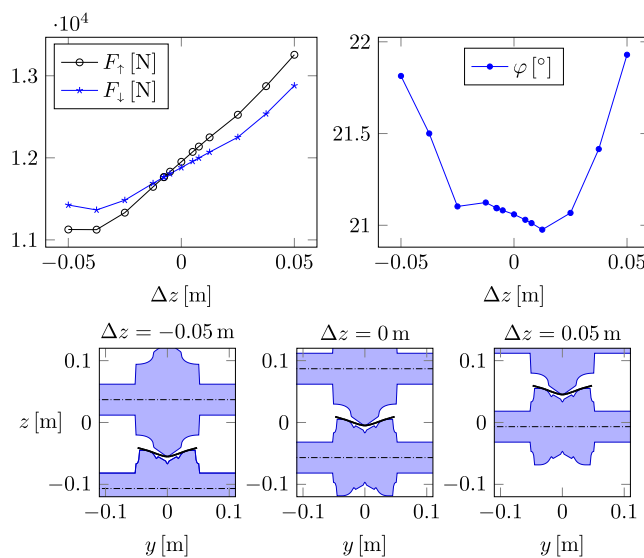


Fig. 13. Evolution of the roll forces ( $F_\uparrow$ ,  $F_\downarrow$ ) and bending angle ( $\varphi$ ) with respect to a vertical offset  $\Delta z$ ; the small graphics visualize the magnitude of this shift in relation to the roll gap geometry.

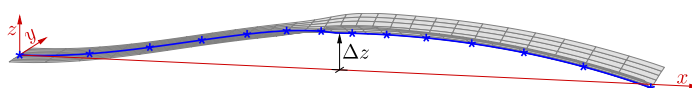


Fig. 14. A vertical offset  $\Delta z$  induces a persistent axial curvature that points in opposite direction of the kinematically induced bend; the path of the center fiber  $\hat{y} = 0$  is highlighted.

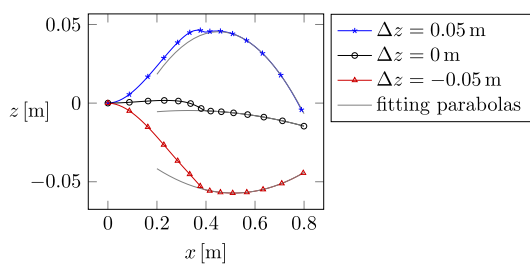


Fig. 15. Deflected paths of the axial fiber  $\hat{y} = 0$  for various values of vertical offset  $\Delta z$ ; a quadratic parabola fit is used to retrieve the persistent curvature of the right segment.

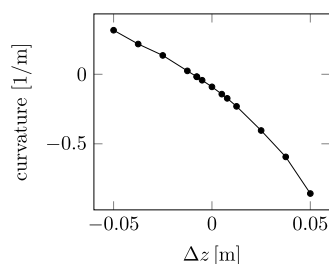


Fig. 16. Persistent curvatures of the center fiber  $\hat{y} = 0$  after roll-forming as derived from parabola fits of the deflected configuration (see Fig. 15) for several values of the vertical offset  $\Delta z$ .

### 9.5. Comparison against physical experiments

The modified simulation model for the comparison against the physical experiment is visualized in Fig. 17, which also provides a glance at

the roll geometry of the pre-forming stand. Most of the parameters of Table 2 still apply, but, in order to accommodate two forming stands, the total length of the spatial domain is extended to  $L = 1.2$  m with the pre-forming stand situated at  $x = 0.4$  m and the main forming stand

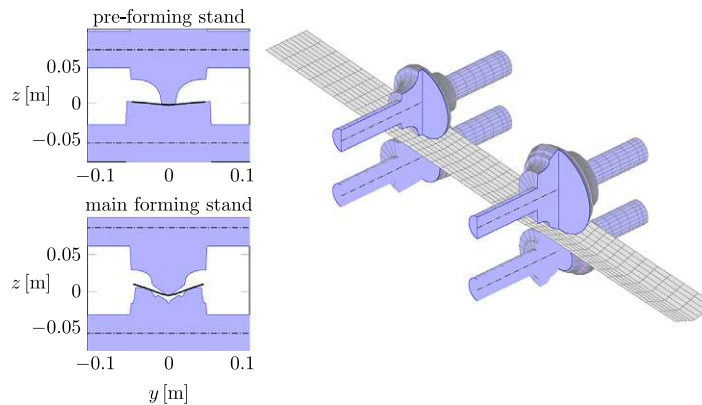


Fig. 17. 3D visualization of the finite element simulation model for comparison against the physical experiments.

Table 9

Validation of simulation results against the physical experiment: the roll-gap-reductions for both roll stands are identified by fitting of  $F_1$  and  $\varphi$  to the measurements of Table 1, which leaves the force  $F_2$  and the roll-gap-reductions  $\rho_2$  at the main forming stand for the comparison.

ID	Roll-gap-reductions		Simulation results			Deviations	
	$\rho_1$ [m]	$\rho_2$ [m]	$F_1$ [N]	$F_2$ [N]	$\varphi$ [°]	$\frac{F_2^{\text{sim}}}{F_2^{\text{measure}}} - 1$	$\frac{\rho_2^{\text{sim}}}{\rho_2^{\text{measure}}} - 1$
a	$4.895e^{-3}$	$9.311e^{-3}$	11 832	10 143	17.9	-0.130	-0.123
b	$4.895e^{-3}$	$1.075e^{-2}$	11 863	10 928	21.0	-0.129	-0.160

at  $x = 0.8$  m, i.e. 0.4 m apart like in the experiment. Owing to this extension and in account for the second roll stand, the corresponding finite element mesh now consists of  $N_x = 42$  elements in axial direction, while the number in width direction remains at  $N_y = 10$ .

In principle, the primary variables to adjust to a particular experiment of Table 1 are the roll-gap-reductions  $\rho_1$  and  $\rho_2$  as well as the vertical offsets  $\Delta z_1$  and  $\Delta z_2$  at the first and second roll stand, respectively. However, the current physical setup does not allow for a measurement of the vertical positions of the roll gaps. Therefore, we simply disregard the vertical offset and set  $\Delta z_1 = \Delta z_2 = 0$  fully aware of the fact that this choice might impact the results in the range of up to  $\pm 5\%$ , see Fig. 13.

The collected simulation results regarding the validation against the measured data of Table 1 are presented in Table 9, which also features the relative deviations of the force  $F_2$  and the roll-gap-reduction  $\rho_2$  at the main roll stand with respect to the physical experiment.

For each experiment, the roll-gap-reductions are chosen such that the measured force at the pre-forming stand  $F_1$  and the bending angle  $\varphi$  are reproduced accurately in the simulation. Hence, the force  $F_2$  and the roll-gap-reduction  $\rho_2$  remain for comparison against the measurements. Direct specification of the roll gap at the main forming stand in the simulation by means of the experimentally identified values according to Eq. (51) is not appropriate as the thickness  $h$  of the metal sheet is not yet consistently accounted for in the kinematic description of the contact interaction. In this regard, the registered deviation for  $\rho_2$  shall be viewed as an error measure which highlights differences between the actual contact interaction (contact at upper and lower face of the shell, at  $\zeta = \pm h/2$ ) and the implemented contact interaction (contact at the middle surface of the shell, at  $\zeta = 0$ ). The discrepancy increases alongside the force  $F_2$  in Table 9 as the roll gap gets smaller, such that the distinction of the two contact interactions becomes more pronounced at higher loads. The validation in terms of  $F_2$  yields a relative error of 13% in both cases. Though still subject to uncertainties as aforementioned, this result gives us confidence that the predictions of the mathematical model at hand reflect the reality both qualitatively and, to a good extent, quantitatively.

## 10. Conclusion

We considered the simulation of the sheet metal roll forming process. The proposed novel simulation model features Kirchhoff–Love shell finite elements in the mixed Eulerian–Lagrangian kinematic description, which efficiently resolves the major drawbacks of the established Lagrangian finite element formulations. Primary variables are parametrized with the coordinates of an intermediate configuration  $\bar{r}$ , which amounts to a Eulerian description of the axial motion and a Lagrangian one for the deflections in transverse and lateral direction. Consequently, material flows through the finite element mesh in axial direction, which facilitates a refined discretization for increased numerical efficiency and, moreover, enables resolution of contact interactions at fixed points in space, thereby preventing the occurrence of spurious numerical oscillations. In this regard, classic Lagrangian finite elements are clearly inferior owing to the strict attachment of nodal points to the motion of material particles.

After a thorough theoretical derivation of the computational model, we performed a series of tests and parameter studies to judge convergence behavior and consistency as well as to identify potential limitations, which shall guide the ongoing development of the scheme towards an application-oriented simulation tool:

- The consistency of the scheme is established in comparison to a reference computation with the commercial software Abaqus in a simplified static setting. The stress resultant plasticity model, reported in [31] and based on the formulation of the plastic constitutive laws in terms of the stress resultants of an elastic–plastic plate, is highly efficient but inaccurate for the purpose of roll forming as compared to the standard continuum plasticity approach. This is due to the complete neglect of membrane stresses in the elastic–plastic constitutive relations of the stress resultant model that are found to have significant effect on the growth of plastic deformations, even though roll forming is a bending-dominant forming process.
- Parameter studies demonstrate the impact of the primary system parameters, which relate to the size and position of the roll gap, on the outcome of the forming process. In addition, results known from engineering practice are successfully reproduced with the simulation model, namely: Plastic deformations already occur before the material establishes contact with the rolls and a vertical offset of the roll gap with respect to the reference plane of the metal sheet induces an axial curvature, i.e. it causes the axis of the steel profile to bend.
- A physical experiment is devised at a roll forming mill to compare the simulation results against actual measurements. This first validation demonstrates the growing relevance of the accurate



kinematic description of the contact interaction, as the roll forces increase, which is not yet fully accounted for in the computational model. The relative deviation in terms of the roll forces at the main forming stand is approximately 13%. Two points to further improve this promising yet not completely satisfactory result in future are: the proper extension of the experimental setup (e.g.: measurement of vertical positioning of the individual roll stands with respect to the planar metal sheet) and the consistent account for the finite thickness of the metal sheet in terms of the contact kinematics.

Ultimately, the proposed finite element scheme is intended as an efficient numerical tool to help improve the design process for roll forming mills and to serve as a basis for model-based control designs. In terms of numerical efficiency, it is worth pursuing the development of the stress resultant plasticity model, which still awaits an appropriate extension regarding the inclusion of membrane effects in the elastic-plastic constitutive relations.

#### CRedit authorship contribution statement

**Emin Kocbay:** Conceptualization, Investigation, Methodology, Software, Validation, Visualization, Writing – original draft, Writing – review & editing. **Jakob Scheidl:** Conceptualization, Investigation, Methodology, Software, Validation, Visualization, Writing – original draft, Writing – review & editing. **Fabian Riegler:** Investigation. **Martin Leonhartsberger:** Investigation, Writing – original draft. **Matthias Lamprecht:** Investigation, Writing – original draft. **Yury Vetyukov:** Conceptualization, Methodology, Software, Supervision, Writing – original draft, Writing – review & editing.

#### Declaration of competing interest

The authors declare that they have no known competing financial interests or personal relationships that could have appeared to influence the work reported in this paper.

#### Data availability

Data will be made available on request.

#### Acknowledgment

The authors acknowledge TU Wien Bibliothek for financial support through its Open Access Funding Programme.

#### Appendix A. Supplementary data

Supplementary material related to this article can be found online at <https://doi.org/10.1016/j.tws.2023.110662>.

#### References

- [1] G.T. Halmos, Roll Forming Handbook, CRC Press, 2005.
- [2] Y. Crutzen, R. Boman, L. Papeleux, J.-P. Ponthot, Lagrangian and arbitrary Lagrangian Eulerian simulations of complex roll-forming processes, *C. R. Mec.* 344 (4–5) (2016) 251–266.
- [3] M.S. Tehrani, P. Hartley, H.M. Naeini, H. Khademizadeh, Localised edge buckling in cold roll-forming of symmetric channel section, *Thin-Walled Struct.* 44 (2) (2006) 184–196.
- [4] F. Heislitz, H. Livatyali, M.A. Ahmetoglu, G.L. Kinzel, T. Altan, Simulation of roll forming process with the 3-D FEM code PAM-STAMP, *J. Mater. Process. Technol.* 59 (1–2) (1996) 59–67.
- [5] Q. Bui, J. Ponthot, Numerical simulation of cold roll-forming processes, *J. Mater. Process. Technol.* 202 (1–3) (2008) 275–282.
- [6] J. Cheng, J. Cao, J. Zhao, J. Liu, R. Zhao, S. Liu, The flower pattern and rolls design for ERW pipes with the different specification in the flexible roll forming process, *Thin-Walled Struct.* 154 (2020) 106809.
- [7] E. Oborin, Y. Vetyukov, I. Steinbrecher, Eulerian description of non-stationary motion of an idealized belt-pulley system with dry friction, *Int. J. Solids Struct.* 147 (2018) 40–51.
- [8] J. Donea, A. Huerta, J.-P. Ponthot, A. Rodriguez-Ferran, Arbitrary Lagrangian-Eulerian methods, in: E. Stein, R. de Borst, T. Hughes (Eds.), *Encyclopedia of Computational Mechanics*, Vol. 1: Fundamentals, John Wiley & Sons, Ltd, 2004.
- [9] V. Longva, S. Sævik, A Lagrangian–Eulerian formulation for reeling analysis of history-dependent multilayered beams, *Comput. Struct.* 146 (2015) 44–58.
- [10] E. Kuhl, H. Askes, P. Steinmann, An ALE formulation based on spatial and material settings of continuum mechanics. Part 1: Generic hyperelastic formulation, *Comput. Methods Appl. Mech. Engrg.* 193 (39–41) (2004) 4207–4222.
- [11] A. Humer, I. Steinbrecher, L. Vu-Quoc, General sliding-beam formulation: A non-material description for analysis of sliding structures and axially moving beams, *J. Sound Vib.* 480 (2020) 115341.
- [12] Y. Vetyukov, P. Gruber, M. Krommer, Nonlinear model of an axially moving plate in a mixed Eulerian-Lagrangian framework, *Acta Mechanica* 227 (2016) 2831–2842.
- [13] Y. Vetyukov, P. Gruber, M. Krommer, J. Gerstmayr, I. Gafur, G. Winter, Mixed Eulerian-Lagrangian description in materials processing: deformation of a metal sheet in a rolling mill, *Internat. J. Numer. Methods Engrg.* 109 (2017) 1371–1390.
- [14] J. Scheidl, Y. Vetyukov, C. Schmidrathner, K. Schulmeister, M. Proschek, Mixed Eulerian–Lagrangian shell model for lateral run-off in a steel belt drive and its experimental validation, *Int. J. Mech. Sci.* 204 (2021) 106572.
- [15] V.V. Eliseev, Y.M. Vetyukov, Finite deformation of thin shells in the context of analytical mechanics of material surfaces, *Acta Mech.* 209 (1–2) (2010) 43.
- [16] Y. Vetyukov, *Nonlinear Mechanics of Thin-Walled Structures: Asymptotics, Direct Approach and Numerical Analysis*, Springer Science & Business Media, 2014.
- [17] F. Bogner, The generation of interelement-compatible stiffness and mass matrices by the use of interpolation formulas, in: *Proc. Conf. Matrix Meth. Struct. Mech.*, Wright-Patterson AFB, 1965, pp. 397–443.
- [18] Y. Vetyukov, Finite element modeling of Kirchhoff-Love shells as smooth material surfaces, *ZAMM* 94 (1–2) (2014) 150–163.
- [19] S. Kaczmarczyk, The dynamic interactions and control of long slender continua and discrete inertial components in vertical transportation systems, in: *Nonlinear Dynamics of Discrete and Continuous Systems*, Springer, 2021, pp. 117–128.
- [20] K. Marynowski, Free vibration analysis of an axially moving multiscale composite plate including thermal effect, *Int. J. Mech. Sci.* 120 (2017) 62–69.
- [21] C. Mueller, X. Gu, L. Baeumer, P. Groche, Influence of friction on the loads in a roll forming simulation with compliant rolls, in: *Key Engineering Materials*, Vol. 611, Trans Tech Publ, 2014, pp. 436–443.
- [22] R. Safdarian, H.M. Naeini, The effects of forming parameters on the cold roll forming of channel section, *Thin-Walled Struct.* 92 (2015) 130–136.
- [23] H. Hetzler, On moving continua with contacts and sliding friction: Modeling, general properties and examples, *Int. J. Solids Struct.* 46 (13) (2009) 2556–2570.
- [24] M. Crisfield, Finite element analysis for combined material and geometric nonlinearities, in: *Nonlinear Finite Element Analysis in Structural Mechanics*, Springer, 1981, pp. 325–338.
- [25] J. Lubliner, *Plasticity Theory*, Dover Publications, Inc, 2008.
- [26] M. Bieniek, J. Funaro, *Elasto-Plastic Behavior of Plates and Shells*, Technical Report, Weidlinger Associates, New York, 1976.
- [27] A. Ibrahimbegović, F. Frey, An efficient implementation of stress resultant plasticity in analysis of Reissner-Mindlin plates, *Internat. J. Numer. Methods Engrg.* 36 (2) (1993) 303–320.
- [28] B. Skallerud, L. Myklebust, B. Haugen, Nonlinear response of shell structures: effects of plasticity modelling and large rotations, *Thin-Walled Struct.* 39 (6) (2001) 463–482.
- [29] J. Dujc, B. Brank, On stress resultant plasticity and viscoplasticity for metal plates, *Finite Elem. Anal. Des.* 44 (4) (2008) 174–185.
- [30] J. Dujc, B. Brank, Stress resultant plasticity for shells revisited, *Comput. Methods Appl. Mech. Engrg.* 247 (2012) 146–165.
- [31] E. Kocbay, Y. Vetyukov, Stress resultant plasticity for plate bending in the context of roll forming of sheet metal, *Internat. J. Numer. Methods Engrg.* 122 (18) (2021) 5144–5168.
- [32] M. Ambati, J. Kiendl, L. De Lorenzis, Isogeometric Kirchhoff-Love shell formulation for elasto-plasticity, *Comput. Methods Appl. Mech. Engrg.* 340 (2018) 320–339.
- [33] J. Simo, R. Taylor, A return mapping algorithm for plane stress elastoplasticity, *Internat. J. Numer. Methods Engrg.* 22 (3) (1986) 649–670.
- [34] M. Crisfield, *Non-Linear Finite Element Analysis of Solids and Structures*. Vol.1, John Wiley & Sons, 1991.
- [35] V. Eliseev, *Mechanics of Deformable Solid Bodies (in Russian)*, St. Petersburg State Polytechnical University Publishing House, St. Petersburg, 2006.
- [36] S. Eisenräger, J. Kiendl, G. Michaloudis, R. Duy, Y. Vetyukov, Stability analysis of plates using cut bogner-fox-schmit elements, *Comput. Struct.* 270 (2022) 106854.
- [37] P.G. Ciarlet, An introduction to differential geometry with applications to elasticity, *J. Elasticity* 78 (1) (2005) 1–215.
- [38] L.P. Lebedev, M.J. Cloud, V.A. Eremeyev, *Tensor Analysis with Applications in Mechanics*, World Scientific, 2010.

- [39] Y. Vetyukov, A. Kuzin, M. Krommer, Asymptotic splitting in the three-dimensional problem of elasticity for non-homogeneous piezoelectric plates, *Int. J. Solids Struct.* 48 (1) (2011) 12–23.
- [40] Q. Hu, X. Li, J. Chen, On the calculation of plastic strain by simple method under non-associated flow rule, *Eur. J. Mech. A Solids* 67 (2018) 45–57.
- [41] H. Kleemola, M. Nieminen, On the strain-hardening parameters of metals, *Metall. Trans.* 5 (8) (1974) 1863–1866.
- [42] M.C. Butuc, C. Teodosiu, F. Barlat, J.J. Gracio, Analysis of sheet metal formability through isotropic and kinematic hardening models, *Eur. J. Mech. A Solids* 30 (4) (2011) 532–546.
- [43] V. Eliseev, Y. Vetyukov, Effects of deformation in the dynamics of belt drive, *Acta Mech.* 223 (8) (2012) 1657–1667.
- [44] U. Nackenhorst, The ALE-formulation of bodies in rolling contact: Theoretical foundations and finite element approach, *Comput. Methods Appl. Mech. Engrg.* 193 (39–41) (2004) 4299–4322.
- [45] J. Simo, R. Taylor, Consistent tangent operators for rate-independent elastoplasticity, *Comput. Methods Appl. Mech. Engrg.* 48 (1) (1985) 101–118.
- [46] J. Scheidl, Y. Vetyukov, Steady motion of a slack belt drive: Dynamics of a beam in frictional contact with rotating pulleys, *J. Appl. Mech.* 87 (12) (2020) 121011.
- [47] D. Bhattacharyya, P. Smith, C. Yee, I. Collins, The prediction of deformation length in cold roll-forming, *J. Mech. Work. Technol.* 9 (2) (1984) 181–191.
- [48] M. Lindgren, An improved model for the longitudinal peak strain in the flange of a roll formed U-channel developed by FE-analyses, *Steel Res. Int.* 78 (1) (2007) 82–87.

## Paper C

*An enhanced stress resultant plasticity model for shell structures with application in sheet metal roll forming*

TU Wien: Emin Kocbay, Jakob Scheidl, Fabian Schwarzinger, Yury Vetyukov  
*The International Journal of Advanced Manufacturing Technology*, December 2023  
<https://doi.org/10.1007/s00170-023-12544-1>

**Keywords:** Metal plasticity, Stress resultant shell plasticity, Kirchhoff–Love shell, roll forming, Finite element analysis, Mixed Eulerian–Lagrangian formulation

**Abstract:** The proposed Kirchhoff–Love shell stress resultant plasticity model extends a previously reported model for plates by complementing the constitutive law of elastoplasticity with membrane effects. This enhanced model is designed for bending dominant settings with small to moderate membrane forces. It is thus implemented in a purpose-built nonlinear mixed Eulerian–Lagrangian finite element scheme for the simulation of sheet metal roll forming. Numerical experiments by imposing artificial strain histories on a through-the-thickness element are conducted to test the model against previously reported stress resultant plasticity models and to validate it against the traditional continuum plasticity approach that features an integration of relations of elastoplasticity in a set of grid points distributed over the thickness. Results of actual roll forming simulations demonstrate the practicality in comparison to the computationally more expensive continuum plasticity approach.

## References of Paper C

- [1] M. Ambati, J. Kiendl and L. De Lorenzis. Isogeometric Kirchhoff–Love shell formulation for elasto-plasticity. *Computer Methods in Applied Mechanics and Engineering* 340 (2018), 320–339. DOI: [10.1016/j.cma.2018.05.023](https://doi.org/10.1016/j.cma.2018.05.023).
- [2] B. Brank, D. Perić and F. B. Damjanić. On large deformations of thin elasto-plastic shells: Implementation of a finite rotation model for quadrilateral shell element. *International Journal for Numerical Methods in Engineering* 40.4 (1997), 689–726. DOI: [10.1002/\(SICI\)1097-0207\(19970228\)40:4<689::AID-NME85>3.0.CO;2-7](https://doi.org/10.1002/(SICI)1097-0207(19970228)40:4<689::AID-NME85>3.0.CO;2-7).
- [3] F. S. Liguori, A. Madeo and G. Garcea. A dual decomposition of the closest point projection in incremental elasto-plasticity using a mixed shell finite element. *International Journal for Numerical Methods in Engineering* 123.24 (2022), 6243–6266. DOI: <https://doi.org/10.1002/nme.7112>.
- [4] M. D. Alaydin, D. J. Benson and Y. Bazilevs. An updated Lagrangian framework for Isogeometric Kirchhoff–Love thin-shell analysis. *Computer Methods in Applied Mechanics and Engineering* 384 (2021), 113977. DOI: <https://doi.org/10.1016/j.cma.2021.113977>.

- [5] J. Li et al. Analysis of elasto-plastic thin-shell structures using layered plastic modeling and absolute nodal coordinate formulation. *Nonlinear Dynamics* 105.4 (2021). DOI: <https://doi.org/10.1007/s11071-021-06766-9>.
- [6] A. Ilyushin. Plasticity (in Russian). GITL, Moscow, Leningrad, 1948.
- [7] Bieniek, MP and Funaro, JR. Elasto-plastic behavior of plates and shells. Tech. rep. Weidlinger Associates New York, 1976.
- [8] M. Crisfield. Finite element analysis for combined material and geometric nonlinearities. *Nonlinear finite element analysis in structural mechanics*. Springer, 1981, 325–338.
- [9] Q. Zeng, A. Combescure and F. Arnaudeau. An efficient plasticity algorithm for shell elements application to metal forming simulation. *Computers & Structures* 79.16 (2001), 1525–1540. DOI: [10.1016/S0045-7949\(01\)00032-3](https://doi.org/10.1016/S0045-7949(01)00032-3).
- [10] J. Dujc and B. Brank. On stress resultant plasticity and viscoplasticity for metal plates. *Finite Elements in Analysis and Design* 44.4 (2008), 174–185. DOI: [10.1016/j.finel.2007.11.011](https://doi.org/10.1016/j.finel.2007.11.011).
- [11] J. Dujc and B. Brank. Stress resultant plasticity for shells revisited. *Computer Methods in Applied Mechanics and Engineering* 247-248 (2012), 146–165. DOI: [10.1016/j.cma.2012.07.012](https://doi.org/10.1016/j.cma.2012.07.012).
- [12] E. Kocbay and Y. Vetyukov. Stress resultant plasticity for plate bending in the context of roll forming of sheet metal. *International Journal for Numerical Methods in Engineering* 122.18 (2021), 5144–5168. DOI: [10.1002/nme.6760](https://doi.org/10.1002/nme.6760).
- [13] E. Kocbay et al. Mixed Eulerian–Lagrangian modeling of sheet metal roll forming. *Thin-Walled Structures* 186 (2023), 110662. DOI: [10.1016/j.tws.2023.110662](https://doi.org/10.1016/j.tws.2023.110662).
- [14] F. Heislitz et al. Simulation of roll forming process with the 3-D FEM code PAM-STAMP. *Journal of Materials Processing Technology* 59.1 (1996), 59–67. DOI: [10.1016/0924-0136\(96\)02287-X](https://doi.org/10.1016/0924-0136(96)02287-X).
- [15] Q. Bui and J. Ponthot. Numerical simulation of cold roll-forming processes. *Journal of Materials Processing Technology* 202.1 (2008), 275–282. DOI: [10.1016/j.jmatprotec.2007.08.073](https://doi.org/10.1016/j.jmatprotec.2007.08.073).
- [16] Y. Vetyukov, P. Gruber and M. Krommer. Nonlinear model of an axially moving plate in a mixed Eulerian-Largangian framework. *Acta Mechanica* 227 (2016), 2831–2842. DOI: <https://doi.org/10.1007/s00707-016-1651-0>.
- [17] Vetyukov, Yu. and Gruber, P. G. and Krommer, M. and Gerstmayr, J. and Gafur, I. and Winter, G. Mixed Eulerian–Lagrangian description in materials processing: deformation of a metal sheet in a rolling mill. *International Journal for Numerical Methods in Engineering* 109.10 (2017), 1371–1390. DOI: [10.1002/nme.5314](https://doi.org/10.1002/nme.5314).
- [18] J. Donea et al. Arbitrary Lagrangian-Eulerian Methods. *Encyclopedia of Computational Mechanics*. Ed. by E. Stein, R. De Borst and T. J. R. Hughes. Chichester, UK: John Wiley & Sons, Ltd, 2004, ecm009. DOI: [10.1002/0470091355.ecm009](https://doi.org/10.1002/0470091355.ecm009).

- [19] Y. Crutzen et al. Lagrangian and arbitrary Lagrangian Eulerian simulations of complex roll-forming processes. *Comptes Rendus Mécanique* 344.4-5 (2016), 251–266. DOI: [10.1016/j.crme.2016.02.005](https://doi.org/10.1016/j.crme.2016.02.005).
- [20] S. Han. Configurational forces and ALE formulation for geometrically exact, sliding shells in non-material domains. *Computer Methods in Applied Mechanics and Engineering* 412 (2023), 116106. DOI: <https://doi.org/10.1016/j.cma.2023.116106>.
- [21] J. Scheidl and Y. Vetyukov. Steady Motion of a Slack Belt Drive: Dynamics of a Beam in Frictional Contact With Rotating Pulleys. *Journal of Applied Mechanics* 87.12 (2020). DOI: [10.1115/1.4048317](https://doi.org/10.1115/1.4048317).
- [22] J. Scheidl et al. Mixed Eulerian–Lagrangian shell model for lateral run-off in a steel belt drive and its experimental validation. *International Journal of Mechanical Sciences* 204 (2021), 106572. DOI: [10.1016/j.ijmecsci.2021.106572](https://doi.org/10.1016/j.ijmecsci.2021.106572).
- [23] V. V. Eliseev and Y. M. Vetyukov. Finite deformation of thin shells in the context of analytical mechanics of material surfaces. *Acta Mechanica* 209.1-2 (2010), 43–57. DOI: [10.1007/s00707-009-0154-7](https://doi.org/10.1007/s00707-009-0154-7).
- [24] Y. Vetyukov. Nonlinear mechanics of thin-walled structures: asymptotics, direct approach and numerical analysis. Springer Science & Business Media, 2014.
- [25] J. Lubliner. Plasticity theory. Dover Publications, Inc., 2008.
- [26] Q. Hu, X. Li and J. Chen. On the calculation of plastic strain by simple method under non-associated flow rule. *European Journal of Mechanics - A/Solids* 67 (2018), 45–57. DOI: [10.1016/j.euromechsol.2017.08.017](https://doi.org/10.1016/j.euromechsol.2017.08.017).
- [27] M. Crisfield and X. Peng. Efficient nonlinear shell formulations with large rotations and plasticity. *DRJ Owen et al. Computational plasticity: models, software and applications, Part 1* (1992), 1979–1997.
- [28] A. K. Mohammed, B. Skallerud and J. Amdahl. Simplified stress resultants plasticity on a geometrically nonlinear constant stress shell element. *Computers & Structures* 79.18 (2001), 1723–1734. DOI: [10.1016/S0045-7949\(01\)00095-5](https://doi.org/10.1016/S0045-7949(01)00095-5).
- [29] F. K. Bogner, R. L. Fox and L. A. Schmit. The generation of interelement compatible stiffness and mass matrices by the use of interpolation formulae. *Proc. Conf. Matrix Methods in Struct. Mech., Airforce Inst. Of Tech.* Wright Patterson AF Base, Ohio, 1965.
- [30] S. Eisenträger et al. Stability analysis of plates using cut Bogner-Fox-Schmit elements. *Computers & Structures* 270 (2022), 106854. DOI: <https://doi.org/10.1016/j.compstruc.2022.106854>.
- [31] C. Mueller et al. Influence of Friction on the Loads in a Roll Forming Simulation with Compliant Rolls. *Material Forming ESAFORM 2014*. Vol. 611. Key Engineering Materials. Trans Tech Publications Ltd, 2014, 436–443. DOI: <https://doi.org/10.4028/www.scientific.net/KEM.611-612.436>.

- [32] J. Paralikas, K. Salonitis and G. Chryssolouris. Investigation of the effects of main roll-forming process parameters on quality for a V-section profile from AHSS. *The International Journal of Advanced Manufacturing Technology* 44.3 (2009), 223–237. DOI: <https://doi.org/10.1007/s00170-008-1822-9>.
- [33] D. Bhattacharyya et al. The prediction of deformation length in cold roll-forming. *Journal of Mechanical Working Technology* 9.2 (1984), 181–191. DOI: [10.1016/0378-3804\(84\)90004-4](https://doi.org/10.1016/0378-3804(84)90004-4).
- [34] M. Lindgren. An Improved Model for the Longitudinal Peak Strain in the Flange of a Roll Formed U-Channel developed by FE-Analyses. *Steel Research International* 78.1 (2007), 82–87. DOI: [10.1002/srin.200705863](https://doi.org/10.1002/srin.200705863).



# An enhanced stress resultant plasticity model for shell structures with application in sheet metal roll forming

Emin Kocbay<sup>1</sup> · Jakob Scheidl<sup>1</sup> · Fabian Schwarzinger<sup>1</sup> · Yury Vetyukov<sup>1</sup>

Received: 23 June 2023 / Accepted: 19 October 2023  
© The Author(s) 2023

## Abstract

The proposed Kirchhoff-Love shell stress resultant plasticity model extends a previously reported model for plates by complementing the constitutive law of elastoplasticity with membrane effects. This enhanced model is designed for bending dominant settings with small to moderate membrane forces. It is thus implemented in a purpose-built nonlinear mixed Eulerian–Lagrangian finite element scheme for the simulation of sheet metal roll forming. Numerical experiments by imposing artificial strain histories on a through-the-thickness element are conducted to test the model against previously reported stress resultant plasticity models and to validate it against the traditional continuum plasticity approach that features an integration of relations of elastoplasticity in a set of grid points distributed over the thickness. Results of actual roll forming simulations demonstrate the practicality in comparison to the computationally more expensive continuum plasticity approach.

**Keywords** Metal plasticity · Stress resultant shell plasticity · Kirchhoff–Love shell · Roll forming · Finite element analysis · Mixed Eulerian–Lagrangian formulation

## Nomenclature

### Geometry, material and numerical parameters

$L, w, h$	length, width and thickness of the metal sheet
$E, \nu$	elastic modulus and Poisson ratio of the metal sheet
$k$	yield strength
$P$	contact penalty

### Coordinates, kinematic description, differential operators and strain measures

$x, y, z$	global Cartesian coordinates of the actual configuration
$i, j, k$	global Cartesian basis
$\overset{\circ}{x}, \overset{\circ}{y}$	material coordinates of the reference configuration of the shell model
$\zeta$	material thickness coordinate in the 3D body of the shell

$\overset{\circ}{r}, r$	position vector of the reference and the actual configuration
$u, u_x, u_y, u_z$	displacement vector and its Cartesian components
$v, \dot{u}_x$	axial material transport rate and axial material velocity
$\overset{\circ}{\nabla}, \nabla$	differential operators of the reference and the actual configuration
$\mathbf{F}$	deformation gradient tensors
$\mathbf{e}_\perp, \mathbf{e}_\perp^e, \mathbf{e}_\perp^p$	in-plane parts of the total strain tensor, elastic strain tensor and plastic strain tensor in the 3D body of the shell
$\mathbf{E}, \mathbf{K}$	total membrane and bending strain tensor of the shell
$\mathbf{E}^e, \mathbf{K}^e$	elastic parts of membrane and bending strain tensor of the shell
$\mathbf{E}^p, \mathbf{K}^p$	plastic parts of membrane and bending strain tensor of the shell

### Stresses and related variables

$\sigma, \mathbf{N}, \mathbf{M}$	tensors of stresses, membrane forces and bending moments
$I_N, I_{NM}, I_M$	invariants of the stress resultants $\mathbf{N}$ and $\mathbf{M}$

✉ Yury Vetyukov  
yury.vetyukov@tuwien.ac.at

<sup>1</sup> Institute of Mechanics and Mechatronics, Technische Universität Wien, Getreidemarkt 9, Vienna 1060, Austria

## Forming parameters and measures of the forming process

$\rho, \varphi$	roll-gap-reduction and bending angle of the profile
$R_{Li}$	resulting contact force (roll force) on lower roll $i$
$A^P, \dot{A}^P$	densities of plastic dissipation work and dissipation power

## 1 Introduction

In this paper a stress resultant shell plasticity model for metals, which is suited for bending dominant applications such as roll forming of sheet metal, is introduced. State-of-the-art finite element schemes to model elastic-plastic forming of thin sheet metal typically rely either on full 3D-continuum elements or on continuum shell elements, where the shell deformations, which obey the kinematic hypothesis of the structural theory, are imposed on the 3D-body to treat plasticity on the continuum level. This approach is accurate and widely established [1–5], but computationally expensive in general, because it requires a through-the-thickness integration of the 3D continuum elastic-plastic constitutive laws to arrive at the stress resultants and the strain energy density of the shell.

Consequently, so-called stress resultant plasticity models are developed [6–12], where the elastic-plastic constitutive laws are stated directly in the space of the stress resultants, thus rendering the through-the-thickness integration obsolete. Oftentimes, these publications make use of some variants of the Ilyushin yield criterion [6]. This criterion represents the von Mises yield surface in terms of stress resultants, meaning bending moments and membrane forces. The Ilyushin criterion is aimed at plastic limit load analysis and merely detects elastic or fully plastic states, but does not account for the gradual spreading of the plastic zone through the thickness. Crisfield [8] augmented the Ilyushin yield criterion by introducing a pseudo-hardening variable, namely the effective plastic curvature, such that the yield criterion is now able to approximate the plastification process through the thickness. Applications of Crisfield's model are available in the open literature [9, 10].

Another attempt to augment the Ilyushin yield criterion was carried out in [12] for geometrically linear plate bending, meaning only the bending moments enter the yield criterion. The evolution of the yield surface was described by means of an isotropic hardening function, which uses the dissipation work as an internal hardening variable. This isotropic hardening function was identified with the help of reference solutions of a continuum through-the-thickness element and by means of analytical solutions for simple cases like elastic-

plastic uniaxial bending. Results were convincing and in a better agreement with continuum solutions when compared to the yield criterion of [8].

To overcome certain limitations of the previously reported stress resultant plasticity models, the plate model of [12] is modified here in an effort to treat large deformation problems of Kirchhoff–Love shells. This enhanced shell stress resultant model is obtained by appropriately pairing the isotropic hardening law of [12] with the augmented yield surface proposed by Crisfield [8]. The thus derived yield criterion is still approximate, but in contrast to the plate-model of [12] features an additional account for small to moderate membrane forces. The two established stress resultant plasticity models and the novel one are put to the test in a series of numerical experiments. The comparison against reference solutions obtained with the continuum plasticity approach reveals the capabilities of the enhanced model, which, as compared to Crisfield's approach, also exhibits an improved convergence of the time integration scheme. Furthermore, the resolution of the plastification process in terms of isotropic work hardening facilitates the account for material hardening, which may be achieved by simple extension of the hardening function that is thus far limited to an elastic ideal-plastic material.

With regard to the aforementioned application of sheet metal roll forming, the model is implemented in the mixed Eulerian–Lagrangian (MEL) finite element framework proposed in [13]. While there are various publications on roll forming simulations [14, 15], most of them utilize a classical Lagrangian kinematic formulation. However, for processes featuring axially moving continua such as a moving metal sheet passing through a roll forming mill, the Lagrangian kinematic formulation is inefficient and causes numerically induced oscillations [16, 17]. An elegant way to mitigate these drawbacks is the use of the Arbitrary Lagrangian Eulerian (ALE) methods [18], where a Lagrangian step is succeeded by a Eulerian step within a time increment. ALE methods have successfully been applied in the context of roll forming [19] and, more recently, in an investigation on configurational forces in problems of sliding shells [20]. Here, the efficient mixed Eulerian–Lagrangian (MEL) kinematic description is employed [13, 21, 22], which – in contrast to more traditional variants of ALE – allows for a solution scheme that limits the Eulerian update step to the transport of plastic variables.

Actual roll forming simulations are carried out to test the proposed stress resultant plasticity model in an application oriented context and to conclude on improvements over its predecessors. The practical relevance of the enhanced model for the simulation of the roll forming process lies in its use as an auxiliary computational tool for the design and optimization of roll forming lines. It is capable of producing accurate results at significantly reduced computation time as compared to the continuum plasticity model.



## 2 Shell plasticity in the framework of the through-the-thickness integration approach

In the following, the essentials of the shell plasticity model in the framework of the usually employed through-the-thickness integration approach, are briefly recapitulated. For the sake of generality, the governing equations of the theory are all presented in invariant form.

The deformation of a Kirchhoff–Love shell is understood as a mapping between the undeformed reference configuration of the material surface and its actual deformed configuration [23, 24]. Material particles in each configuration are identified with the position vectors  $\overset{\circ}{\mathbf{r}}$  and  $\mathbf{r}$  for the reference and the actual state, respectively. Two corresponding differential operators  $\overset{\circ}{\nabla}$  and  $\nabla$  may be defined with the help of the total differential of a field quantity  $\phi$  on the surface:

$$d\phi = d\overset{\circ}{\mathbf{r}} \cdot \overset{\circ}{\nabla}\phi = d\mathbf{r} \cdot \nabla\phi. \tag{1}$$

These planar operators implicitly contain the derivatives with respect to the two material (Lagrangian) coordinates that are typically used to parametrize the surface. The gradients of  $\overset{\circ}{\mathbf{r}}$  and  $\mathbf{r}$  are the first metric tensors:

$$\overset{\circ}{\mathbf{a}} = \overset{\circ}{\nabla}\overset{\circ}{\mathbf{r}}, \quad \mathbf{a} = \nabla\mathbf{r}, \tag{2}$$

which define lengths and angles of the surface in the two configurations. In accordance with (1), the deformation gradient tensor  $\mathbf{F}$  provides a mapping between the differential line elements:

$$d\mathbf{r} = \mathbf{F} \cdot d\overset{\circ}{\mathbf{r}}, \quad \mathbf{F} = \overset{\circ}{\nabla}\mathbf{r}^T. \tag{3}$$

The bending deformation in terms of the unsharable Kirchhoff–Love theory is connected to the change of the unit normal vector to the deformed surface  $\mathbf{n}$ , which is expressed through the second metric tensor  $\mathbf{b}$ :

$$\mathbf{b} = -\nabla\mathbf{n}, \tag{4}$$

where  $\mathbf{n}$  fulfills the constraint of orthogonality  $\mathbf{a} \cdot \mathbf{n} = 0$ . The membrane and bending strain measures correspond to the change of the components of the first and second metric tensors, respectively. Their invariant forms read:

$$\mathbf{E} = \frac{1}{2} (\mathbf{F}^T \cdot \mathbf{F} - \overset{\circ}{\mathbf{a}}), \quad \mathbf{K} = \mathbf{F}^T \cdot \mathbf{b} \cdot \mathbf{F}, \tag{5}$$

where a planar reference configuration is assumed in the definition of the curvature tensor  $\mathbf{K}$ .

In terms of the through-the-thickness approach, the shell deformations are kinematically imposed on the three-dimensional continuum, which allows to resolve the elastic-plastic rate equations on the continuum level. In accordance with the Kirchhoff kinematic hypothesis, the in-plane part of the strain tensor of the 3D body  $\boldsymbol{\epsilon}_\perp$  varies linearly in thickness direction  $\zeta$ :

$$\boldsymbol{\epsilon}_\perp = \mathbf{E} - \zeta\mathbf{K}. \tag{6}$$

The now employed additive decomposition of the planar strain tensor into an elastic and a plastic part

$$\boldsymbol{\epsilon}_\perp = \boldsymbol{\epsilon}_\perp^e + \boldsymbol{\epsilon}_\perp^p \tag{7}$$

rests on the small strain assumption for  $\boldsymbol{\epsilon}_\perp$ . This prerequisite does not preclude large overall deformations, but it does require the membrane strains  $\mathbf{E}$  to remain small and the thickness coordinate to vary in a narrow range  $-h/2 \leq \zeta \leq h/2$ . An elastic-ideal plastic material behavior with constant yield strength  $k$  is assumed for simplicity and the von Mises yield criterion is adopted to distinguish elastic and elastic-plastic states with the function

$$f = \frac{3}{2} \boldsymbol{\sigma} \cdot \boldsymbol{\sigma} - \frac{1}{2} (\text{tr } \boldsymbol{\sigma})^2 \leq k^2. \tag{8}$$

Elastic states are identified by  $f < k^2$  and yield happens at  $f = k^2$ . The planar stress tensor  $\boldsymbol{\sigma}$  is connected to the elastic part of the planar strain tensor according to Hooke’s law for the plane stress assumption:

$$\boldsymbol{\sigma} = \frac{E}{1+\nu} \boldsymbol{\epsilon}_\perp^e + \frac{E\nu}{1-\nu^2} \overset{\circ}{\mathbf{a}} \text{tr } \boldsymbol{\epsilon}_\perp^e = {}^4\mathbb{C} \cdot \boldsymbol{\epsilon}_\perp^e, \tag{9}$$

with the elastic modulus  $E$  and the Poisson ratio  $\nu$ ; the fourth rank plane stress elasticity tensor  ${}^4\mathbb{C}$  provides a more concise representation. It is important to acknowledge the inconsistency introduced through (9) that connects the Cauchy stresses  $\boldsymbol{\sigma}$  related to the actual state to the Green type of strain measure  $\boldsymbol{\epsilon}_\perp$  related to the reference state. However, owing to the small strain assumption this subtle distinction is of little importance here [13]. The system of equations is complemented by the associated flow rule, which determines the evolution of the plastic strains and follows from the postulate of maximum plastic dissipation [25]:

$$\dot{\boldsymbol{\epsilon}}_\perp^p = \dot{\lambda} \frac{\partial f}{\partial \boldsymbol{\sigma}}, \quad \frac{\partial f}{\partial \boldsymbol{\sigma}} = 3\boldsymbol{\sigma} - \overset{\circ}{\mathbf{a}} \text{tr } \boldsymbol{\sigma}. \tag{10}$$

The consistency parameter  $\dot{\lambda} \geq 0$  is either zero (elastic state,  $\dot{\boldsymbol{\epsilon}}_\perp^p = 0$ ) or positive (elastic-plastic state,  $\dot{\boldsymbol{\epsilon}}_\perp^p \neq 0$ ). At yield the consistency condition  $\dot{f} = 0$  requires the stress state to remain on the yield surface. It is evaluated in the usual way

[25], to derive the stress-strain relation in terms of time rates for elastic-plastic states:

$$\dot{\sigma} = \left( {}^4\mathbb{C} - \frac{{}^4\mathbb{C} \cdot \cdot \frac{\partial f}{\partial \sigma} \frac{\partial f}{\partial \sigma} \cdot \cdot {}^4\mathbb{C}}{\frac{\partial f}{\partial \sigma} \cdot \cdot {}^4\mathbb{C} \cdot \cdot \frac{\partial f}{\partial \sigma}} \right) \cdot \cdot \dot{\epsilon}_{\perp}. \quad (11)$$

The fourth rank tangent stiffness tensor in brackets is symmetric in consequence of the associated flow rule [26]. The strain energy density per unit reference area expressed in terms of the through-the-thickness integration approach reads:

$$U = \int_{-h/2}^{h/2} \frac{1}{2} \epsilon_{\perp}^e \cdot \cdot {}^4\mathbb{C} \cdot \cdot \epsilon_{\perp}^e d\zeta, \quad \epsilon_{\perp}^e = \epsilon_{\perp} - \epsilon_{\perp}^p. \quad (12)$$

Since the energy density of the shell is obtained via a thickness integration, this approach is henceforth referred to as “continuum plasticity model” or “cp-model” in short. Regarding the finite element implementation of Sect. 5, the integration with respect to  $\zeta$  is accomplished by means of a Gaussian quadrature rule with several points  $\zeta_i$  in thickness direction.

### 3 Stress resultant model of elastic-plastic Kirchhoff-Love shell for large overall deformations

In order to avoid the computationally expensive time integration of the constitutive equations of elastoplasticity in multiple points over the thickness, inherent to the cp-model discussed above, a stress resultant model to treat elastoplasticity directly in the framework of the direct approach featuring the shell as material surface is developed here. In particular, a representation of the strain energy density in terms of the elastic parts of the shell strain measures is sought:

$$U = \frac{1}{2} (A_1 (\text{tr } \mathbf{E}^e)^2 + A_2 \mathbf{E}^e \cdot \cdot \mathbf{E}^e + D_1 (\text{tr } \mathbf{K}^e)^2 + D_2 \mathbf{K}^e \cdot \cdot \mathbf{K}^e), \quad (13)$$

which stands in contrast to the definition (12) used in the through-the-thickness approach. Like in (7) the additive decomposition of shell strain components

$$\mathbf{E} = \mathbf{E}^e + \mathbf{E}^p, \quad \mathbf{K} = \mathbf{K}^e + \mathbf{K}^p \quad (14)$$

is based on the assumption of small local strains, which also justifies the particular choice of the strain energy density as a quadratic form in the elastic strain measures with the usual stiffness coefficients:  $A_1 = E\nu h/(1 - \nu^2)$ ,  $A_2 = Eh/(1 + \nu)$ ,  $D_1 = A_1 h^2/12$  and  $D_2 = A_2 h^2/12$ . The tensors of membrane and bending stress resultants follow from (13) by means of partial differentiation:

$$\mathbf{N} = \frac{\partial U}{\partial \mathbf{E}^e} = A_1 \hat{\mathbf{a}} \text{tr } \mathbf{E}^e + A_2 \mathbf{E}^e, \quad \mathbf{M} = \frac{\partial U}{\partial \mathbf{K}^e} = D_1 \hat{\mathbf{a}} \text{tr } \mathbf{K}^e + D_2 \mathbf{K}^e. \quad (15)$$

To close the formulation, the governing equations of plasticity in terms of these stress resultants and a small number of internal plastic variables are restated following the concept developed in [12]. It features the plastic dissipation work  $A^p$  as internal variable that governs the evolution law for the effective yield stress. This approach is based on the observation that the yield progress in a thickness element from initial yield up to limit yield (plastic hinge) resembles isotropic hardening. This phenomenon of “structural hardening” is not to be confused with actual material hardening, which is neglected here owing to the elastic-ideal plastic material law. The model proposed in [12] is limited to the geometrically linearized framework of the plate bending problem, where  $\mathbf{N}$  can be neglected and only the bending moments  $\mathbf{M}$  need to be considered. This simplification is no longer feasible in the present context of the geometrically nonlinear shell theory owing to the inherent coupling of membrane and bending forces. The enhanced stress resultant plasticity model for the Kirchhoff-Love shell to be developed in the following shall be addressed as “shell srp-model”, in contrast to the “plate srp-model” model proposed in [12].

The derivation rests upon an augmentation of the von Mises yield criterion (8), which is defined with respect to the plane stress tensor  $\sigma$ . Provided the current state is purely elastic, it is possible to reconstruct  $\sigma$  in terms of the stress resultants:

$$\sigma = -\frac{12}{h^3} \mathbf{M} \zeta + \frac{1}{h} \mathbf{N}, \quad (16)$$

which can be easily verified by means of a substitution of (6) in the elasticity law (9) and comparison to the constitutive relation (15) for the stress resultants. Initial yield occurs in an elastic limit state that is first reached at an outer fiber (upper surface or lower surface of the shell) at  $\zeta = \pm h/2$ :

$$\sigma^{\max} = \mp \frac{6}{h^2} \mathbf{M} + \frac{1}{h} \mathbf{N}. \quad (17)$$

Hence, the initial yield surface follows by substitution of (17) in (8), which is rearranged to reach the convenient representation:

$$f_0 = I_N + 2|I_{NM}| + I_M - 1, \quad (18)$$

with  $f_0 = 0$  corresponding to first yield; the absolute value of  $|I_{NM}|$  ensures positivity of the corresponding term. The scalar variables  $I_N$ ,  $I_{NM}$  and  $I_M$  are invariants of the membrane force tensor and the bending moment tensor:

$$I_N = \frac{1}{N_0^2} \left( \frac{3}{2} \mathbf{N} \cdot \cdot \mathbf{N} - \frac{1}{2} (\text{tr } \mathbf{N})^2 \right),$$

$$I_{NM} = \frac{1}{N_0 M_0} \left( \frac{3}{2} \mathbf{N} \cdot \cdot \mathbf{M} - \frac{1}{2} \text{tr } \mathbf{N} \text{ tr } \mathbf{M} \right), \quad (19)$$

$$I_M = \frac{1}{M_0^2} \left( \frac{3}{2} \mathbf{M} \cdot \cdot \mathbf{M} - \frac{1}{2} (\text{tr } \mathbf{M})^2 \right).$$

For later usage, the partial derivatives of these invariants are also provided:

$$\begin{aligned} \frac{\partial I_N}{\partial \mathbf{N}} &= \frac{1}{N_0^2} (3\mathbf{N} - \mathring{\mathbf{a}} \text{tr } \mathbf{N}), \\ \frac{\partial I_{NM}}{\partial \mathbf{N}} &= \frac{1}{N_0 M_0} \left( \frac{3}{2} \mathbf{M} - \frac{1}{2} \mathring{\mathbf{a}} \text{tr } \mathbf{M} \right), \\ \frac{\partial I_{NM}}{\partial \mathbf{M}} &= \frac{1}{N_0 M_0} \left( \frac{3}{2} \mathbf{N} - \frac{1}{2} \mathring{\mathbf{a}} \text{tr } \mathbf{N} \right), \\ \frac{\partial I_M}{\partial \mathbf{M}} &= \frac{1}{M_0^2} (3\mathbf{M} - \mathring{\mathbf{a}} \text{tr } \mathbf{M}). \end{aligned} \quad (20)$$

The expressions are normalized with respect to the membrane force  $N_0$  and the bending moment  $M_0$  that correspond to first yield under the distinguished load cases of uniaxial tension and uniaxial bending, respectively:

$$N_0 = kh, \quad M_0 = \frac{kh^2}{6}. \quad (21)$$

The yield surface of (18) describes initial yielding exactly, but is incapable of capturing the advancement of the plastic zone in the thickness element beyond that.

In an attempt to resolve this issue, the limit yield surface is considered as the second limiting case, which corresponds to the fully plastified thickness element. Lacking exact means of derivation for this case, it is assumed that the state of limit yield can be mathematically described in the same way as initial yield. Therefore, the limit yield surface is sought as a linear combination of the invariants in the form of (18) but with a-priori unknown coefficients  $a$ ,  $b$  and  $c$ :

$$f_L = aI_N + b|I_{NM}| + cI_M - 1. \quad (22)$$

Simple thought-experiments based on the general uniaxial stress state  $\mathbf{N} = N_x \mathbf{i}\mathbf{i}$  and  $\mathbf{M} = M_x \mathbf{i}\mathbf{i}$  in direction  $\mathbf{i}$  are carried out to determine these constants. In the limit state, the uniaxial stress distribution is piecewise constant and the position of the neutral fiber is offset by an amount  $\eta$  owing to the action of the tensile force  $N_x$ :

$$\sigma_x = \begin{cases} k, & -h/2 \leq \zeta < \eta \\ -k, & \eta < \zeta \leq h/2 \end{cases}, \quad (23)$$

with the neutral fiber being located at  $\zeta = \eta$ . The magnitudes of the stress resultants follow by thickness integration to:

$$\begin{aligned} N_x(\eta) &= \int_{-h/2}^{h/2} \sigma_x \, d\zeta = 2k\eta, \\ M_x(\eta) &= - \int_{-h/2}^{h/2} \zeta \sigma_x \, d\zeta = 1/4k(h^2 - 4\eta^2). \end{aligned} \quad (24)$$

These distributions are evaluated for three distinguished types of uniaxial stress states defined by:

$$\eta_1 = \frac{h}{2}, \quad \eta_2 = 0, \quad \eta_3 = \frac{h}{2\sqrt{3}}, \quad (25)$$

where the first corresponds to uniaxial tension, the second to uniaxial bending and the third to the special state, where the mixed invariant  $I_{NM}$  becomes maximal:

$$\frac{\partial I_{NM}}{\partial \eta} = 0 \Rightarrow \eta_3 = \frac{h}{2\sqrt{3}}. \quad (26)$$

Evaluation of (22) for all three cases yields a system of linear equations, with the solution:

$$a = 1, \quad b = \frac{2}{3\sqrt{3}}, \quad c = \frac{4}{9}. \quad (27)$$

The resulting limit yield surface of (22) turns out to be identical to the one proposed by Ilyushin [6]. In an effort to represent states in-between initial and limit yielding, Crisfield [8] augmented the Ilyushin yield criterion by introducing a dimensionless pseudo-hardening variable  $\gamma$  which is identified by the uniaxial bending experiment:

$$f_{Cr} = I_N + \frac{1}{\sqrt{3}\gamma} |I_{NM}| + \frac{1}{\gamma^2} I_M - 1, \quad \gamma = \frac{1}{2} (3 - e^{-4\chi^P}). \quad (28)$$

Here,  $\chi^P$  corresponds to the dimensionless effective plastic curvature that is derived from the plastic curvature tensor  $\mathbf{K}^P$ :

$$\chi^P = \frac{Eh}{3k} \sqrt{\frac{2}{3} (\mathbf{K}^P \cdot \cdot \mathbf{K}^P + (\text{tr } \mathbf{K}^P)^2)} \quad (29)$$

By comparison to (18) and (22) with constants according to (27) one can observe that for pure bending the Crisfield yield surface exactly captures the initial yield surface;  $\chi^P = 0$  and  $\gamma = 1$  as well as the limit yield surface;  $\chi^P \rightarrow \infty$  and  $\gamma = 3/2$ .

Instead of  $\gamma$ , the newly proposed model makes use of the isotropic hardening function of the dissipative work  $k_M(A^P)$  introduced for the plate srp-model developed in [12], which was identified for the uniaxial bending continuum reference

solution. This modification amounts to the replacement of  $\gamma$  in (28) with  $k_M(A^P)/M_0$ :

$$f = I_N + \frac{1}{\sqrt{3} \frac{k_M(A^P)}{M_0}} |I_{NM}| + \frac{1}{\frac{k_M^2(A^P)}{M_0^2}} I_M - 1, \quad (30)$$

where the hardening function is defined such, that it reproduces the elastic-plastic response of a plate at pure uni-axial bending:

$$k_M^2(A^P) = -\frac{1}{36} h^3 \left( 3EA^P - 3\sqrt{EA^P} \sqrt{2hk^2 + EA^P} + 2\sqrt{3}hk^2 \arctan \frac{\sqrt{EA^P}}{\sqrt{6hk^2 + 3EA^P}} \right) + \frac{h^4 k^2}{36}. \quad (31)$$

In contrast to Crisfield’s approach, the dissipation work per unit surface of the shell  $A^P$  appears as additional state variable that determines the hardening behavior in terms of the evolution of the effective yield strength  $k_M^2(A^P)$ . This implementation in the spirit of work hardening not only captures initial yield ( $k_M^2 = M_0^2, A^P = 0$ ) and limit yield ( $k_M^2 = M_L^2, A^P \rightarrow \infty$ ) accurately for the case of pure bending, but also facilitates the additional account for actual isotropic material hardening by means of a proper augmentation of  $k_M^2(A^P)$  [12]. Moreover, the contribution of plastic membrane strains to the work hardening can be consistently accounted for in the definition of the dissipation power:

$$\dot{A}^P = \mathbf{N} \cdot \dot{\mathbf{E}}^P + \mathbf{M} \cdot \dot{\mathbf{K}}^P. \quad (32)$$

The plate srp-model and the one suggested by Crisfield lack this ability. Two associated flow rules with a single consistency parameter  $\lambda$  are stated for the plastic strain rates:

$$\dot{\mathbf{E}}^P = \lambda \frac{\partial F}{\partial \mathbf{N}}, \quad \dot{\mathbf{K}}^P = \lambda \frac{\partial F}{\partial \mathbf{M}}, \quad (33)$$

where the original yield equation  $f = 0$  has been replaced with the modified one  $F(\mathbf{N}, \mathbf{M}) = k_M^2(A^P)$ , which in terms of the stress invariants reads:

$$F = \frac{h^4 k^2 \left( |I_{NM}| + \sqrt{12I_M(1 - I_N) + I_{NM}^2} \right)^2}{432(1 - I_N)^2} = k_M^2(A^P). \quad (34)$$

The thus achieved separation of yield criterion and effective yield strength is beneficial when it comes to the evaluation of the consistency condition:

$$\dot{F} = \frac{\partial F}{\partial \mathbf{N}} \cdot \dot{\mathbf{N}} + \frac{\partial F}{\partial \mathbf{M}} \cdot \dot{\mathbf{M}} = 2k_M k'_M \dot{A}^P, \quad (35)$$

which binds the stress state to the actual yield surface in case of plastic flow. Application of the chain rule of differentiation yields:

$$\begin{aligned} \frac{\partial F}{\partial \mathbf{N}} &= \frac{\partial F}{\partial I_N} \frac{\partial I_N}{\partial \mathbf{N}} + \frac{\partial F}{\partial I_{NM}} \frac{\partial I_{NM}}{\partial \mathbf{N}}, \\ \frac{\partial F}{\partial \mathbf{M}} &= \frac{\partial F}{\partial I_M} \frac{\partial I_M}{\partial \mathbf{M}} + \frac{\partial F}{\partial I_{NM}} \frac{\partial I_{NM}}{\partial \mathbf{M}}, \end{aligned} \quad (36)$$

which, for the sake of conciseness, is not expanded further with the help of (20). Likewise, the lengthy total derivative of  $k_M^2(A^P)$  that follows from (31) is omitted. With the dissipation power given in (32), it remains to evaluate the constitutive law (15) to relate the rates of the stress and strain resultants:

$$\begin{aligned} \dot{\mathbf{N}} &= A_1 \overset{\circ}{\mathbf{a}} \text{tr} \dot{\mathbf{E}}^e + A_2 \dot{\mathbf{E}}^e = \frac{\partial \mathbf{N}}{\partial \mathbf{E}^e} \cdot \cdot (\dot{\mathbf{E}} - \dot{\mathbf{E}}^P), \\ \dot{\mathbf{M}} &= D_1 \overset{\circ}{\mathbf{a}} \text{tr} \dot{\mathbf{K}}^e + D_2 \dot{\mathbf{K}}^e = \frac{\partial \mathbf{M}}{\partial \mathbf{K}^e} \cdot \cdot (\dot{\mathbf{K}} - \dot{\mathbf{K}}^P), \end{aligned} \quad (37)$$

where the elastic strain rates are replaced according to the additive decomposition (7). The tensor derivatives of  $\mathbf{N}$  and  $\mathbf{M}$  with respect to the corresponding elastic strain tensors constitute two fourth order tensors that resemble the elasticity tensor  ${}^4C$  of the continuum theory (9). With the rates of the stress resultants (37) as well as the dissipation power (32) written in terms of strain rates, we utilize the flow rules (33) to solve (35) for the consistency parameter:

$$\lambda = \frac{\frac{\partial F}{\partial \mathbf{N}} \cdot \cdot \frac{\partial \mathbf{N}}{\partial \mathbf{E}^e} \cdot \cdot \dot{\mathbf{E}} + \frac{\partial F}{\partial \mathbf{M}} \cdot \cdot \frac{\partial \mathbf{M}}{\partial \mathbf{K}^e} \cdot \cdot \dot{\mathbf{K}}}{\frac{\partial F}{\partial \mathbf{N}} \cdot \cdot \frac{\partial \mathbf{N}}{\partial \mathbf{E}^e} \cdot \cdot \frac{\partial F}{\partial \mathbf{N}} + \frac{\partial F}{\partial \mathbf{M}} \cdot \cdot \frac{\partial \mathbf{M}}{\partial \mathbf{K}^e} \cdot \cdot \frac{\partial F}{\partial \mathbf{M}} + 2k_M k'_M (\mathbf{N} \cdot \cdot \frac{\partial F}{\partial \mathbf{N}} + \mathbf{M} \cdot \cdot \frac{\partial F}{\partial \mathbf{M}})}. \quad (38)$$

In analogy to (11), backward substitution in (37) reveals the tangential elastic-plastic constitutive law in the framework of the stress resultant plasticity theory. The appearance of the total strain rates  $\dot{\mathbf{E}}$  and  $\dot{\mathbf{K}}$  in (38) expresses the inherent coupling of membrane and bending deformations in the elastic-plastic regime. Therefore, curvature rates will in general evoke plastic membrane strain rates according to the flow rules (33) and vice versa.

Now that all prerequisites for the implementation of a numerical solution scheme are met, the return mapping algorithm from [12] is adapted by replacing the governing equations of the original plate srp-model with the ones of the enhanced shell srp-model.

#### 4 Elastic-plastic response of a through-the-thickness element

Here, all three previously mentioned stress resultant plasticity models (Crisfield srp-model, plate srp-model, shell

srp-model) are subjected to simple load cases and are compared to the results of reference solutions obtained with the continuum plasticity model (cp-model) of Sect. 2. Specifically, different kinds of kinematic loading are imposed on a through-the-thickness element by means of a time incrementation of the membrane strain and curvature tensor:

$$\mathbf{K} = \alpha_K(t) K_{\max} (\mathbf{ii} - \nu \mathbf{jj}), \quad \mathbf{E} = \alpha_E(t) E_{\max} \mathbf{P} \cdot (\mathbf{ii} - \nu \mathbf{jj}) \cdot \mathbf{P}^T, \quad (39)$$

where  $\mathbf{i}$  and  $\mathbf{j}$  denote the in-plane Cartesian basis vectors of the element. The rotation tensor  $\mathbf{P}$  is used to adjust the relative angular alignment of the strain measures:

$$\mathbf{P} = \mathbf{P}(\Theta) = \cos \Theta (\mathbf{ii} + \mathbf{jj}) - \sin \Theta (\mathbf{ij} - \mathbf{ji}). \quad (40)$$

The primary directions coincide for  $\Theta = 0$ , in which case an uniaxial stress state in  $\mathbf{i}$ -direction is obtained in the elastic range; small additional components of membrane forces and bending moments in the orthogonal direction arise once plastic flow occurs. A multi-axial state may be enforced by  $\Theta \neq 0$ . Alternatively, a force driven approach that would allow for a direct specification of stress states could be pursued, but the deformation driven one is preferred for ease of implementation. The kinematic loading (39) is biased towards a bending dominant application (like roll forming) with the maximum amplitudes:

$$K_{\max} = 4 \frac{12M_0}{Eh^3} = \frac{8k}{Eh}, \quad E_{\max} = \frac{1}{2} \frac{N_0}{Eh} = \frac{1}{2} \frac{k}{E}, \quad (41)$$

that correspond to four-times the curvature of first yield for pure bending and just half of the membrane strains required for yielding in the state of pure tension, respectively. The actual values are controlled with the load factors  $\alpha_K$  and  $\alpha_E$  that range from zero to one and are defined as piecewise linear functions in the timespan  $0 \leq t \leq 1$ .

The rate equations of the particular plasticity models under consideration are integrated numerically with a simple explicit scheme and a sufficiently fine time discretization. The parameters of the particular numerical experiments are specified in Table 1;  $N_\zeta$  is the number of thickness integration

points that are used for the continuum plasticity model. The element with the given material parameters and thickness  $h$  is subjected to four different load histories that are stated in terms of the angle  $\Theta$  and tabulated values for the load factors  $\alpha_E$  and  $\alpha_K$ , which are interpolated linearly between the designated points  $t = \{0.0, 0.5, 1.0\}$ . Cases 1 and 2 feature a simultaneous increase of the imposed strains (41) and differ solely in the angle  $\Theta$ . The angular alignment is varied in cases 3 and 4 as well, but, more importantly, the kinematic loads are applied sequentially, i.e.: first bending then tensioning and vice versa.

The tabulated values for the load factors are indicated at the top of the respective grid lines in the corresponding graphs of Figs. 1, 2, 3 and 4 that depict the simulated time histories of the primary invariants  $I_N$  and  $I_M$ . These variables are bounded by their uniaxial limit yield values, namely:  $I_N \leq 1$  and  $I_M \leq 9/4$ . An exception is the plate stress resultant model of [12], which may be recovered from (30) by simply setting  $I_N = I_{MN} = 0$ . Hence, the membrane stress resultants do not enter the elastic-plastic constitutive of the plate srp-model in any way and the invariant  $I_N$  is unbounded in consequence thereof. Analyzing the results presented in Figs. 1 – 4, good agreement of the novel shell srp-model with the exact continuum model is observed, which in terms of  $I_M$  also poses a slight improvement over the stress resultant plasticity model of Crisfield; regarding  $I_N$ , both models are almost indistinguishable. The great importance of including the membrane forces in the plasticity model is highlighted in comparison to the plate srp-model, which produces the same purely elastic response for  $I_N$  regardless of the imposed loading. This deficiency is most pronounced for the cases 1, 2 and 4, where the corresponding graphs of the plate srp-model for  $I_N$  deviate from the others as soon as plastic flow occurs and the purely elastic regime, for which all models are equal, is left. Interestingly, the coupling of membrane and bending resultants in these cases primarily affects the distribution of the membrane forces, but its impact on the bending behavior is weak, such that the distributions for  $I_M$  remain in close proximity to the continuum reference model. In this respect case 3 of Fig. 3 is different, because the late application of the kinematic membrane loading must cause additional plas-

**Table 1** Parameters and specific load histories for the numerical experiments on the through-the-thickness element: The angle  $\Theta$  determines the angular alignment of the prescribed strain states

$E$ [N/m <sup>2</sup> ]	$\nu$	$k$ [N/m <sup>2</sup> ]	$h$ [m]	$N_\zeta$			
$2.8 \times 10^{11}$	0.3	$362 \times 10^6$	0.003	50			
load case	$\Theta$ [rad]	$\alpha_E(0)$	$\alpha_E(0.5)$	$\alpha_E(1.0)$	$\alpha_K(0)$	$\alpha_K(0.5)$	$\alpha_K(1.0)$
1	0	0.0	0.5	1.0	0.0	0.5	1.0
2	$\pi/2$	0.0	0.5	1.0	0.0	0.5	1.0
3	$\pi/4$	0.0	0.0	1.0	0.0	1.0	1.0
4	0	0.0	1.0	1.0	0.0	0.0	1.0

The time evolution of the load factors  $\alpha_E$  and  $\alpha_K$  is given by piecewise linear interpolation of the tabulated values for  $t = \{0.0, 0.5, 1.0\}$

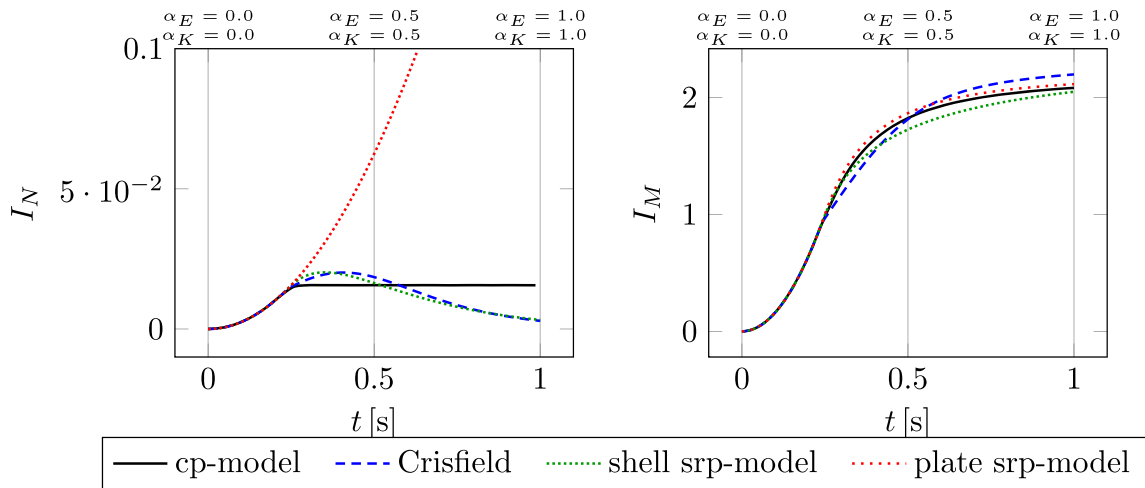


**Fig. 1** Comparison of simulation results of the through-the-thickness element between the four different plasticity models for the load case 1 of Table 1

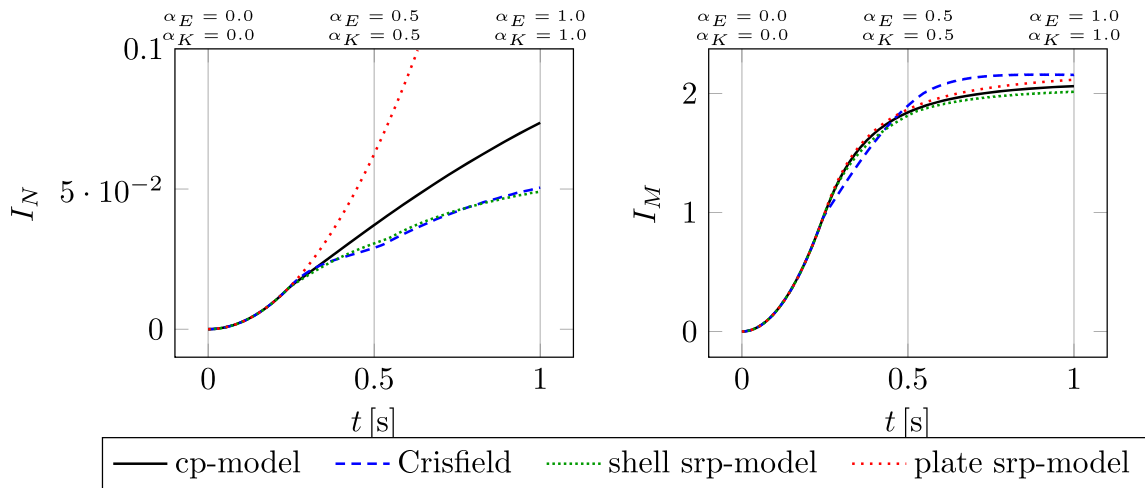


**Fig. 2** Comparison of simulation results of the through-the-thickness element between the four different plasticity models for the load case 2 of Table 1

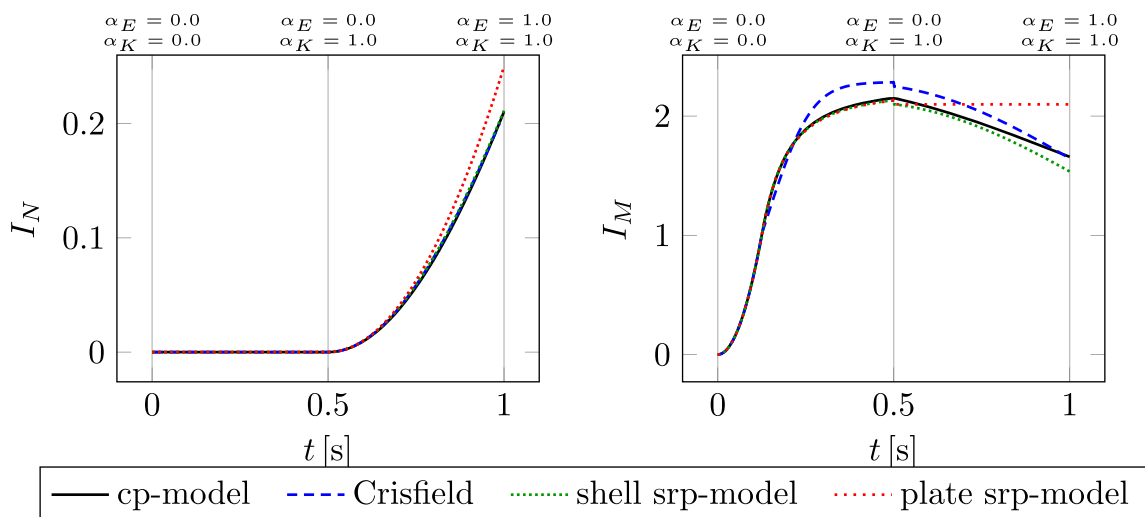


**Fig. 3** Comparison of simulation results of the through-the-thickness element between the four different plasticity models for the load case 3 of Table 1

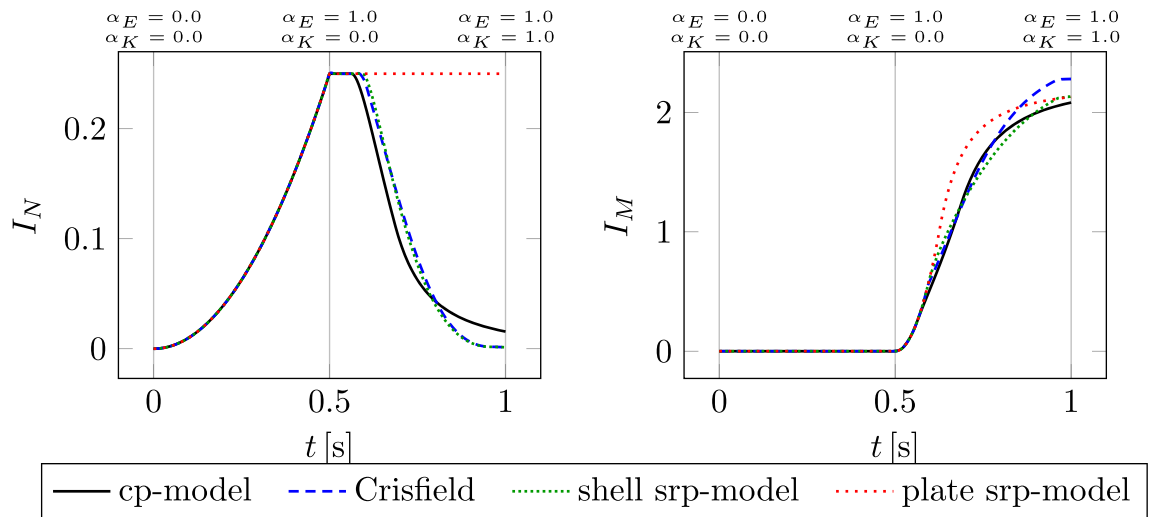


Fig. 4 Comparison of simulation results of the through-the-thickness element between the four different plasticity models for the load case 4 of Table 1

tic curvature strains in the extended models owing to the inherent coupling best illustrated by (38). Hence, the limited capabilities of the plate srp-model show in the distribution for  $I_M$  in this special case. Evidently, the inclusion of plastic membrane strains is crucial for an accurate resolution of the stress resultants.

To investigate the essential differences of the novel shell srp-model and the one proposed by Crisfield, comparisons of the respective hardening functions  $k_M(A^P)/M_0$  and  $\gamma(\chi^P)$  are presented in Figs. 5 and 6 for all considered load cases. The values of both dimensionless hardening functions are initialized with 1, which is the limit for initial yielding. Once plastic flow occurs, the hardening functions grow towards the

limit yield value  $3/2$ . Owing to the exponential law (28), the Crisfield model always saturates very quickly. In contrast, the shell srp-model approaches the limit yield boundary slower without ever reaching it. Being based on work hardening, this model also accounts for the contribution of plastic membrane strains to the plastic work  $A^P$  that determines the progression of plastic flow in the thickness element. However, the impact is negligible in all cases, which is best illustrated by the graphs corresponding to load case 3 in Fig. 6, where the hardening function  $k_M/M_0$  remains practically constant for  $t > 0.5$  after the curvature loading has been fully applied.

The results presented so far, demonstrate the obvious advantages of the proposed shell srp-model over its prede-

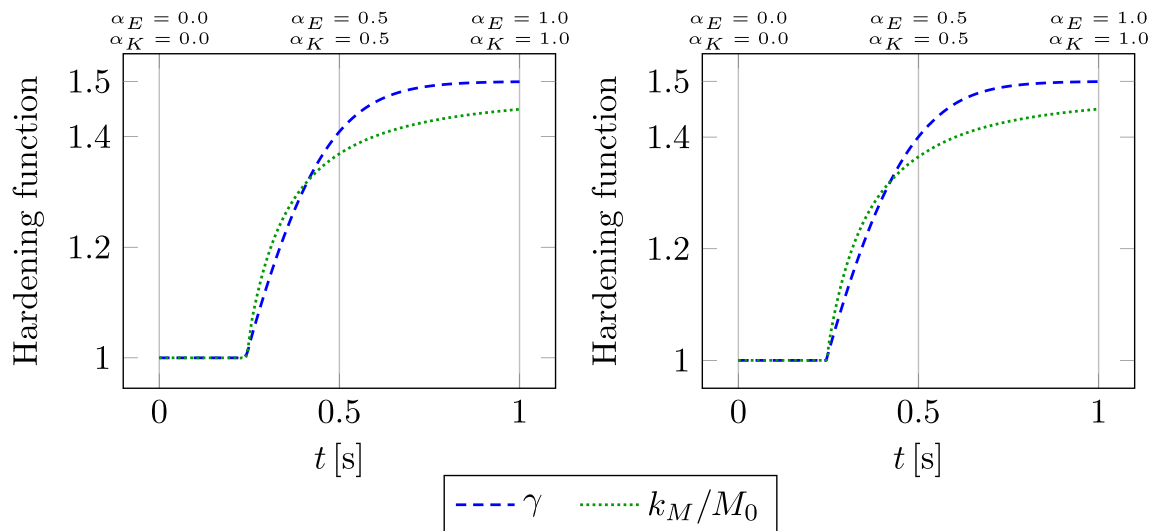
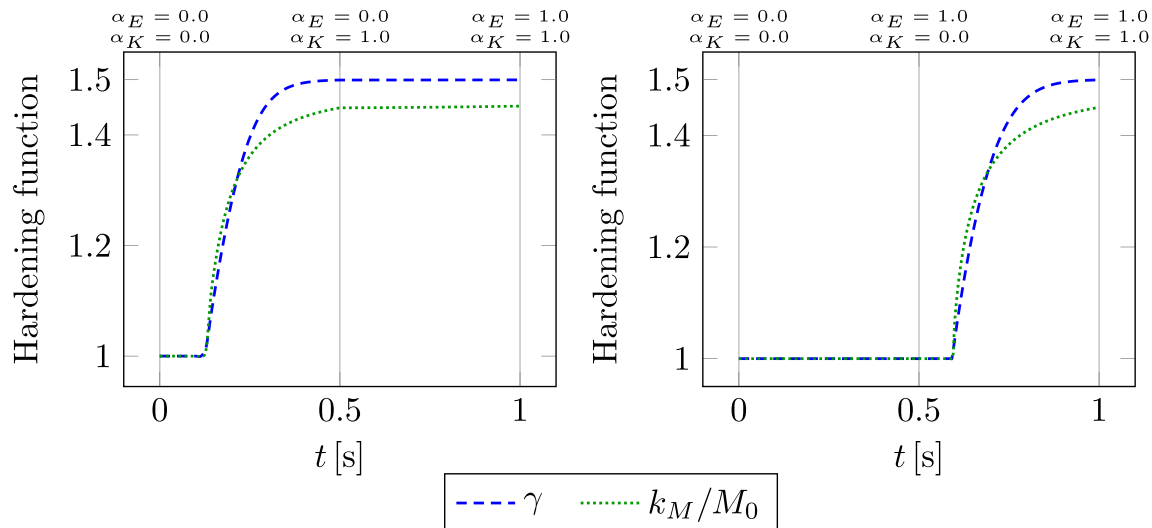


Fig. 5 Comparison of the hardening functions for load case 1 (left) and load case 2 (right) of Table 1



**Fig. 6** Comparison of the hardening functions for load case 3 (left) and load case 4 (right) of Table 1

cessor for the plate bending problem discussed in [12]. The primary benefits in comparison to the Crisfield stress resultant model comprise:

- modest improvements of accuracy with respect to the continuum reference solution
- the formulation in terms of a work hardening law that facilitates the inclusion of isotropic material hardening
- a significantly better convergence of the numerical time integration scheme

Regarding the last point, it is found, that the Crisfield model requires about three times more time steps than the shell srp-model in order to reach results of comparable numerical accuracy. An elaborate discussion on the time integration scheme of the Crisfield model and related limitations of [10] is available in [10]. Similar concerns regarding actual implementations of the Crisfield model were expressed in [27, 28]. Later in Sect. 7, the comparison of plasticity models by imposing the results of actual roll forming simulations on a through-the-thickness element is continued.

## 5 Mixed Eulerian–Lagrangian finite element scheme

The different plasticity models, except for the one proposed by Crisfield, are implemented in a mixed Eulerian–Lagrangian shell finite element scheme that is designed for the simulation of sheet metal roll forming. Since a detailed discussion of this program is available [13], only a brief explanation of the most essential aspects is provided, namely:

- the mixed Eulerian–Lagrangian kinematic description

- the contributions that constitute the total potential energy in the weak formulation
- frictionless contact
- the convective transport of internal plastic variables in the two-step solution procedure

Though purpose-built for the process of sheet metal forming, the simulation framework is equally applicable to certain static problems [13]; actual roll forming simulations are addressed in Sects. 6 to 8.

Since the raw material of the roll forming process is a flat metal sheet a rectangular reference configuration can now explicitly be stated:

$$\overset{\circ}{\mathbf{r}} = \overset{\circ}{x}\mathbf{i} + \overset{\circ}{y}\mathbf{j}, \quad -w/2 \leq \overset{\circ}{y} \leq w/2, \quad (42)$$

where  $\overset{\circ}{x}$  and  $\overset{\circ}{y}$  denote the Lagrangian material coordinates in axial direction and lateral (width) direction, respectively. Originally, the undeformed sheet is aligned in the  $xy$ -plane of the spatial Cartesian coordinate frame with the basis vectors  $\mathbf{i}$  and  $\mathbf{j}$ ; the complementary vector  $\mathbf{k} = \mathbf{i} \times \mathbf{j}$  points in  $z$ -direction. The lateral coordinate  $\overset{\circ}{y}$  is bounded by the total width  $w$  of the metal sheet, but the axial coordinate  $\overset{\circ}{x}$  is unbounded, because roll forming is viewed as a continuous process in a spatial control domain  $0 \leq x \leq L$ . Therefore, as forming progresses the axially moving sheet (and its material particles) will be continuously transported through this domain, which renders the purely Lagrangian perspective inefficient and suggests a coordinate transformation to a mixed set that decouples the actual deformations sustained during the forming process from the axial travel of the structure. Thus, the position vector to a material particle  $\mathbf{r}$  in the actual configuration is parametrized in a mixed coordinate



space that comprises the Eulerian axial coordinate  $x$  and the Lagrangian lateral coordinate  $\overset{\circ}{y}$ :

$$\mathbf{r} = x\mathbf{i} + (\overset{\circ}{y} + u_y)\mathbf{j} + u_z\mathbf{k}, \quad \overset{\circ}{x} = x - u_x. \quad (43)$$

Together the mixed pair  $\{x, \overset{\circ}{y}\}$  constitute a rectangular intermediate configuration of the part of the metal sheet currently enclosed by the boundaries of  $x \in [0, L]$  (active material volume). The Cartesian components of the displacement vector

$$\mathbf{u}(x, \overset{\circ}{y}, t) = u_x(x, \overset{\circ}{y}, t)\mathbf{i} + u_y(x, \overset{\circ}{y}, t)\mathbf{j} + u_z(x, \overset{\circ}{y}, t)\mathbf{k} \quad (44)$$

serve as primary unknowns. More specifically, the nodal variables of a single four-node rectangular finite element, which resides in the intermediate configuration, comprise the displacements themselves, their first derivatives and the mixed second derivative with respect to the local finite element coordinates. This choice of nodal degrees of freedom paired up with bi-cubic polynomial shape functions ensures a  $C^1$  continuous approximation of the position vector. The used finite elements are therefore an extension of the Bogner-Fox-Schmit plate elements [29, 30].

The mixed parametrization is advantageous because it enables a spatial resolution of the deformations imposed by the roll stands at given  $x$ -positions. Consequently, material particles are free to travel through the finite element mesh that is fixed in axial direction. This change of perspective necessitates a corresponding transformation of the basic kinematic relations. In particular, the material differential operator needs to be restated in terms of the partial derivatives with respect to  $x$  and  $\overset{\circ}{y}$ :

$$\overset{\circ}{\nabla} = \mathbf{i} (1 - \partial_x u_x)^{-1} \partial_x + \mathbf{j} \partial_{\overset{\circ}{y}}, \quad (45)$$

such that its application to  $\overset{\circ}{\mathbf{r}}$  with  $\overset{\circ}{x} = x - u_x$  still yields the planar unit tensor. The first coefficient represents the derivative of the Eulerian coordinate  $x$  with respect to its material counterpart  $\overset{\circ}{x}$ . Consequently, its reciprocal value determines the Jacobian determinant to transform the material area integral for the total strain energy:

$$U^\Sigma = \iint U d\overset{\circ}{x}d\overset{\circ}{y} = \int_0^L dx \int_{-w/2}^{w/2} (1 - \partial_x u_x) U d\overset{\circ}{y}, \quad (46)$$

where either (13) or (12) need to be inserted for the strain energy density  $U$  depending on the particular choice of plasticity model.

The second contribution to the total potential energy is attributed to the contact of the metal sheet with the rolls that impose the plastic bending on the initially flat metal sheet during the roll forming process. It is modelled as a frictionless contact of a solid body (metal sheet) with rigid

bodies of revolution (rolls). The assumption of frictionless contact is justified with the following reasoning:

- In reality, the interface between rolls and sheet metal is lubricated to reduce tool wear, which reduces friction and significantly complicates the identification of the friction parameters [31].
- Friction seems to have no significant impact on resulting geometry and contact normal forces [15, 31, 32].

The penalty-regularization method is employed to state the contact potential as

$$V^\Sigma = \int_0^L dx \int_{-w/2}^{w/2} (1 - \partial_x u_x) \frac{1}{2} P \gamma^2 d\overset{\circ}{y}, \quad (47)$$

with a large factor  $P$  to penalize any penetration  $\gamma \geq 0$  of the metal sheet into the roll surface; details are provided in [13]. The sum of  $U^\Sigma$  and  $V^\Sigma$  constitutes the total potential energy, which is minimized numerically to compute a quasistatic equilibrium state in the first phase of the transient simulation procedure.

Since the inner variables that identify the plastic state are strictly attached to the material particles, their flow through the Eulerian–Lagrangian finite element mesh in axial direction must be rigorously accounted for. This is done by means of solving an advection equation, which constitutes the second (Eulerian) step of the solution scheme and concludes the time increment. A forward in time backwards in space finite difference method is used to perform the incremental time integration of this equation; its implementation in the finite element scheme is discussed in [13].

## 6 Roll forming simulation for a single roll stand

In this section the enhanced shell srp-model is tested in an actual roll forming simulation with a single roll stand and its response is compared to corresponding simulations conducted with the plate srp-model of [12] and the continuum plasticity model. The same assumptions (rigid rolls, frictionless contact etc.) and simulation procedure as described in [13] is followed, which features the mixed Eulerian–Lagrangian finite element scheme outlined in Sect. 5

A control domain  $0 \leq x \leq 0.8$  m with one roll stand acting at  $x = 0.4$  m is considered, with simulation parameters according to Table 2; an axial mesh refinement (with  $N_x$  elements) such, that the elements at the contact region are half the size of the elements in the outer regions is employed. The edge at  $x = 0$  corresponds to a fully (in-plane and out-of-plane) clamped edge with material particles flowing through at the constant transport rate  $v$ . The final (steady state) con-

**Table 2** Default parameters of the simulation model with one roll stand

Geometry			Material			
$L$ [m]	$w$ [m]	$h$ [m]	$E$ [N/m <sup>2</sup> ]	$\nu$	$k$ [N/m <sup>2</sup> ]	
0.8	0.1	0.003	$2.08 \times 10^{11}$	0.3	$362 \times 10^6$	
Forming		Transport	Numerical			
$\rho$ [m]	$v$ [m/s]	$\Delta t$ [s]	$N_x$	$N_y$	$N_\xi$	$P$ [N/m <sup>3</sup> ]
0.004	0.8	0.005	26	10	8	$1 \times 10^{13}$

figuration with a cross-sectional view of the roll gap in the center is depicted in Fig. 7.

It visualizes the symmetrical roll profiles and also shows the forming angle  $\varphi$  as well as the roll-gap-reduction parameter  $\rho$ . The latter is used to position the rolls vertically by means of a symmetrical shift of  $\rho/2$  towards each other and the angle  $\varphi$  corresponds to the tangential direction at the end of the cross section. As postprocessing variables the resulting contact force acting on the lower rolls  $R_L$  and the bending angle  $\varphi(x = 0.6 \text{ m})$  are viewed. The angle is evaluated at this particular x-coordinate because the forming angle of an endless profile is best approximated about halfway between the roll-stand and the free end, i.e.: sufficiently far away from the rolls and the right boundary. A parameter study for varying roll-gap-reduction  $\rho$  is carried out and the resulting force  $R_L$  and the bending angle  $\varphi(x = 0.6 \text{ m})$  are plotted in Fig. 8. Evidently, the results produced by the proposed shell srp-model are mostly in line with the ones of the reference computation with the cp-model.

The good correspondence of all models regarding the bending angle is owed to the fact that the shape of the final cross section is primarily determined by the kinematically imposed roll profiles. However, the force distribution obtained for the plate srp-model deviates significantly, which can be attributed to the neglect of the membrane forces in the elastic-plastic constitutive law. Hence, though the forming operation is bending dominant, the impact of membrane effects on the forming forces is not negligible. The slight “waviness” of the curves in Fig. 8 is owed to the coarse discretization according to Table 2. This does not impede the comparison of plasticity models, but could, in principle, be

resolved by a mesh-refinement to improve the contact resolution [13].

To conclude this experiment the intensities of the membrane forces represented by  $I_N$  as a contour plot for the cp-model, the novel shell srp-model and the plate srp-model are plotted in Figs. 9, 10 and 11, respectively. Expectedly, the proposed shell srp-model matches the continuum behavior significantly better than the plate srp-model. It is also noteworthy, that the largest intensities of  $I_N$  occur at the outermost fibers before entering the roll gap. This is a well established fact in practice: Material particles moving along the curved side edges are stretched as they must travel a greater distance than particles following the shorter path in the center.

## 7 Response of a through-the-thickness element subjected to a roll forming strain history

To facilitate a comparison of the shell srp-model with Crisfield’s model in the practical scenario of roll forming, the numerical experiments on the through-the-thickness element of Sect. 4 are reconsidered, but this time the thickness element is subjected to strain histories of actual roll forming simulations. This presents an easy way to continue the validation without having to implement Crisfield’s model in the finite element framework.

For this sake, the results obtained in Sect. 6, from the reference simulations with the cp-model for the particular choice  $\rho = 0.004 \text{ m}$  are taken. More specifically, the steady

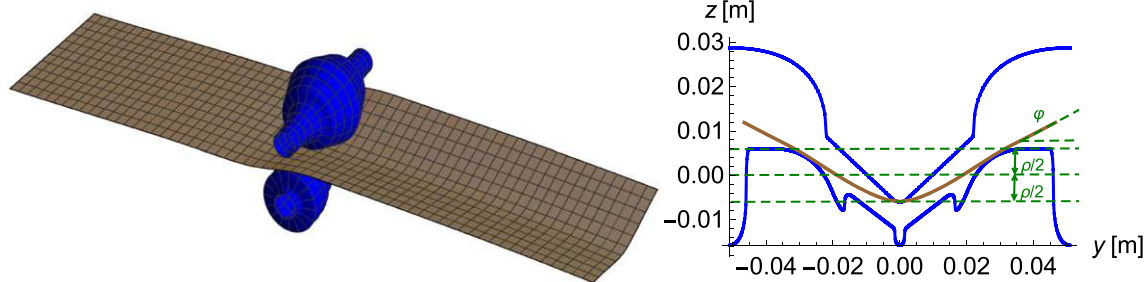


**Fig. 7** Final, steady state configuration of the roll forming experiment with one roll stand (left); annotated view of the cross section at the roll stand showing the roll-gap-reduction parameter  $\rho$  and the bending angle  $\varphi$  (right)

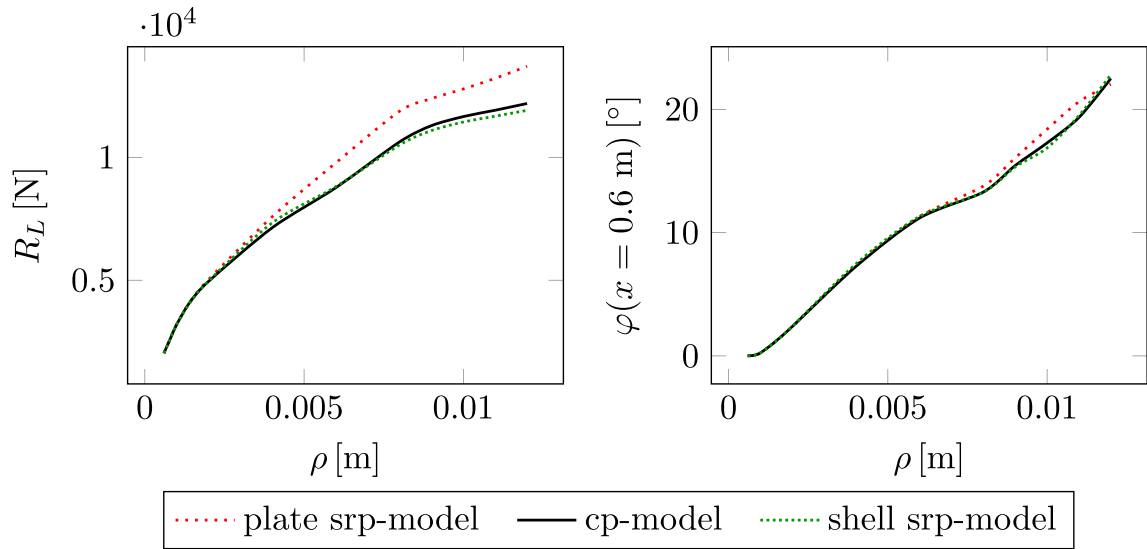


**Fig. 8** Comparison of the different plasticity models in terms of the roll force on the lower roll  $R_L$  and the bending angle  $\varphi(x = 0.6 \text{ m})$  for increasing values of the roll-gap-reduction  $\rho$

**Fig. 9** Intensities  $I_N$  of the shell as obtained for the continuum plasticity model of [13] in the steady state configuration of the roll forming experiment with one roll stand and  $\rho = 0.004\text{m}$

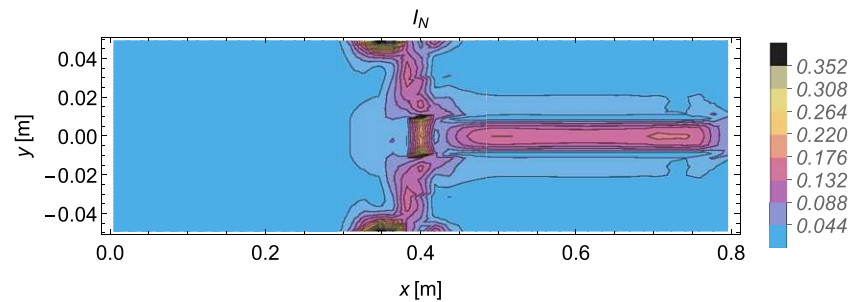


**Fig. 10** Intensities  $I_N$  of the shell as obtained for the proposed shell stress resultant plasticity model in the steady state configuration of the roll forming experiment with one roll stand and  $\rho = 0.004\text{m}$

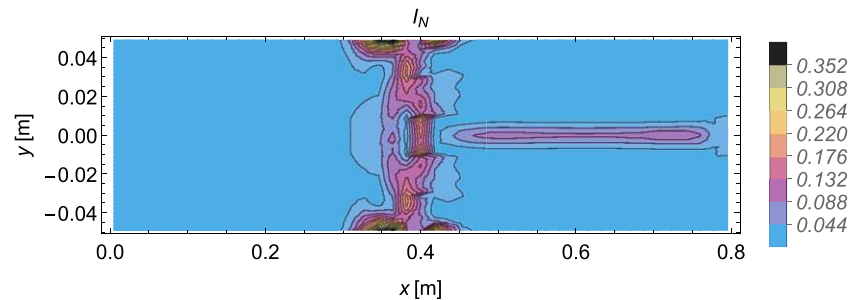
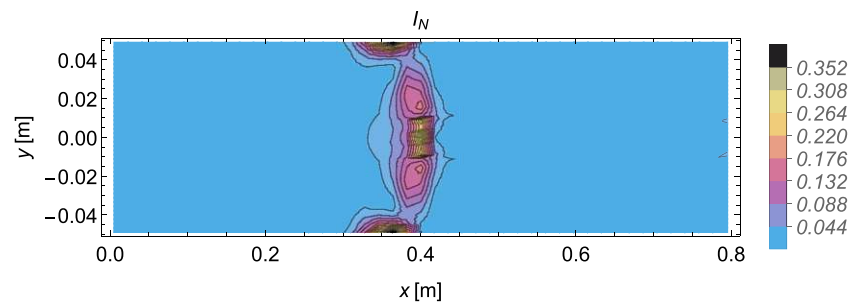


**Fig. 11** Intensities  $I_N$  of the shell as obtained for the plate stress resultant plasticity model of [12] in the steady state configuration of the roll forming experiment with one roll stand and  $\rho = 0.004\text{m}$



state strains  $\mathbf{E}$  and  $\mathbf{K}$  encountered by a material particle on its way through the control domain  $0 \leq x \leq L$  are imposed on the through-the-thickness element by means of:

$$\mathbf{E}(x(t), y^*), \quad \mathbf{K}(x(t), y^*), \quad x(t) = t/L, \quad (48)$$

where  $y^*$  is the lateral position of an axial fiber and the load-application is controlled with the pseudo-time  $0 < t \leq 1$  in resemblance of (39). The strain histories are evaluated for the outermost line of integration points at  $y^* = 0.049\text{m}$  and the innermost line at  $y^* = 0.0011\text{m}$ . A piecewise quadratic interpolation is used to obtain a smooth strain history from the discrete integration point values. The time-histories of  $I_N$  and  $I_M$  as well as the hardening functions are depicted in Figs. 12, 13 and 14.

It is important to note that the thus produced time histories for the plate srp-model, the shell srp-model and the Crisfield model are artificial to a varying degree. This is due to the fact, that the strain history of the simulation with the continuum plasticity model is imposed, which generally differs from the corresponding strain histories obtained from simulations with the stress resultant plasticity models.

From Fig. 12 it can be concluded that the shell srp-model very closely replicates the reference solution of the cp-model for the outermost fiber. The plate srp-model is equally accurate with regard to the bending invariant  $I_M$  but exhibits a strong deviation in the membrane invariant  $I_N$ . Crisfield's model produces reasonably accurate results, which are however harder to obtain numerically owing to the less favorable convergence behavior of the time integration scheme already noted in Sect. 4.

The time histories for the innermost fiber depicted in Fig. 13 show, however, significant differences between the continuum and the stress resultant plasticity models. In order to investigate this discrepancy, the time history of the dominant components of the bending moments  $M_x(t)$  and  $M_y(t)$  are presented in Fig. 15. Here, the non-monotonous characteristic of the axial bending moment  $M_x$ , which relates to the axial curvature induced by the rolls, entails a significant change of the load case that even induces reverse plasticity. The stress resultant plasticity models fail to reproduce such load histories accurately, because the employed isotropic hardening functions that govern the progression of plastic flow rest upon the assumption of a monotonously increasing loading. However, for the considered type of profile geometry these discrepancies remain confined to the proximity of the center fiber and, as depicted in Fig. 8, do not perceptively deteriorate the correspondence in terms of the primary variables of the forming process.

Finally, Fig. 14 demonstrates, that plastic flow at outer- and inner- fiber is initiated even before the sheet enters the roll gap at  $x = 0.4\text{m}$ , which is a well established observation in the engineering practice of roll forming [33, 34].

## 8 Practical example of U-shaped profile formed by three roll stands

Here, a simulation with three roll stands in which a simple U-shaped geometry with a final forming angle of  $\varphi = \pi/4$  is produced, is considered. The steady state configuration with fully closed roll gaps is depicted in Fig. 16. The simulation parameters are provided in Table 3. The edge at  $x = 0$  is again fully clamped (in- and out-of-plane) and the three roll stands are positioned at  $x_i = \{0.39, 0.78, 1.17\}\text{m}$ .

Table 4 presents the resulting forming forces  $R_{Li}$  (resultant contact forces) on the lower rolls as obtained from the stress resultant plasticity models and the relative errors  $\epsilon_{Li}$  in comparison to the continuum plasticity approach, which serves as reference solution. The shell srp-model provides highly accurate results (at significantly lower computational cost), whereas the plate srp-model significantly overestimates these forces. This inability to produce accurate forming forces is a consequence of the incomplete description of plasticity with respect to the membrane forces. On the other hand, the evolution of bending angles along the axis  $x$  as depicted in Fig. 17 shows good correspondence of all three considered models. Hence, in accordance with the observations made for the experiment with a single roll stand in Sect. 6, the estimated membrane forces have a strong influence on the required forming forces to obtain a given profile geometry.

In comparison to the cp-model the primary advantage of the shell srp-model is, that it produces practically accurate results at approximately one-fifth of the total simulation time.<sup>1</sup>

## 9 Conclusion

The proposed Kirchhoff–Love shell stress resultant plasticity model is designed for a bending dominant framework in which membrane forces remain small to moderate. The derivation rests upon a proper combination of a previously reported stress resultant plasticity model for elastic-plastic plate bending and an augmented version of the Ilyushin yield criterion proposed by Crisfield. The thus deduced stress resultant plasticity formulation presents a computationally more efficient alternative to the usually applied continuum approach with a through-the-thickness resolution of plastic states. This advantage is of crucial importance since econ-

<sup>1</sup> Reaching a quasi-steady state solution for the parameter set from Table 3 takes about 45 days for the cp-model vs. 9 days for the shell srp-model and vs. 8 days for the plate srp-model on a 6-core Intel(R) Core(TM) i7-8850H CPU at 2.60GHz. This comparison of simulation times stands regardless of the inherent inefficiency of the in-house finite element code. In the latter respect, preliminary studies show, that limited optimization measures are easily capable of reducing the simulation time with the shell srp-model to less than a day.

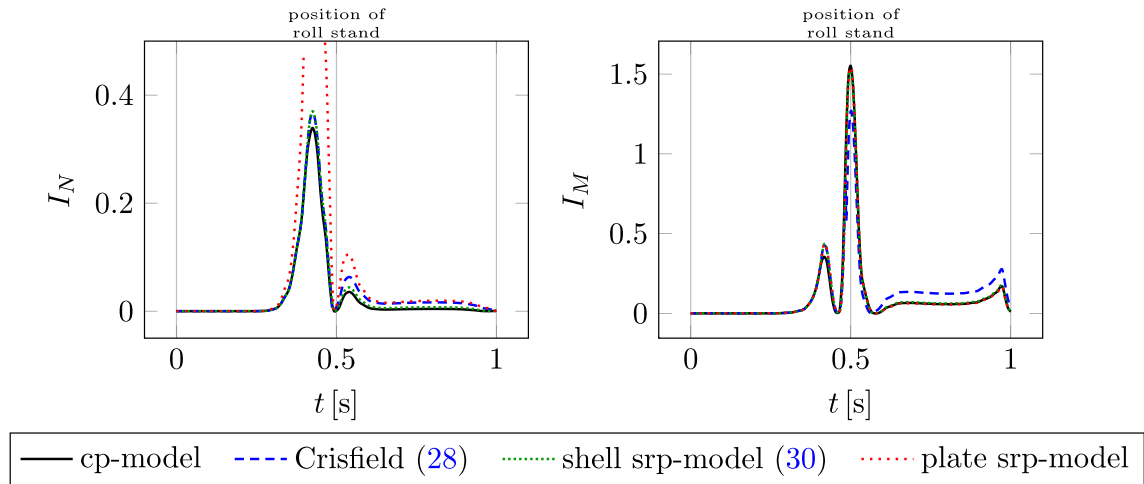


**Fig. 12** Comparison of simulation results of the through-the-thickness element between the four different plasticity models with the strain history of the outermost fiber;  $y^* = 0.049m$  and  $\rho = 0.004m$

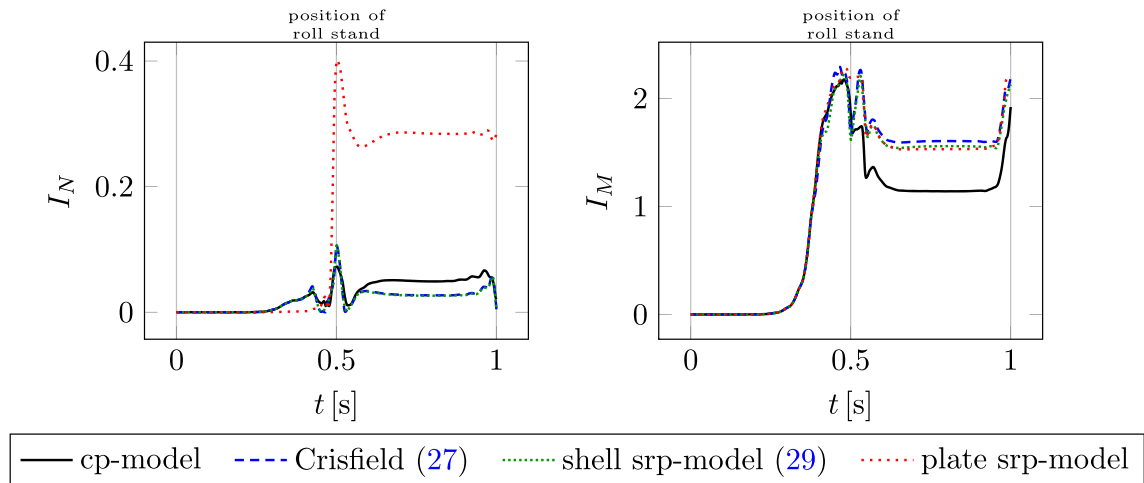


**Fig. 13** Comparison of simulation results of the through-the-thickness element between the four different plasticity models with the strain history of the innermost fiber;  $y^* = 0.0011m$  and  $\rho = 0.004m$

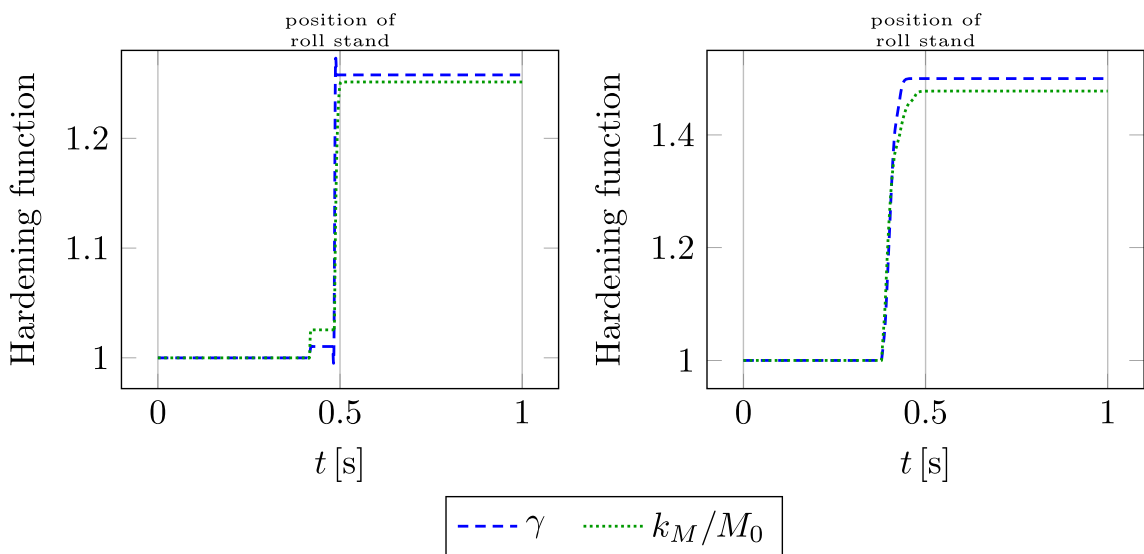


**Fig. 14** Comparison of the hardening functions for outermost fiber (left) and innermost fiber (right)

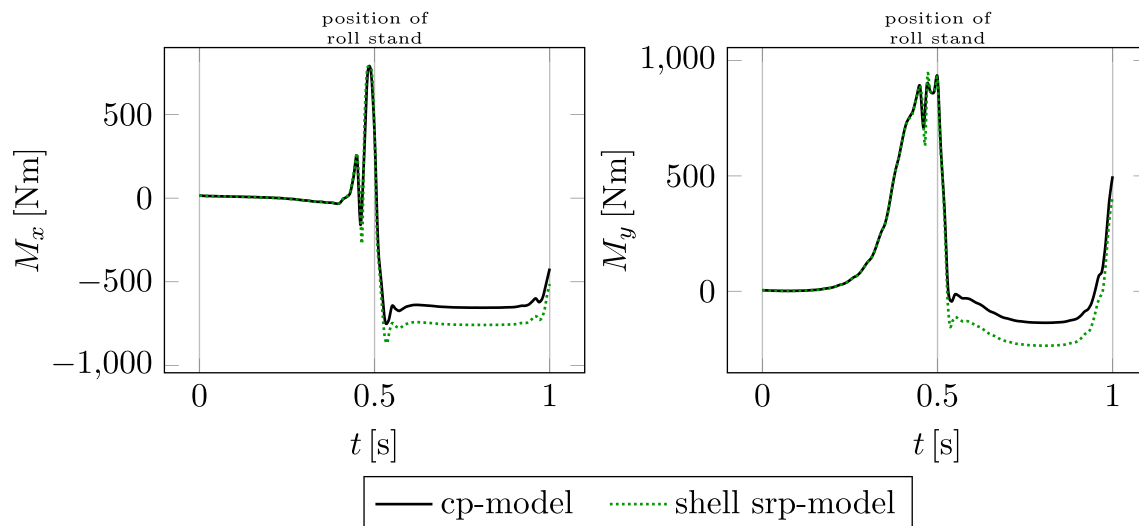


**Fig. 15** Comparison of simulation results of the bending moments of the through-the-thickness element for the innermost fiber with  $y^* = 0.0011m$  and for  $\rho = 0.004m$

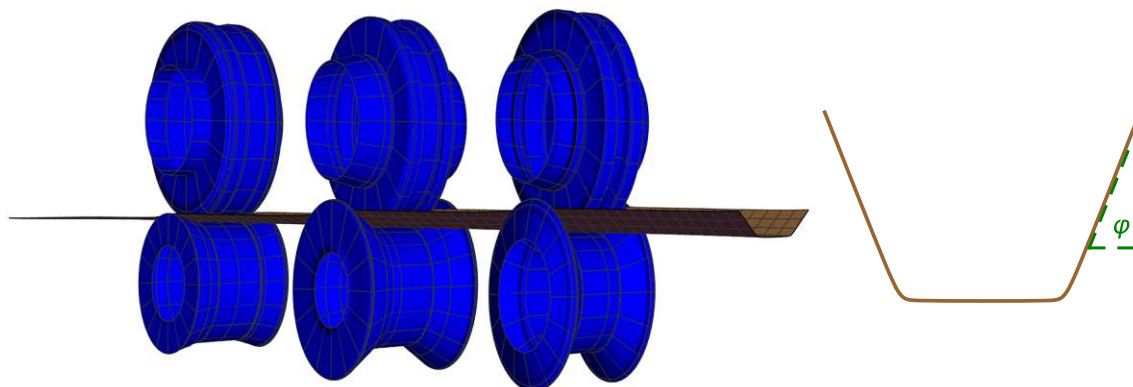


**Fig. 16** Final, steady state configuration of the roll forming experiment with three roll stands

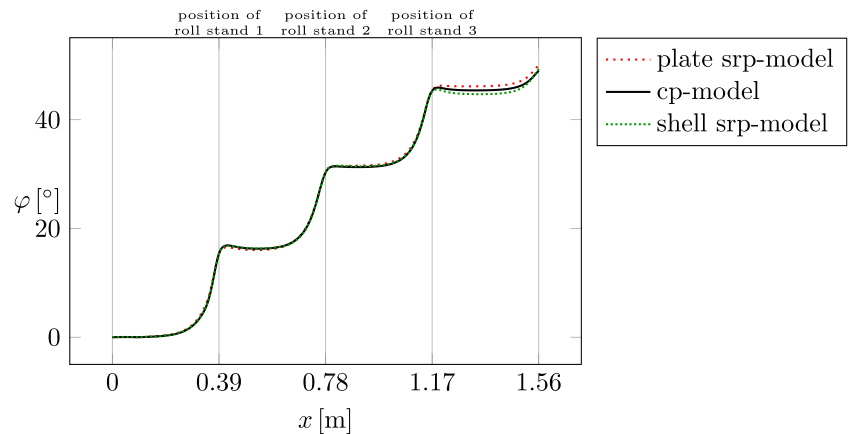
**Table 3** Parameters of the roll forming simulation with three roll stands

Geometry			Material			
$L$ [m]	$w$ [m]	$h$ [m]	$E$ [N/m <sup>2</sup> ]	$\nu$	$k$ [N/m <sup>2</sup> ]	
1.56	0.12	0.0015	$2.08 \times 10^{11}$	0.3	$362 \times 10^6$	
Forming		Transport		Numerical		
$\rho$ [m]	$v$ [m/s]	$\Delta t$ [s]		$N_x$	$N_y$	$N_\zeta$
$\rho_{max}$	0.8	0.005		56	20	8
				$P$ [N/m <sup>3</sup> ]		
				$1 \times 10^{13}$		

**Table 4** Stationary forces and relative errors with respect to the continuum reference solution for the simulation with three roll stands

Model	$R_{L1}$ [N]	$R_{L2}$ [N]	$R_{L3}$ [N]	$\epsilon_{L1}$ [%]	$\epsilon_{L2}$ [%]	$\epsilon_{L3}$ [%]
cp-model	5396	7493	10710	-	-	-
shell srp-model	5480	7487	10491	1.56	-0.08	-2.05
plate srp-model	5838	10008	15607	8.19	33.57	45.72

**Fig. 17** Comparison of the resulting stationary bending angles  $\varphi(x)$  for the three different plasticity models in the simulation with three roll stands



omy of time is an important design goal when developing simulation tools for industrial applications like the here considered process of sheet metal roll forming.

The proposed model is tested in a series of experiments on a through-the-thickness element by imposing bending and membrane strain histories. Moreover, it is implemented in an existing mixed Eulerian–Lagrangian finite element scheme that is designed for the simulation of the sheet metal roll forming process. For the purpose of validation, reference solutions are obtained with the established continuum plasticity approach. In the considered scenarios, the new model surpasses the previously reported stress resultant plasticity models in terms of accuracy and computational efficiency.

Like its predecessors the model captures the evolution of plastic zones through the thickness by means of a custom isotropic hardening law. As such it is well applicable to cases that feature a monotonous increase of a given type of loading, whereas non-monotonous load histories that induce reverse plastic bending cannot be captured accurately. It is interesting to note that even in case of the roll forming process, which features a progressive bending of an initially flat metal sheet, the phenomenon of reverse plasticity may occur in certain parts of the cross section. This is due to the curvature in axial direction that the rolls impose on the sheet as it is passing through the roll gap. Future research may focus on the resolution of this persistent limitation, which nonetheless does not inhibit the usability of the proposed model as long as reverse plasticity has no dominant impact on the outcome of the forming process.

In the roll forming scenarios considered so far, which featured simulation models with one and three roll stands to produce a V-shaped and a U-shaped profile, the novel shell stress resultant plasticity model produces accurate results in terms of contact forces and bending angles when compared to reference simulations conducted with the continuum plasticity approach. In contrast to the previously reported model for elastic-plastic plate bending, the additional account for membrane effects in the plasticity model significantly improves

the estimates of the forming forces. Ultimately, the enhanced shell stress resultant plasticity model paired with the mixed Eulerian–Lagrangian finite element framework presents a major step towards a both computationally efficient and accurate simulation of the sheet metal roll forming process.

**Acknowledgements** The authors acknowledge TU Wien Bibliothek for financial support through its Open Access Funding Programme.

**Author Contributions** All authors contributed to the study conception and design. Material preparation, data collection and analysis were performed by all authors. The first draft of the manuscript was written by [Emin Kocbay] and all authors commented on previous versions of the manuscript. All authors read and approved the final manuscript.

**Funding** Open access funding provided by TU Wien (TUW). The authors declare that no funds, grants, or other support were received during the preparation of this manuscript.

## Declarations

**Competing Interests** The authors have no relevant financial or non-financial interests to disclose.

**Open Access** This article is licensed under a Creative Commons Attribution 4.0 International License, which permits use, sharing, adaptation, distribution and reproduction in any medium or format, as long as you give appropriate credit to the original author(s) and the source, provide a link to the Creative Commons licence, and indicate if changes were made. The images or other third party material in this article are included in the article's Creative Commons licence, unless indicated otherwise in a credit line to the material. If material is not included in the article's Creative Commons licence and your intended use is not permitted by statutory regulation or exceeds the permitted use, you will need to obtain permission directly from the copyright holder. To view a copy of this licence, visit <http://creativecommons.org/licenses/by/4.0/>.

## References

1. Ambati M, Kiendl J, De Lorenzis L (2018) Isogeometric Kirchhoff-Love shell formulation for elasto-plasticity. *Comput Methods Appl Mech Eng* 340:320–339. <https://doi.org/10.1016/j.cma.2018.05.023>

2. Brank B, Perić D, Damjanić FB (1997) On large deformations of thin elasto-plastic shells: implementation of a finite rotation model for quadrilateral shell element. *Int J Numer Methods Eng* 40(4):689–726. [https://doi.org/10.1002/\(SICI\)1097-0207\(19970228\)40:4<689::AID-NME85>3.0.CO;2-7](https://doi.org/10.1002/(SICI)1097-0207(19970228)40:4<689::AID-NME85>3.0.CO;2-7)
3. Liguori FS, Madeo A, Garcea G (2022) A dual decomposition of the closest point projection in incremental elasto-plasticity using a mixed shell finite element. *Int J Numer Methods Eng* 123(24):6243–6266. <https://doi.org/10.1002/nme.7112>
4. Alaydin MD, Benson DJ, Bazilevs Y (2021) An updated Lagrangian framework for isogeometric Kirchhoff-Love thin-shell analysis. *Comput Methods Appl Mech Eng* 384. <https://doi.org/10.1016/j.cma.2021.113977>
5. Li J, Liu C, Hu H, et al (2021) Analysis of elasto-plastic thin-shell structures using layered plastic modeling and absolute nodal coordinate formulation. *Nonlinear Dynamics* 105(4). <https://doi.org/10.1007/s11071-021-06766-9>
6. Ilyushin A (1948) Plasticity. GITL, Moscow, Leningrad ((in Russian))
7. Bieniek MP, Funaro JR (1976) Elasto-plastic behavior of plates and shells. Tech. rep, Weidlinger Associates New York
8. Crisfield M (1981) Finite element analysis for combined material and geometric nonlinearities. In: *Nonlinear finite element analysis in structural mechanics*. Springer, pp 325–338
9. Zeng Q, Combescurie A, Arnaudéou F (2001) An efficient plasticity algorithm for shell elements application to metal forming simulation. *Comput Struct* 79(16):1525–1540. [https://doi.org/10.1016/S0045-7949\(01\)00032-3](https://doi.org/10.1016/S0045-7949(01)00032-3)
10. Dujc J, Brank B (2008) On stress resultant plasticity and viscoplasticity for metal plates. *Finite Elem Anal Des* 44(4):174–185. <https://doi.org/10.1016/j.finel.2007.11.011>
11. Dujc J, Brank B (2012) Stress resultant plasticity for shells revisited. *Comput Methods Appl Mech Eng* 247–248:146–165. <https://doi.org/10.1016/j.cma.2012.07.012>
12. Kocbay E, Vetyukov Y (2021) Stress resultant plasticity for plate bending in the context of roll forming of sheet metal. *Int J Numer Methods Eng* 122(18):5144–5168. <https://doi.org/10.1002/nme.6760>
13. Kocbay E, Scheidl J, Riegler F et al (2023) Mixed Eulerian-Lagrangian modeling of sheet metal roll forming. *Thin-Walled Structures* 186:110662. <https://doi.org/10.1016/j.tws.2023.110662>
14. Heislitz F, Livatyali H, Ahmetoglu MA, et al (1996) Simulation of roll forming process with the 3-D FEM code PAM-STAMP. *J Mater Process Technol* 59(1):59–67. [https://doi.org/10.1016/0924-0136\(96\)02287-X](https://doi.org/10.1016/0924-0136(96)02287-X), selected Papers on Metal Forming and Machining
15. Bui Q, Ponthot J (2008) Numerical simulation of cold roll-forming processes. *J Mater Process Technol* 202(1):275–282. <https://doi.org/10.1016/j.jmatprotec.2007.08.073>
16. Vetyukov Y, Gruber P, Krommer M (2016) Nonlinear model of an axially moving plate in a mixed Eulerian-Lagrangian framework. *Acta Mechanica* 227:2831–2842. <https://doi.org/10.1007/s00707-016-1651-0>
17. Vetyukov Y, Gruber P, Krommer M et al (2017) Mixed Eulerian-Lagrangian description in materials processing: deformation of a metal sheet in a rolling mill. *Int J Numer Methods Eng* 109(10):1371–1390. <https://doi.org/10.1002/nme.5314>
18. Donea J, Huerta A, Ponthot JP, et al (2004) Arbitrary Lagrangian-Eulerian methods. In: Stein E, de Borst R, Hughes T (eds) *Encyclopedia of computational mechanics*, vol 1: Fundamentals. Wiley, Ltd, chap 14
19. Crutzen Y, Boman R, Papeleux L, et al (2016) Lagrangian and arbitrary Lagrangian Eulerian simulations of complex roll-forming processes. *Comptes Rendus Mécanique* 344(4):251–266. <https://doi.org/10.1016/j.crme.2016.02.005>, computational simulation of manufacturing processes
20. Han S (2023) Configurational forces and ALE formulation for geometrically exact, sliding shells in non-material domains. *Comput Methods Appl Mech Eng* 412:116106. <https://doi.org/10.1016/j.cma.2023.116106>
21. Scheidl J, Vetyukov Y (2020) Steady motion of a slack belt drive: dynamics of a beam in frictional contact with rotating pulleys. *J Appl Mech* 87(12). <https://doi.org/10.1115/1.4048317>, 121011
22. Scheidl J, Vetyukov Y, Schmidrathner C et al (2021) Mixed Eulerian-Lagrangian shell model for lateral run-off in a steel belt drive and its experimental validation. *Int J Mech Sci* 204:106572. <https://doi.org/10.1016/j.ijmecsci.2021.106572>
23. Eliseev VV, Vetyukov YM (2010) Finite deformation of thin shells in the context of analytical mechanics of material surfaces. *Acta Mechanica* 209(1–2):43. <https://doi.org/10.1007/s00707-009-0154-7>
24. Vetyukov Y (2014) *Nonlinear mechanics of thin-walled structures: asymptotics, direct approach and numerical analysis*. Springer Sci Bus Media
25. Lubliner J (2008) *Plasticity theory*. Dover Publications, Inc
26. Hu Q, Li X, Chen J (2018) On the calculation of plastic strain by simple method under non-associated flow rule. *Eur J Mech-A/Solids* 67:45–57. <https://doi.org/10.1016/j.euromechsol.2017.08.017>
27. Crisfield M, Peng X (1992) Efficient nonlinear shell formulations with large rotations and plasticity. *DRJ Owen et al Computational plasticity: models, software and applications, Part 1:1979–1997*
28. Mohammed AK, Skallerud B, Amdahl J (2001) Simplified stress resultants plasticity on a geometrically nonlinear constant stress shell element. *Comput Struct* 79(18):1723–1734. [https://doi.org/10.1016/S0045-7949\(01\)00095-5](https://doi.org/10.1016/S0045-7949(01)00095-5)
29. Bogner FK, Fox RL, Schmit LA (1965) The generation of interelement compatible stiffness and mass matrices by the use of interpolation formulae. In: *Proc. Conf. Matrix Methods in Struct. Mech.*, Airforce Inst. Of Tech., Wright Patterson AF Base, Ohio
30. Eisenträger S, Kiendl J, Michaloudis G et al (2022) Stability analysis of plates using cut Bogner-Fox-Schmit elements. *Comput Struct* 270:106854. <https://doi.org/10.1016/j.compstruc.2022.106854>
31. Mueller C, Gu X, Baeumer L, et al (2014) Influence of friction on the loads in a roll forming simulation with compliant rolls. In: *Material forming ESAFORM 2014, key engineering materials*, vol 611. Trans Tech Publications Ltd, pp 436–443. <https://doi.org/10.4028/www.scientific.net/KEM.611-612.436>
32. Paralikas J, Salonitis K, Chryssoulouris G (2009) Investigation of the effects of main roll-forming process parameters on quality for a V-section profile from AHSS. *Int J Adv Manuf Technol* 44(3):223–237. <https://doi.org/10.1007/s00170-008-1822-9>
33. Bhattacharyya D, Smith P, Yee C et al (1984) The prediction of deformation length in cold roll-forming. *J Mech Work Technol* 9(2):181–191. [https://doi.org/10.1016/0378-3804\(84\)90004-4](https://doi.org/10.1016/0378-3804(84)90004-4)
34. Lindgren M (2007) An improved model for the longitudinal peak strain in the flange of a roll formed U-channel developed by FE-analyses. *Steel Res Int* 78(1):82–87. <https://doi.org/10.1002/srin.200705863>

**Publisher's Note** Springer Nature remains neutral with regard to jurisdictional claims in published maps and institutional affiliations.



# Emin Kocbay

Curriculum Vitae

## Contact

2340 Mödling, Austria  
[e.kocbay@gmx.at](mailto:e.kocbay@gmx.at)

## Education

**AHS Keimgasse**  
*High school* 2003-2007

## Personal profile

DOB: 22<sup>nd</sup> March, 1992  
Military Service: 2012

**BHS HTL Mödling**  
*High school* 2007-2012

## Languages

German, English, Turkish

### TU Wien

*Bachelor Program Mechanical Engineering* 2013–2018

Thesis: Influence of Micropillar Shape and Layer Configuration on the Stress State Caused by Compression Tests on Micropillars of Circular Cross Section

## Computer literacy

Math: Mathematica,  
Matlab

Typesetting: L<sup>A</sup>T<sub>E</sub>X, TikZ,  
pgfplots, MS-Office

Programming: F#,  
Python

FEM: Abaqus

CAD: Catia

### TU Wien

*Master Program Mechanical Engineering* 2018–2019

Thesis: Mechanical model to predict the shaft stiffness of a roll stand

### TU Wien

*Doctoral Program Technical Sciences* 2019–2023

Thesis: Stress resultant plasticity model and mixed kinematic description in roll forming simulations

## Expertise

Structural mechanics,  
Finite Element Method,  
Analytical Mechanics,  
Metal plasticity

## Experience

### TU Wien, Institute of Mechanics and Mechatronics

*Research Assistant* 2019–2023

Research Group: Mechanics of Solids

### TU Wien, Institute of Mechanics and Mechatronics

*Tutor* 2016–2019

Courses on mechanics

### Knorr-Bremse Mödling, Assembly Brake-Control

*Working Student* 2016–2019

Implementing test protocols and working instructions